JIME - The Exoplanet Ionospheric Model

A. D. C. Williams

Submitted for the Degree of *Doctor of Philosophy*

Department of Physics and Astronomy

University College London

November 23, 2004

ProQuest LLC
789 East Eisenhower Parkway
P.O. Box 1346
Ann Arbor, MI 48106-1346

Acknowledgements

Huge and thunderous thanks must go to **Steve Miller**, my supervisor and enemy of Austria, **Alan Aylward**, head of APL and knower of all things atmospheric, **Callum Wright**, HiPerSPACE manager, provider of unlimited disk space and Linux fan (hoorah!), **George Millward**, an atmospheric modeller beyond the ken of mortal man, **Tom Stallard**, who seems to know a lot about spectroscopy, despite which he seems remarkably cheerful. All of whom have, in various ways, nudged, forced or hauled this thesis towards its conclusion.

Also great and deafening thanks to all the occupants of APL who made life at APL enjoyable, **PPARC** for giving me lots of money and assorted family members for the same reason.

Finally, thanks go to **Imogen** for showing me my true station in life.

Typeset using LaTeX

JIME *Jim"my*, n.; pl. *Jimmies. Cf. Jemmy.*

n : A short crowbar used by burglars in breaking open doors. A numerical model of exoplanet ionospheres.

v : to move or force, esp. in an effort to get something open; "The burglar jimmied the lock", "Raccoons managed to pry the lid off the garbage pail" syn: pry, prise, prize, lever

As an adolescent I aspired to lasting fame, I craved factual certainty, and I thirsted for a meaningful vision of human life - so I became a scientist. This is like becoming an archbishop so you can meet girls.

M. Cartmill

Abstract

Recent discoveries in the field of planetary astronomy have yielded a large number of Jupiter-mass planets orbiting main sequence stars such as the sun. A significant number of these are what as known as *51-Peg* type planets, whose primary characteristics are their very small orbital radii (0.1AU or less), tidally locked rotation period and circularised orbits.

This thesis describes the modifications made to JIM, the University College London Jovian Ionospheric Model in order to simulate the upper atmospheric conditions that may be expected to exist in a 51-Peg planet, notably the addition of H_3^+ cooling and stability improvements.

Modelling simulations using the new **JIME** have determined that the subsolar H_3^+ column density for a 51-Peg planet are two orders of magnitude greater than on Jupiter with a corresponding increase in H_3^+ cooling, leading to the conclusion that the upper atmosphere temperature will be lower than expected. This has consequences for both planetary detection due to infrared radiation emission and survivability due to atmospheric evaporation.

Contents

Chapter 1

Introduction

The research conducted for this thesis has used as its base JIM, the Jovian Ionospheric Model (Achilleos et al., 1998) developed by the Atmospheric Physics Group at University College London. The model itself will be discussed in Chapter 3, but as an introduction it is important to understand the physical laws upon which it is based. This chapter will lay out the basic laws of atmospheric physics, then going on to focus upon the specific characteristics of the Jovian system, such as the magnetosphere and specific chemistry.

1.1 Atmospheric Structure

A typical atmosphere is divided up into several distinct regions, depending on their chemical properties, dominant physical processes and temperature gradients. These regions are broadly comparable between planets and a diagram showing the vertical structure of Jupiter's atmosphere may be seen in Figure 1.1.

The troposphere in the case of a terrestrial planet is heated by the ground and consists of a region of convective mixing; hot air parcels rise into cooler air. Above the tropopause the temperature gradient inverts due to ozone heating, stabilising

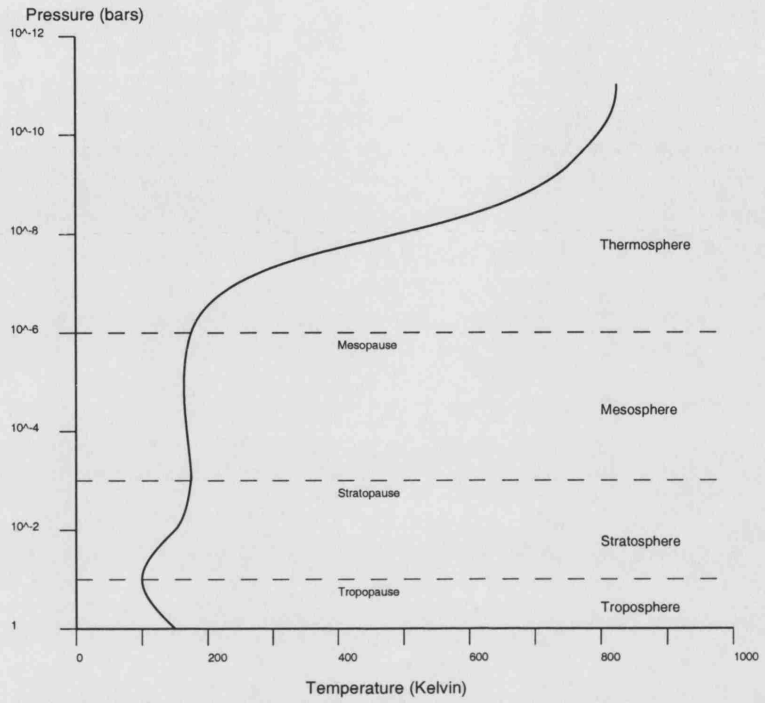

Figure 1.1: Temperature profile for Jupiter's atmosphere showing layer and boundary names.

convection in a region known as the stratosphere. In the Earth's atmosphere this region is heated by ozone molecules absorbing ultraviolet radiation.

Above the stratopause lies the mesosphere. In this region the temperature gradient is again negative with height in Earth's atmosphere, and broadly constant in the case of Jupiter. Beyond the mesopause lies the Thermosphere, so called because the temperature rises dramatically due to absorption of solar extreme ultraviolet (EUV) radiation. In this region on Earth the atmosphere becomes stratified according to molecular mass due to gravitational separation above the homopause which marks the boundary between the homosphere, where the atmosphere is well mixed, and heterosphere with the individual gasses separate due to diffusion. The final region, the Exosphere has little significance in atmospheric dynamics and is regarded as a transition region between atmosphere and space.

Roughly coincident with the thermosphere is the ionosphere. In this region neutral molecules are ionised by high energy particles and ultraviolet radiation from the sun, forming a highly ionised region extending to high altitudes and merging into a region of space enclosed by low latitude magnetic field lines known as the plasmasphere. Charged particles move under the influence of the Earth's magnetic field and can form current systems extending into the magnetosphere which play a significant part in energy and particle transport.

In order to determine the structure and physical properties of an atmosphere we must define the laws governing the physical processes occurring within that atmosphere. This provides the basic set of equations that can be used to build a model atmosphere.

1.1.1 Effective Temperature

A simple estimate of a planetary temperature in our solar system may be made by assuming that the inwards energy flux due to solar radiation input is equal to the outgoing flux due to infrared emission. This produces an equation of the form

$$4\pi a^2 \sigma T_e^4 = \pi a^2 (1 - A) F / R^2 \tag{1.1}$$

where the left hand side is the Black Body emission and the right hand side is the absorbed solar radiation. Here a is the radius of the planet at distance R AUs, F is the solar flux in Wm^{-2} at the surface of the Earth, σ is the Stefan-Boltzmann constant and A is the Albedo, defined as the ratio of reflected to incident solar energy.

Clearly this basic calculation can only be considered an accurate determination of surface temperature for a planet with no significant atmosphere, such as Mercury.

For other terrestrial planets with significant absorbing atmospheres and cloud layers or gas giants with no effective surface this equation has only symbolic value, lacking the ability to describe the variable temperature profile with height. How does one then mathematically define the properties of an atmosphere?

1.1.2 Hydrostatic Equilibrium

The classical simple expression of a model atmosphere is that of a gravitationally bound and spherically symmetric body in hydrostatic equilibrium (Chamberlain, 1978), governed by three relationships. The first, the hydrostatic equilibrium pressure gradient is given by:

$$\frac{dp}{dr} = -\frac{G\mathcal{M}}{r^2}(MN) = -g(r)\rho \tag{1.2}$$

where $\mathcal{M}$ is the planetary mass, M is the mean mass of the molecules in the mixed atmosphere, N is the number density, ρ is the mass density and r is the distance from the centre of the planet.

Secondly, the equation of state is given by the perfect gas law:

$$p = NkT = \rho RT \tag{1.3}$$

where $R = k/M$ is the local gas constant and k=Boltzmann's constant.

The local gas constant is related to the universal gas constant, R_g as follows:

$$R = \frac{R_g}{M} \tag{1.4}$$

Combining 1.2 and 1.3 gives:

$$\frac{dp}{p} = -\frac{dz}{H} \tag{1.5}$$

where z is the height above the surface and

$$H = \frac{kT}{Mg} = \frac{RT}{g} \tag{1.6}$$

which is known as the Pressure Scale Height, defined as the increase in altitude necessary to reduce the pressure by a factor e.

Integrating Equation 1.5 (Houghton, 2002) provides the pressure p at altitude z

$$p = p_0 exp\left\{-\int_0^z \frac{dz}{H}\right\} \tag{1.7}$$

where p_0 is the surface pressure.

1.1.3 Adiabatic Lapse Rate

Assuming a simple model of a planetary atmosphere that is transparent to radiation, it is possible to understand the convective motion of gas by means of considering isolated parcels of atmosphere, defined as having interior pressure equal to the local exterior pressure. Since the parcels are isolated no gas can be exchanged between the parcel and the rest of the atmosphere so as the parcel rises or falls it must expand or contract to equalise pressure.

The act of changing volume alters the temperature of the parcel, which is assumed to occur adiabatically so that the energy exchange is zero. Recalling the first

law of thermodynamics and applying to unit mass we get

$$dq = c_v dT + pdV \tag{1.8}$$

where c_v is the specific heat at constant volume. Since $dq = 0$ as stated above and $\rho = 1/V$, differentiating equation 1.3, the equation of state, gives

$$\begin{aligned} pdV + Vdp &= RdT/M_r \\ &= (c_p - c_v)dT \end{aligned} \tag{1.9}$$

as for a perfect gas $c_p - c_v = R_g/M_r$ where c_p is the specific heat at constant pressure.

Substituting pdV from equation 1.9 in equation 1.8 gives

$$c_p dT - Vdp = dq = 0 \tag{1.10}$$

and substituting dp from equation 1.2 where $dr \equiv dz$ gives

$$\frac{dT}{dz} = -\frac{g}{c_p} = -\Gamma_d \tag{1.11}$$

where Γ_d is known as the *Dry Adiabatic Lapse Rate* which generally has the units $K\,km^{-1}$ and describes the rate at which rising air cools due to natural expansion, and therefore the local temperature gradient. More specifically this is the *Dry* adiabatic lapse rate where an alternate case known as the *Saturated* adiabatic lapse rate describes the temperature change of a saturated parcel of air and has to take into account the condensation of water and the associated change of latent heat.

Consider that the weight of a parcel of air with volume V and density ρ has

weight ρVg then the upwards force due to the displacement of surrounding air with density ρ' is $\rho' Vg$. The *net buoyant force F per unit mass* is

$$F = \frac{(\rho' - \rho)g}{\rho} \tag{1.12}$$

which can be written as

$$F = (T - T')g/T' \tag{1.13}$$

where T and T' are the temperatures of a parcel or air and the surrounding air respectively.

Examining the adiabatic lapse rate allows one to examine the stability to vertical motion of our parcel of air depending on the temperature gradient of the local atmosphere. The lapse rate of the air surrounding the parcel, Γ_a, is defined as (Exell, 2001)

$$\Gamma_a = -\frac{dT'}{dz} \tag{1.14}$$

where T' is the temperature of the surrounding atmosphere.

Therefore suppose $\Gamma_a < \Gamma_d$. Initially $T = T'$. After an upwards displacement $T < T'$, and the buoyancy force on the air parcel is downwards. After a downwards displacement $T > T'$, and the buoyancy force is upwards so this condition is stable. If $\Gamma_a > \Gamma_d$ the opposite situation occurs so this condition is unstable. Finally if $\Gamma_a = \Gamma_d$ the condition is neutral.

Adiabatic lapse rate therefore represents the largest negative temperature gradient that the atmosphere can support and still remain stable to convection.

1.1.4 Radiative Equilibrium

Analogous to Hydrostatic Equilibrium is Radiative Equilibrium which, balancing the radiative emission and absorption, defines the temperature of the atmosphere at a certain point, assuming the atmosphere is vertically static. This situation may be regarded as appropriate when convection and conduction are negligible.

The following section will define the conditions for radiative equilibrium in a *Grey* atmosphere, a somewhat simplified model which allows for a constant average level of absorption with no dependence on wavelength.

Lambert's law states that, in a plane-parallel atmosphere provided that the pressure, temperature and composition are held constant, extinction due to radiation of intensity I traversing an elementary section of atmosphere of thickness dz is proportional to the mass of the absorber ρdz in unit cross-section and to the incident intensity of the radiation. Written mathematically this becomes

$$dI = -Ik\rho dz \tag{1.15}$$

where k is the absorption coefficient. The integral form of Equation 1.15 is

$$I = I_o exp\left(-\int k\rho dz\right) \tag{1.16}$$

where $exp(-\int k\rho dz)$ is known as the fractional transmission τ of the path and $\int k\rho dz$ is the optical path, χ, or optical depth when measured down from the top of the atmosphere.

This section of atmosphere will also emit radiation which, assuming Thermodynamic Equilibrium, may be determined by the application of Kirchhoff's law which results in $\kappa\rho dz B(T)$ Joules per unit area, where $B(T)$ is the black-body emission

per unit solid angle per unit area of a surface at temperature T. From the Stefan-Boltzmann law, the integral of B(T) over a hemisphere is proportional to T^4:

$$\int_{2\pi} BdScos\theta d\omega = \sigma T^4 dS \tag{1.17}$$

Solving this results in

$$B = \pi^{-1}\sigma T^4 \tag{1.18}$$

where σ is the Stefan-Boltzmann constant and dw is an element of solid angle at an angle θ to the normal to the element of surface area dS.

As stated above we have assumed Thermodynamic Equilibrium for our atmosphere, which requires that the kinetic temperature is equal to the Planckian temperature used in Kirchhoff's law. This is generally not the case in real atmospheres but it can usually be assumed to be a good approximation if you exclude extreme conditions such as those found in the rarefied upper atmosphere, where departures from equilibrium have to be taken into account (Yelle and Miller, 2004). This local assumption is known as Local Thermodynamic Equilibrium has been taken to be sufficiently accurate for the purposes of the JIM model. Whether it applies in the extreme conditions in the upper thermosphere of a hot exoplanet where collision rates are low must be doubtful. In this case the molecular energy levels may deviate significantly from the LTE case. The significance of this has been investigated by Kim et al. (1992) who calculated that that $H_2(v = 4)$ population was significantly enhanced above $0.5\,\mu bar$, leading to a greater formation rate of H_2^+, and therefore H_3^+. The significance of this in the context of exoplanets has yet to be investigated.

Now introducing Schwarzschild's Law of Radiative Transfer (Farrell, 2002)

through the slab of atmosphere:

$$dI = -Ik\rho dz + Bk\rho dz \tag{1.19}$$

where the first component on the right hand side corresponds to the absorption due to the atmosphere and the second component is the emission. This equation described the net rate at which the intensity of a pencil of radiation changes in the dz direction.

Recalling the definition of χ, the optical depth allows Equation 1.19 to be rewritten as

$$\frac{dI}{d\chi} = I - B \tag{1.20}$$

This derivation assumes the simplified case of vertically upward and downward streams of radiation, $F^{\uparrow}$ and $F^{\downarrow}$, ignoring all radiation that is not travelling perpendicularly to the surface of the planet. This is known as the *Two-Stream Approximation.* Detailed analysis shows that this can account for the non-perpendicular radiation by replacing the optical depth with a commonly accepted 5/3 increase (ie $dz = (5/3)dz$) in the radiative transfer equations, replacing B with πB and replacing I with F.

Now, assuming infrared radiation is the only method of energy transfer and assuming a lower temperature boundary condition to be that of the surface, T_g

$$\rho c_p \frac{dT}{dt} = \frac{d}{dz}(F^{\downarrow} - F^{\uparrow}) \tag{1.21}$$

where c_p is the specific heat at constant pressure and dT/dt is the net rate of

temperature change. Assuming a constant net flux, ϕ

$$\phi = F^{\uparrow} - F^{\downarrow} \tag{1.22}$$

Applying the conditions for the two-stream approximation to the radiative transfer equation 1.20 to the two directions of flux results in

$$\begin{aligned} \frac{dF^{\uparrow}}{d\chi^*} &= F^{\uparrow} - \pi B \\ -\frac{dF^{\downarrow}}{d\chi^*} &= F^{\downarrow} - \pi B \end{aligned} \tag{1.23}$$

where χ^* denotes that the 5/3 factor has been applied to the optical depth. Setting

$$\psi = F^{\uparrow} + F^{\downarrow} \tag{1.24}$$

allows Equation 1.23 to be rewritten as

$$\frac{d\psi}{d\chi^*} = \phi \tag{1.25}$$

$$\frac{d\phi}{d\chi^*} = \psi - 2\pi B \tag{1.26}$$

Since ϕ is a constant then Equation 1.26 becomes

$$\psi = 2\pi B \tag{1.27}$$

which on substitution into Equation 1.25 gives

$$2\pi B = \phi\chi^* + constant \tag{1.28}$$

To determine the value of this constant we consider the boundary condition $F^{\downarrow}$

where $\chi^* = 0$ which exists at the top of the atmosphere. From Equations 1.22 and 1.24 it can be seen that here $\phi = \psi$ and substituting into Equation 1.28 reveals that the constant value is equal to ϕ.

Hence

$$B = \frac{\phi}{2\pi}(\chi^* + 1) \tag{1.29}$$

At the base of the atmosphere $\chi^* = \chi_0^*$ and $F^{\uparrow} = \pi B_g$ where B_g is the black body function of ground temperature. The black body function for the temperature at the lower boundary of the atmosphere is

$$B_g - B_0 = \frac{\phi}{2\pi} \tag{1.30}$$

where B_0 is the black body function of air close to the ground.

Figure 1.2 shows the black-body function, B, plotted against χ^* and figure 1.3 shows the equivalent in terms of height and temperature. The latter plot shows that in radiative-convective equilibrium the temperature distribution is represented by the adiabatic curve at low altitudes, becoming a purely radiative solution at high altitudes.

The upper boundary of the atmosphere is radiating at a constant temperature known as the *Skin temperature.* Comparing this relatively simplistic model to Earth's atmosphere it is notable how the model appears to predict the convective nature of the troposphere and the static stability of the stratosphere.

1.2 Numerically Modelling an Atmosphere

Any time-dependent numerical model of an atmosphere must include the equations describing the dynamic and chemical processes ongoing in that atmosphere. What

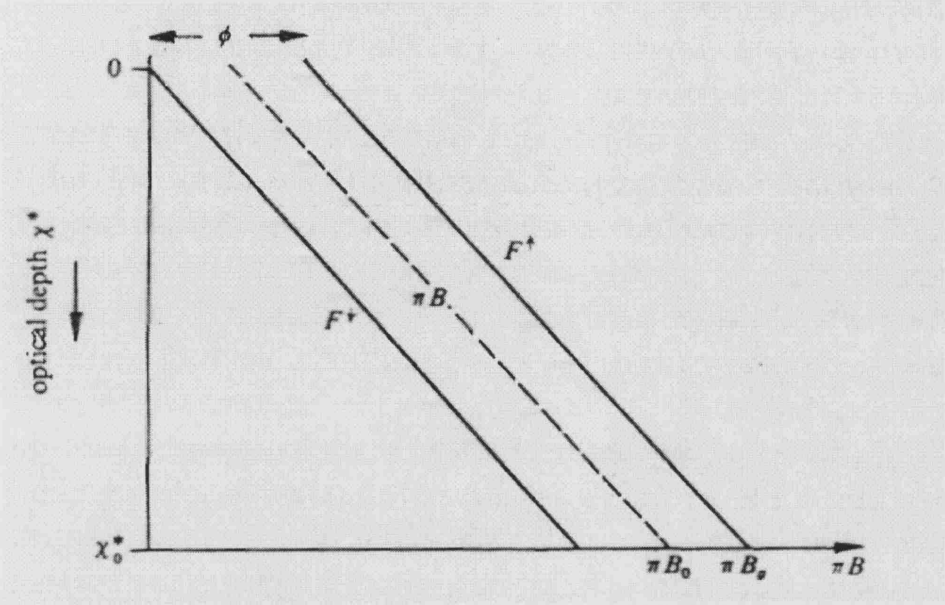

Figure 1.2: Upwards and downwards radiation flux and black body function πB at atmospheric temperature plotted against optical depth for a radiative equilibrium atmosphere (Houghton, 2002)

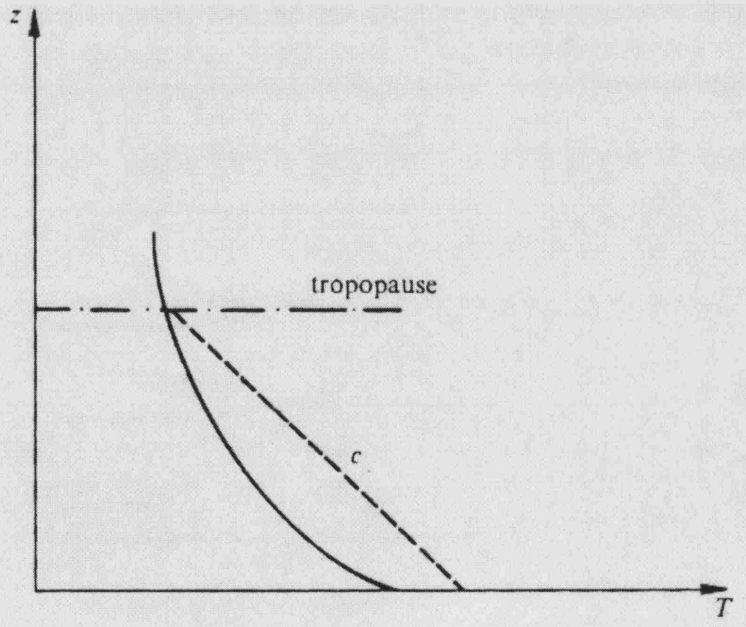

Figure 1.3: Radiative equilibrium temperature plotted against altitude. The dashed line shows an adiabatic solution continuing to an altitude where the radiative solution is convectively stable and below which convection dominates.

equations are included depends on what one is choosing to model and which physical processes one chooses to include. For each *tick* of the model clock the particular equations have to be solved for each element of atmosphere. The more detailed the model, the smaller the atmospheric elements that make it up, reducing the coarseness of the granularity, and the more physical processes solved for each element. Clearly there must be a trade-off between time and detail.

No matter which processes one chooses to include in a model atmosphere there are some basic equations that define the structure of the atmosphere and the physical and energy balances occurring in it. A short description of these main processes and their application follows. [1]

1.2.1 Continuity

The continuity equation is the law of conservation of mass that describes the net flux of particles through a surface. Consider an infinitesimal volume $\Delta x \Delta y \Delta z$ (Fuller-Rowell, 1982). The mass inflow to the x face is

$$\rho U_x \Delta y \Delta z \tag{1.31}$$

where ρ is the density and U_x is the x component of velocity. The corresponding outflow from the opposite face is

$$\left[\rho U_x + \frac{\delta}{\delta x}\rho U_x\right] \Delta y \Delta z \tag{1.32}$$

[1]Partially obtained from an Ionosphere modelling course presented by George Millward of the Atmospheric Physics Laboratory, University College London.

The difference between inflow and outflow per unit volume is

$$-\frac{\delta}{\delta x}\rho U_x \tag{1.33}$$

which represents the x contribution to the local rate of density change. In three dimensions this becomes

$$\frac{\delta\rho}{\delta t} = -\nabla\rho\underline{V} \tag{1.34}$$

for the case of a compressible fluid.

1.2.2 Momentum

The atmosphere can be considered to act as the flow of an incompressible fluid. The thermosphere, which is modelled by JIME, is more complex in that it is highly ionised and pervaded by a magnetic field which separates the motion of the neutral and ionic species and introduces a frictional ion drag on the neutral component. The neutral momentum equation is described by Fuller-Rowell (1982) in respect to the thermospheric model upon which JIME is based and was in turn developed from formulations by Rishbeth (1972):

$$\frac{d\underline{V}}{dt} = -2\underline{\Omega}\wedge\underline{V} + \underline{g} - \frac{1}{\rho}\nabla P + \frac{1}{\rho}\nabla\cdot(\mu_m\nabla)\underline{V} - \nu_{ni}(\underline{V}-\underline{U}) \tag{1.35}$$

In equation 1.35 $\underline{V}$ and $\underline{U}$ are the neutral wind and ion drift velocities in $m\,s^{-1}$, $\underline{g}$ is the gravitational acceleration, $\underline{\Omega}$ is the planetary angular velocity (s^{-1}), ρ is the neutral density ($kg\,m^{-2}$), P is the pressure ($kg\,m^{-2}$), ν_{ni} is the effective collision frequency for momentum transfer to ions, μ_m is the molecular coefficient of viscosity and ∇ is the del operator.

The above equation contains contributions due to

dV/dt, the Inertial term,

$(2\underline{\Omega} \wedge \underline{V})$, the Coriolis term,

$(1/\rho)\nabla\ P$, the Pressure Gradient term,

$(1/\rho)\nabla \cdot\ (\mu_m \nabla)\underline{V}$, the Viscous Drag term, and

$\nu_{ni}(\underline{V} - \underline{U})$, the Ion Drag term.

1.2.3 Energy

The third of the major equations used in the model, the energy equation, describes the balance of energy processes on an element of gas (Peters, 2001),(Fuller-Rowell, 1982):

$$\frac{d}{dt}(\epsilon + \Phi) = -\frac{1}{\rho}\underline{V} \cdot \nabla\ P + \underline{V} \cdot \underline{F} + \dot{Q} + \frac{1}{\rho}\frac{dP}{dt} \tag{1.36}$$

where

$$\epsilon\ = C_p T + \frac{1}{2}\underline{V} \cdot \underline{V} \tag{1.37}$$

is known as the enthalpy, the sum of the internal and kinetic energy, Φ is the potential energy per unit mass, $\dot{Q}$ represents the sum of energy sources and sinks, such as stellar UV input and H_3^+ cooling. The first two terms on the right hand side in equation 1.36 represent the rate of change of kinetic energy per unit mass, including the effects of viscosity and ion drag and the final term represents the work done on the gas.

1.3 H_3^+

It is important at this stage to provide information on the molecular ion H_3^+, knowledge of which will prove invaluable later in this thesis. H_3^+ is one of the major ionic components in the JIM atmosphere and additional use of its unique properties

was used in the expanded JIME to provide a more realistic process of atmospheric cooling.

H_3^+ is the simplest of all polyatomic molecules, consisting of just 3 hydrogen atoms in a high symmetry equilateral triangle configuration (McCall, 2000). It was first discovered in 1911 by J.J. Thomson using a primitive mass spectrometer.

After decades of research it was concluded that H_3^+ had no stable electronically excited states and that its only sharp spectrum would be the vibrational-rotational spectrum in the infrared (Oka, 2000). The first laboratory observation of the infrared v_2 band was achieved by Takeshi Oka in 1980 (Oka, 1980) and since that time it has proved to be an invaluable observational probe for both the astronomer and the planetary scientist.

1.3.1 H_3^+ in interstellar space

For the astronomer it is found in dense molecular clouds, a product of cosmic-ray ionisation of H_2 and the following efficient ion-molecule reaction (Pan and Oka, 1986).

$$H_2 + H_2^+ \rightarrow H_3^+ + H \tag{1.38}$$

It is then destroyed primarily as follows (Herbst and Klemperer, 1973):

$$CO + H_3^+ \rightarrow HCO^+ + H_2 \tag{1.39}$$

The above class of efficient protonating reaction is responsible, amongst many others, for the production of abundant molecular ions such as HCO^+ and HNN^+ (Oka, 1981). Hence it can be seen that the detection of H_3^+ in interstellar clouds (McCall et al., 1999) allows us to infer the presence of these ongoing molecular

reactions; an important step towards understanding the processes involved in the evolution of these clouds.

1.3.2 H_3^+ in planetary atmospheres

The first spectroscopic detection of H_3^+ in Jupiter's atmosphere was achieved by a team led by Pierre Drossart of L'Observatoire de Paris in 1989 (Drossart et al., 1989). These observations were taken of Jupiter's southern auroral zone and correspond to the 2μm overtone band. Later observations, initially by Oka & Geballe (1990) achieved detection of the $4\mu m$ fundamental v_2 band of H_3^+. These two regions correspond to infrared wavelengths where Earth's atmosphere is relatively transparent, known as the K-window and L-window respectively, allowing convenient ground-based observations.

Apart from Jupiter H_3^+ has also been discovered in the atmospheres of Saturn (Geballe et al., 1993) and Uranus (Trafton et al., 1993), although at peak intensities some two orders of magnitude lower. It is of interest that despite its smaller size and greater distance from the Sun that emission from Uranus is stronger than Saturn.

H_3^+ is produced by the ionisation of neutral molecular hydrogen followed by the extremely favourable ion-molecule reaction between H_2 and H_2^+ as shown in equation 1.40.

$$\begin{aligned} H_2 + e^- &\rightarrow H_2^+ + e^- + e^- \\ H_2 + hv &\rightarrow H_2^+ + e^- \\ H_2(v \geq 4) + H^+ &\rightarrow H_2^+ + H \\ H_2 + H_2^+ &\rightarrow H_3^+ + H \end{aligned} \tag{1.40}$$

where e^- represents precipitating energetic electrons and $h\nu$ represents solar EUV radiation.

The third term in reaction 1.40 represents the charge exchange reaction between ionised hydrogen and vibrationally excited molecular hydrogen, the rate constant of which is not well constrained. JIM uses the rate constant $k_c = 10^{-14}\, cm^3 s^{-1}$ as described in Achilleos et al. (1998).

In the absence of organic molecules, as in the Jovian atmosphere above the homopause the H_3^+ chemistry is relatively simple, being primarily destroyed by electron capture as follows

$$\begin{aligned} H_3^+ + e^- &\rightarrow H_2 + H \\ &\rightarrow H + H + H \end{aligned} \tag{1.41}$$

in a process known as dissociative recombination. The organic chemistry of H_3^+ is extremely complex and will not be considered in this thesis.

This can also be considered a valid assumption in the case of an exoplanet. The pressure scale height will decrease with increasing atomic mass. Thus, as temperature increases, increasing altitude will reduce higher mass partial pressure over lower mass (ie, H, He). So as the exoplanet warms up the homopause will retreat further below the bottom level of the model.

Reaction 1.41 is very important in that its rate is determined by the density of free electrons, and therefore by extension the level of ionisation of the gas. The greater the ion density, the greater the density of associated free electrons and therefore the shorter the lifetime of H_3^+. As we shall see in chapter 4 as H^+ becomes the dominant ion at the top of the thermosphere, due to its long lifetime and high levels of photoionisation, this can lead to a large pool of free electrons (see equation

1.42) with a corresponding reduction of the H_3^+ ion density, and associated cooling, from what would be expected in isolation.

$$H + hv \rightarrow H^+ + e^- \tag{1.42}$$

This increasing dominance of $[H^+]$ over $[H_3^+]$ with increasing stellar flux has been predicted computationally by Moore et al. (2003), solving the one-dimensional photochemical ion continuity equations

$$\frac{d[n_i^+]}{dt} = P_i - L_i \tag{1.43}$$

where the ion production and loss components, $P_i = A_i[n_i]$ and $L_i = B_i[n_i^+]$ may be due to photoionisation ($A_i = j_i$) or charge-exchange ($A_i = k_i[n_j^+]$), or dissociative recombination ($B_i = \alpha_i[n_e]$) or charge-exchange ($B_i = k_i[n_j]$) respectively. A_i and B_i represent generic production and loss rates (sec^{-1}) for species $[n_i^+]$, j_i is the photoionisation rate (sec^{-1}) of $[n_i]$, k_i is the recombination rate coefficient for a charge exchange reaction between $[n_i]$ and $[n_j^+]$ ($cm^3\, sec^{-1}$), and α_i is the dissociative recombination coefficient for $[n_i^+]$ ($cm^3\, sec^{-1}$). As with JIME, electron density, $[n_e]$ is taken to be the sum of the individual ion densities.

Where changes in electron density are small, equation 1.43 can be solved to get

$$[n_i^+] = [n_i^+]_0 e^{-B_i \Delta t} + P_i/B_i(1 - e^{-B_i \Delta t}) \tag{1.44}$$

Analysis of equation 1.43 reveals that under photochemical equilibrium the densities of H^+ and H_3^+ may be represented by

$$[H^+] \sim \frac{j_3}{k_1} \tag{1.45}$$

and

$$[H_3^+] \sim \{[H_2]/(\alpha_4 + \alpha_5)\} j_2/[n_e] \tag{1.46}$$

where j_2, j_3, k_1, α_4 and α_5 represent the appropriate rate constants as shown in equation 1.47.

$$\begin{aligned}
j_2&: \quad H_2 + h\upsilon \rightarrow H_2^+ + e^- \\
j_3&: \quad H_2 + h\upsilon \rightarrow H^+ + H + e^- \\
k_1&: \quad H^+ + H_2(\upsilon \geq 4) \rightarrow H_2^+ + H \\
\alpha_4&: \quad H_3^+ + e^- \rightarrow H_2 + H \\
\alpha_5&: \quad H_3^+ + e^- \rightarrow 3H
\end{aligned} \tag{1.47}$$

Since j_2 and j_3 scale at the same rate and $[n_e]$ decreases with decreasing solar flux it is predicted that H^+/H_3^+ should also decrease with solar flux.

Moore et al. also examine how variation in the value of the poorly constrained rate constant in the charge exchange reaction producing H_2^+, shown in equation 1.48 can dramatically alter the composition of the atmosphere.

$$H^+ + H_2(\upsilon \geq 4) \rightarrow H_2^+ + H \tag{1.48}$$

A span of 10^4 either side of their chosen value of the rate constant results in a significant difference in the relative densities of H^+ and H_3^+, tipping the balance of dominance from H_3^+ on the high side, to H^+ on the low side. However, this aspect of the work of Moore et al. is beyond the scope of this thesis and is cited in order demonstrate that there is room for improvement in the understanding of the chemical processes ongoing in a model Jupiter.

H_3^+ is of particular interest in the field of exoplanet research because it has

been suggested (Miller et al., 1997), (Miller et al., 2000), (Satoh and Connerney, 1999), (Rego et al., 2000) that the ion may play a major role in atmospheric cooling, with postulated Jovian planet-wide IR emission of the order of 10^{13}W. At infrared wavelengths the dominant atmospheric species, H_2, is a poor radiator due to its lack of either a permanent or vibrational induced dipole moment but the high radiative efficiency H_3^+ makes it the dominant cooling mechanism.

In the 51-Peg region the stellar energy input is some three orders of magnitude greater than at Jupiter, with correspondingly higher levels of EUV input leading to expected greater ion densities; the increase in $[H_3^+]$ being moderated by the increased value of $[e^-]$ as described above. A higher density of H_3^+ should lead to increased levels of cooling, with the result being that the thermospheric temperatures may be considerably lower than predicted. The existence and significance of this enhanced H_3^+ cooling is explored in depth in this thesis.

1.4 Jupiter - A Model Gas Giant

Jupiter is the most massive and closest of the four gas giants in our solar system and the planet which JIM has been designed to model. Considering the structure of the Jovian system will help to understand the processes involved in the model and the potential similarities and differences to the *51-Peg* type exoplanets of the type JIM-E is seeking to simulate.

1.4.1 Atmosphere

Unlike the inner terrestrial planets which consist of a large rocky body with a relatively thin skin of atmosphere the so-called Jovian planets have no solid surface, simply deep gaseous layers increasing in density and temperature down to a hypo-

thetical rock and iron core. Jupiter's atmosphere consists of gases of near-primordial composition with a H:He ratio of approximately 75:25 by mass with trace levels of water and organic compounds.

At the immense pressure of the planet's deep interior hydrogen acts as a metallic liquid consisting of a sea of individual protons and electrons, able to conduct electricity. It is the rapid spin ($\sim$10 hours at the 1 bar region) of the planet that generates the immense magnetic field, greater than 4 Gauss at the equatorial surface, by a process known as hydromagnetic-dynamo action (Smoluchowski, 1971).

Above the metallic region comes a layer of liquid molecular hydrogen thought to extend up to a region where the pressure is of the order of 10 bars, beyond which lies the uppermost regions where the atmosphere is considered to behave as described in section 1.1

Until recently the temperature profile of the upper atmosphere was not well established; occultations observed by the Voyager probes yielded exospheric temperatures greater than expected if solar energy input was the only source of heating. It was not until the Galileo vehicle arrived at Jupiter more than a decade later with its atmospheric entry probe that a more detailed profile could be obtained, plots of which are shown in figures 1.4 and 1.5 (Seiff et al., 1997).

These results were derived from the entry probe deceleration data which yielded an atmospheric density profile allowing pressure and, using the equation of state, temperature to be calculated for a range of predicted exospheric temperatures.

Jupiter's latitudinally banded cloud belts delineate the pattern of zonal winds that dominate the visible atmosphere. The origin of these jets has long thought to be the alternately rising and falling convective cells that give the belts their respective bright and dark colours, although the precise mechanism that could explain strong prograde winds of the order of 100 ms^{-1} had yet to be determined. Recently,

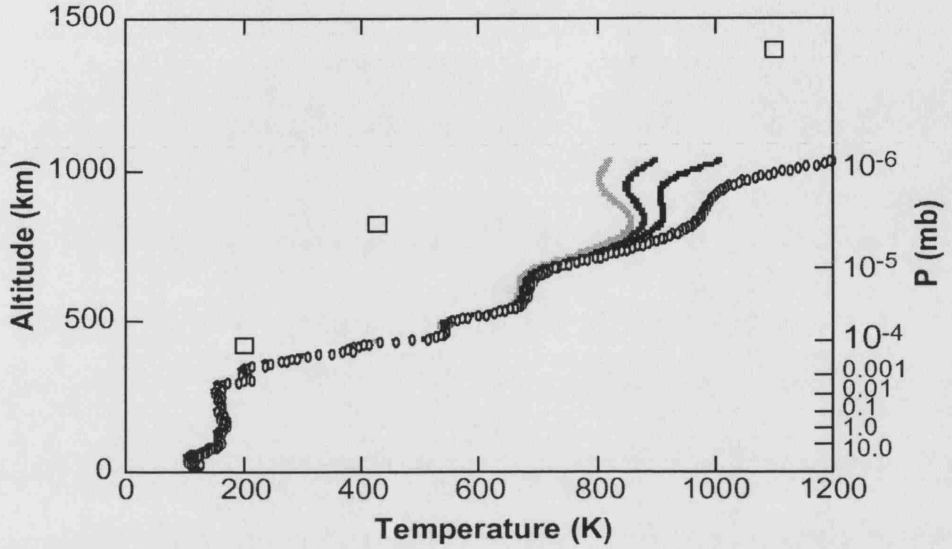

Figure 1.4: Galileo probe derived temperature profiles from the measured density, predicted equation of state and variable initial exospheric temperature. Voyager IRIS results are represented by squares.

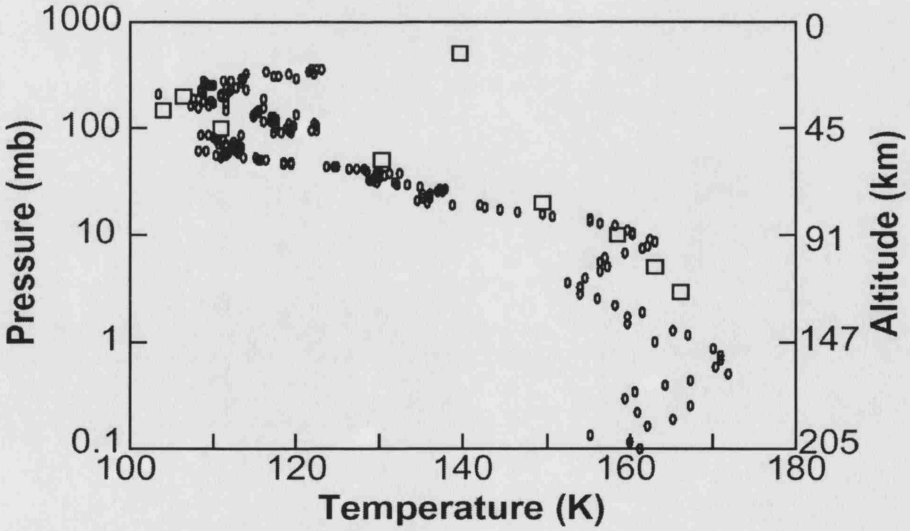

Figure 1.5: Expansion of figure 1.4 around the tropopause region.

however, (Yano et al., 2003) have applied a two-dimensional deep-turbulence model, allowing a convectively well-mixed interior to the problem and report that it predicts the observed wind features well.

1.4.2 Magnetospheric Region

Understandably given the great strength of the Jovian magnetic dipole the magnetosphere of the planet is correspondingly huge; the inner region being large enough to swallow the sun and with a magnetotail extending as far as the orbit of Saturn.

Due to the size of the magnetosphere Jupiter's giant Galilean satellites orbit within a strongly magnetised region. The closest of the four satellites, Io, undergoes strong tidal kneading resulting in internal heating and turning Io into the most volcanic body in the solar system. Gases ejected from the interior either condense back onto the surface or escape into local space, forming a corona and extended neutral gas cloud around the satellite. Neutral species within this cloud are constantly being ionised by interaction with magnetospheric particles, and are consequently brought into corotation with Jupiter's ionosphere due to interaction with the planetary magnetic field. Thus is formed an ionised torus enclosing Io's orbit at $6R_j$ and extending as a flattened plasma sheet out to around $30R_j$ where corotation breaks down (Bagenal, 1992).

Within the magnetospheric region plasma moves under the influence of the Jovian magnetic field. Where the direction of bulk flow of ions and electrons is different a current is set up. The most apparent of these current systems are those which introduce visible effects in Jupiter's atmosphere.

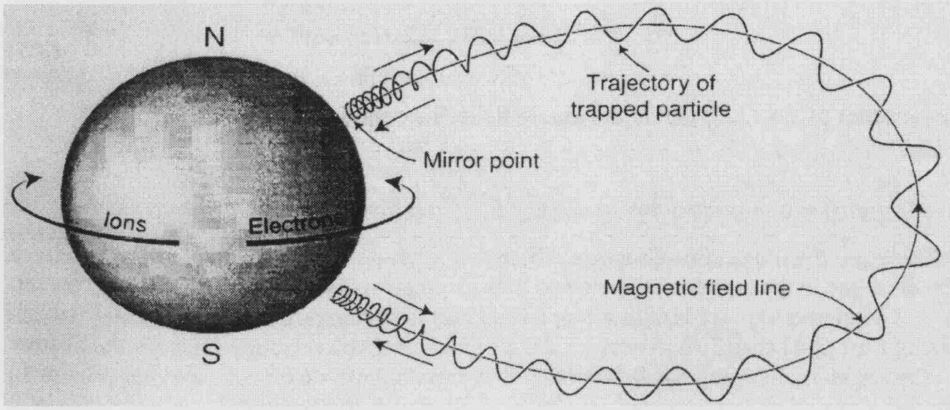

Figure 1.6: Trajectory of a charged particle in a dipolar field (Baumjohann and Treumann, 1997).

1.4.3 Auroral Region

Within what is known as Jupiter's aurorae are a number of separate regions associated with electron precipitation from different parts of the magnetosphere. By examining the auroral structure it is possible to infer the physical processes that cause them. A charged particle in a dipole magnetic field may become trapped and oscillate between the two extreme *mirror points* as shown in figure 1.6.

As can be seen from this diagram the latitude at which ions precipitate into the atmosphere along a particular field line is dependent upon the radius from the centre of the magnetic dipole at which they are injected into the magnetic field.

The *main auroral oval* encircles the magnetic pole at co-latitude $\sim 15°$. Studies of this region by various authors have demonstrated that the main oval couples to the equator beyond $\sim 20R_J$, around the region at which plasma corotation begins to break down (Cowley and Bunce, 2001). This shearing of the plasma sheet induces electric fields caused by the $\mathbf{j} \times \mathbf{B}$ force produced as the sub-corotating plasma moves within the magnetic field. The circuit is completed through the ionosphere by an equatorial-directed current system. Precipitating particles, primarily high energy electrons guided by the Jovian magnetic field, excite neutral atmospheric

species giving rise to bright extreme ultraviolet (EUV) aurorae. Particle ionisation gives rise to such species as H_3^+, which emits strongly in the infrared, detectable as Jupiter's IR aurora.

The other striking auroral signature is produced by Io's progression through the magnetic field, generating an enormous potential which is discharged through a field-aligned current system known as the *Io flux tube.*

The Jovian auroral emission has been an invaluable probe of the chemistry occurring in Jupiter's upper atmosphere. In particular the aforementioned infrared aurora has been widely used to examine the abundance and location of the H_3^+ molecule.

Chapter 2

Exoplanets

The first question to ask when being shown a model of a gas giant in a circular orbit around a main sequence star at 0.1AU is *Why*? Why 0.1AU? Why a gas giant? In order to answer these questions it is necessary to understand how planets end up as they are today. If we look at our solar system we see three small rocky planets, Mercury, Venus and Earth, two gas giants, Jupiter and Saturn and two ice giants, Uranus and Neptune. The latter category contains planets with an icy mantle surrounding a rocky core with only a relatively thin layer of atmosphere above compared to the gas giants. Consensus of opinion is moving towards the theory that Pluto is an irregularity, a visitor from the Kuiper belt possibly disturbed by Neptune's gravitational pull, allowing its disturbing presence to be conveniently ignored.

In this chapter I will be commenting on the present methods of exoplanet detection, exploring the results so far obtained and explaining the current theories of planetary formation and evolution that are required to justify the development of the JIME project and answer the initial question of why this specific configuration of planet is being studied.

2.1 Exoplanet Search Methods

The difficulty in detecting planets exterior to our solar system is demonstrated by the fact that it is only in the last ten years that the field of exoplanet research has existed as a legitimate science, as opposed to speculation. The combination of faintness, distance and atmospheric turbulence had confounded detection until Wolszczan & Frail (1992) detected planetary bodies orbiting the millisecond pulsar PSR1257 + 12.

Despite this boost it was another three years until a planet was detected around a main sequence star like the sun (Mayor and Queloz, 1995), the now legendary *51-Pegasi b* which gave its name to a new class of super hot Jupiters with orbits of 0.1 AU or less.

This section discusses the main planetary detection techniques and some of the problems encountered. A selected listing of some of the more successful current experimental groups may be found in Appendix B, along with some future space-based missions which are currently in planning or under construction. Although the vast majority of planets have been discovered using the Doppler spectroscopy method it was felt that a more general coverage was required in order to understand the difficulties involved in detecting exoplanets and to cover the theories, particularly astrometry and microlensing, that will have a big part to play in future space-based experiments, some of which are already in the planning stage.

2.1.1 Direct Imaging

The most straightforward method of detecting extrasolar planets, at least in principle, is to search for signatures in the image of a selected star. Since planets generally have no intrinsic emission we are only able to detect reflected stellar radiation. The

ratio of planetary to stellar luminosities is (Perryman, 2000)

$$\frac{L_p}{L_\star} = p(\lambda, \alpha) \left(\frac{R_p}{a} \right)^2 \tag{2.1}$$

where λ is a particular wavelength and $p(\lambda, \alpha)$ is a phase dependent function which includes the effects of orbital inclination and takes into account the various sources of scattering in the planetary atmosphere, α is the angle between the star and the observer as seen from the planet, and R_p and a are the planet's size and orbital radius respectively. This equation does not take into account any thermal emission from the planet itself.

Unfortunately, $L_p/L_\star$ is generally extremely small; of the order of 10^{-9} for the Jupiter-Sun system (Schneider, 1999). If this were not discouraging enough, a star observed through a telescope of diameter Δ produces a diffraction peak with an angular radius $\theta = 1.2\lambda/\Delta$ (Schneider, 1999), of a similar order of magnitude to θ_p, where θ_p is the angular distance of the planet from the star. The interference due to the broad diffraction peak at a typical planetary radius tends to swamp the relatively feeble light from the planet and makes direct detection extremely difficult, with integration times required to achieve a satisfactory signal to noise ratio of the order of months for a reasonably sized telescope, effectively unfeasible. The alternative is to use different technologies to attempt to remove the diffraction peak or at least reduce its influence to the point where reasonable integration times are achieved.

Nulling Interferometry

Nulling Interferometry, unlike many of the other methods discussed is potentially sensitive enough to be able to detect Earth-sized planets (Angel and Woolf, 1997).

It uses the principle of superposing the light from multiple telescopes so that the stellar wavefronts interfere destructively, while the planet signal interferes constructively, thus selectively removing the starlight from the image (Hinz et al., 1998). The interferometer is pointed at the star and the distance between the individual telescopes is set so that at the pointing centre light from one instrument is exactly half a wavelength out of step with the other, effectively cancelling out the star. At planetary distance the delay is not exactly half a wavelength and so light from the planet is not nulled. The array is then rotated around the axis, thus providing a modulation for the signal of the planet, which crosses alternately bright and dark fringes (Mennesson and Mariotti, 1997) caused by the varying optical paths through of the array whilst the star remains nulled on axis. The baseline of such an interferometer may be adjusted so that constructive interference occurs at a selected angular radius from the star (Perryman, 2000), thus allowing 'tuning' of the instrument to specific planetary orbital radii. Figure 2.1 demonstrates the layout of the Multiple Mirror Telescope as described by Hinz et al. (1998) used to prove the viability of the nulling process, and figure 2.2 shows the procedure in action.

The most useful wavelength range for the nulling process is the infrared, in which the star is faintest and the planet warmest. This effectively rules out ground-based interferometry where the Earth's atmosphere would dominate the signal. There are a number of space-based projects currently in development, the most promising of which will be discussed in detail in appendix B.

Mennesson and Mariotti summarise the important requirements that a nulling interferometer must have in order to be able to detect extrasolar planetary systems; namely very strong suppression of starlight, good spectral coverage (from 6 to 18 μm) and the ability to distinguish planets from local dust. The spectral range stated above contains the absorption features of water, ozone and carbon dioxide and so

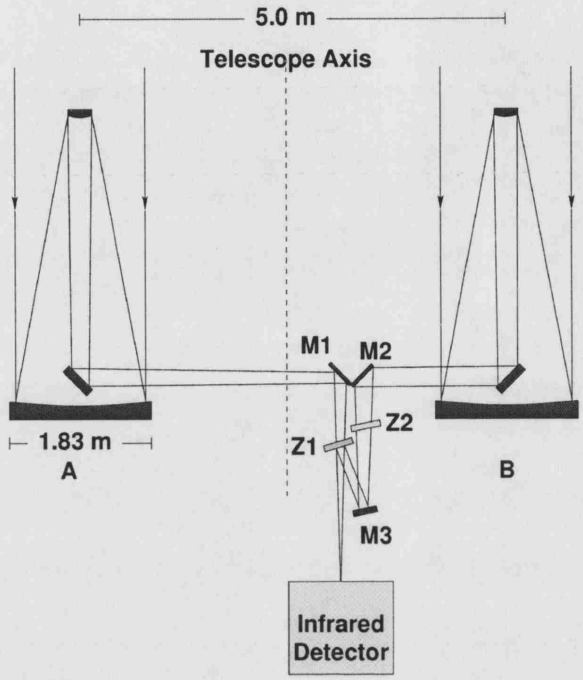

Figure 2.1: Nulling interferometer using the MMT (Hinz et al., 1998). The two telescopes are co-mounted for rigidity. Z1 and Z2 are beam splitters and mirror M3 is used to adjust the light path length.

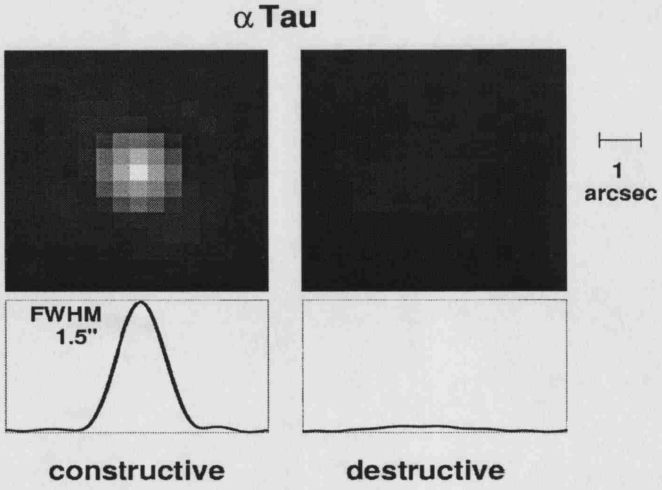

Figure 2.2: Short exposure demonstration of the apparatus shown in figure 2.1 (Hinz et al., 1998).

would provide a great deal of information about the planets under observation. The authors also provide a solution to these requirements that goes beyond the basic two-telescope system and uses five 1.5m telescopes in an elliptical array, 50 by 25m in size.

Adaptive Optics

When observing from the ground atmospheric turbulence introduces random perturbations into the plane wavefront received from an astronomical target, distorting the image. For large telescopes this effectively introduces a limit on the resolution they can achieve, above the maximum diffraction limited resolution they were designed for. This is why telescopes are usually located to be above as much of the atmosphere as possible. Ideally, putting a telescope into space would be the ultimate solution but the cost and weight limit is prohibitive and so a system of adaptive optics have been developed.

An adaptive optics system samples the point spread function (PSF) of a suitably bright guide star or artificial laser-generated object in the frame using a wavefront sensor around 1000 times per second (O'Byrne, 1996), thereby enabling the calculation of an appropriate counter wavefront distortion which both spatially and temporally follows the fluctuations of the original signal (Beckers, 1993). A computer may then deform the primary telescope mirror using numerous actuators located behind the mirror itself to apply the corrected wavefront to the signal, thereby attempting to reproduce the original undistorted wavefront before it entered the atmosphere. This process is known as closed loop adaptive optics.

2.1.2 Dynamical Perturbation

As described by Perryman (2000), a star orbited by a single planet will be seen to undergo elliptical motion about the two-body system barycentre. Considering that the mass of the planet relative to the star is negligible, this motion can be described as a circular orbit with a radius

$$a_\star = a(M_p/M_\star) \tag{2.2}$$

where M_p and $M_\star$ are the masses of the planet and star respectively and a is the orbital separation between the two bodies (Schneider, 1999). Accurate measurement of the motion of the star will therefore describe a regular periodicity, the measurement of which may be used to infer the orbital period of the planet. There are a number of methods in which this measurement may be obtained, descriptions which follow.

Radial Velocity

The observed velocity amplitude K of a star of mass $M_\star$ due to a companion body with mass M_p, orbital inclination $\sin i$ with respect to the observer, orbital period P and eccentricity e(Cumming et al., 1999) is:

$$K = \left(\frac{2\pi G}{P}\right)^{1/3} \frac{M_p \sin i}{(M_p + M_\star)^{2/3}} \frac{1}{(1-e^2)^{1/2}} \tag{2.3}$$

It is important at this point to note why the mass of the companion planet is represented by $M_p \sin i$. Imagine observing a stellar system edge on to the orbital plane of the planet. In this configuration M_p may be accurately determined as the full amplitude of the stellar perturbation is in the radial direction. However, if the system was observed face on then the component in the radial direction would be

zero. The mass of the planet is the same but the radial velocity we see is very different. Since without directly imaging the planet it is impossible to tell the angle of the orbital plane of the system we can only state the minimum mass if we were seeing the system edge on, and the unknown angle, i.

For a circular orbit, the variations in velocity can be considered sinusoidal and since $M_p \ll M_\star$, K is measured as:

$$K = 28.4 \left(\frac{P}{1year}\right)^{-1/3} \left(\frac{M_p \sin i}{M_J}\right) \left(\frac{M_\star}{M_\odot}\right)^{-2/3} ms^{-1} \tag{2.4}$$

where M_J is the mass of Jupiter and P and a, measured in AU, are related by Kepler's third law:

$$P = \left(\frac{a}{1AU}\right)^{3/2} \left(\frac{M_\star}{M_\odot}\right)^{-1/2} year. \tag{2.5}$$

This simple result has extraordinary implications for the field of extrasolar planet detection and much effort has been expended by a number of research groups across the world in order to produce a catalogue of stellar perturbations which can then be individually examined for traces of periodicity.

The most popular method of perturbation detection and indeed extrasolar planet detection in general, the radial velocity method is employed by the majority of research groups and has detected the vast majority of planets.

In order to detect the variance in radial velocity caused by an orbiting planet a spectrograph is generally used. The dispersing element can be either a prism or, as is more likely in the case of astronomical detectors, a diffraction grating. The general equation for diffraction by a grating is(Hollas, 1987)

$$m\lambda = d(\sin i + \sin \theta) \tag{2.6}$$

corresponding to the position of maxima in a diffraction pattern, where i and θ are the angles of incidence and reflection, d is the groove spacing, λ is the wavelength and m is the order of diffraction.

For normal incidence

$$m\lambda = d\sin\theta \tag{2.7}$$

The angular dispersion is

$$\frac{d\theta}{d\lambda} = \frac{m}{d\cos\theta} \tag{2.8}$$

and the resolving power is

$$R = \frac{\lambda}{\Delta\lambda} = mN \tag{2.9}$$

where N is the total number of grooves and $\Delta\lambda$ is the smallest resolvable wavelength difference defined by the Rayleigh criterion, where the maxima of one lies at the first minimum of the other.

Spectral lines from a gas absorption cell, typically containing Iodine or Thorium-Argon are used to provide a fixed reference and the lines from the star are superimposed during the image reduction process, allowing a time-varying redshift signal to be plotted.

2.1.3 Astrometry

An alternative to the radial velocity method of perturbation detection is to observe directly the movement of the target star relative to the stellar background in a process known as Astrometry. The position of a star orbiting a star-planet barycentre

appears projected on the plane of the sky as an ellipse with angular semi-major axis α as given by (Perryman, 2000)

$$\alpha = \frac{M_p}{M_\star}\frac{a}{d} \tag{2.10}$$

where d is in parsecs, a is in AU and M_p and $M_\star$ are in common units.

Clearly α is going to be an extremely small number, even for the closest stars and demands extremely high accuracy from the telescope and detector. For a ground-based visible band experiment using a CCD detector the sources of noise include photon noise, atmospheric noise, sky background noise, uncalibrated differential chromatic refraction, detector noise, uncalibrated geometric errors on the detector and uncalibrated optical aberrations, making an already daunting detection process even more of a challenge. Adaptive optics would reduce the atmospheric noise, as would a space-based telescope, but what are the prospects of success without these luxuries? With the above sources of error in mind Pravdo & Shaklan (1996) set out to examine whether and astrometric extrasolar planet survey could feasibly be attempted with a ground-based telescope. For the purposes of their experiment they used the 5m Palomar telescope to observe the open cluster NGC 2420 using a 2048x2048 pixel CCD. Pravdo & Shaklan determined that for a feasible planet search program, a minimum of 40 nights per year would be necessary in order to obtain sufficient data. The program would be run for 20 years in order to sample a large range of orbital periods. Their experiment yielded astrometric precisions of 0.1 milliarcseconds (*mas*) over periods of minutes in a 90" field of view, which let them to conclude that such a ground-based observation program would yield significant results and would be able to detect the existence of Jovian planets in solar-system-type orbits. This would require considerably more precise instruments than

the detection of close-orbiting planets due to the correspondingly smaller periodic movement induced on the star by the planet.

2.1.4 Photometric Transits

The orbital plane of a planet orbiting its parent star may be orientated at any angle to the observer. If the configuration of a system is such that the angle of the plane is closely aligned with the line of sight, then there is a chance that for a small proportion of its orbit, the planet will pass in front of the star, thus reducing the apparent luminosity of the star by a fractional amount. The reduction in light is in direct proportion to the ratio of the projected areas of the planet to the star as shown (Howell et al., 1999):

$$\frac{\Delta I}{I} = \left(\frac{R_{Planet}}{R_{Star}}\right)^2 \tag{2.11}$$

Associated transit times can be approximated to be

$$t = 13R_{*}\sqrt{\frac{a}{M_{\star}}} \tag{2.12}$$

for the case of a star of identical properties to the Sun where $R_{\star}$ and $M_{\star}$ are the radius and mass of the star in solar units, a is the radius of the planet's orbit in AU and t is the transit time in hours.

This solution assumes that the star has uniform surface brightness. However, as stated by Deeg (1998), the exact shape of the light curve during the transit depends on such phenomenon as the size ratio of the planet and star, the latitude of the transit across the stellar disc, the star's limb darkening and the eccentricity of the planet's orbit. Figure 2.3 demonstrates how the brightness variation evolves for non-zero transit latitude and figure 2.4 shows actual data obtained by Charbonneau

et al. (Charbonneau et al., 2000) from a planet transiting the star HD 209458.

Taking into account the variable properties of the star and the inclination of the orbital plane, the duration of the transit is now given by:

$$t_{tr} = \frac{T_{pl}}{\pi}\left(\frac{R_* \cos(\delta) + R_{pl}}{a_{pl}}\right) \tag{2.13}$$

where δ is the latitude of the transit, R_{pl} is the radius of the planet, a_{pl} is the major halfaxis of the planetary orbit and T_{pl} is the orbital period. T_{pl} may be determined simply by observing repeated transits and calculating the time interval between each ingress.

It is here where one of the significant advantages of the transit method over radial velocity searches is made clear. Whereas radial searches simply allow us to calculate the minimum mass from the obtained period, transit observations provide dramatically more information about the target planet. Deeg suggests that repeated observations of a transit may demonstrate minor fluctuations in T_{pl}, suggesting the existence of further non-transiting planets. In addition, if the radius of the star can be estimated, as would be the case if the spectral classification is known, then the *radius* of the planet may be calculated from equation 2.11. The orbital halfaxis, a_{pl}, may then be derived from Kepler's third law and an estimation of the latitude, δ may be made using equation 2.13. The inclination of the orbital plane of the planet may now be obtained as follows:

$$\cos i = \frac{R_* \sin \delta}{a_{pl}} \tag{2.14}$$

Using the mass estimate of the planet obtained using the radial velocity method and the inclination calculated in equation 2.14, a significantly more accurate determination of the mass may be obtained which, together with the above estimation

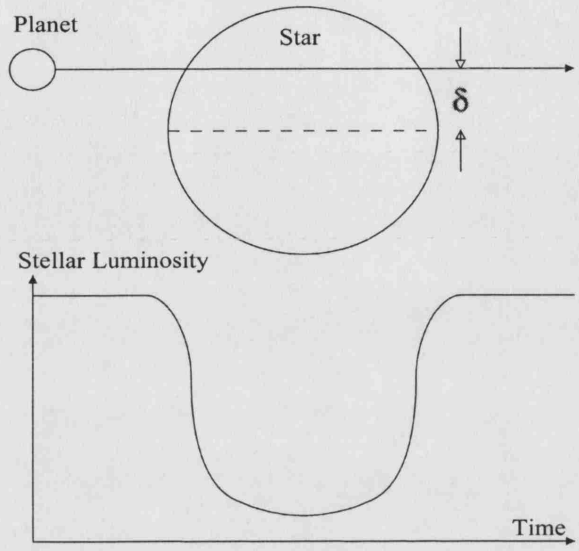

Figure 2.3: Evolution of brightness variation due to a planetary transit. δ is the latitude of the transit and $L_\star$ is the brightness of the star.

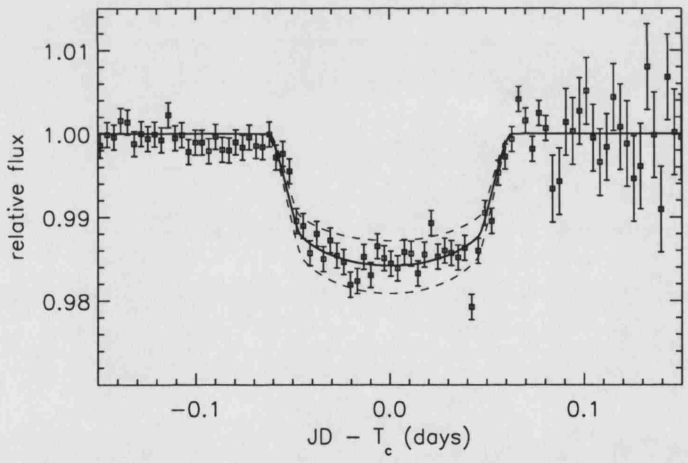

Figure 2.4: Processed photometric data from the star HD 209458 with fitted light curve.

of the radius of the planet allows values to be placed on the planetary density and albedo. Clearly this is of great importance in probing the properties of extrasolar planets and demonstrates how the two methods discussed so far may complement each other.

Giampapa et al. (1995) consider the prospects of detecting an extrasolar planet

using the transit method as follows. For a sample of N stars containing a fraction f_p with at least one planet, a planet may be detected where the angular displacement of the orbital plane from the line of sight is small, allowing a transit to occur. If the allowed angular displacement for a successful transit event is given by $\Delta\theta$, which is simply the fraction of the possible angular inclinations over the total solid angle, then the fraction of such systems with the correct geometry is therefore $\Delta\theta$. The probability of observing such a transit at any given time is the ratio of the transit duration to the orbital period, which can be shown to be $R_s/\pi a$, where R_s is the stellar radius and a is the orbital radius of the planet, assuming a circular orbit. The number of systems with a potentially observable transit at any given time of observation is $n_d = f_p N R_s \Delta\theta/\pi a$ or

$$n_d = \frac{f_p N}{\pi}\left(\frac{R_s}{a}\right)\sin^{-1}\left(\frac{R_s}{a}\right) \tag{2.15}$$

where $\Delta\theta$ is $\sin^{-1}(R_s/a)$.

In the case where $a \gg R_s$,

$$\frac{n_d}{N} = \frac{f_p}{\pi}\left(\frac{R_s}{a}\right)^2 \tag{2.16}$$

From these last two equations it can be seen that the greatest chance of observing a transit occurs in systems containing a large star with a close-orbiting planet, as there is the greatest range of orbital plane angles for which a transit may be viewed, and the frequency of transits is highest.

Comparing the likelihood of detecting a planet for different star/planet mass and separation combinations, for both the transit and Doppler spectroscopy method reveals certain similarities and differences. The transit method favours closely spaced bodies with a high mass (and therefore physically large) star, allowing a larger

range of orbital inclinations in which a transit may occur. Planetary size would not significantly increase this range, but would provide a stronger signal. The Doppler method also favours closely spaced bodies in order for the planet's gravitational influence on the star to be as strong as possible. For this same reason the mass ratio of the two bodies should be as small as possible, i.e. a high mass planet and a low mass star.

Howell et al. (1999) consider that the class of stars that are potential targets for a current transit mission is of significantly wider spectral range. Their simulations based on the development of a low-cost photometric search program, using a Meade LX-200 telescope and 'off the shelf' components suggest that even modest ground based experiments could easily detect transits of a Jupiter-mass planet across a star of spectral type F-M, down to ~13.5 magnitudes. In addition, terrestrial-type planets could theoretically be detected transiting M-dwarfs.

2.1.5 Gravitational Microlensing

As reported by Gould (2001), microlensing occurs when a massive object which shall be known as the lens becomes closely aligned with a more distant object known as the source. General relativity predicts that a lens of mass M will deflect the light from the source by an angle (Gould, 2000)

$$\alpha = \frac{4GM}{r_E c^2} \tag{2.17}$$

where M is the lens mass and r_E is known as the *Einstein Radius*, analogous to the impact parameter of the light ray. Light from the source will therefore be deflected by an angle θ_E from its true position as demonstrated in figure 2.5. If the source and lens are directly aligned then the source image will be detected as a ring,

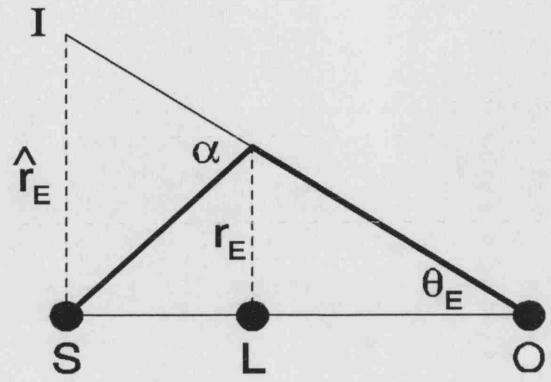

Figure 2.5: Microlensing geometry (Gould, 2001). Bold line is path of light from source, S, past lens, L, to observer, O. The image is displaced from the source by the angular Einstein radius θ_E.

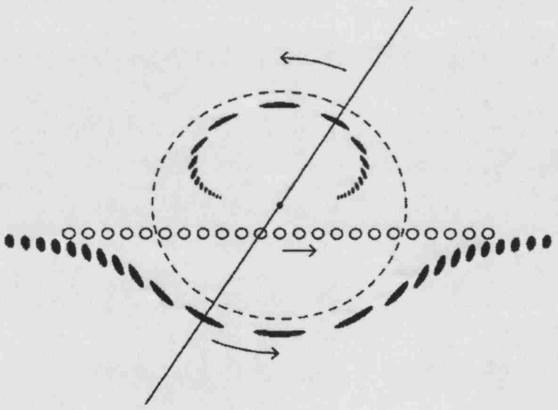

Figure 2.6: Diagram showing the distorted and magnified images (black smudges) of the source (open circle) as it passes behind the lens(central point) (Paczyński, 1996). The Einstein ring is the large dotted circle and the solid line passing through the lens and the source shows which magnified images are associated with it.

known as the Einstein Ring, of size $\hat{r}_E$, the *Projected Einstein Radius.*

If axial symmetry is broken then the ring is broken up into two individual images, one exterior to the Einstein ring and one interior, as shown in figure 2.6.

For such an event, the combined magnification of the two images, A_+ and A_- as a function of time may be calculated to be (Wambsganss, 1997)

$$A = A_+ + A_- = \frac{u(t)^2 + 2}{u(t)\sqrt{u(t)^2 + 4}} \tag{2.18}$$

where $u(t)$ is the projected distance between lens and source at time t (in units of Einstein radius). Clearly demonstrated is the increasing magnification as the two components become more directly aligned. Note that this number is always larger than unity and allows the lensing effect to be demonstrated when the individual components may not be resolvable, a matter of particular interest in the detection of exoplanets.

How, then, does one apply gravitational microlensing to exoplanet detection? In order to understand this we must consider what an event light curve would look like if the lens was not a single body but multiple, such as a planetary system. In the general case of a double lens with the angular separation of the two components being of the order of the individual Einstein rings, it is possible to obtain (Paczyński, 1996) the following equations describing the positions of light rays crossing the source plane at co-ordinates X_s, Y_s under the influence of lens components $m_1(x_1, y_1)$ $m_2(x_2, y_2)$

$$x_s = x - \frac{m_1(x - x_1)}{r_1^2} - \frac{m_2(x - x_2)}{r_2^2} \tag{2.19}$$

$$y_s = y - \frac{m_1(y - y_1)}{r_1^2} - \frac{m_2(y - y_2)}{r_2^2} \tag{2.20}$$

where $x_s = X_s/D_s$, $y_s = Y_s/D_s$, $x = X/D_d$, $y = Y/D_d$, D_s is the source distance, D_d is the deflector (lens) distance and m_1 and m_2 are the individual lens component masses. All except X_s and Y_s are measured in the deflector plane.

Plotting the three-dimensional light paths onto a graph reveals a new feature called a *caustic* created as an artifact of lens astigmatism. When a point source crosses a caustic it undergoes infinite magnification, whereas a source of finite size is magnified by a finite but large amount. The shape of the caustic is determined my the mass ratio and separation of the lens components and determines the form of the light curve produced by a source passing behind.

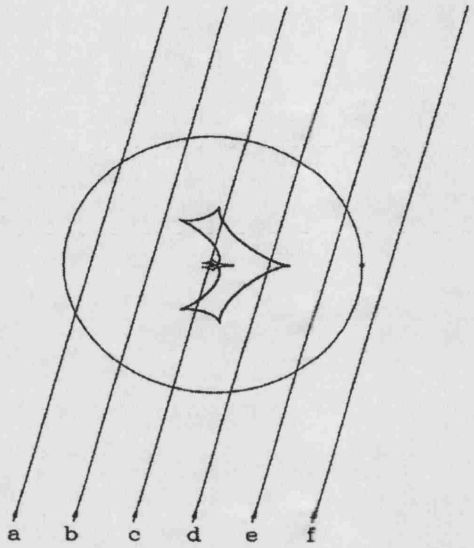

Figure 2.7: Geometry of binary microlensing, with a $1M_{\odot}$ primary star surrounded by a caustic (irregular line) and a $0.1M_{\odot}$ secondary located on the Einstein Ring of the primary (circle). The lines labelled a-f are paths of a source object behind the caustic.

As the separation between the two components of the lens increases the angular size of the caustic shrinks rapidly (Han and Kang, 2003), and if the separation is significantly greater than the Einstein ring radius the two bodies will act as separate lenses. Therefore, for a group of potential lenses such as the stars in the Magellanic clouds, all of which are of effectively the same distance, there is a limited range of planetary orbital radii outside which the caustic angular size is reduced sufficiently to make source crossing considerably less likely.

Some very impressive plots of the microlensing phenomenon have been produced by Mao & Paczyński (1991) and are shown in figures 2.7 and 2.8.

As the mass ratio between the two lens components increases the caustic structure becomes more and more distorted. For a typical extrasolar system where the mass of the planet is of the order of one thousandth of the mass of the star, the Einstein ring of the planet is subsumed by that of the star and the angular area of the caustic is very much smaller than for components of similar masses. Therefore it

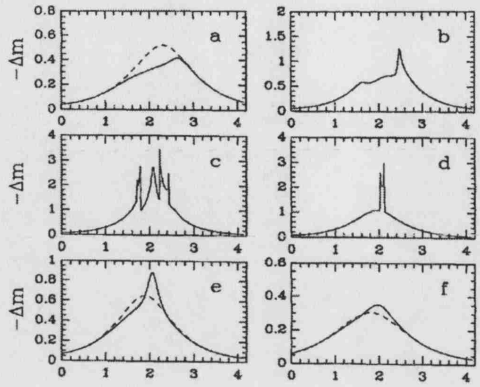

Figure 2.8: Light curves corresponding to source trajectories shown in figure 2.7. Note the sharp increase in magnification when the source crosses the caustic.

is less likely that a source would pass behind the caustic, and the duration of transit would be considerably smaller. Whilst the chances of this situation occurring are of course extremely small it does at least show the potential of planet detection at large distances from the parent star.

Unlike the other planetary detection methods, where a likely system is targeted and observed for a period of time, the gravitational microlensing technique allows, and indeed requires a large number of stars to be considered simultaneously, as the likelihood of an individual lensing event is extremely small. In this case telescopes are trained on a wide field of densely clustered stars, such as the galactic core or the Magellanic clouds in order to encompass as many events as possible, and wait for an event to take place.

Clearly a lens consisting of a planetary system containing planets with masses even of the order of the Earth could produce distinctive features in the magnification profile of a transiting source under certain conditions. It is this feature, the ability to detect planets with masses far smaller than can currently be achieved by the radial velocity method, and without the long-term commitment of telescope time required by transit method that makes gravitational microlensing so attractive. The

relatively low likelihood of a microlensing event occurring is offset by the large number of stars that can be examined in one field, yielding a somewhat scattershot approach to detection. The major weakness is that outside of a particular range of planetary orbit radii at a certain lens distance the angular caustic size drops off rapidly, reducing the chances of producing a detectable event. Of course, such events are also one-off processes with no opportunity to re-observe the lensing system, but it would allow other telescopes to be focused on to it and the use of other methods to examine the system in more detail.

2.2 Planet Detections

In a field as fast moving as Extrasolar planets producing a list of current results is akin to following a moving target. Since the first planet orbiting a main sequence star, *51-Pegasi*, was detected by Mayor & Queloz (1995) in 1995 there has been a near continuous stream of new discoveries, with the current total topping one hundred. Therefore I must recommend that anyone who would like to see an up to date snapshot of current planet detections should visit the excellent website of the California & Carnegie Planet Search team at **http://exoplanets.org/** , which is regularly updated.

With this caveat in mind I will now lay out the current status of planet detections and what has been inferred from the admittedly limited data available.

2.2.1 Current Results

Of the current known planets all but one have been detected using the dynamical perturbation method. Prior to the new discovery of OGLE-TR-56b (Konacki et al., 2003) even the single transiting planet known, HD 209458b (Charbon-

neau et al., 2000) was first detected by this method. This is to be expected given the large set of phase space that an orbital plane may exist in, but the more planets discovered the more are likely to be capable of transits, which will provide a great deal more information about the planets involved.

Shown in figure 2.9 is a current plot of the masses and orbital radii of all known exoplanets, obtained from the California & Carnegie web page.

Immediately obvious is the large number of planets with extremely small orbital radii and the dominance of observed single planetary systems. While in the early days of exoplanet detection the predominance of extremely close orbiting planets was pronounced, now with more sensitive detections and the encouraging evidence that such planets exist, more are being discovered with what we would deem *solar-type* orbital radii, and in multiple systems.

Utilising data obtained from the planet catalogue of *l'Observatoire de Paris* at **http://www.obspm.fr/planets** , which holds a regularly updated list of exoplanet properties, it is possible to examine the mass and orbital properties of these planets. Firstly, and most relevantly given this thesis aims to discover the properties of very close orbiting *51-Peg* type planets, is there a relationship between orbital radius and eccentricity? One would expect tidal circularisation to reduce the eccentricity of the very closest planets. Looking at figure 2.10 no relationship is immediately obvious. However, a logarithmic plot (figure 2.11) clearly shows the trend of increasing eccentricity with orbital radius. Zooming in to the closest orbiting planets in figure 2.12 allows the eccentricities of those planets with orbital radii less than 0.1AU to be observed with the very closest, those in the $\sim$0.1AU region, almost exclusively having near circular orbits as predicted in section 2.4.2.

A plot of orbital radius versus mass in figure 2.13 is somewhat indeterminate, suggesting no general trend but displaying an apparent dearth of high mass planets

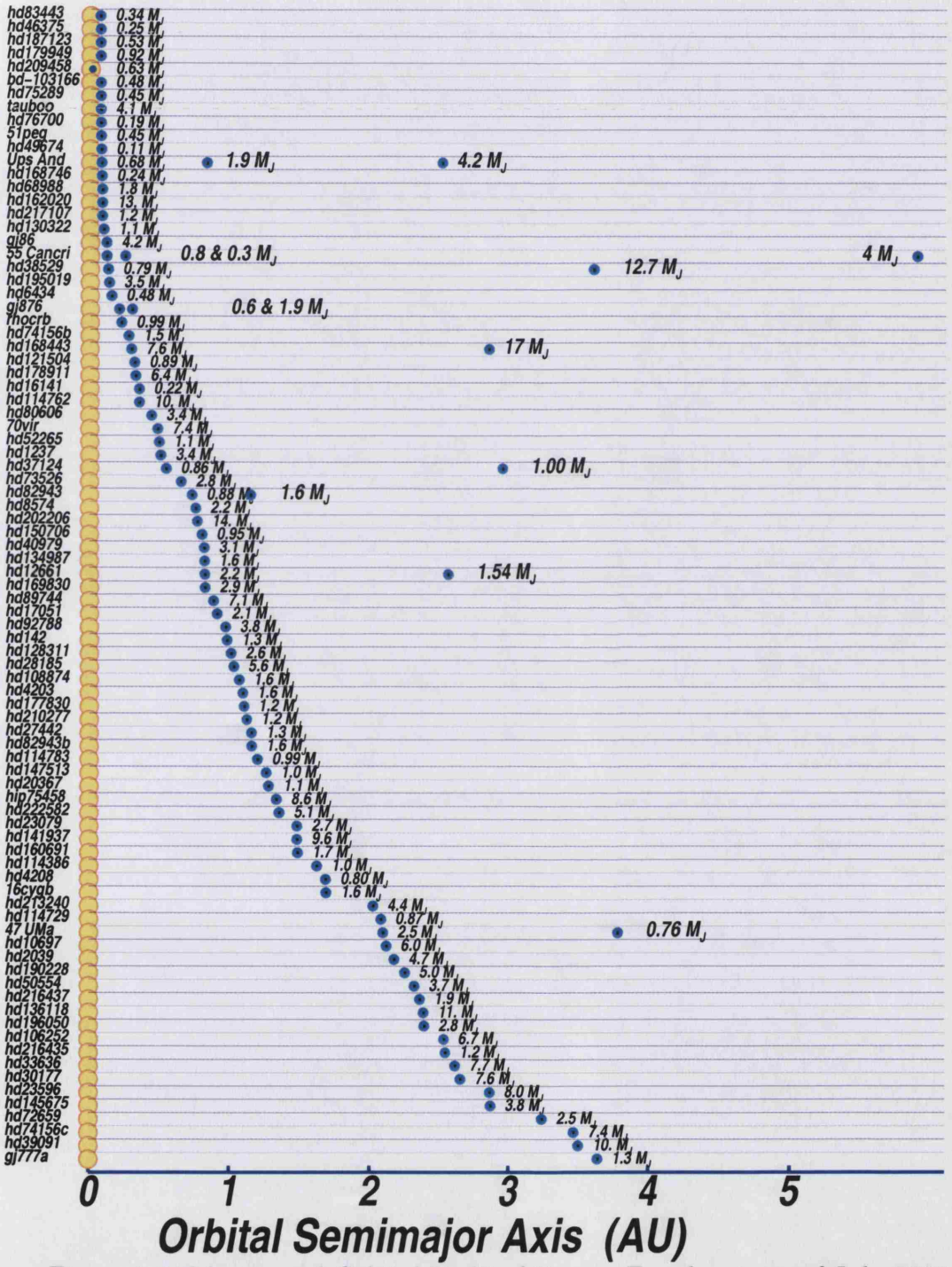

Figure 2.9: Masses and Orbital Radii of Known Exoplanets as of July 2003.

.

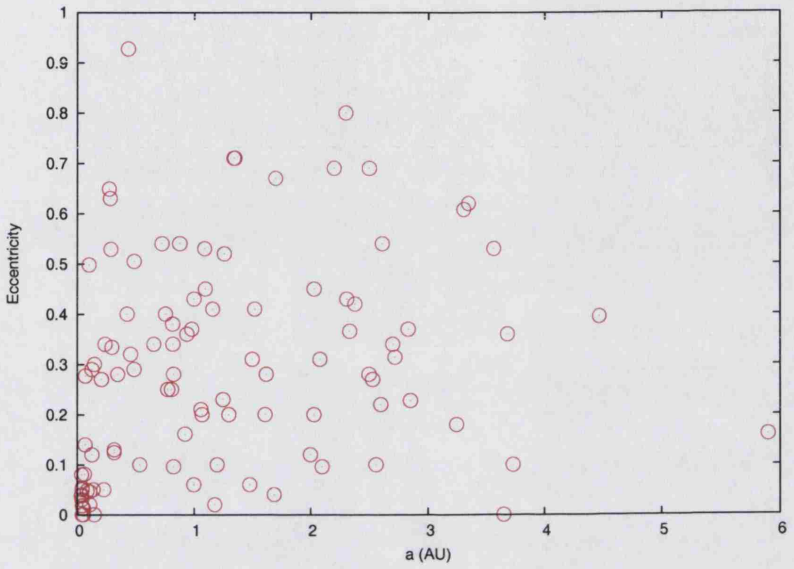

Figure 2.10: Plot of eccentricity versus orbital radius in astronomical units.

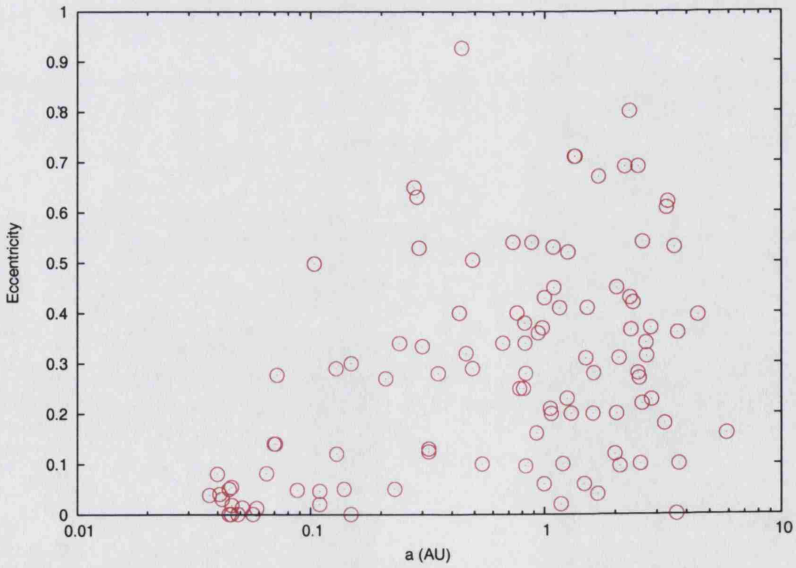

Figure 2.11: As figure 2.10 but with orbital radius logarithmically spaced.

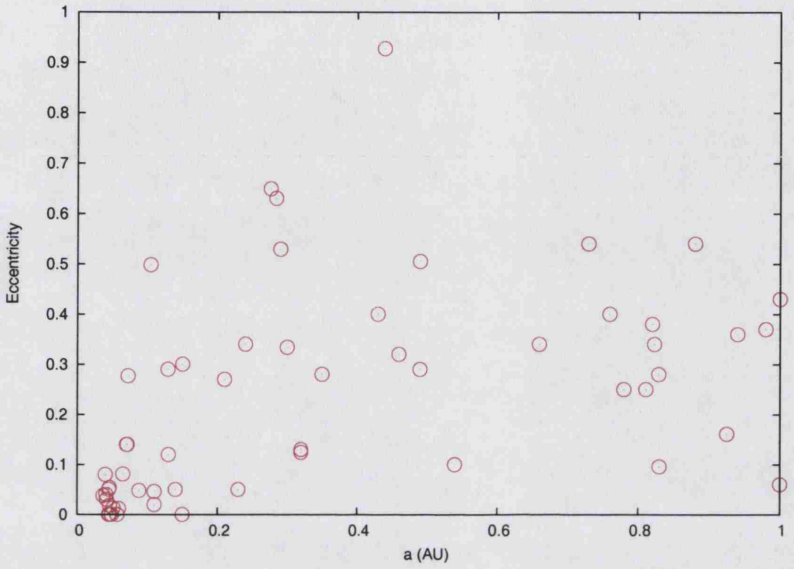

Figure 2.12: Zoomed in region of figure 2.10.

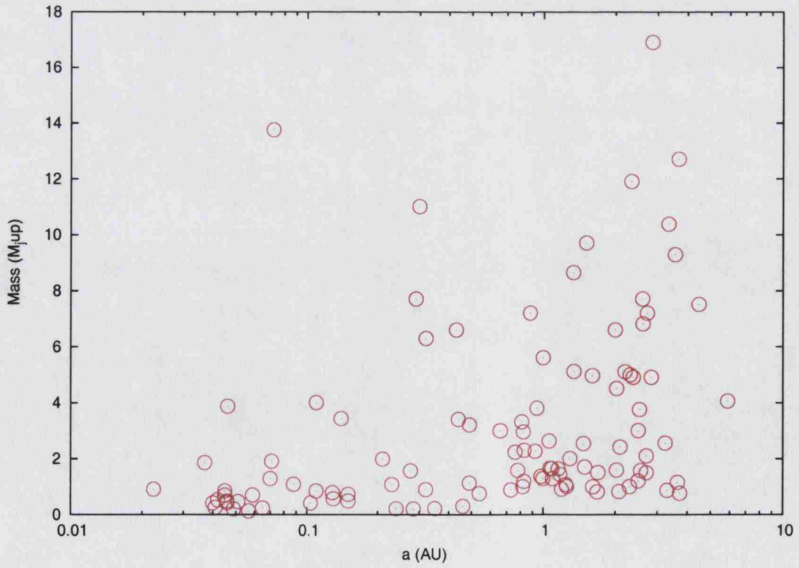

Figure 2.13: Plot of logarithmic orbital radius (in AU) versus mass (in Jovian masses) for the current set of exoplanets.

interior to 1 AU, corresponding to the circularised region. It could be that planets in this region undergo mass loss due to the extreme irradiation by the parent star or possibly orbital decay timescale in this region is dependent on planetary mass, allowing low mass companions to survive longer.

2.2.2 Stellar Metallicity

Stellar metallicity is designated by the logarithm of $[Fe/H]$, i.e. the iron ratio in relation to hydrogen. In astronomy, to give this value context, metallicity is generally presented relative to the solar value:

$$Z = log_{10}\left[\frac{Fe}{H}\right]_{\star} - log_{10}\left[\frac{Fe}{H}\right]_{\odot} \tag{2.21}$$

Since terrestrial planets and the cores of giants are made up of metals and rocky material it is important to ask whether the metallicity of the host star has a bearing on the likelihood of planetary formation, particularly in light of the core accretion theory discussed in section 2.3.1. Beyond this, could there be a correlation between metallicity and orbital or other planetary properties?

There have been a number of studies of planet-bearing stellar metallicities (Butler et al., 2000), (Gonzalez et al., 2001), (Santos et al., 2000) and others. In each case the results show a general trend towards planet-bearing stars having a higher $[Fe/H]$ ratio that that of the stellar field, as shown in figure 2.14.

Taken at face value this result should confirm a metallicity dependency on planetary formation. However it is important to consider the possibility that the metal content of the star may not be of primordial origin. Murray & Chaboyer (2002) note the fact that the lowest mass stars with planets are notably iron poor with several having $[Fe/H] < -0.2$, demonstrating that high metallicity is not required

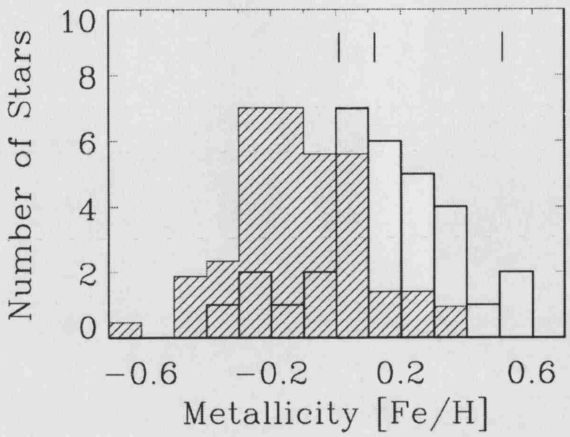

Figure 2.14: Metallicities of planet-bearing stars (outlined) compared to nearest field stars (dashed) relative to solar abundance (Butler et al., 2000).

for formation of Jupiter-mass planets. Moreover, they show that, up to $1.2M_{\odot}$ average $[Fe/H]$ increases with increasing stellar mass and demonstrate that the mass-metallicity trend can be explained by the accretion of $\sim 5M_{\oplus}$ of iron to stars with known radial velocity planets, suggesting that the high metallicity of these stars may be down to absorption of their inner planets or planetesimals. They conclude by suggesting that the observed enhanced metallicity in stars with planets is a combination of metal accretion, selection effects and genuine high intrinsic metallicity. This is a somewhat indeterminate result but one that implies that the prior requirement of high metallicity for planet formation may not be as rigid as previously thought.

Could the accreted material be in the form of a captured planet? Sandquist et al. (2002) suggest the possibility, noting that hydrodynamical simulations indicate a hot planet would be destroyed and thoroughly mixed into the convection zone of the host star, increasing the detected metallicity, and notes that the increase should be dependent on the depth of the stellar convection layer, with varying survival times for different isotopes.

Interestingly Santos et al. (2003) have plotted stellar metallicity against convective envelope mass, the result being no detectable trend that would be expected if metallicity excess were a result of inflow of material. This evidence would appear to point strongly towards the primordial source as the best explanation of stellar metallicity.

Santos et al have also attempted to determine if there is any relationship between metallicity and orbital eccentricity, and have detected none.

2.3 Planetary Formation Theory

Until recently all models of planetary system formation had exactly one physical example to test themselves against, our own. Therefore the model would have to predict the interior terrestrial planets, the outer gas giants and the predominantly non-eccentric orbits. Since the detection of planetary systems other than our own solar system, theories have had to explain not just the familiar layout of terrestrial and gas planets, but the wide variability in eccentricity and orbital radius observed. Whilst the basic theories have been in place for some time, the new data has given rise to a flurry of research as each planet has to be accommodated. What follows is a snapshot of the current theories of planetary formation and evolution.

From stellar formation theory it has been common knowledge for some considerable time that shocks driven by highly energetic events, such as supernovae, trigger gravitational collapse of clouds of interstellar gas and dust. Conserving angular momentum the collapsing cloud forms a flattened disc of material accreting onto a protostar at the centre. From this *accretion disc* it is thought that planets are formed.

There are two general theories of massive planet formation (ice giant and up-

wards), *Core Accretion* and *Disc Instability* and both have their advantages and disadvantages (Boss, 2002) which will be detailed as follows.

2.3.1 Core Accretion

The prevailing theory prior to the discovery of exoplanets, Core Accretion cites that individual planets form by collisional agglomeration via gravitational instability or non-gravitational cohesion of successively larger particles, from sub-micron dust grains up to planetesimals a few kilometres across (Wetherill, 1990). These bodies then undergo merger to form a small number of dominant planetary embryos around the size of the Moon up to Mercury, which grow extremely rapidly due to gravitationally enhanced collision cross-sections (Greenberg et al., 1978). These dominant protoplanets cease accretion when their orbits are sufficiently separated so that mutual perturbation becomes negligible and the orbits may be considered stable.

Depending on the supply of available disc material some of these embryos may accrete further. At Earth's orbital radius the temperature is low enough to allow silicate crystals and iron to condense but not volatile ices, explaining the rocky structure of the terrestrial planets and the icy composition of most giant planet satellites. The outer planets were able to accrete large quantities of gas along with solid material allowing them to attain a larger mass.

The gas giants are thought to form when the planetary embryo reaches a mass of $\sim 10 M_{\oplus}$, although the exact core mass is a matter for some debate (eg. Mizuno (1980), Sasaki (1989), Guillot et al. (1997)).

Once a critical mass has been reached the growing planet cannot sustain its atmosphere via hydrostatic equilibrium and it contracts, allowing further gas accretion in a process of runaway growth (Pollack et al., 1996).

Although able to explain the delineation between the terrestrial and gas giant planets the core accretion theory is not without its problems. Chief among these is the formation timescale. In order for the gas giants to form they must have reached their approximate present size within the lifetime of the stellar nebula. The nebula is steadily absorbed by the star and forming planets and blown away by stellar UV radiation and solar wind on a timescale of a few million years (Briceno et al., 2001). Stars forming in high density regions with a number of nearby bright O and B type stars have correspondingly shorter disc lifetimes.

Given a *minimum mass solar nebula*, the hypothetical minimum mass of the primordial nebular from which the solar system formed, obtained by taking the present mass of all the planets and adding whatever material is required to bring their relative abundance to that of the sun, present theories predict planetary embryo formation timescales significantly longer than predicted nebula lifetimes. Given planetary formation rates which are dependent on σ_s, the surface density of planetesimals in the region, Pollack et al. (1996) calculated that for $\sigma_s = 10 g\,cm^{-2}$ at 5.2AU, formation time is approximately 8×10^6 years. Further out from the sun at the orbit of Uranus, where planetesimal density is decreased, orbital speeds are lower and the planetesimals less tightly bound to the central star, formation timescales reach nearly 2×10^7 years. Decreasing σ_{init}, the initial mass of the planetary nebula increases formation times still further. The authors, however, note that these timescales should be regarded as conservatively long, although they still pose something of a conundrum, particularly in regard to ice giant formation.

Increasing the surface density of the nebula would bring the corresponding formation timescale down, although at the expense of producing a larger solid core than is presently favoured.

Interesting solutions to the ice-giant formation timescale problem have been pro-

posed, such as the runaway growth of a single embryo as disc interaction causes it to radially migrate into undepleted regions (Levison and Stewart, 2001). More radical, however, is a theory (Thommes et al., 1999) that suggests that the ice giants' cores were formed in the Jupiter-Saturn region and scattered outwards as the gas giant planets accrete material, stabilising into orbits resembling their present forms due to gravitational interaction with small bodies in the region.

2.3.2 Disc Instability

Given the range of problems and uncertainties associated with the core accretion theory it is reasonable to ask if it is really a valid scenario, despite its ability to predict the formation of the terrestrial and gas giants. In particular, should the cores of the gas giants be found to be of lower mass than previously thought (Boss, 1997) then runaway gas accretion may not be possible.

Hydrodynamic models of early phase protoplanetary discs have shown the formation of trailing spiral arms (Boss, 1998) which transport mass inwards. Near the end of this large scale instability phase the temperature and surface density may be right for disc instability to operate from about 5 AU to 20 AU, forming clumps of gas and dust which collapse under self gravity.

The primary advantage of this theory is the rapid timescale involved. Simulations have suggested that the disc could break up into massive protoplanets with nearly their final mass in only about 10^3 years. Sedimentation of dust grains then causes the core to form *after* the protoplanet.

Doubts, however, arise as to whether disc instability could form planets as small as Saturn without some additional process to potentially remove some proportion of the gaseous envelope prior to sedimentation, such as stellar UV radiation. In addition, observations show that the giant planets have substantially non-stellar

abundance, which would require considerable cometary impact and a lack of deep mixing which would dilute the surface composition.

Furthermore, unless there were some aforementioned method of reducing proto-planet mass prior to sedimentation it would be expected that the core mass would depend on total planetary mass, a situation at odds with the core accretion model.

Clearly, these two very different planetary formation methods have a number of advantages and disadvantages and neither can currently be unambiguously considered the dominant. Boss (1998) suggests that one way of definitively testing for disc instability would be the detection of the presence of planets around a very young star ($\sim 10^5$ years) which would not have had time to form under the core accretion model. This would provide unambiguous evidence of the unsuitability of this model and lend weight to the disc instability theory. Additionally, disc instability would appear to be independent of stellar metallicity although, as previously suggested, this issue of metallicity with regard to planet formation is unresolved. Until these issues is settled, the theory of planetary formation is still in flux, making this an interesting time for the exoplanetary scientist.

2.4 Orbital Evolution

Considering the number of planets discovered orbiting in the region of 0.1AU from their parent star and considering earlier evidence which suggests that gas giants are unable to form in this region it is reasonable to pose the question as to whether the theory of planetary formation is flawed of if it were possible that the planets formed further from the star, beyond the snow line and migrated inwards over time. In this section I will be putting forward the evidence for the latter conclusion.

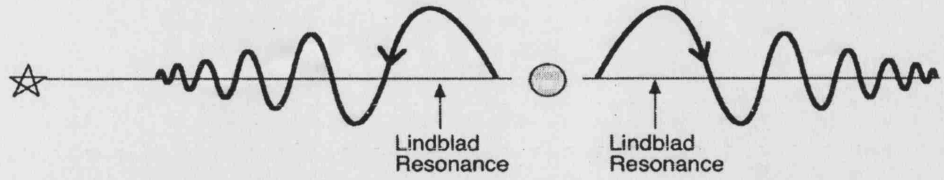

Figure 2.15: Wave Propagation in a Circumstellar Disc (Takeuchi et al., 1996).

2.4.1 Migration

A disc with non-zero viscosity will transport angular momentum outward, resulting in the spreading of the disc (Thommes and Lissauer, 2002) and leading to a net inwards transport of mass (Lynden-Bell and Pringle, 1974).

A massive, still accreting protoplanet and the circumstellar disc interact tidally (Trilling et al., 1998) resulting in angular momentum transfer between the disc and the planet (Goldreich and Tremaine, 1980). The planet's motion through the disc creates spiral density waves that propagate away from corotation (Ward, 1997b) both interior and exterior to the orbit of the planet due to the presence of *Lindblad resonance* sites, located where the natural epicyclic period of the gas in the disc is $p(m+1)/m$ (Kuchner and Lecar, 2002) where p is the orbital period of the planet and m is an integer value. A schematic of the wave propagation in the disc is shown in figure 2.15.

The protoplanet's gravitational interaction with the density waves results in a reaction torque on the planet, due to the inequality of the exterior and interior resonance torques and causes the planet to drift relative to the disc material with a velocity (Ward, 1997b)

$$\frac{dr}{dt} \sim c_1 \left(\frac{M}{M_\star}\right)\left(\frac{\sigma r^2}{M_\star}\right)\left(\frac{r\Omega}{c}\right)^3 r\Omega \tag{2.22}$$

where Ω is the orbital frequency of the protoplanet, $M_\star$ is the mass of the primary,

σ is the disc surface density, c is the gas sound speed, r is the protoplanet orbital distance, M is the protoplanet mass and c_1 is a measure of the torque asymmetry, essentially the ratio of the inner and outer torques, and is generally of order unity and negative in the case of inward migration.

Dimensional arguments suggest that the migration rate, v scales with h/r (Ward, 1997a) and:

$$v \propto \left(\frac{r\Omega}{c}\right)^2 \tag{2.23}$$

The larger the mass of the planet in a particular disc, the more rapid the orbital migration. This method of orbital migration is known as *Type I Migration* and applies to planets which are embedded in the disc. Recent calculations (Tanaka et al., 2002) and hydrodynamical models (Bate et al., 2003) have produced orbital decay times of the order of 10^5 years or less, clearly dramatically shorter than the predicted life of the circumstellar disc.

The second form of migration, *Type II Migration*, requires that the protoplanet be massive enough that nonlinear gravitational interactions between the disc and the planet clear out a gap in the disc surrounding its orbit (Winters et al., 2003) thus establishing a barrier to radial disc flow by viscous diffusion. The planet becomes tidally locked to the disc and evolves with it on a viscous timescale (Lin and Papaloizou, 1986).

If the viscosity of the disc is of the Shakura-Sunyaev form,

$$\nu \sim \frac{\alpha c^2}{\Omega} \tag{2.24}$$

where α is the S-S viscosity parameter (Shakura and Sunyaev, 1973) then the

characteristic velocity may be represented as

$$\frac{dr}{dt} = c_2 \alpha \left(r\Omega\right) \left(\frac{c}{r\Omega}\right)^2 \tag{2.25}$$

where c_2 is a constant of order unity.

Type II orbital decay timescale is longer that Type I, up to 10^8 years depending on the disc viscosity, suggesting that a planet undergoing Type II orbital decay may be able to survive until the disc has dissipated, although as stated this would depend on the disc viscosity.

In a well known paper on the subject of planetary survival strategies, William Ward (1997b) lays out the rules. In order to migrate at a slow enough speed a protoplanet must either be sufficiently small to survive type I migration or it must grow at a sufficient rate in order to transit to type II migration before its orbit has decayed.

This leaves us with an intriguing question; considering the number of exoplanets discovered orbiting so close to their parent stars, is there some mechanism that could halt migration at these small orbital radii or, given the number of stars in existence, do most of the planets that form spiral to their doom and what we see are simply those that are left stranded when the circumstellar disc evaporates? Looking at figure 4.1 there appears to be a sharp cutoff at the lower end of the plot of orbital radii with a number of planets clustered just above this point, giving credence to the existence of a possible migration halting process.

Interestingly, the planet in this plot with the smallest orbital radius, OGLE-TR-56b, is something of an anomaly, having an orbital radius of only 0.023AU, well inside the inner edge (Konacki et al., 2003).

Theories that attempt to explain migration halting include taking into account

the existence of a toroidal magnetic field in the disc (Terquem, 2003), which could dominate the Lindblad resonances if sufficiently strong. A planet migrating into a magnetised region may stall or even begin migrating outwards. If the magnetic field is stable over long timescales then a protoplanet could migrate a certain distance before reaching a stable region and completing its evolution.

Alternately it has been hypothesised that migration may be halted by photoevaporation of the interior disc due to the central star. Matsuyama et al. (2003) have suggested that photoevaporation may produce a gap in the disc at several AU from the star, preventing planets outside the gap from migrating inwards and introducing a surfeit of planets just outside the photoevaporation radius, a result which may be tested. In addition Kuchner and Lecar (2002) postulate that dust grains reach sublimation temperature at $\sim 1500K$, corresponding to an orbital period of ~ 6 days around a Sun-like star. Interior to this turbulent accretion due to magnetorotational instability may evacuate the disc centre. This would explain the large number of planets with orbital periods of 3-4 days and lack of any with periods less than three days in that migrating planets would halt once the evacuated region contains the site of their exterior 2:1 Lindblad resonance.

Finally, the presence of numerous close-orbiting planets may be explained as simply a selection effect resulting from the preferential detectability of high mass planets in short period orbits. This is not expected to be the case due to the fact that planets have been detected several AU from their parent star, demonstrating that if they exist then they can be detected. Clearly this is another aspect of exoplanet theory that would benefit greatly from a larger and more varied group of detections. Fortunately as shown above there are a number of theories already in existence that may explain the features of the planetary systems that we see.

So, assuming that migration halting is a genuine process, how does one explain

the presence of the oddity, OGLE-TR-56b? A study of the planet (Sasselov, 2003) has suggested that it may be the result of a different migration halting process (Trilling et al., 1998) where a close-orbiting planet that is losing mass due to Roche-lobe overflow balances the inward torque from the disc with outward torque from a fast spinning pre-main-sequence star. If the disc dissipates sufficiently quickly that the planet is not completely consumed ($t \leq 10^6$ yrs) then it may be left in a stable orbit inside the inner cutoff.

The presence of OGLE-TR-56b appears to provide compelling evidence of the fact that the previously discussed migration halting conditions do not apply in all cases. OGLE-TR-56b has passed beyond the supposed point where migration is halted due to evacuation of the inner disc, suggesting that maybe in this system the disc extended inwards almost to the star during the epoch of planetary migration, perhaps due to the young star's stellar wind strength or some property of the disc itself. If any further planets beyond the inner cutoff point are discovered it will allow a comparison of their parent stars to be made and possibly go some way towards answering this question.

2.4.2 Eccentricity

Given that accreting protoplanets in a circumstellar disc are expected to form in near circular orbits (Ward and Hahn, 2000), (Agnor and Ward, 2000), the number so far discovered in sometimes exceptionally eccentric orbits up to e$\sim$0.9 is initially puzzling. The most natural explanation for the theorised increase in eccentricity is by gravitational disturbance by a nearby companion. Considering the vast majority of planets have been detected orbiting a single isolated star, the likely suspect would be an additional planet or planets.

Numerical simulations studying the dynamical evolution of two giant planets

in nearly circular orbits very close to the dynamical stability limit (Ford et al., 2001) have produced a number of resultant systems containing either a single planet resulting from a collision or ejection of one planet, or two planets with significant eccentricities in a new quasi-stable configuration. The main problem with this theory is the lack of observed near-circular orbits which would be readily produced by direct collisions.

A more promising theory involves the convergent migration of two planets, which may occur if the two planets are sufficiently close together that they clear out the disc material between them. Unopposed torques exerted by the disc drive the planets together. This process can lead to capture into a 2:1 mean-motion resonance (Lee and Peale, 2002). As the two planets migrate inwards in tandem on the disc viscous timescale, the eccentricities are pumped up until eccentricity damping processes such as tidal dissipation and planet-nebula interaction allow equilibrium to be reached.

Alternatively, planets undergoing divergent migration (Chiang et al., 2002) may traverse a series of mean-motion resonances that amplify their eccentricities in approximate inverse proportion to their masses.

Whereas both the previous theories involve perturbations by a companion, an alternative has been suggested by Goldreich and Sari (2003) in which the planet interacts with the extant circumstellar disc. Planetary interaction with the disc may either excite or damp eccentricity depending on resonance configuration and if the balance it tipped towards the former then eccentricity can increase.

Once a planet migrates inwards sufficiently it may undergo tidal circularisation by the parent star on a timescale smaller than the age of the system, which explains why all the very closest exoplanets which are apparently unperturbed by companion bodies have eccentricities ~ 0.1 or less.

Interestingly, Witte and Savonije (2002) apply numerical studies to the theory of

tidal interaction and conclude that, over a main sequence timescale for slow stellar rotation it is only possible for circularisation to occur for planets with initial orbital periods of ~ 4.5 days or less, possibly explaining why only the very closest orbiting planets have truly circular orbits.

In addition to orbital circularisation, tidal forces will tend to slow the planetary rotation rate of a planet until it becomes synchronised with the orbital period, with one side permanently facing the star. Planetary spin down occurs on a timescale of (Guillot et al., 1996)

$$\tau \sim Q\left(\frac{R_p^3}{GM_p}\right)\omega_p\left(\frac{M_p}{M_\star}\right)^2\left(\frac{D}{R_p}\right)^6 \tag{2.26}$$

where Q is the planet's tidal dissipation factor, ω_p is the planet's primordial rotation rate, $M_\star$ is the star's mass, M_p is the mass of the planet, R_p is the radius of the planet, D is the orbital radius and G is the gravitational constant.

Taking Jupiter's values of $Q \sim 10^5$ and $w_p \sim 1.7 \times 10^{-4} s^{-1}$ along with a value of D equivalent to the distance of 51-Pegasi from its star gives $\tau \sim 2 \times 10^6 yr$, suggesting that spin period locking occurs on a much faster timescale than tidal circularisation and we can expect the majority of close orbiting planets to present one face to their parent star.

Chapter 3

JIME - The Enhanced Jovian Ionospheric Model

Having provided a background to exoplanet studies and a demonstration of the necessity of a planetary model that can simulate the conditions expected in the region of 0.1AU from a sun-like star, it is time to introduce JIME. In this chapter I will provide a basic description of the previously existing JIM and detail the concepts and work that went into developing a new model capable of simulating a super-hot 51-Peg type planet. More specifically, whereas JIM is hard coded to support Jupiter, JIME is intended to be more flexible, allowing additional input parameters to be specified at runtime without recourse to recompilation.

Included are a number of the problems that were encountered in this process and how they were solved.

3.1 Introduction to JIM

JIM is a time-dependent, three-dimensional model for the thermosphere and ionosphere of Jupiter. It was developed by Nicholas Achilleos and based on the prior University College London Thermosphere Model of Fuller-Rowell and Rees. For an in-depth report on the development of JIM it is recommended that the reader follow the reference to the original JIM paper (Achilleos et al., 1998), hereafter referred to as Paper I. This thesis will provide basic details but aims to concentrate on the development of JIME.

JIM is a numerical model based on a three-dimensional Cartesian grid of 30 pressure elements, 40 longitudinal elements and 91 latitudinal elements, in which the equations of momentum, energy and continuity are solved self-consistently on a user-defined timescale.

3.1.1 Dynamics

The equation of conservation of horizontal momentum for a neutral gas

$$\frac{D\mathbf{v}}{Dt} = -\frac{\nabla_z P}{\rho} + \mathbf{F} \tag{3.1}$$

where $\mathbf{v}$ is the horizontal velocity and $\mathbf{F}$ is the Coriolis force, is transformed into the P coordinate system (Fuller-Rowell and Rees, 1980)

$$\frac{D\mathbf{v}}{Dt} = \left(\frac{\delta \mathbf{v}}{\delta t}\right)_P + \mathbf{v}.\nabla_P \mathbf{v} + w\frac{\delta \mathbf{v}}{\delta P} \tag{3.2}$$

where $w = DP/dt$, to allow for the use of pressure rather than altitude as a vertical coordinate. This more conveniently allows for the effects of atmospheric expansion.

$P(n)$	$P(Pa)$	$P(mb)$
1	2.026×10^{-1}	2.026×10^{-3}
5	4.090×10^{-2}	4.090×10^{-4}
10	5.536×10^{-3}	5.536×10^{-5}
15	7.492×10^{-4}	7.492×10^{-6}
20	1.014×10^{-4}	1.014×10^{-6}
25	1.372×10^{-5}	1.372×10^{-7}
30	1.857×10^{-6}	1.857×10^{-8}

Table 3.1: JIM Pressure levels with associated pressure.

It can be shown that

$$\nabla_z P = \rho \nabla_P \Phi \tag{3.3}$$

where $\Phi = gz$ is the gravitational potential and ∇_P and ∇_z are the gradient operators in the corresponding directions, leading to

$$\left(\frac{\delta \mathbf{v}}{\delta t}\right)_P = -\mathbf{v}.\nabla_P \mathbf{v} - \omega \frac{\delta \mathbf{v}}{\delta P} - \nabla_P \Phi + \mathbf{F} \tag{3.4}$$

which is the form of the momentum equation used in the model.

The vertical grid spacing is chosen to be uniform with respect to the logarithm of pressure

$$P_n = P_1 exp\{-\gamma(n-1)\} \tag{3.5}$$

where $\gamma = 0.4$.

The relationship between pressure level, $P(n)$, and absolute pressure measured in pascals and millibars is represented in table 3.1. Pressure level 1 is fixed at a constant altitude of 357 km above the P=1 *bar* level.

3.1.2 Viscosity

The viscosity force in the horizontal momentum equation is determined by the vertical transport of horizontal momentum due to intermolecular collisions

$$(\mathbf{F}_v)_j \approx \frac{\mu_m + \mu_t}{\rho} \nabla_P^2 v_j + g^2 \frac{\delta}{\delta P}((\mu_m + \mu_t)\rho \frac{\delta v_j}{\delta P}) \tag{3.6}$$

where j represents the x or y component of the acceleration and μ_m and μ_t are the coefficients of molecular and turbulent viscosity.

3.1.3 Ion/Neutral Collisions and Electric Field

The motion of ions and electrons represents a current which exerts an electromagnetic force on the neutral gas of the form

$$\mathbf{F}_L = \mathbf{J} \times \mathbf{B}/\rho \tag{3.7}$$

where J is the current density and B is the local magnetic field.

The J term is dependent on the local electric field and the effect of this component is most obvious in the auroral region where magnetic field lines intersect non-corotating regions of the Io plasma torus, introducing a local potential superimposed on general electric field morphology.

This leads again to the consideration of which features in the Jovian model should be considered general to gas giants and which are particular to Jupiter. The magnetic field and its possible dependence on a rotating body has been discussed, but the Io plasma torus and its contribution to the Jovian aurora is a unique feature in the solar system. Given the probability of a gas giant harbouring large satellites (all the giant planets in the solar system are orbited by at least one satellite that

could be considered large) it is not unreasonable to assume that this is a repeatable event. Given, however, that the plasma torus depends not only on a large satellite in sufficiently close orbit but also a sufficiently strong magnetic field to confine any potential ionised particles sublimated from the surface then the common presence of a Jovian-type auroral electric field system must be questioned.

However, considering the decision to retain the magnetic field it is therefore important to also retain the auroral electric field for consistency reasons. However, since the ion density profile due to magnetospheric particle precipitation should remain approximately constant with orbital radius they will provide a useful comparison with global photoionisation processes which should dominate in the subsolar region.

The electric field in JIME consists of two major components, the implementation of which is discussed in Paper I:

- A high-latitude field due to the solar wind impinging on the magnetosphere, based on analytical work by Spiro et al (1978).
- An cross-auroral component due to closing of field-aligned currents flowing through the plasmasheet.
- A global Lorentz $\mathbf{U} \times \mathbf{B}$ component due charge motion through the magnetic field.

The global electric field consists of the three components described above added together at each grid point. A plot showing the three components taken from actual JIME output can be found in figure 4.19(a). Clearly distinguishable are the two high latitude components and the weaker global field.

3.1.4 Continuity

The continuity equation of mass is likewise transformed into the P-coordinate system with added effects of chemistry not included in the original thermosphere model

$$\nabla_P.\mathbf{v} + \frac{\delta w}{\delta P} = \frac{1}{\rho}\sum_j m_j(q_j - l_j) \tag{3.8}$$

where $w = DP/Dt$ and m_j, q_j and l_j are the mass and chemical creation and destruction rates of each neutral species, H, H_2 and He.

3.1.5 Energy

Energy transport is implemented by considering the change of enthalpy per unit mass of neutral gas

$$c_P\frac{DT}{Dt} - \frac{1}{\rho}\frac{DP}{Dt} = \dot{Q} \tag{3.9}$$

where c_P is the heat capacity at constant pressure per unit mass and $\dot{Q}$ represents heating and cooling processes. In JIME these include

- **Joule Heating** due to electrical energy liberated from current flow and the $J \times B$ force.
- **Energy Deposition** due to auroral precipitating electrons and high energy photoelectrons. The auroral region in this case is defined as between the magnetic field lines attached to the plasma sheet between $6\,R_J$ and $30\,R_J$. In the model auroral electrons are considered monochromatic with an initial energy of $10keV$ which degrades with altitude. The number flux is set to 2×10^{12}.

- **Solar Heating** due to solar EUV input, dependent on the optical depth:

$$\dot{Q}_s = f_s \int_\lambda F_u(\lambda)\, exp\{-\tau(\lambda, \chi)\} d\lambda \tag{3.10}$$

where $F_u(\lambda)$ is the solar flux per unit wavelength interval about λ at the upper boundary, f_s is the neutral heating efficiency and τ is the optical depth parameter which is in turn dependent on solar zenith angle, height and extinction due to photoionisation of H, H_2 and He and photodissociation of H.

- **Thermal Conduction** in the vertical and horizontal directions using molecular and turbulent conduction coefficients.

- H_3^+ **Cooling**, which is a new feature in JIME and is described in section 3.3.2.

In chapter 4 will be demonstrated that by the time the planet has been brought in to 0.3AU, solar heating and H_3^+ cooling are by far the dominant energy transport mechanisms during the day. At night H_3^+ is no longer formed, producing only residual H_3^+ cooling and allowing other mechanisms such as thermal conduction to dominate.

3.1.6 Chemistry

The JIM atmosphere is assumed to exist above the Jovian homopause, allowing complex organic chemistry to be ignored. The neutral components of the JIM atmosphere are monatomic H and He and molecular H_2, whilst the major ionic species are H^+, H_2^+, H_3^+ and He^+.

A complete list of the ionic chemical reactions, which includes photon and electron impact ionisation/dissociation and radiative/dissociative recombination may be found in Paper I. For the purposes of JIME the most important reactions are

those involving photoionisation, where there will be a clear increase in the rate of reaction for a 51-Peg type planet over Jupiter.

It is particularly important to consider the processes involved in the life-cycle of H_3^+ and its relationship with H^+ as the relative abundance of the two species is indelibly related as will be demonstrated in chapter 4. H_3^+ is formed by the reactions listed in equation 1.40, where the intermediate species H_2^+ is considered to react instantly to form H_3^+, and primarily destroyed by dissociative recombination shown in equation 1.41.

In JIM, in order to prevent local charge build-up and agree with the observed neutrality of the Jovian atmosphere, the ambient electron number density is set to be equal to the sum of the densities of all the positive ions. Under the conditions which JIME will be simulating H^+ is the dominant ion by a significant margin. High H^+ density is therefore associated with high e^- density which, from the equation for H_3^+ recombination timescale

$$\tau_r(H_3^+) = (\kappa_r[e^-])^{-1} \tag{3.11}$$

where κ_r, the rate constant used in JIME is taken to be $\sim 10^{-7} cm^3 s^{-1}$ at 300K (Mitchell et al., 1983), can be seen to lead to proportionately increased H_3^+ recombination rate and hence reduced H_3^+ lifetime. By and large processes which produce H^+ will cause the destruction of H_3^+. This is an interesting phenomenon in that one would expect the increased UV photoionisation rate at 0.1AU to increase the H_3^+ density, but this may be at least partially offset by the increased H^+ and related e^- density, and will be an important point when it comes to interpreting the results produced by JIME.

3.1.7 Magnetic Field

The JIM magnetic field consists of a tilted, offset dipole whose strength and configuration may be modified by the input parameters. The energy input and density of auroral electron precipitation and the extent of the auroral region may likewise be set. For the main JIME runs the magnetic field and auroral electron properties have not been changed in order to limit the range of free parameters when it comes to interpreting the results. This raises an important question with regard to 51-Peg planet magnetic fields. Since the field is generated due to fluid motions in an electrically conducting medium, thought to be influenced by the rotation of the planet (Cardin et al., 2002), there is some question as to whether a planet rotationally synchronised with its star would have a significant magnetic field. There is limited evidence either way but research into rotation of binary stars (Yildiz, 2003) has suggested that the tidally synchronised outer layers of a gaseous body may be decoupled from the rapidly rotating core, allowing a dynamo generated magnetic field to be extant. Due to this uncertainty JIME has also been used to simulate a tidally synchronised planet with no magnetic field in order to investigate the similarities and differences induced in the thermosphere by the two differing regimes.

3.2 JIME Input/Output

JIM is designed to run non-interactively. That is, invocation of the JIM executable requires the passing of an input file containing a number of runtime parameters and an output file to where the run log is stored. An annotated copy of the additional parameters unique to JIME may be found in Appendix C. Once invoked JIM will run to completion with no further user input.

During initialisation JIM creates a number of binary files where relevant calcu-

lated values of ion and molecular densities, temperature, wind velocities etc. are written every specified number of timesteps. In addition JIME now also writes two additional formatted text files, one containing the densities of the major components in atmospheric energy balance, stellar UV heating and H_3^+ cooling and a second containing the Joviographic coordinates of the magnetic field zero dip angle.

For output file visualisation an IDL program named *Jimview.pro* was used, written by George Millward of the UCL Atmospheric Physics Group and modified by myself. For conversion between architecture specific binary JIM output and Jimview input file formats the twin programs *toascii* and *toidlbinary2.pro* were used, also slightly modified from the George Millward originals. Additional programs named *av.pro*, *avhc* and *ch.pro* were written by myself and used to manipulate and extract data in preparation for plotting.

3.3 JIME Development

3.3.1 Planetary Orbital Radius

The first stage in the development of JIME was to allow the stellar radiation input to be varied, allowing the effective orbital radius of the planet to be changed. JIM uses a solar radiation dilution factor, *Dfac*, in its calculations, amounting to the planet's distance in AU squared. At Earth's orbit Dfac would be equal to 1, whilst for Jupiter Dfac is set to 27 (Jupiter's orbital radius being 5.2AU). However, being that JIM was never intended to simulate anything but Jupiter, the value of 27 is hard coded into every subroutine. This required a lengthy process of examination and replacement of the hard coded value by a variable which could be read from the JIM input file.

3.3.2 H_3^+ Cooling

It has been suggested (see section 1.3.2) that H_3^+ may play an important part in atmospheric cooling, and would be of particular relevance to 51-Peg type exoplanets. JIM does not support H_3^+ cooling and therefore it must be implemented. This was achieved by adding a function named **coolh3** (see Appendix D.1), to be called once per timestep with the objective of calculating the energy loss at each grid element.

Data concerning the energy emission per H_3^+ molecule at a specified temperature obtained from first principles calculations by Dinelli et al. (1992) had been curve fitted to a polynomial by Tom Stallard of APL, but this fit extended only up to 2000K. It was considered that given the as yet unknown temperatures expected in JIME it would be wise to revisit the original data and refit over a wider range of temperatures.

For this purpose an IDL-based curve fitting routine called **MPFIT** (Markwardt, 2002) was used to fit the data between 500K and 3500K, producing the polynomial

$$\begin{aligned} E &= 1.420 \times 10^{-13} - 3.072 \times 10^{-16}T - 2.312 \times 10^{-19}T^2 \\ &+ 7.463 \times 10^{-22}T^3 - 1.358 \times 10^{-25}T^4 \end{aligned} \tag{3.12}$$

The quality of the fit can be assessed by overlaying a plot of the original data points between 500K and 3500K with that of the fitted function as shown in figure 3.1. As can be seen the two curves are indistinguishable.

This function was then incorporated into the coolh3 subroutine so that at each grid element the energy emission in $Joules\, s^{-1}$ is calculated. This is then divided by the volume of the element and the neutral mass density to obtain the cooling rate per unit mass.

Initial test at Jupiter distance showed that the energy balance remained relatively

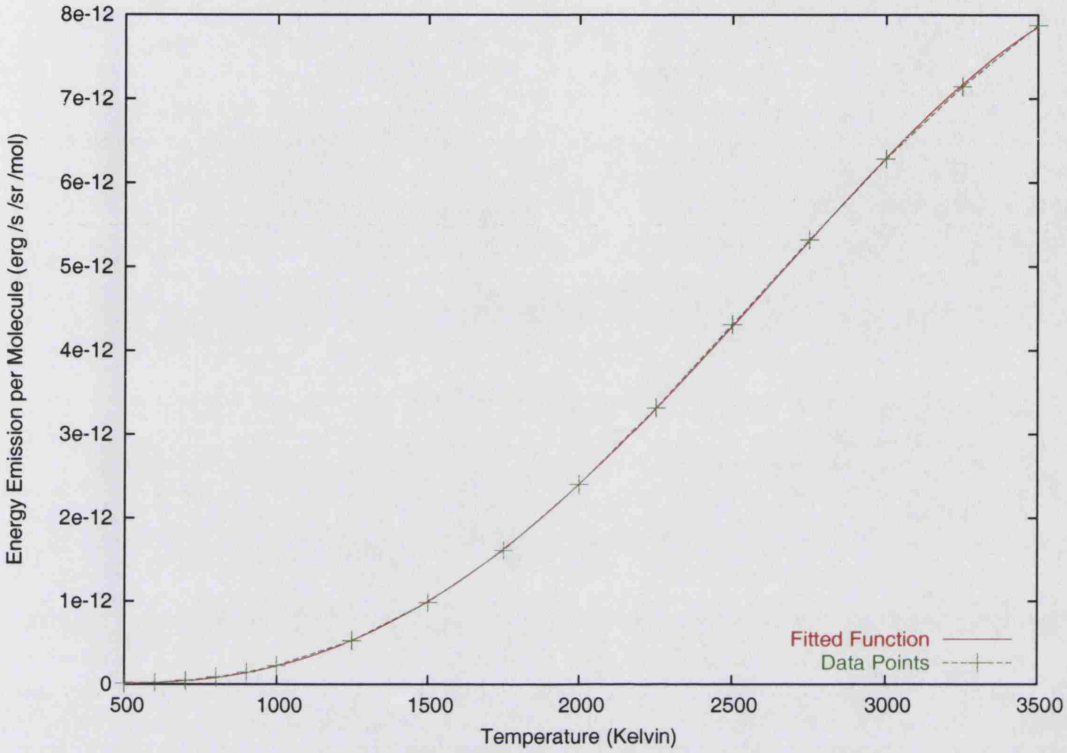

Figure 3.1: Overlay of fitted function and original data for H_3^+ emission with temperature.

steady with altitude until approximately half way up the model atmosphere where rapid cooling began to set in, increasing with altitude to the point where the highest pressure levels were cooling of the order 200K over the course of a Jovian rotation with no sign of slowing down. This was clearly a worrying situation and appeared to be at odds with studies of the Jovian thermosphere which predict flat or increasing temperature with altitude.

A physical explanation of why this phenomenon is not seen observationally is suggested as a consequence of the breakdown of Local Thermodynamic Equilibrium (LTE) in the upper thermosphere (Collins, 1991). Conditions of LTE can only exist where the mean free path of individual atmospheric species is small compared to the temperature scale height. As the local density decreases, the mean free path increases and collisions capable of exciting the H_3^+ molecule into an emitting level

are reduced. Thus the emission rate of H_3^+ is reduced below what would be expected if one assumed that the kinetic temperature specified the population levels.

A solution to this would be the introduction of modifier term to the code that artificially restrains the cooling rate dependent on altitude, and hence collision frequency. The restraining factor, an exponential modifier, has been chosen as follows:

$$f = e^{f1(n-f2)} - e^{-f3} \tag{3.13}$$

where $f1$, $f2$ and $f3$ are user specified parameters and n is the pressure level. The value of $f3$ is dependent on the other two parameters and is chosen so that the second term in equation 3.13 cancels out the first term at pressure level 30; i.e. the cooling rate at the top of the atmosphere is set to zero.

This function would activate if the pressure level were higher than a certain value, reducing the emission rate with altitude. Since the energy transfer properties of the upper atmosphere of Jupiter are virtually unknown it was necessary to experiment with the parameters over a number of JIME runs in order to find a set that prevented the dramatic high level cooling previously seen whilst still allowing for a reasonable fraction of the calculated energy emission in the mid atmosphere.

Eventually the values of $f1 = -0.1$, $f2 = 9$ & $f3 = -2.1$ for pressure levels above 10 were chosen. These values provided for a cooling rate at Jovian distance that preserved the temperature profile over a Jovian rotation whilst retaining the ability to keep up with the increased energy input as the planet is brought towards the star. Below pressure level 10 the stellar UV input is low enough that relative H_3^+ density is not sufficient to cool the planet to a significant extent over a small number of planetary rotations. It is important to note that the cooling rate is *very* sensitive, with small changes of the order of 10% in $f1$ and $f2$ leading to dramatic cooling at

the top of the atmosphere, causing a deep temperature inversion and significantly reducing the stability of the model. Clearly modification of these parameters will affect the equilibrium temperature of the model at a certain orbital radius, making the initial choices extremely important. This fact should be kept in mind when examining the data produced by JIME.

3.4 Stability Issues

A feature of JIM is that it is not designed for long runs. At 5.2AU it is sufficiently stable for runs of a simulated Jovian day or longer, but with increasing energy input driving faster chemistry and dynamics the length of stable runtime reduces dramatically, to the point where at 0.1AU it was only possible to achieve runs of approximately 5 Jovian *minutes* before the model crashed. At this orbital radius the chemistry timescale is reduced to the point where it is of the order of the numerical timestep, Δt used in the model, at which point statistical noise dominates the calculation. A discussion of the importance of the timestep and its relation to the chemistry timescale is make in sections 3.4.2 and 3.4.3. However, whilst reducing the timestep will reduce the noise it will also increase the computation time required to perform a JIME run, requiring a compromise to be made.

Initially undertaken using *Miracle*, a Silicon Graphics Origin 2000 supercomputer designed for multiple users and parallel tasks, a 6000 timestep run with a 4 second timestep would complete in approximately a week. Reducing the timestep in order to increase temporal accuracy would correspondingly increase the run time to the point where the time required to complete a single run would be unacceptable. Clearly these stability issues with a standard timestep length would have to be resolved if JIME were going to be an effective tool.

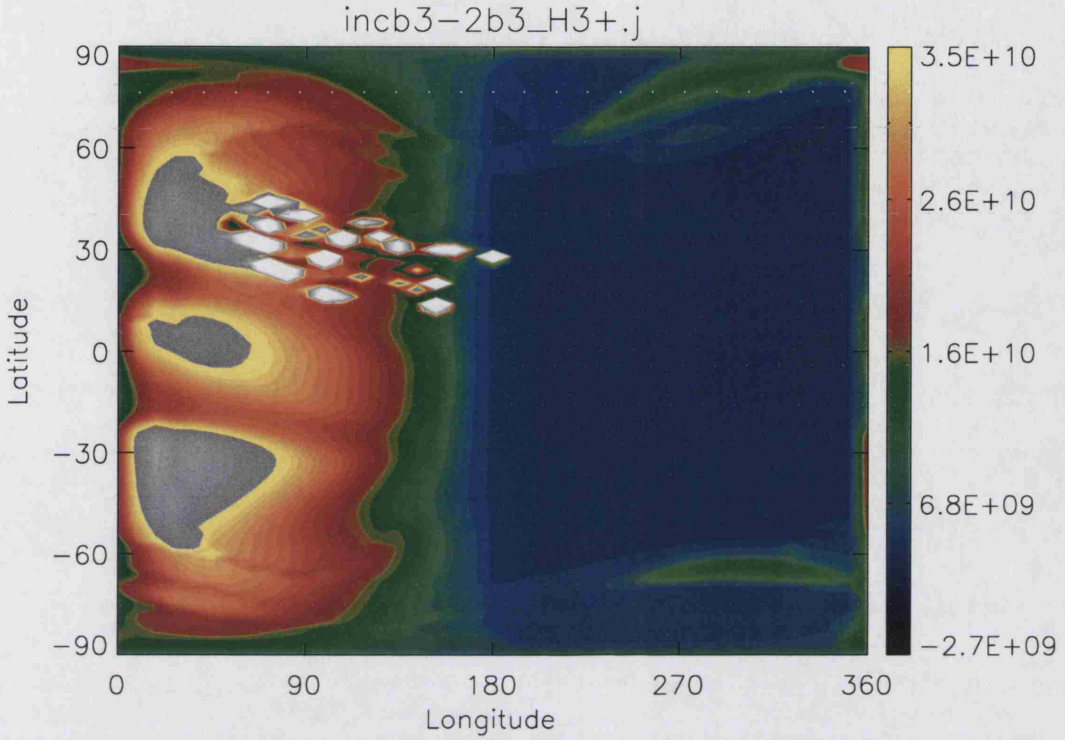

Figure 3.2: Example of a forest of H_3^+ spikes.

Roughly two-thirds of the way through the data-gathering process Miracle failed due to overheating and both JIME and all backups were lost. At this point a year-old copy of the model was salvaged, updated and transferred to *Enigma*, a Sun Sunfire V880, which was able to complete runs between 20 and 50 percent faster than Miracle. However, the version of JIME used for the non-magnetised and magnetic field-aligned models as described in section 4 is somewhat less complete than that used for the others and some of the following features are visible. They are, however, isolated and do not significantly effect the overall results.

3.4.1 H_3^+ Spikes

The most obvious of the stability issues was the detection of H_3^+ spikes in the atmosphere as shown in figure 3.2

These spikes appear to occur pseudo-randomly with no obvious latitudinal preference and can exist for several simulated hours before rapidly increasing by two orders of magnitude in the space of a minute, causing a number of fatal errors such as wind speed and temperature rolling over and becoming negative, leading to a crash shortly afterwards.

It was noticed that shortly before the rapid spike growth the mixing ratio of neutral elements became highly distorted with fractional composition exceeding unity. Artificially limiting neutral species mixing ratio change to 0.1% per timestep delayed the rapid ion density growth but did not prevent it. Therefore it was decided to turn neutral chemistry off in the hope that this would prevent invalid mixing ratios occuring which may me a cause of the spike growth. It was decided that this would not render the model unphysical as the neutral mixing ratio was not expected to change significantly over the course of time. However, despite postponing the crashes for a number of timesteps, it did not prevent them.

Other attempts to source the problem led nowhere as spike growth was initially so slow that it left no signature and it was decided that the most effective solution would be introduce a smoothing routine that would check for spikes by comparing the density with an average value taken from the surrounding elements.

The first attempt at smoothing code named *sprtime* was designed so that every set number of timesteps the routine would be called and calculate the average ion density over each latitude. Every ion density would then be compared with the average density of its latitude and if it were greater than a set fraction over the average then it would be replaced by the average value.

Clearly this solution has a glaring deficiency in that averaging over the entire latitude does not take into account any diurnal variability and therefore the catch density (the density that would trigger the detection of a spike) for spikes has to

be high in order to avoid smoothing out genuine features. This allows spikes to get through unless one is smoothing every timestep, a processor intensive solution, and even then would only detect spikes after they had reached a level significantly higher than the greatest H_3^+ density for that particular latitude.

The second and definitive attempt, named *arcsprtime* and listed in Appendix D.2 started off as a modification of sprtime in which the average ion density of a short arc of elements on either side of the current element was taken. This has the advantage of allowing a varying average with longitude, taking into account the changing ion density with solar position, and so the spike catch density could be set to a smaller fraction over the average. In addition to the arc, the latitudinal elements on either side of the current element were added to the average to provide a larger pool of surrounding values.

Whilst the stability of the model was vastly improved over the non-smoothed edition, there was a concern about using the average value of elements. It was considered that should a large spike of an order of magnitude greater than the background appear within a group of elements it would more than double the calculated average.

When comparing the density of a spike to this skewed average the density catch would be triggered and the density set to the average value. But this new value would still be double that of the surrounding elements. If the smoothing code were activated every timestep then the spike would steadily be lowered until it reached the density catch fraction over the average but no further. This results in the same problem as for the *sprtime*; processor intensive smoothing or the risk of letting spikes through the net.

There is an even larger problem if there is also a minimum density set that would trigger smoothing, as has been added to the code in an attempt to correct

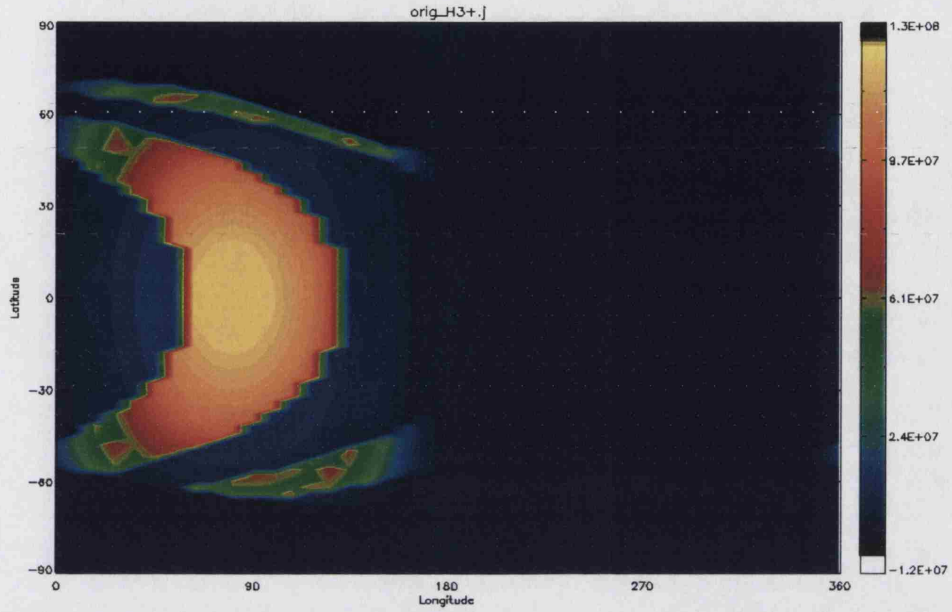

Figure 3.3: H_3^+ density bug at pressure level 2 for a planet at 5.2AU orbital radius.

for H_3^+ holes as described in section 3.4.3. In this case every *normal* density would be compared to this skewed average, found to be below the catch level and raised artificially. The consequence of this would be to raise the density value for *all* elements in the region, the exact opposite for which the smoothing code had been designed!

The solution to this problem was to calculate the median of a set of values instead of the average. If a large spike was amongst this set it would not effect the value of the median, and so would be more successful in removing spikes without influencing the values of any of the other elements.

3.4.2 Low Level Ion Bug

When one looks at a latitude-longitude plot of one of the lower pressure levels of a typical JIM run (figure 3.3) there is an obvious and distinctly non-physical crescent-shaped bite out of the density profile of both the H^+ and H_3^+ ions.

This feature is fixed to the numerical grid, as opposed to following the movement of the subsolar point, and can therefore be considered a model-induced feature.

Investigation reveals that this is a consistent feature throughout all previous JIM runs and quite possibly present in the precursors to JIM on which the code is based. It appears that blank regions of variable shape and size occur between pressure levels 2 and 4. Although it does not appear to effect the densities of pressure levels higher than this it is a disturbing occurrence that may have unseen consequences for stability.

Studying the code it appears that there are some serious calculation errors in the computation of H_3^+ density time derivatives, used to set the density of the ion at the following timestep.

The three components that dictate the change in ion density at a point are

- Bulk flow.
- Divergence of diffusive velocity.
- Chemical reaction rates.

Of these three terms, particularly in the 51-Peg region, the chemical component is by far the dominant by several orders of magnitude.

The problem appears to occur where the variables holding values of the first two components are extremely low, of the order of 10^{-14} or less. Printing out the contents of the variable shows that it is assigned correctly. However, *any other operation* on the variable, even assigning the contents to another variable will corrupt the value. As an example for a particular model run at 0.8AU the contents of some typical corrupted values were output. For the variable *xbulk*, the bulk flow, the calculated value was -4.31×10^{-14} whereas the assigned value used to compute the time derivative was changed to -74.0!

Clearly such a massive negative derivative would explain the holes in the ion densities, but what is causing this error? Attempts at reassigning the variables as double precision had no effect. Recompilation of JIME on three separate architectures under three compilers, one of them using 64bit floating point math produced exactly the same errors.

On the face of it this is a baffling statement; any action using a variable causes that variable to change. It is also one that makes debugging difficult.

The consolation must be that this bug only manifests itself between pressure levels 2 and 4 (pressure level 1 has constant uniform density), below the levels that will be of interest in the JIME results. However it will be important to bear this information in mind when viewing ion densities in this region. Code has been added to check for the existence of this computational bug and throw out any bad values that are detected (see section D.3), using only the chemical component. Preliminary tests suggest that despite the prevention of massive negative values, the holes never fill in satisfactorily, with the same arc-shaped bite out of the ion density profile remaining stationary with respect to the JIME longitudinal grid. This suggests that there is a fundamental flaw in the code. Fortunately this feature has never occurred above pressure level 4 and examination of bulk flow calculations above this level show that errors do not occur.

3.4.3 H_3^+ Holes

At first glance related to the previously described Low Level Ion bug are the H_3^+ Holes. Although similar in appearance (see figure 3.4) they are of a different source and apparently not related to the computational error described in section 3.4.2. The major obvious difference between the two phenomenon is whereas the Low Level bug produced a distinctive arc shaped slice out of the ion density, the H_3^+

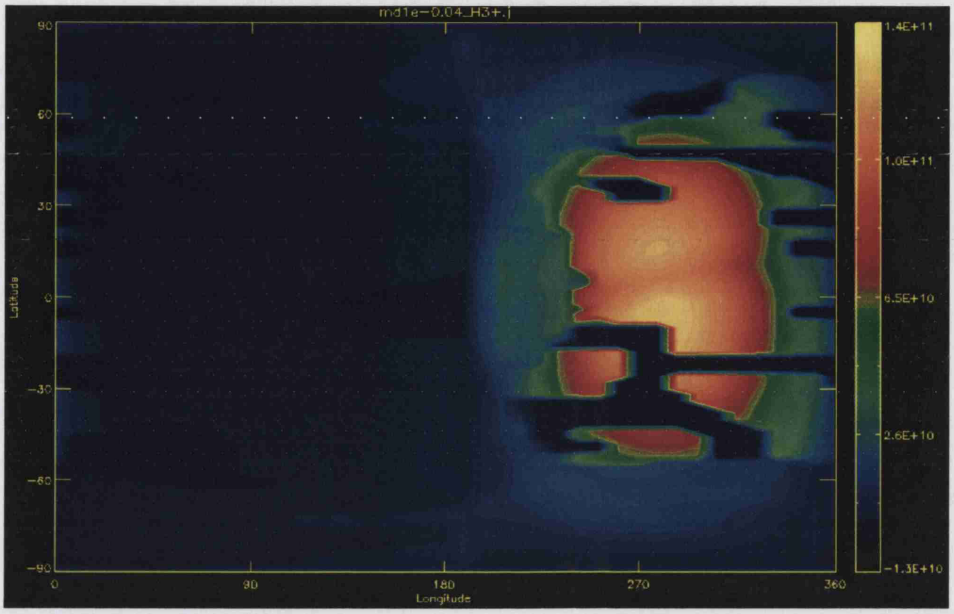

Figure 3.4: H_3^+ hole example at pressure level 16 and at an orbital radius of 0.2AU.

holes show random occurrence and are not apparently related to a JIM bug, but rather a fundamental feature of the numerical model.

Occurring approximately between pressure levels 15 and 25 and only afflicting the H_3^+ density, this particular feature appears to be related to chemical reaction rate as its intensity increases with decreasing orbital radius, first manifesting itself around 0.5AU and becoming more severe as stellar input increases.

As previously mentioned the JIME numerical timestep is a tradeoff between computation time and accuracy. It might be expected that the major destruction reaction of H_3^+, dissociative recombination, would determine the time resolution required to accurately simulate ion chemistry. The timescale for H_3^+ recombination is stated in equation 3.11.

As stated in Paper I, the peak e^- number densities in the Jovian auroral and non-auroral ionosphere are $10^6 cm^{-3}$ and $10^4 cm^{-3}$ respectively, corresponding to H_3^+ lifetimes of the order of $10\,s$ and $10^3\,s$. At 0.2AU e^- non-auroral number densities peak at approximately $2 \times 10^6 cm^{-3}$ at pressure level 20 and are above $10^6 cm^{-3}$

between pressure levels 15 and 25. This peak number density corresponds to an H_3^+ lifetime approximately equal to the timestep, a situation in which the chemistry in not able to be modelled accurately and would explain the unpredictable nature of the H_3^+ density profile in this region.

Given that the e^- density requires a lower timestep for accurate chemistry modelling and the constraints on the timestep due to available computer processor time a compromise solution was arrived at with the intention of limiting the time derivative of the H_3^+ density to a maximum fraction of the density. Although this solution appeared to prevent the holes appearing it did yield a artificial slowing of the build up of H_3^+ at dawn, as ion densities are very low and therefore the set rate of change of density is proportionally low.

The was replaced by the far simpler routine shown in appendix D.3 which simply throws out any time derivative values that are greater than a set proportion of the number density and replaces them with either 1% of the ion density or the time derivative calculated for the dissociative recombination rate, whichever is the smaller. Since this code was introduced there have been no further instances of the H_3^+ 'holes' leading to the conclusion that where resolution is not essential and runtime is important JIME may still be used with a larger timestep than might otherwise be required.

3.4.4 H_3^+ Speckling

The speckling of H_3^+ density, best described by an example as shown in figure 3.5, is another manifestation of the comparative H_3^+ lifetime to timestep problem.

Consider a particular atmospheric element with number density $[H_3^+]$, density time derivative $\delta[H_3^+]$, timestep T and timestep length, t. JIME calculates the time derivative due to the balance of constructive and destructive processes and uses this

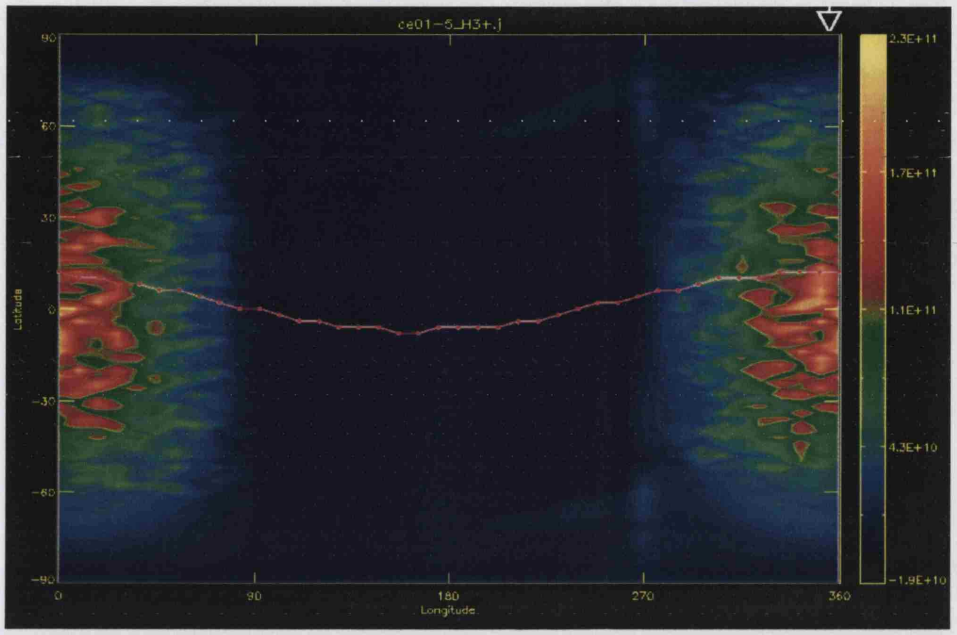

Figure 3.5: H_3^+ speckling due to timestep length at 0.1AU.

to compute the number density at timestep $T + t$ like so:

$$[H_3^+]_{(T+t)} = [H_3^+]_{(T)} + \delta[H_3^+]t \tag{3.14}$$

For short timesteps compared to the H_3^+ lifetime, the density difference at timestep $T + t$ compared to T will be a small compared to the density itself. For long timesteps, however, quick density changes are extrapolated over a comparatively long time period, introducing unpredictable fluctuations of the kind shown in figure 3.5, commonly known as noise.

If these fluctuations are indeed noise then it should be possible to filter them out by taking the average of a number of sets of output one timestep apart, and this has been done at 0.1AU where noise has become particularly intrusive. In this case (figure A.20(b)), averaged over 100 timesteps) it is possible to see how the noise has been removed compared to the original plot (figure 3.5).

This averaging process has only been used for the 4 second timestep model at

0.1AU due to disk space and time limitations.

3.4.5 Determining Reliable Features

With the above additional code specifically designed to remove certain features from the data it is important to question whether a particular observed feature can be considered a 'bug' and removed or whether it is genuine and should be explained and not smoothed out.

It has been standard practise when adding any code that may potentially effect the output to compare data plots over long runs, ensuring that only the intended features are effected and that the remaining plot is identical.

It must be remembered that the model is comprised of a grid of cells, and that any features on the scale of a single cell should be treated with suspicion, particularly when their value deviates significantly from those surrounding it. This is in essence what the previously described spikes are. Geometric artifacts such as those seen in figure 3.4 overlaying otherwise smooth profiles clearly have no physical cause.

Whereas some features are clearly artifacts, others are not so clear cut. Examining the plots in Appendix A shows a number of apparently smooth features, such as the H_3^+ peak at dawn, that are not seen in the original JIM data. Are these also model-induced artifacts?

Fundamentally, any new features observed in JIME must be explained using the known physics incorporated in the model in order to be considered genuine. However, an attempt must be made to explain even those features considered artifacts, in order to better understand the processes occuring numerically.

Chapter 4

Results

The stated aim from the beginning of this thesis has been to simulate the conditions expected to exist in the thermosphere of close-orbiting exoplanets. Chapter 2 describes the processes of orbital and rotational evolution that conclude with a planet in a 51-Peg type orbit and it is important to begin by explaining how these theories are interpreted and the JIME run series that are performed in order obtain the final goal.

4.1 Properties of a JIME Model Planet

From figure 2.11 it can clearly be seen that the population of circularised planets lies interior to 0.1AU. As previously stated this is due to the timescale for circularisation dropping to that of a typical dwarf star main sequence lifetime at an orbital period of approximately 4.5 days, which is equivalent to approximately 0.06AU as shown in figure 4.1.

A closer look at the region around 0.1AU (figure 4.2) does indeed appear to show a demarcation between the planetary population interior to 0.06AU with eccentricities $\leq$ 0.1 and that further out in which not all have had sufficient time to

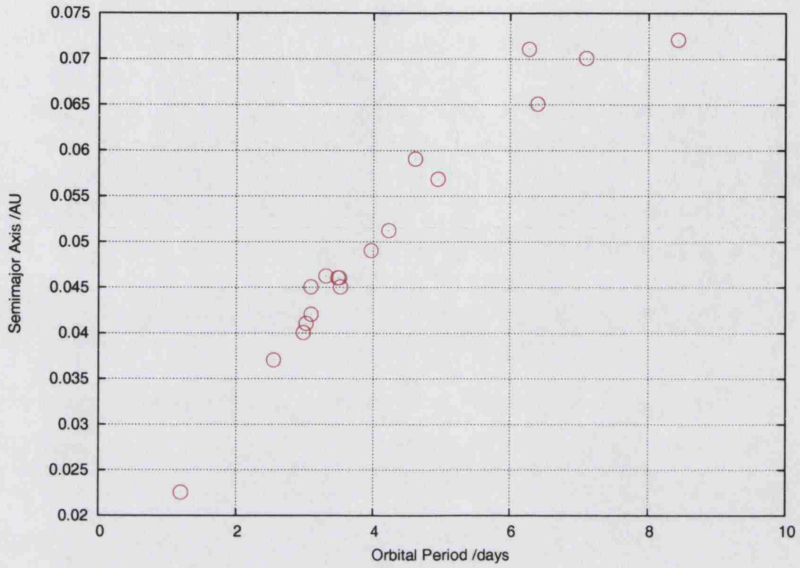

Figure 4.1: Orbital period versus semimajor axis for exoplanets with periods less than 10 days.

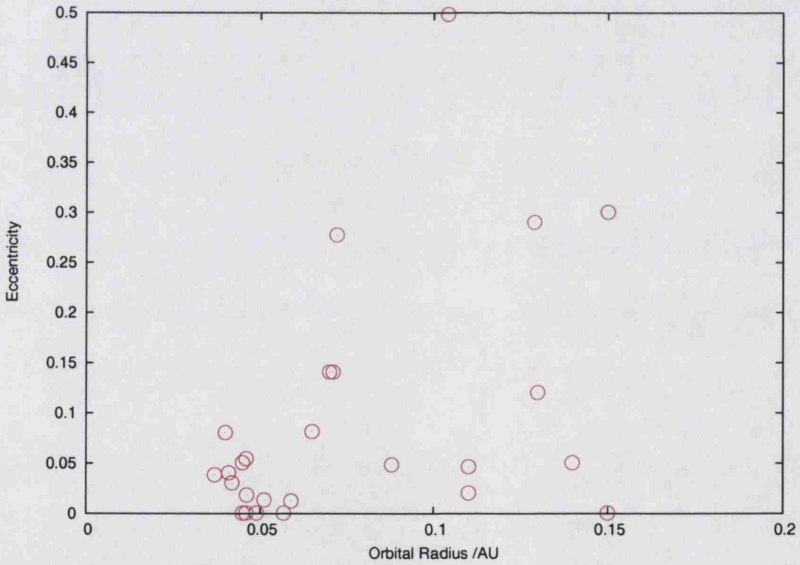

Figure 4.2: Eccentricity of exoplanets in the 51-Pegasi region.

circularise their orbits.

However, balancing this figure with the capabilities of JIME, it was considered that 0.1AU would be an appropriate position to set the final orbital radius of a model planet. The figure itself is somewhat arbitrary in that the only expected difference between a low eccentricity planet at 0.1AU and 0.06AU is the near threefold

increase in stellar radiation intensity which, considering the intensity increases from Jupiter's orbital radius to 0.1AU by 2700 times and taking into account the additional time that would be required to obtain model stability and the expected lack of extra information that would make this worthwhile, is considered an acceptable compromise.

Additionally, in section 2.4.2 it was stated that planetary spin down leading to tidal locking occurs on a much shorter timescale that circularisation. Using equation 2.26 it is possible to calculate that for a main sequence star 10^9 years old, tidal spin down has had time to occur for Jupiter mass planets out to an orbital radius of approximately 0.7AU. Therefore at 0.1AU tidal forces are considered to have slowed the rotation of the planet so that, with a circular orbit, one hemisphere permanently faces the star and the other is perpetually in darkness. However, given the timescale for planetary spin down it is probable that the majority of planets with orbital radii in the 0.1 to 1 AU region shown some level of rotational retardation. Therefore the major distinction between those planets with orbital radii sub 0.06AU and the rest is that the former population are all rotationally synchronised whereas the latter are made up of both rotationally synchronised planets (in the case of circular orbits) and simply slow rotating (where orbital eccentricity causes libration over the course of the orbit).

Taken at face value this would appear to suggest that the planetary magnetic field is at best residual, with no dynamo action occurring in the core. However, as discussed in section 3.1.7 there is uncertainty regarding the effect of tidal spin-down acting throughout the layers of the planet. It has been proposed that the surface layers of the planet may be brought into synchronous rotation with the star whilst the core may be decoupled and still rotate independently, allowing a significant magnetic field to be generated.

Run Series	Magnetic Field	Rotation	Page
cm-j0	None	Synchronised	207
cm-me	Rotationally Aligned	Synchronised	200
ce	Jovian	Jovian	157
cm	Jovian	Synchronised	186

Table 4.1: Summary of the model runs described in this section in the order in which they are discussed, including the start page of the output data as shown in Appendix A.

Given the caveats stated above it has been concluded that three separate strategies are required in order to cover the full range of possibilities of orbital evolution. The final goal in each case is to achieve a stable planet at 0.1AU from the Sun. Whilst this does not take into account the different spectrum of the host star, the majority of planets so far detected orbit main sequence G dwarfs such as the Sun, allowing this generalisation to be made. This is not a physical property of the host star, simply a selection effect in that astronomers have been primarily searching for planets around Sun-like stars where they know planets are capable of forming. In each run path once 0.1AU has been reached a separate model is branched off and is run to the point of model floating point overflow with a timestep of 1.3 seconds, the aim being to approach as close to equilibrium energy balance as possible

4.2 The JIME Run Series

The JIME model planet properties are shown in table 4.1, along with the page where the start of the output data is located.

The first planet, codenamed **ce**, is the control, being an exact copy of Jupiter. It is brought in from its initial location at 5.2 AU to 2AU, 1AU, 0.8AU and then in steps of 0.1 AU until it reaches an orbital radius of 0.1AU. At each location the model is run for 6000 timesteps, with each timestep being 4 seconds, this being

equal to 6.67 terrestrial hours. This is less than one planetary rotation, meaning that the entire surface of the planet would not be illuminated in a single run. This may raise the question as to whether the subsequent lack of equilibration may allow non-physical features to persist as orbital radius is reduced. However, this situation has been considered acceptable for the following reasons:

Firstly, as we shall see H_3^+ formation rates and lifetimes are of sufficiently short scale that chemical equilibrium can be approximated in a fraction of a rotation. Evolution over the majority of a run at a particular orbital radius consists primarily of temperature rise, which is not a concern until the 0.2 to 0.1 AU region, where the planets this thesis is attempting to study reside. H^+ lifetimes are so long that it would take several rotations for equilibrium to occur, which is not practical due to time considerations. The goal is to reach equilibrium if possible at 0.1AU.

Secondly, a number of runs were branched at 0.3AU and run to thermal equilibrium. These extended runs showed all the ion features observed in the transient runs, suggesting that they are stable and not an artifact of the lack of equilibration.

The second planet, codenamed **cl** is branched from the ce runs at a distance of 0.8AU and mirrors the first run path from there in to 0.1AU. The major difference between the two paths is that the planetary rotation period of the cl branch is decreased at each position, from 20 hours at 0.8AU to 200 hours at 0.2AU, at which period JIME sets the rotation rate to be zero. This is done in order simulate a rotationally synchronised planet at 0.2AU and it is achieved in several steps not for physical reasons but in an attempt to minimise the impact on the JIME atmosphere of a sudden halt in planetary rotation. This run series may be considered an experimental set; clearly such rapid spiral in and rotational synchronisation would never happen but it was useful to examine how ion density reacts to both increasing stellar UV input and decreasing rotational period.

The third planet, codenamed **cm** is branched from the ce runs at a distance of 0.4AU and immediately sets the rotation rate to be zero. This run takes a different approach from the cl runs in that it attempts to allow the impact of a sudden rotation rate halt to occur at sufficient distance from the star that there is time for the chemistry and wind patterns to recover before entering the 51-Peg region. Also the region of rotational synchronisation as calculated earlier suggests that planets with one hemisphere permanently facing the parent star may extend far beyond the circularisation region, and this series of runs attempts to simulate this.

It is important to remember that all the above models are based on the characteristic properties of the planet Jupiter, such as the inclination of the rotational axis to the orbital plane and offset and tilt of the magnetic dipole. When considering a tidally locked planet it must be expected that such assumptions will not be valid for two reasons. Firstly, by definition the rotation axis of a tidally locked planet will be orthogonal to the orbital plane, with the consequence that setting this to any other value would be unphysical. The planetary equator would therefore be parallel to the orbital plane. Secondly, the magnetic field will be primarily generated by planetary rotation. In the case of a tidally locked planet the rotation period is equal to the orbital period, which for a 51-Peg type planet would be in the order of 10 days. It is unlikely that such a slow rate of rotation would be able to generate a magnetic field of any great strength. Therefore additional runs were obtained, codenamed **cm-me**, with identical properties to the cm series but with rotational axis set to 90° to the orbital plane and the magnetic dipole directly aligned with the rotational axis. The fact of the rotationally aligned dipole should mean that the cm-me runs will be symmetric about the Joviographic equator, allowing field-generated features in the cm runs to be identified.

The final planet, **cm-j0** is a second extension to the original cm series and is the

Orbital Radius /*AU*	Rotational Period /*hours*		
	ce	*cl*	*cm*
5.2	9.92		
2.0	9.92		
1.0	9.92		
0.8	9.92	20.0	
0.7	9.92	30.0	
0.6	9.92	40.0	
0.5	9.92	60.0	
0.4	9.92	80.0	RS
0.3	9.92	100.0	RS
0.2	9.92	RS	RS
0.1	9.92	RS	RS

Table 4.2: Summary of JIME runs. Rotationally synchronised (**RS**) planets are assumed to present one face permanently to their parent star.

simplest of all in that the magnetic field is effectively turned off. This should provide the cleanest set of results of all the models, being uncontaminated by ion drift effects, and should provide the most accurate simulation of what might be expected to be the textbook 51-Peg type planet; unmagnetised and rotationally synchronised.

A complete summary of the model runs may be found in table 4.2. When referring to a particular run I shall use the codename plus the orbital radius of the planet so, for example, a *cl* run at 0.5AU would be referred to as **cl05**. The runs at 0.1AU using a 1.3 second timestep are referred to by removing the first letter of the codename and replacing it with a number 1, for example **1e01**.

Output from each run is plotted after 1000 timesteps. This was done initially as the model was not sufficiently stable to guarantee long runs when the stellar UV intensity was incremented. Subsequent tests have proved that the ion densities do not vary greatly between timestep 1000 and 6000 and so this strategy was continued for the sake of consistency. As I have stated earlier, achieving thermal equilibrium at a particular orbital radius is not of primary concern until the 51-Pegasi region is reached.

4.3 Selecting the JIME Output

In producing the results which follow I have decided to take latitude-longitude ion density profiles at two separate pressure levels, 16 and 26, corresponding approximately to pressures of 5×10^{-6} and 10^{-7} *millibars* (*mb*) respectively. These two levels were chosen after some experimentation in that they capture separate atmospheric features at middle and upper regions of the simulated thermosphere. Both the stellar EUV input and the H_3^+ cooling decrease from a peak around pressure level 26 and fade to negligible around pressure level 16 so plots of ion densities at the lower altitude are expected to show few features produced by these processes. At pressure level 26 the stellar EUV input is expected to be near a peak so it will be interesting to see how this effects the atmospheric composition.

Considering the wealth of available data that has been produced it is important to recognise which is important and which may be discarded. Therefore I have decided to include the plots of the **ce** run at 0.8AU, 0.3AU and 0.1AU, and the **cl** and **cm** runs at 0.3AU and 0.1AU. In addition I have provided the original JIM output for reference, produced by Nick Achilleos, and additional output at 0.1AU when the model has run with a 1.3 second timestep for as long as possible. Where further intermediate information is important the plots will be referenced as required when discussing the results.

In selecting the range of orbital radii displayed it has been decided to take an order of magnitude increase in $Dfac$ from 0.01 at 0.1AU to 0.1 at approximately 0.3AU, and another further approximate order of magnitude increase to 0.64 at 0.8AU. Experimentation has revealed a progressive graduation of atmospheric properties between the selected radii, rendering the remaining data superfluous.

The plots to be displayed are shown in the following order in Appendix A:

- **H^+ and H_3^+ local density at pressure levels 16 and 26.** This will enable local patterns in the ionisation profile to be observed.

- **H^+ and H_3^+ column densities.** This will allow the total extent of the ionisation of these two major species to be observed with increasing stellar input.

- **H^+ and H_3^+ longitude-local density profiles at pressure level 26 on the Joviographic equator.** This will allow the balance between the two primary ions to be observed over the course of the day-night cycle.

- **Temperature profile at the subsolar point and midnight.** These two plots allow the two extremes of the heating profile to be illustrated.

- **Energy balance at subsolar point and midnight.** These two plots each allow the stellar EUV input, H_3^+ cooling rate and total energy balance to be compared. The energy balance plot includes all forms of heating and cooling, not just the two dominant processes, allowing the significance of H_3^+ cooling and stellar EUV to be assessed.

It is important to note that each of these plots represents a snapshot of the model in its path towards the ultimate goal of 0.1 AU and are, due to time constraints, not fully equilibrated. As will be shown, however, the ion densities in particular achieve their equilibrium levels within a short timescale. Data obtained from fully equilibrated models at 0.3 AU and 0.1 AU, approximately the orbital radii of Mercury and a 51-Peg planet respectively are discussed later in this chapter.

In each of the latitude-longitude plots that follow the Jovimagnetic equator is represented by a sinusoidal line and the position of the subsolar longitude is always located at 180° unless otherwise stated. The longitudinal axis scale from 0 to 360°

originates at the zero point of the model grid and is not meant the actual Jovio-graphic co-ordinates. As such they can always be considered as a way of displaying angles duskwards (> 180°) and dawnwards (< 180°) of the subsolar point. The plots themselves may be found in Appendix A and a discussion of the results follows below.

4.4 cm-j0 - Non-Magnetised and Rotationally Synchronised

The location of data plots referred to in this section is shown in table 4.3.

Model	Orbital Radius	Page
cm03-j0	0.3 AU	207
cm01-j0	0.1 AU	212

Table 4.3: Location of output data of the cm-j0 model run.

Despite the fact that the non-magnetised model planet was obtained last after branching from the cm series at 0.4AU, it is useful to examine it first as it provides a generic base from which the special cases of rotating and magnetised planets may be considered.

In examining the data for this planet it is useful to compare the results with the magnetised-synchronised planet (**cm-me**) at the same orbital radius, as the only altered variable is presence of a magnetic field aligned with the rotation axis.

4.4.1 Ion Density

Observing the H^+ ion density at pressure level 26 for the non-magnetised planet at 0.3AU (figure A.51(a) on page 209) reveals a near rotationally symmetric plot about the subsolar point, as would be expected for a planet where the only variable

determining ion density should be distance from the subsolar point. It is important to take into account when examining these ion profiles that:

- The latitude grid resolution of JIME is more than double that of the longitude grid.
- The longitude and latitude axes of the JIME output use different scales.
- The longitude axis is open and wrapped round on itself, whereas the latitude axis starts and ends at a point. This entails treating the grid cells connected to the poles separately from the rest of the numerical grid, as they are three-sided.
- Shadows of the auroral regions still remain due to residual ion precipitation.

Also, it is possible to see an extended H^+ peak following what would have been the magnetic equator. This is due to the fact that this model had been branched from the magnetised rotating model 70 simulated minutes previously and the long lifetime of H^+ under these conditions ($\sim$60 hours) means that magnetic field generated features still exist.

An examination of the initial H^+ and H_3^+ densities for this model planet at 0.3AU (pages 208-209) and 0.1AU (pages 213-214) in comparison to that of Jupiter (pages 151-152) reveals a shift in the relative abundance of these ions. In Jupiter's atmosphere the low latitude local density of H^+ and H_3^+ at pressure level 26 is near identical, being $\simeq 3 \times 10^9\, m^{-3}$. The equatorial column density for H^+ is $\simeq 5 \times 10^{15}\, m^{-2}$ and that of H_3^+ is $\simeq 7 \times 10^{15}\, m^{-2}$. The low latitude density of both ions is dominated by that of the auroral region.

At 0.3AU the peak density now occurs at the subsolar point due to the lack of significant auroral precipitation in this model. The H^+ and H_3^+ peak densities at

pressure level 26 are now $\simeq 6 \times 10^{11}\, m^{-3}$ and $\simeq 9 \times 10^{9}\, m^{-3}$ respectively and the column densities are $\simeq 10^{18}\, m^{-2}$ and $\simeq 5 \times 10^{16}\, m^{-2}$.

The corresponding H^+ and H_3^+ densities at 0.1AU are $\simeq 10^{12}\, m^{-3}$ and $\simeq 2 \times 10^{10}\, m^{-3}$ respectively with column densities of $\simeq 5 \times 10^{18}\, m^{-2}$ and $\simeq 2 \times 10^{17}\, m^{-2}$.

In addition to the expected greater ion density with stellar flux the most interesting result is the increasing dominance of H^+ over H_3^+ with reducing orbital radius, a phenomenon anticipated by Moore et al. (2003) and described in section 1.3.2. Whereas the high level H^+ density increases by nearly three orders of magnitude from 5.2AU to 0.1AU, the H_3^+ density increases by less than one order of magnitude. This has the effect of reducing the contribution to planetary cooling by H_3^+ emission below what would be expected by simple scaling of overall ion density.

4.4.2 Density Evolution

Given the residual magnetic field features in the above data it is useful to examine the planet at 0.3AU for a longer period, at an orbital radius that is still quite highly irradiated but sufficiently stable for the model to run for a long period of time. In particular it would be useful to examine both how the H^+ and H_3^+ ion densities evolve over time, possibly achieving equilibrium, and whether the magnetic field-induced impurities will dissolve, allowing a cleaner view of the ion profile. The result is a run series that lasts for over 30,000 timesteps, a discussion of which follows.

Looking at the H_3^+ plot (figure 4.3) reveals two interesting features. Firstly, the subsolar region shows a minimum that anticorrelates with the H^+ density as predicted in section 1.3.2. Secondly, whereas the H^+ plot (figure 4.4) shows a pronounced peak at the subsolar point, the H_3^+ profile (figure 4.5) appears to be almost flat over much of the hemisphere. This is due to the increased level of H_3^+ production due to photoionisation as the solar zenith angle decreases being offset by

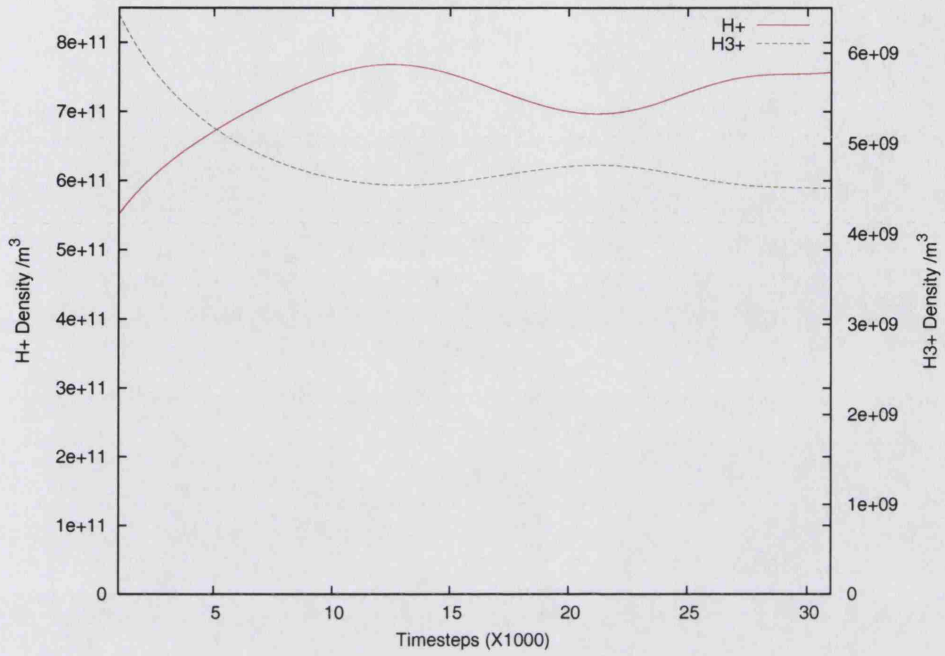

Figure 4.3: Comparison of H^+ and H_3^+ number densities at the subsolar point at pressure level 26 for a non-magnetised planet at 0.3AU.

the reduced H_3^+ lifetime due to increased e^- density as a consequence of rising H^+ density. This feature is easier to see in a plot through the subsolar longitude at the very top of the atmosphere as shown in figure 4.6. This phenomenon is considered in more detail when discussing the magnetised rotating planet.

Figure 4.3 shows the relative densities of H^+ and H_3^+ over time. The anticorrelation of the two species can clearly be seen in the figure, with H^+ density reaching a asymptotic peak after approximately 14 hours, corresponding to a H_3^+ minimum. After this the H^+ density dips and rises again, remaining approximately constant for the next 20 hours. The start of the H^+ dip at 13000 timesteps coincides with the start of a new run and therefore may simply be model-induced. It can be seen, however, that after the initial rise of H^+ the density remains roughly flat. Unfortunately the temporal resolution of the JIME output is not sufficiently fine to catch the initial features in the H_3^+ output below 1000 timesteps. It is expected that as

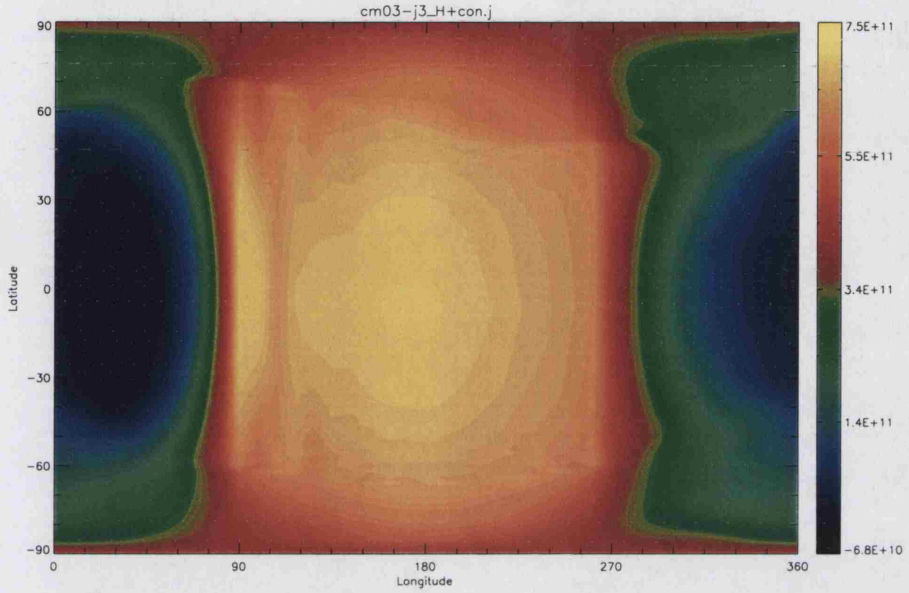

Figure 4.4: H^+ density at pressure level 26 after 21000 timesteps.

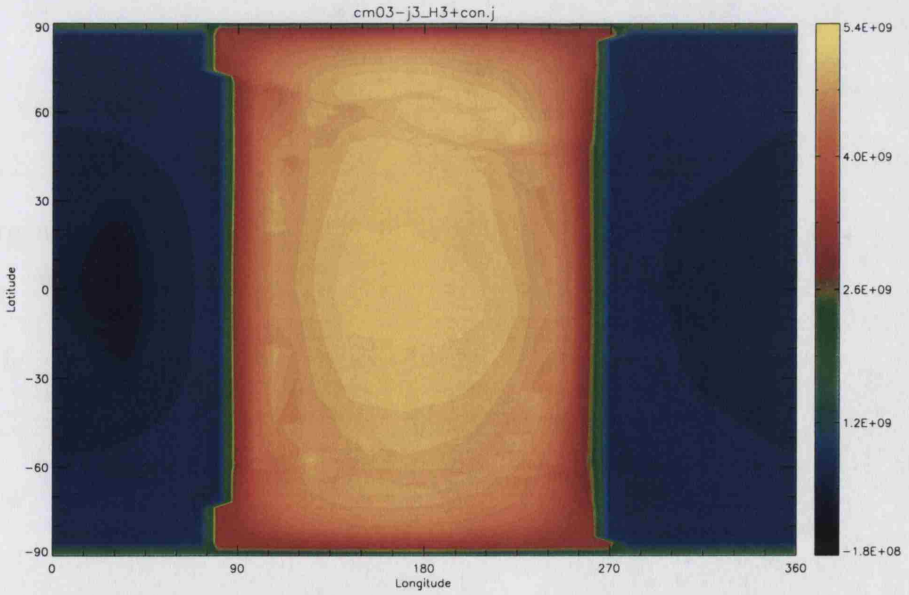

Figure 4.5: H_3^+ density at pressure level 26 after 21000 timesteps.

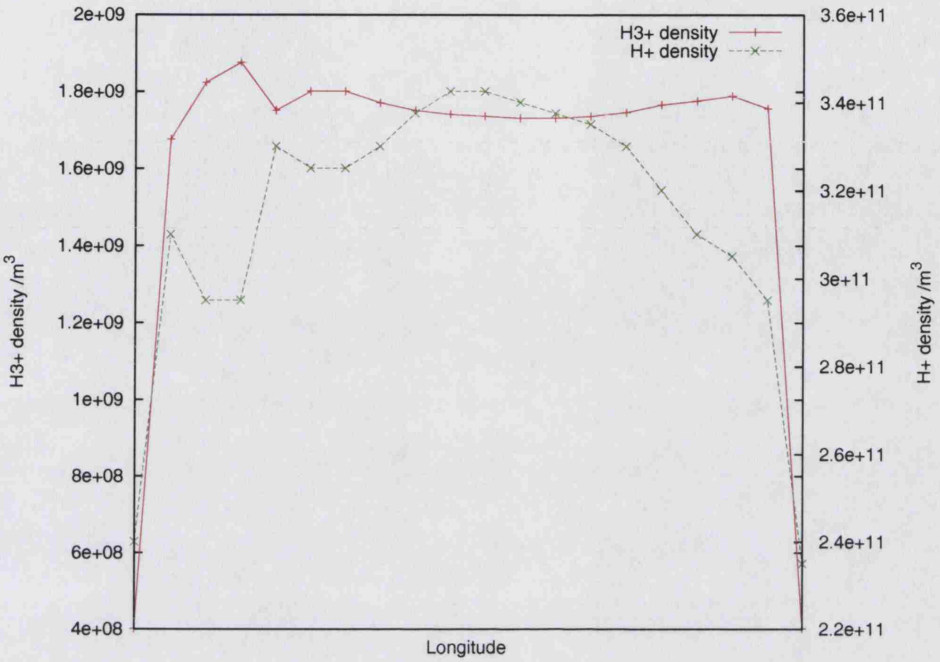

Figure 4.6: Plot of relative H^+ and H_3^+ densities from dawn to dusk through the subsolar longitude, showing flattened H_3^+ profile and H^+ peak.

the planet is moved in from 0.4AU to 0.3AU the H_3^+ density should rise rapidly, due to it's higher production rate than H^+, and then start to fall as H^+ density rises. In figure 4.3 we catch the tail end of the initial H_3^+ fluctuation. It should be noted that the variation in density of both ions over the course of this graph is $\sim 25\%$, considerably smaller than the difference between runs at different orbital radii.

Figures 4.4 and 4.5 show the ion profiles at pressure 26 for the non-magnetised planet at the equilibrated final position from figure 4.3. Visible in these plots are residual features due to the position of the auroral region, most clearly in the H^+ profile. Given that the lifetime of H^+ at this altitude is nearly 60 hours (see table 4.6 on page 116), it might be expected that the global ion profile would not be free of magnetic field effects, and some low-energy auroral ion precipitation is still present. However, observing the low latitudes near the Joviographic equator it is clear that both plots show a peak at the subsolar point, with density falling off approximately

equally in all directions and no extraneous features. This observation will be of importance when comparing this model with the magnetised ce and cm runs, where equatorial features come to dominate the ion profile.

4.5 cm-me - Rotationally Synchronised with Aligned Magnetic Field

The location of data plots referred to in this section is shown in table 4.4.

Model	Orbital Radius	Page
cm03-me	0.3 AU	200

Table 4.4: Location of output data of the cm-me model run.

The **cm-me** model is identical to the **cm-j0** model with the exception of a Jovian strength magnetic field aligned with the nominal rotation axis, i.e. passing through the poles of the numerical grid, and Jovian levels of auroral particle precipitation. This model is an attempt to simulate a rotationally synchronised planet with a decoupled core generating a strong magnetic field.

4.5.1 Ion Density

Looking at figure A.45(a) on page 202 reveals a striking new feature, a H^+ peak following the magnetic equator with symmetric minima on either side. Figure A.45(b) reveals the expected H_3^+ anticorrelation. Looking further down in the thermosphere at pressure level 16 (figures A.44(a) and A.44(b) on page 201) reveals an opposite profile; a H^+ trough at the equator and a H_3^+ peak. The H_3^+ profile is somewhat unclear due to the necessity of using an older version of JIME for this model. Given that the only new physical process in this model is the presence of a low latitude

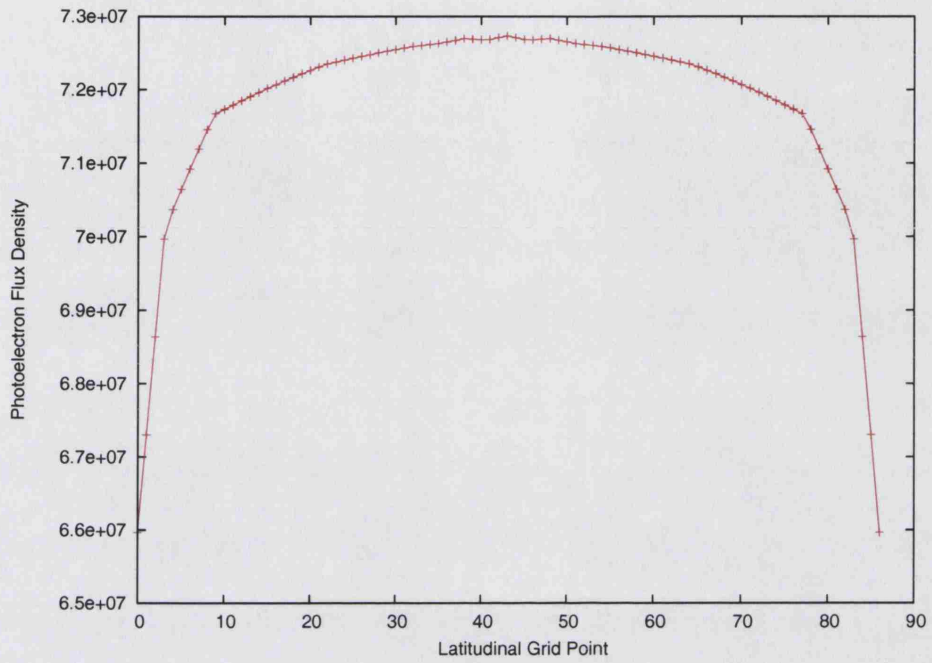

Figure 4.7: Photoelectron flux across the subsolar longitude at pressure level 26.

magnetic field it is logical to assume that this is the cause of the equatorial peak.

Examining Paper I reveals a similar equatorial peak that the author considered to be due to

> the near-horizontal orientation of the magnetic field in this region, preventing ionising photoelectrons from penetrating to the deeper layers of the thermosphere.

Thus, an excess of photoelectrons contributes to a high altitude peak of H^+ ionisation and produces a deficit resulting in a local H^+ minimum at lower altitudes.

In order to determine whether this process could explain the sharp H^+ peak it is necessary to examine the latitudinal variation in H^+ production along the line of subsolar longitude due to photoelectron flux. Figure 4.7 shows that at high altitudes there is a equatorial photoelectron enhancement, as would be expected if they were prevented from penetrating deeply. The profile is, however, extremely shallow.

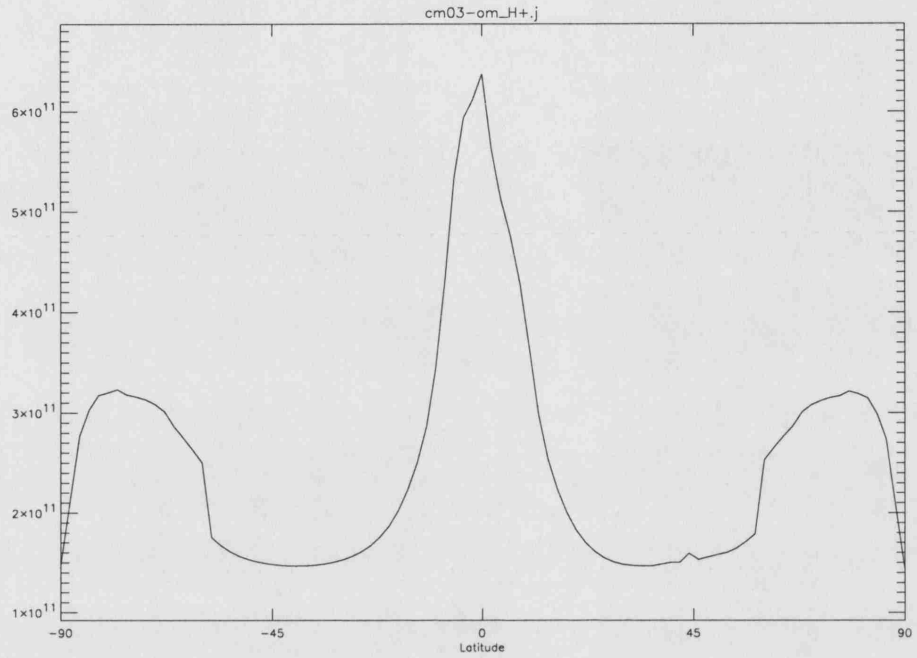

Figure 4.8: H^+ density at the same positions as shown in figure 4.7.

Comparing this with the H^+ density along the same line as shown in figure 4.8 reveals a notable discrepancy at the equator (the enhanced density in the polar regions is due to auroral particle precipitation); the peak is too great to be explained by a build-up of ionising photoelectrons.

An explanation is possible by examining the processes governing charged particle drift. As described in Paper I, JIM uses a Spiro type high latitude field based on the study by Quegan et al. (1982). At the lower latitudes which are of interest, fields are generated by wind flow across magnetic field lines.

The equatorial H^+ peak is similar to a structure known to occur on Earth, called the Appleton anomaly or, more recently, the Equatorial Ionisation Anomaly (EIA) (see for example Sambou et al. (1998) and Lui and Wan (2001)). In this case the combination of low magnetic dip angle and east-west electric field produces what is known as a *fountain effect*, where $\mathbf{E} \times \mathbf{B}$ vertical drift causes ions to rise up at the equator before field-aligned diffusion due to gravity, neutral winds and plasma

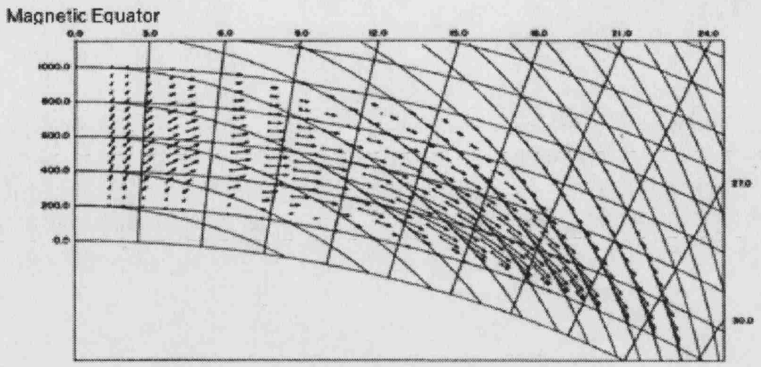

Figure 4.9: Demonstration of the ion velocity vectors under the influence of the Appleton Anomaly (Hanson and Moffett, 1966). Radial lines represent electric field and solid curved lines represent magnetic field.

pressure gradient causes them to sink down on either side of the zero dip angle equator. See figure 4.9.

An examination of the relevant JIME code reveals that ion drift is dependent on the $\mathbf{U} \times \mathbf{B}$ electric field caused by neutral particle flow across magnetic field lines. The correlation between electric field and ion drift velocity can clearly be seen in figure 4.10.

Now, examining the vertical ion drift along the line of subsolar longitude (figure 4.11 shows an equatorial structure similar to the H^+ density.

Notable from this plot is the near zero vertical velocity at the equator, with significant downflow on either side.

This last result would appear to suggest a solution to the H^+ equatorial peak. Charged particle winds flowing north and south away from the subsolar point due to temperature gradients pass through the vertical component of the magnetic field forming a crossed, longitudinally-directed electric field. This has the same direction on either side of the magnetic equator due to both the wind flow and vertical component of the magnetic field being oppositely directed. Ions then experience a downwards-directed force due to this electric field crossed with the horizontal

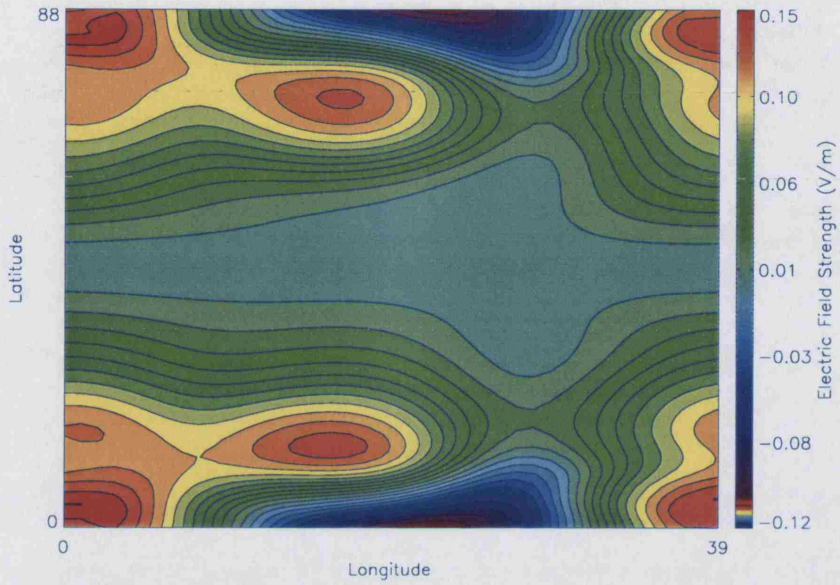

(a) Longitudinally-directed electric field

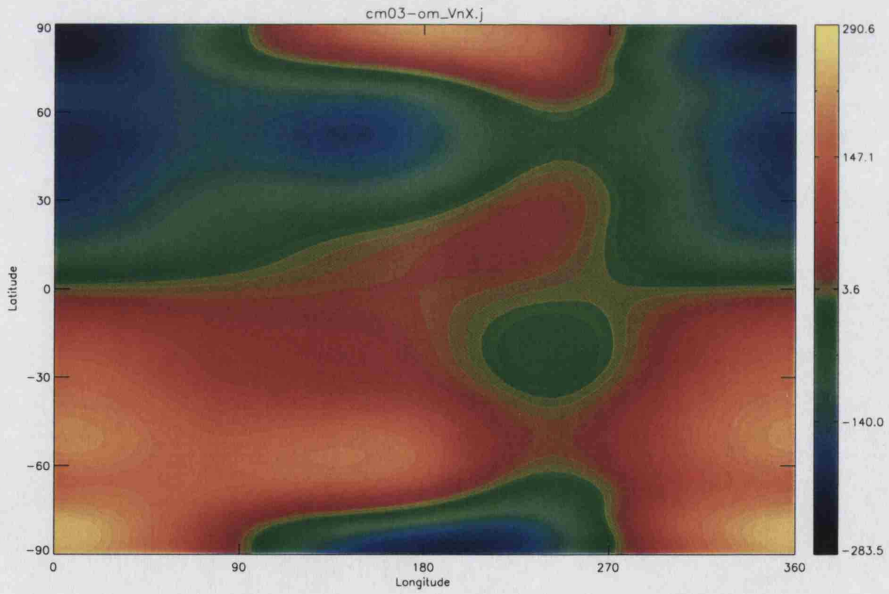

(b) Latitudinally-directed neutral wind velocity (ms^{-1})

Figure 4.10: Demonstration of the association between electric field and neutral wind velocity at pressure level 26 of a planet with an orbital radius of 0.3AU. The subsolar point is at longitude zero.

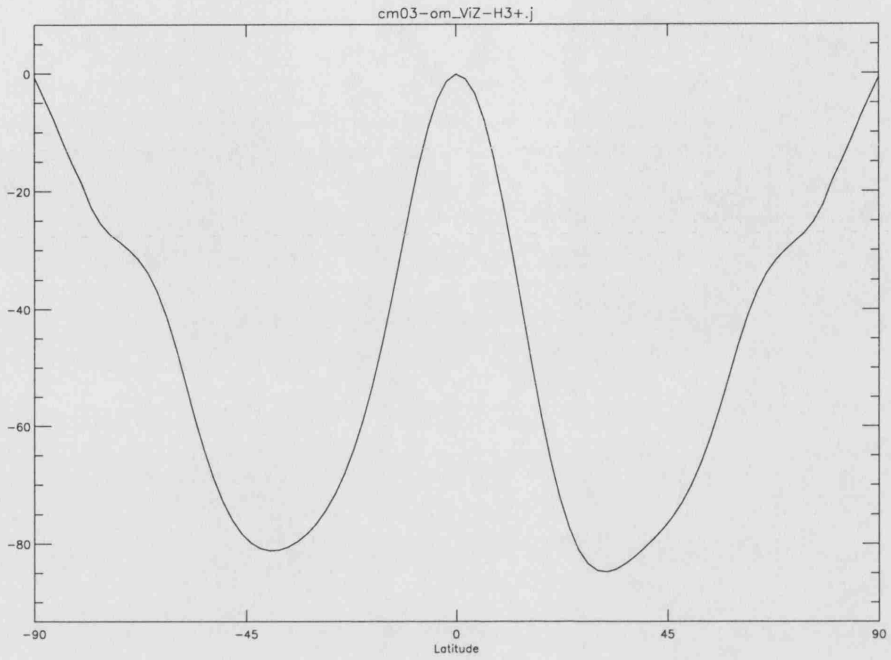

Figure 4.11: Vertical ion velocity at pressure level 26 at the subsolar longitude (ms^{-1}).

latitudinal component of the B-field, which has the same direction vector in both hemispheres.

Figure 4.10 shows the negligible electric field strength along the magnetic equator, implying a near-zero vertical ion drift which is indeed what is seen. At higher and lower latitudes the electric field is stronger and therefore the vertical drift velocity will be greater. Thus, away from the magnetic equator ions suffer a strong downwards force leading to the observed sharp dip in the H^+ ion profile.

Although the above results explain the equatorial phenomenon, examination of the JIME code reveals that the processes involved are unfinished. The unidirectional calculation of electric fields due to neutral wind flow is uncoupled and cannot be considered to be an self-consistent implementation of the physics involved. Therefore it is essential to examine the equatorial features of the magnetised planets with this consideration in mind, placing importance on the large scale ion densities rather

than local features.

Examining the overall ion density of the two planetary models discussed thus far reveals that although the magnetised model has a more complicated ion profile, explained above, the column densities of H^+ and H_3^+ are nearly identical. Although the peak H_3^+ density at pressure level 26 is higher, the presence of a central trough suggests the overall ion numbers at this altitude, taking into account the entire hemisphere, are practically the same.

4.5.2 Atmospheric Dynamics

A more detailed study of the heating and cooling of the rotating model will be discussed in section 4.6 but a glance at the temperature profiles at the subsolar and midnight points of the rotationally synchronised planet at 0.3AU (figure A.48) shows, as would be expected, a clear temperature imbalance between the day and night sides.

The wind patterns in a rotating planet are complex; Earth has three global circulation cells in each hemisphere, but it might be expected that for a rotationally synchronised planet the wind flow would be considerably simpler. With axial symmetry about the line through the subsolar and midnight points the atmospheric dynamics could theoretically be modelled two dimensionally. A plot of the high altitude wind flow for the magnetised-synchronised planet may be seen in figure 4.12.

The wind vectors in this plot reveals the neutral wind speeds that may be expected at pressure level 26. It would be expected that the temperature gradient from midday to midnight would produce extremely strong winds towards the night side, and this is indeed the case, with the speeds corresponding to the longest arrows being approximately $1200ms^{-1}$, a remarkable figure.

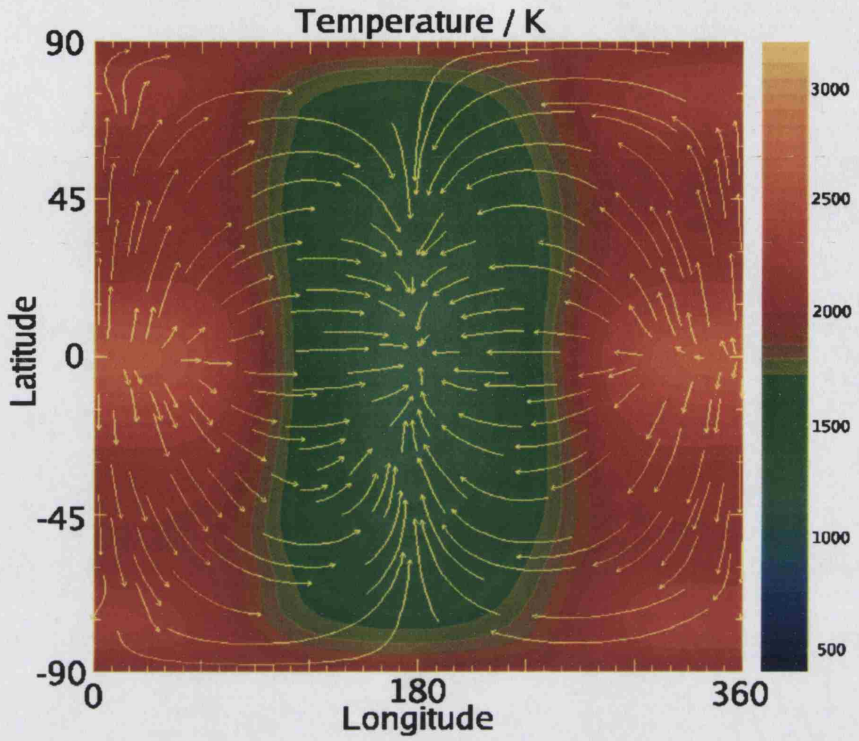

Figure 4.12: Neutral winds for cm01-me at pressure level 26. Midnight is at 180° longitude.

With this results in mind it is possible to infer the nature of thermospheric circulation for a rotationally synchronised planet at small orbital radius. The atmosphere around the subsolar point is strongly heated by incident UV flux and thus expands and rises. Around the midnight point the atmosphere cools and descends creating a single enormous circulation cell which keeps the atmosphere well mixed.

4.6 ce - Rotating with Tilted Magnetic Field

The location of data plots referred to in this section is shown in table 4.5.

The two models described previously have shown relatively simple structure due to the absence of or symmetrical nature of the magnetic field. This has made it easy to examine the variation of ion density with orbital radius and has shown the large

Model	Orbital Radius	Page
ce08	0.8 AU	157
ce03	0.3 AU	165
ce01	0.1 AU	172

Table 4.5: Location of output data of the ce model run.

scale atmospheric circulation pattern of the planet.

In this section I will be examining the case of a rotating planet with a tilted magnetic field; in effect what would happen if Jupiter was brought in to 0.1AU. This will make a direct comparison with the original Jupiter plots easier.

4.6.1 Ion Density

For the ce08 run ion density plots are also obtained at pressure level 11, corresponding to approximately $50\,nb$, in order to examine the composition lower down in the thermosphere. It also allows one to compare these plots directly with the ion profiles obtained in Paper I for the JIM model. Output at this pressure level is not repeated as at this depth ionising UV photons are rare and H_3^+ variation with orbital radius follows a similar, symmetrical, pattern to that at pressure level 16, with a density increase from 5.2AU to 0.1AU of $\sim$ an order of magnitude.

Observing the H^+ and H_3^+ plots at pressure level 11 (page 158) shows that both ion profiles show an approximate symmetry about the subsolar point, with the H^+ plot slightly offset towards dusk. Calculating the lifetimes of the two species one finds that H_3^+, which is dominated by dissociative recombination, has a typical destruction time of $\approx 500\,s$, agreeing with the observations that the species will not survive long enough to be carried through a significant proportion of an planetary revolution. Hence the density profile will be dominated by the balance of creation and destruction timescales. The dominant H^+ destruction reaction will be the

charge exchange reaction

$$H^+ + H_2(v \geq 4) \rightarrow H + H_2^+ \tag{4.1}$$

which has a rate coefficient of $10^{-14}\, cm^3 s^{-1}$, using the value provided in Paper I for consistency. This provides a H^+ lifetime of $\approx 300\, s$, even shorter than the H_3^+ lifetime.

Moving up to pressure level 16 (page 159), the H_3^+ lifetime is $\approx 100\, s$ and the H^+ lifetime is $\approx 2000\, s$. The longer destruction timescale of H^+ manifests itself as an offset of the maxima towards towards increasing longitude (nightwards), as the species tends to linger after formation. Note the slight offset of the H_3^+ peak towards dawn, a feature than is even more pronounced at higher altitude as we shall see.

At pressure level 26 (page 160) the H_3^+ lifetime is once again $\approx 100\, s$ at the subsolar longitude and the H^+ lifetime is $\approx 2 \times 10^5\, s$, corresponding to more than 5 Jovian days. As can be seen more clearly in figure A.11, the H^+ density increases roughly monotonically throughout the day.

The combination of relatively high H^+ density and long destruction timescale has a remarkable effect on the H_3^+ density. As can be seen in figure A.9(b) the density peaks shortly after dawn and decays throughout the day. The phenomenon of H^+ subduing H_3^+ formation has been discussed in relation to the rotationally synchronised model. Here, however, H^+ density variation is not simply temporal but longitudinal. For example, shortly after dawn $[e^-]$ is approximately $3 \times 10^{10}\, m^{-3}$, corresponding to a H_3^+ lifetime of $\approx 330\, s$. At dusk, however, $[e^-]$ has risen to 2×10^{11}, with the associated H_3^+ lifetime having dropped to only $\approx 50\, s$, a nearly sevenfold decrease. Thus, at dawn H_3^+ is allowed to build up to a certain extent, whereas at dusk it is destroyed almost as soon as it is formed. This *Dawn Peak* is a

new feature not seen in JIM due to the increased ion densities and correspondingly shorter chemistry timescales in the new model, and it becomes even more prominent with increasing energy input, as can be seen in the output from the ce03 and ce01 runs in sections A.3 and A.4.

Now turning to the ce03 run series. If one looks at pressure level 16 (page 166) it is possible to see a similar pattern to that of ce08. Since the H^+ charge exchange reaction depends primarily on the density, and this will not change significantly with increasing temperature, the lifetime of H^+ at each pressure level can be considered approximately constant throughout the ce run series.

H_3^+ lifetime, however, will change, although it is clear that at pressure level 26 (page 167) the lifetime will only get shorter with increasing ionisation and will therefore always be several orders of magnitude less than H^+, leading us to expect a similar *dawn peak* at both ce03 and ce01, as indeed there is. Out of interest the subsolar H_3^+ lifetime at pressure level 26 is $\approx 10\,s$, getting dangerously close to the timestep length.

Notable at ce03 in the H^+ plots is the equatorial cavity as seen in the **cm-me** series. Here, however, it is clear that this feature follows the magnetic rather than Joviographic equator. As expressed previously, this is a feature that may not be considered genuine in terms of magnitude due to the incomplete electric field code in JIME. Also clear is the same increasing dominance of H^+ over H_3^+ as seen in the previous models.

The ion profile at ce01 (pages 173-174) is essentially identical to that at ce03, with a couple of minor yet interesting differences. All the features described above are present, but in the case of H_3^+ the increasing dominance of H^+ results in the shortening of the dawn peak in terms of longitudinal extent. In addition the central H^+ ridge has become so pronounced that it clearly separates that northern and

Orbital Radius (AU)	Pressure Level	Ion Lifetime (seconds)					
		Dawn		Midday		Dusk	
		H^+	H_3^+	H^+	H_3^+	H^+	H_3^+
0.8	16	2000	5000	2000	100	2000	220
	26	1.7×10^5	650	1.7×10^5	150	1.7×10^5	120
0.3	16	2000	650	2000	17	2000	40
	26	2.1×10^5	100	2.1×10^5	28	2.1×10^5	25
0.1	16	2500	250	2500	2.2	2500	5.0
	26	2.9×10^5	65	2.9×10^5	6.5	2.9×10^5	6.5

Table 4.6: Variable ion lifetime with altitude and decreasing orbital radius.

southern components of the H_3^+ dawn peak.

A summary of the principal ion lifetimes with altitude and orbital radius may be found in table 4.6, and clearly shows both the shortening H_3^+ ion lifetime with increasing irradiation and the imbalance between dawn and dusk. These lifetimes were calculated by hand using ion density output from the model.

These results are interesting in that they clearly show that the H_3^+ lifetime asymmetry occurs at pressure level 16 as well as 26, and yet the H_3^+ density at pressure level 16 is close to symmetric about the subsolar point, showing little of the pronounced dawn peak that is so evident at the top of the atmosphere.

To understand this apparent anomaly one must examine the stellar UV input at both pressure levels as seen in figure 4.13. Notice the very different shapes of the two energy input curves. At pressure level 16 the curve is almost Gaussian with a slow rise and decay and a very narrow peak at the subsolar point. At pressure level 26, however, the curve rises and decays sharply with a broad plateau. The shape of the pressure level 16 curve can be explained by the greater optical depth near dawn and dusk with correspondingly higher UV absorption, reducing the UV flux in comparison to the subsolar point. At pressure level 26 there is considerably less atmosphere with which to absorb the incident radiation and hence the more uniform distribution and sharper day/night boundary.

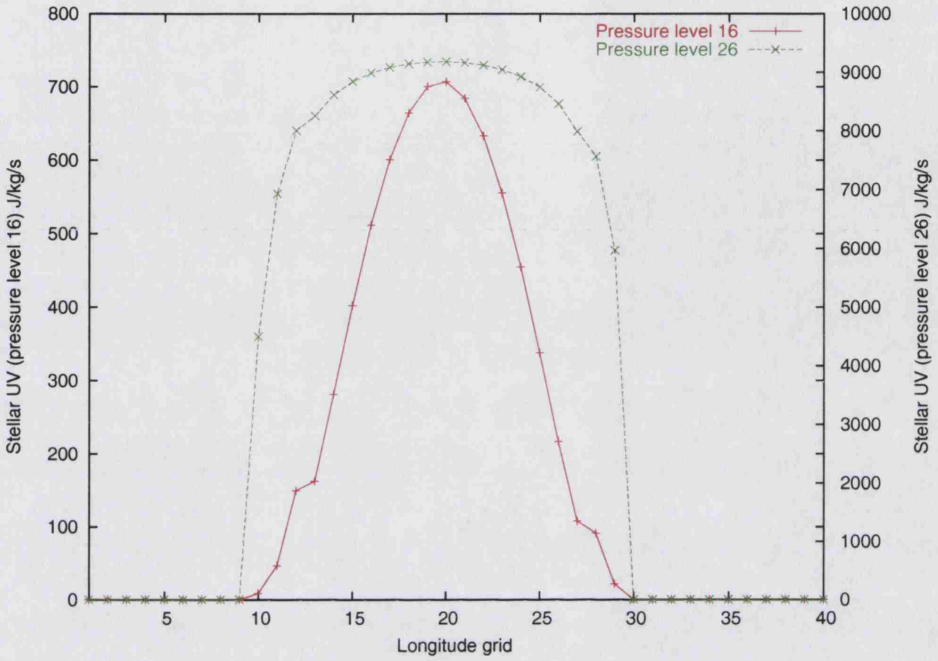

Figure 4.13: Stellar UV input at the Joviographic equator centred on subsolar point for pressure levels 16 and 26 of run ce01.

Thus at pressure level 16, despite the long H_3^+ lifetime at dawn, the stellar UV input is not sufficiently large to produce a high density of the ion, whereas at pressure level 26 the stellar UV input is a significant proportion of that at midday, allowing a H_3^+ buildup whilst the e^- density is still relatively low.

4.6.2 Temperature and Energy Balance

Plotted in figures A.12 (page 163) and A.13 (page 164) are the temperature profiles and energy balance for the ce08 model at the subsolar point and the exact Joviographic opposite point on the planet, referred to as midday and midnight respectively. There are corresponding plots for the ce03 and ce01 runs on pages 170-171 and 177-178 respectively. The energy balance diagrams show the energy input due to the dominant physical processes at these distances, stellar EUV heating and H_3^+ cooling. Also plotted is the **total** energy balance at this point due to all processes.

If one looks at the temperature profiles at ce08 it is clear that the temperature has actually *decreased* as the planet was brought in towards the star. This feature is partially due to the uncertain cooling efficiency at high altitudes and also due to the fact that the upper thermosphere temperature in JIM has possibly been set artificially high, with the H_3^+ cooling code bringing it back down to more realistic levels. Looking at the Galileo plot shown in figure 1.4 it can be seen that the most common interpretations of the upper thermosphere temperature at the probe impact site predict temperatures of approximately 900K at $10^{-6}mb$, corresponding to around pressure level 20 in the model. In the original JIM the temperature at pressure level 20 is 1200K, a clear deviation from the observed results.

Whichever is the case it can be seen that for ce08 the temperature has been decreasing preferentially in the upper atmosphere around pressure level 25, and if one looks at the original JIM output with H_3^+ cooling briefly turned on (figure A.6(a) on page 156), it can be seen that this altitude corresponds with the peak of the H_3^+ cooling. At ce08 distance, however, stellar heating has caught up with cooling (figure A.13(a) on page 164) and the energy balance is positive. The main altitude at which H_3^+ cooling dominates is around pressure level 16, at which altitude stellar EUV heating has dropped almost to zero. It must be stated again that this can be considered an artificial situation. With the H_3^+ cooling profile presently unknown, the efficiency of removal of energy from the neutral atmosphere is parameterised as described in section 3.3.2, from 100% at pressure level 16 to 0% at pressure level 30. Therefore it is probably not wise to take the exact shape of the temperature profile as read, but rather consider it a guide to the approximate upper atmosphere temperatures that may be expected in Jovian planets at these distances from a main sequence star.

Looking at the plot of the midnight energy balance it can be seen that there is

still some residual H_3^+ cooling, but the majority of local energy loss would be due to thermal conduction with some bulk flow in the form of winds.

At ce03 the energy balance is now dominated by the stellar EUV input, as would be expected, with the energy balance being positive throughout the upper atmosphere, apart from a couple of pressure levels around 13 where the energy input has still not quite caught up with the H_3^+ cooling yet. The night side is once again dominated by non-chemical energy processes.

Turning to the temperature profiles it is clear that there is a significant temperature increase in the region of maximum stellar energy input, where the positive energy balance is large, with a transient temperature inversion around pressure level 15 again, where H_3^+ cooling is dominant.

Looking at the figures for ce01 (A.24 on page 177 and A.25 on page 178) it is apparent that H_3^+ cooling is beginning to catch up with stellar input and the energy balance curve is beginning to flatten out. This is encouraging in that it suggests that we are approaching thermal equilibrium, with subsolar temperatures reaching a peak at approximately 2800K. At midnight the temperature has dropped to approximately 2200K. This rapid drop can potentially be explained by the fact that, although at a high temperature, the upper atmosphere is extremely diffuse and thus has a low heat capacity. During the night downwards vertical neutral bulk flow of gas of the order of $50\,ms^{-1}$ over the unlit hemisphere is sufficient to remove that energy and dump it in the lower atmosphere where its contribution would not be felt as strongly as higher up.

4.6.3 Achieving Temperature Equilibrium

Given these temperatures it is intriguing to consider if and when a temperature equilibrium may be reached. For this I am using a 1.3 second timestep model 1e01,

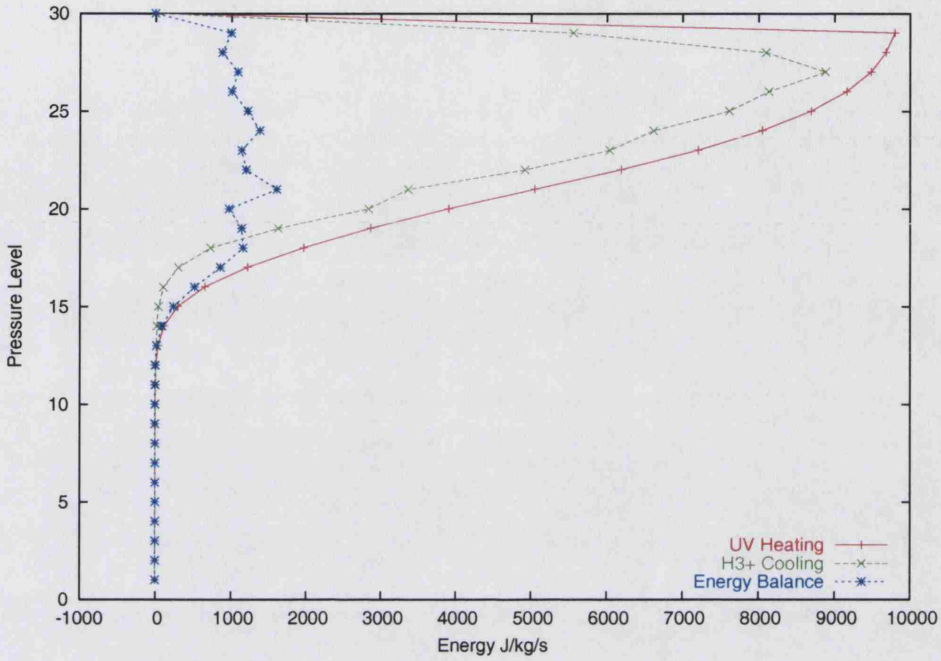

Figure 4.14: Subsolar energy balance for 1e01 run; 390 minutes on from ce01.

which was able to continue on from the end of a prior ce01 run for another 390 simulated minutes (or just under one Jovian rotation) and was timed to coincide with a simultaneous 1m01 run with a tidally locked planet.

A plot of the subsolar energy balance at the end point may be found in figure 4.14 and the temperature profile is shown in figure 4.15.

As can be seen from these plots, the energy balance is still approaching equilibrium, particularly closely at the highest altitudes The maximum H_3^+ local density at pressure level 26 is only 6% greater than at ce01, suggesting that it is not likely to rise a great deal further. Thus H_3^+ cooling rate will depend primarily on increasing temperature. The maximum temperature has now risen to over 3000K. Intriguingly, further plots have shown that the maximum temperature at high altitudes does not occur at the subsolar point, but close to dusk, where H_3^+ cooling is reduced, as shown in figure 4.16.

A study of when equilibrium temperature is reached is clearly required. It is

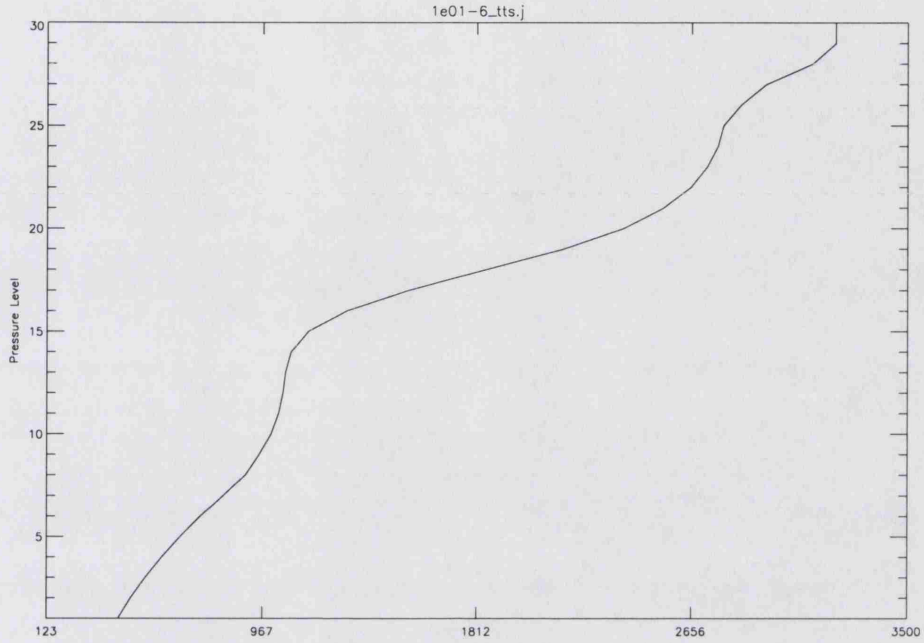

Figure 4.15: Temperature profile at subsolar point as in figure 4.14.

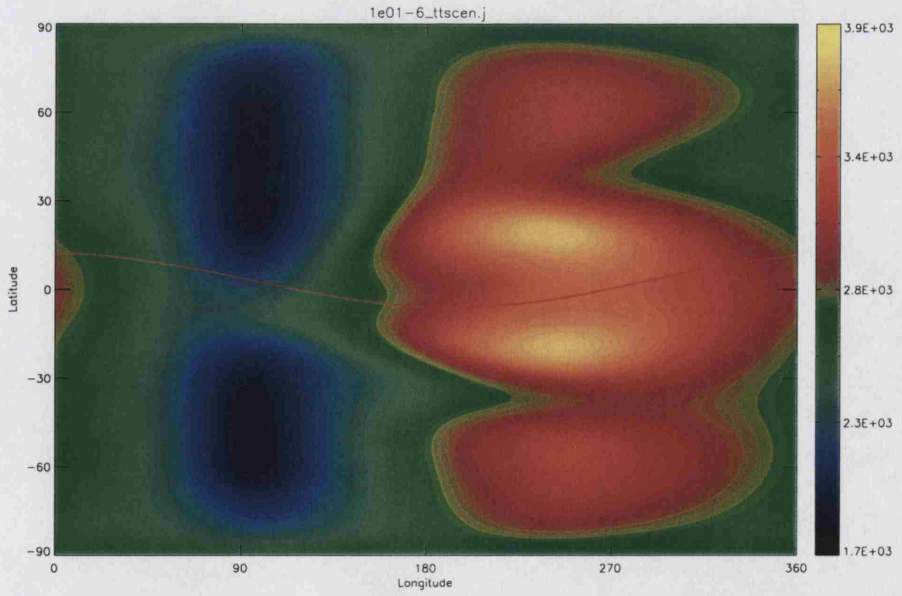

Figure 4.16: Temperature plot for 1e01 at pressure level 26 in units of Kelvin.

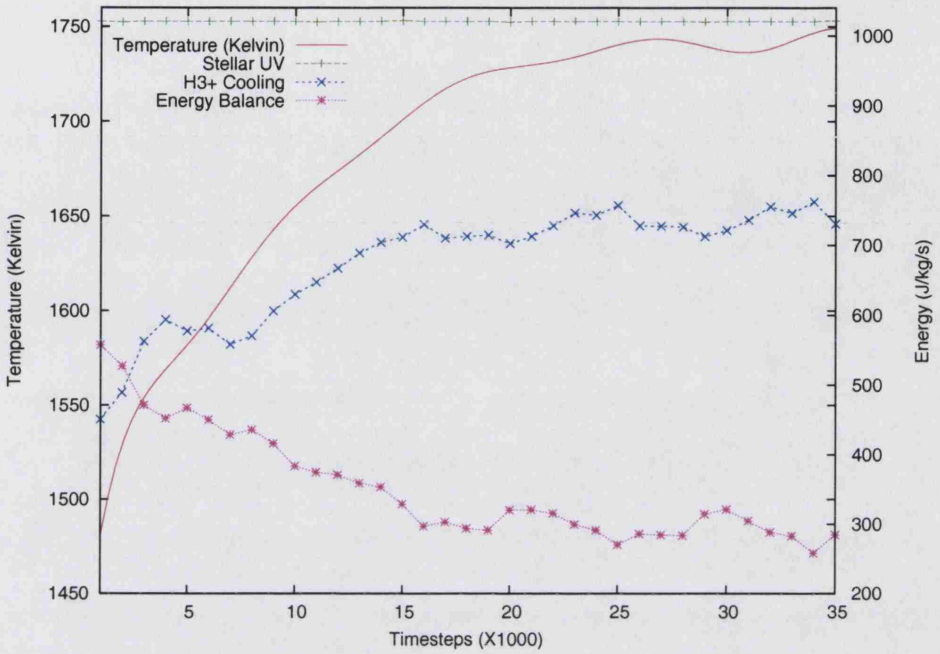

Figure 4.17: Temperature (left scale) and energy balance (right scale) at the subsolar point and pressure level 26 for a 4 second timestep run at 0.3AU.

also practical to measure the temperature at constant altitude and sub-stellar co-ordinates, rather that simply using the maximum temperature which observations suggest varies in Joviographic longitude with increasing stellar input. For this I am once again using pressure level 26 at the subsolar point.

In addition to the previously described 1e01 model a ce03 model at 0.3AU with a 4 second timestep has been used in an attempt to run the model for as long as possible, in this case 36000 timesteps, which is equivalent to 40 hours or just over 4 Jovian rotations. This should allow any diurnal variations to be identified.

Figure 4.17 shows the result from the ce03 run. It clearly demonstrates that temperature equilibrium is reached on a remarkably short timescale in the upper thermosphere, the trend line showing that plateau temperature is achieved after only approximately 18000 timesteps, or 20 hours. It can be seen at this distance that H_3^+ cooling is by far the dominant cooling process, with approximately three

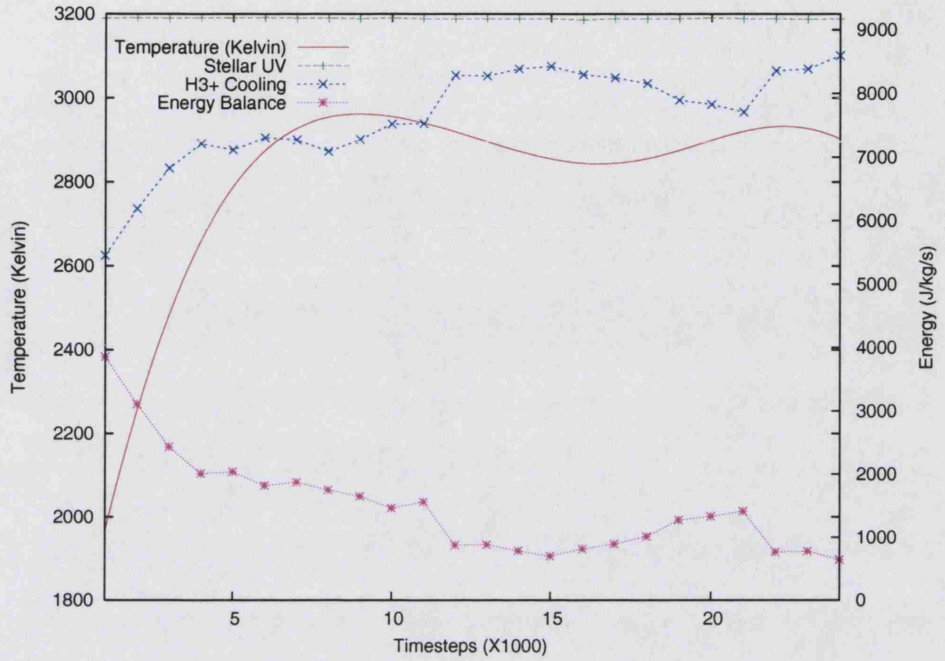

Figure 4.18: Temperature (left scale) and energy balance (right scale) for 1.3 second timestep run at 0.1AU.

quarters of the stellar UV energy input radiated back into space.

Figure 4.18 shows plots of both the temperature and energy balance of a series of runs at 0.1AU. This plot begins where the ce02 output ends, with a 1.3 second timestep for approximately 550 minutes, or one Jovian day.

It is clear from this figure that a temperature maximum at the subsolar point is reached at approximately 150 minutes after the planet is brought in to this orbital position, after which the temperature begins to oscillate about an equilibrium value. This is despite the fact that H_3^+ cooling is still less than stellar UV heating and can be explained by energy conduction downwards and temperature gradient wind flow.

The above argument reveals two notable results. Firstly that temperature equilibrium at 0.1AU may occur on a remarkable short timescale in the upper thermosphere. Secondly, the equilibrium temperature is considerably lower than might be expected, considering the greater than three orders of magnitude stellar UV increase

from Jupiter's orbit. This can be considered primarily due to H_3^+ cooling. For an example of the effectiveness of H_3^+ cooling when applied to the tidally locked model see figure 4.21.

4.7 cm - Rotationally Synchronised with Tilted Magnetic Field

I have chosen to only examine the **cm** series in this section as opposed to the textbfcl series, partially because both series model the same planetary configuration, but mainly because the act of slowing rotation rate down every seven hours in the case of the **cl** series caused large jumps in the subsolar longitude, preventing a stable H^+ pattern from forming. In the case of the **cm** series the sudden halting of planetary rotation at 0.4AU allows the stable H^+ profile time to reform by the time the planet enters the 51-Peg region.

The major consequences of increasing stellar input, such as decreased chemistry timescales, increased temperatures, and greater bulk flow rates have been covered when describing the CE run series, and therefore I will aim to concentrate on the similarities and differences from the CE run model that come from selectively illuminating a single hemisphere only.

4.7.1 Asymmetry due to Tilted Magnetic Field

In many ways the CM series of runs may be expected to be a good deal simpler to predict and explain than the CE series, in that with a single hemisphere illuminated and zero planetary rotation it is not expected that we should see any of the longitudinal features that are a result of periodic illumination, such as ion peaks

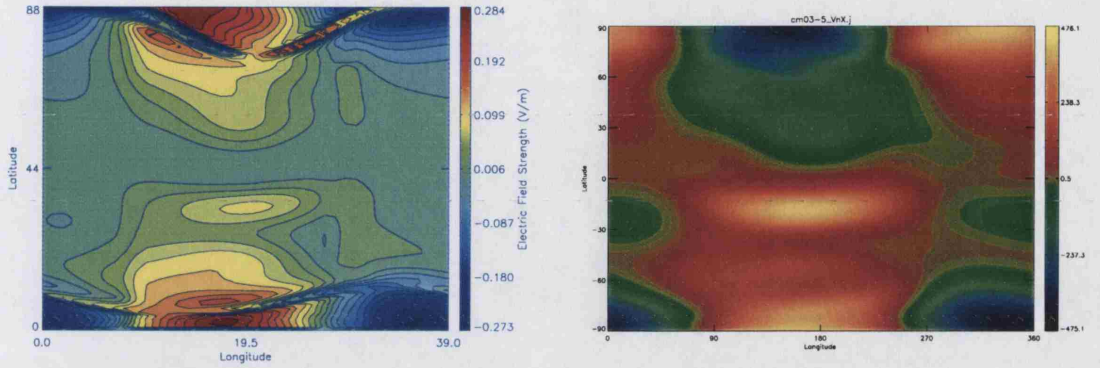

(a) Longitudinally-directed electric field

(b) Latitudinally-directed neutral wind velocity (ms^{-1})

Figure 4.19: Electric field and neutral wind correlation.

shifted away from the subsolar point. Indeed, if one looks as figure A.32 on page 187, showing the ion profiles at pressure level 16, the H^+ and H_3^+ profiles are essentially identical, with both peak densities occurring at the subsolar longitude.

At pressure level 26 (page 188) we still see longitudinal symmetry, but now with some new features obscuring what might be, for H^+, a similar profile. We have already seen the ion profiles of a rotationally synchronised planet with a non-tilted magnetic field and it can therefore be concluded that these features are solely due to the fact that at each longitudinal position the latitude of the magnetic equator differs from the Joviographic equator. Thus, the asymmetry of these features is simply the equatorial pattern seen in section 4.5 twisted to follow the magnetic equator.

It is interesting to examine the longitudinal electric field and latitudinal neutral wind flow in order to examine if there is the predicted correlation. Figure 4.19 shows it is clearly present.

The difference between this case and that of the rotationally aligned magnetic field is that now the magnetic equator is not located on the Joviographic equator.

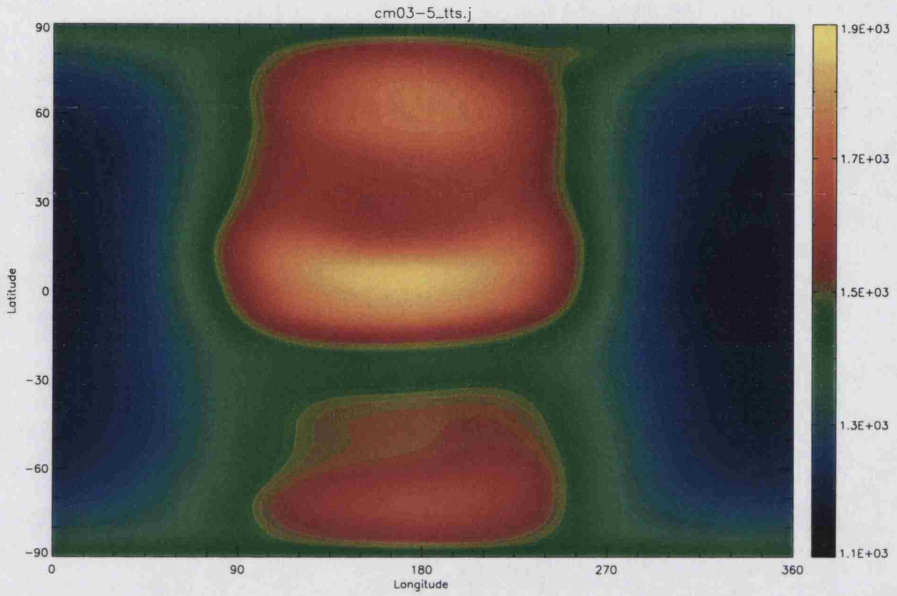

Figure 4.20: Temperature plot for cm03 at pressure level 26.

Temperature gradient driven winds from the subsolar point now pass across the region of zero dip angle in one direction, resulting in oppositely directed longitudinal $U \times B$ electric fields on either side of the magnetic equator. Thus, on one side of the magnetic equator ions will experience an negligible or upwards $E \times B$ force depending on the strength of the temperature gradient, and on the other side a downwards force, resulting in the north-south asymmetry seen in figure 4.19 and A.33 on page 188.

Therefore it appears that these distinctive features in the upper thermosphere of the non-rotating models are a result of the asymmetry of the Joviographic magnetic dip angle at the subsolar longitude.

4.7.2 Temperature and Energy Balance

Considering cm03 and looking at the temperature profiles for the subsolar and midnight points (figure A.36) one would expect the temperature differential to be significantly greater than for a rotating planet due to selective stellar heating of a single hemisphere. This is indeed the case, with an approximate 800K temperature difference between the two opposing points compared to less than 100K for the equivalent rotating planet.

Turning to the energy balance plots reveals something of a surprise. The subsolar plot (figure A.36(a)) shows the H_3^+ emission shadowing the stellar input, although somewhat closer than for the rotating planet. This can be explained by the higher daytime temperature of the tidally locked planet, remembering that nightside temperature has negligible effect on H_3^+ cooling due to the ion's short lifespan. What is remarkable is the deep drop-off in total energy balance between pressure levels 23 and 27, which would require H_3^+ cooling to match the stellar input which it clearly doesn't.

If one looks at the midnight energy balance (figure A.36(b)) the situation is even more unexpected, with a positive energy balance, despite zero stellar input and a small amount of residual H_3^+ cooling. Where is this energy coming from? Returning to the wind flow plot obtained in section 4.5.2 it can be inferred that what is being seen here is the effect of the atmospheric circulation dumping heat on the night side of the planet.

Up to this point I have discussed the effectiveness of H_3^+ cooling and how it may considerably lower the thermospheric temperatures of a 51-Peg type planet. The plots provided so far have demonstrated that thermal equilibrium may be reached in the order of a Jovian rotation for a rotating planet. In order to gauge its importance

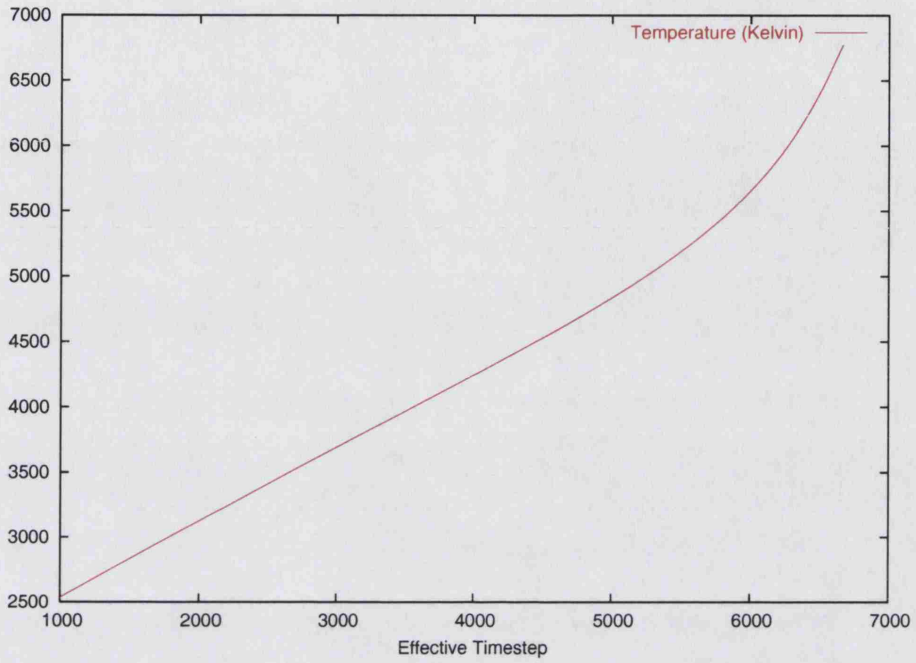

Figure 4.21: **cm** temperature at subsolar point with H_3^+ cooling off, commencing at 0.2AU for 6000 timesteps and then at 0.1AU with 1.3 second timestep until end of plot.

it would be useful to examine what sort of temperatures may be predicted in the absence of H_3^+ cooling. A plot taken from the **cm** series with cooling turned off is shown in figure 4.21.

This plot uses the output from the cm03 run and commences at 0.2AU for 6000 seconds with a 4 second timestep before switching to 0.1AU with a 1.3 second timestep in order to achieve as long a run at 0.1AU as possible. As can be seen even at 0.2AU the temperature rises to 5000K almost linearly. Moving the planet in to 0.1AU causes the rate of increase to rise dramatically. At this point the simulated wind speeds are beyond $2000\,ms^{-1}$ and JIME's atmospheric dynamics calculations collapse. This is a convincing demonstration of the importance of H_3^+ cooling in regulating the thermospheric temperature.

4.8 Trends due to Shrinking Orbital Radius

In presenting the previous results an attempt has been made to examine and explain the atmospheric features shown in the model. However, the goal of this thesis has been to determine the importance of H_3^+ cooling and for that global ion density is more important than local structure. This section will attempt to bring together the results obtained thus far and examine how the physical properties of a planet vary with orbital radius.

4.8.1 Ion Density

Of primary importance is the relation between the two principal ions, H^+ and H_3^+. We have seen examples of the anticorrelation between the two and the increasing dominance of H^+ with decreasing orbital radius due to the increasing production rate versus static destruction rate.

Figure 4.22 shows that the H^+ density profile at the subsolar point increases dramatically with increased stellar UV input. The peak density increases by more than three orders of magnitude from 5.2AU to 0.1AU. This is roughly equivalent to the near three thousandfold increase in UV intensity.

Figure 4.23 shows that, as predicted, the subsolar H^+ density for a rotationally synchronised planet is greater than for a rotating planet. The difference is not as great as might be expected due to the long lifetime of H^+ in the model atmosphere (see table 4.6) allowing the bulk of the ion in the upper thermosphere to survive the night.

The difference in H^+ density at the top of the atmosphere, where the level of photoionisation is greatest may be seen in figure 4.24. Plotting the column density at the subsolar point (figure 4.25) shows a similar profile.

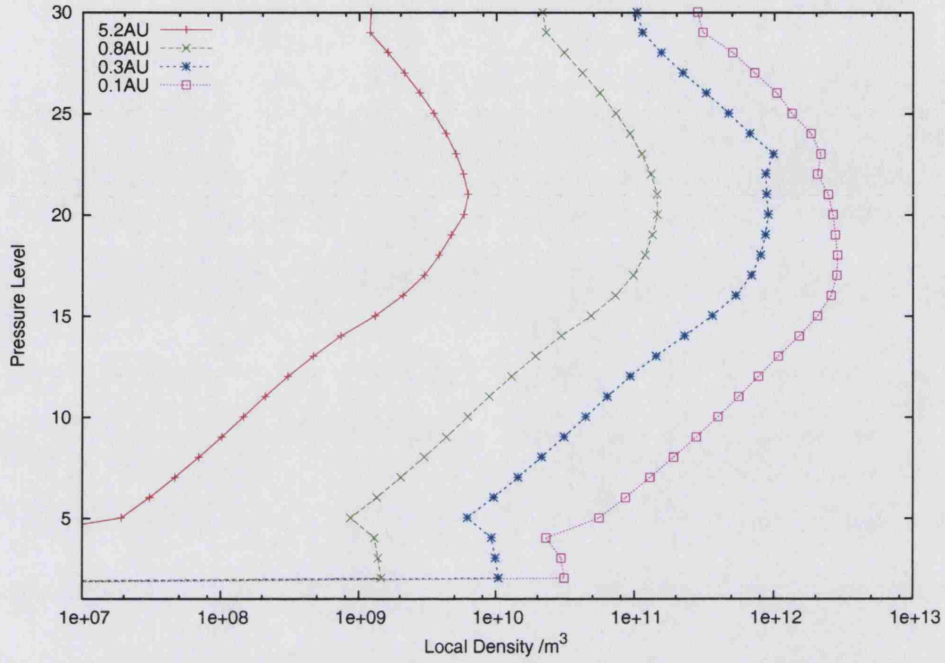

Figure 4.22: H^+ density profile at the subsolar point for the rotating-magnetised model.

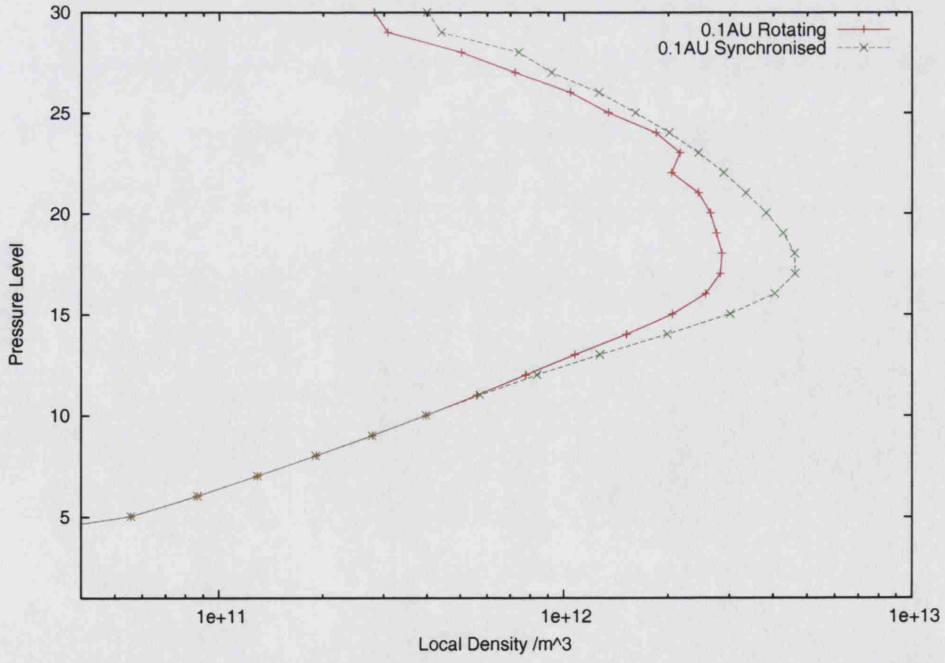

Figure 4.23: Comparison of H^+ density profiles of the rotating and rotationally synchronised planets at the subsolar point.

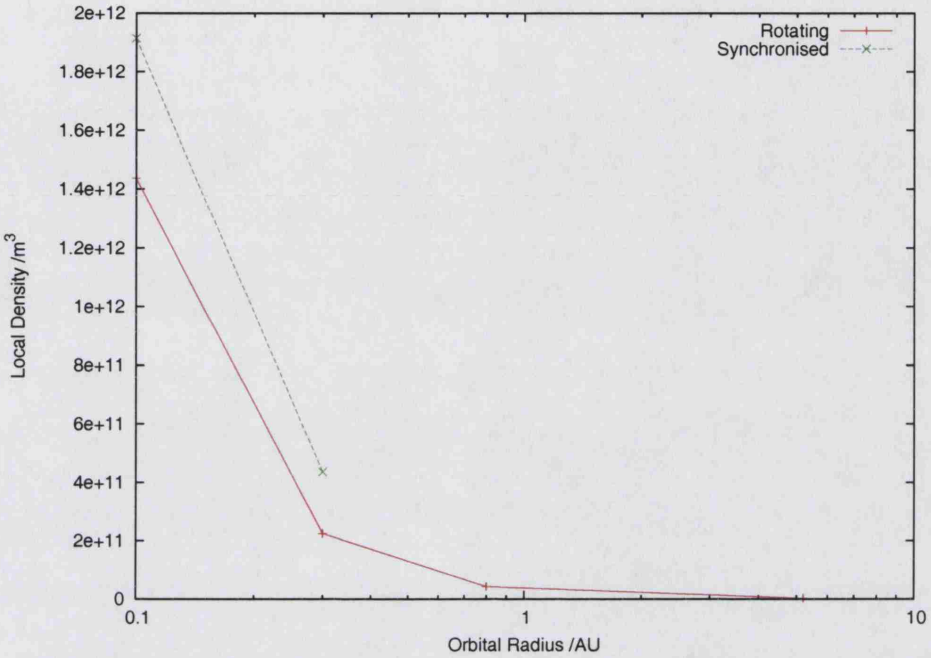

Figure 4.24: Subsolar H^+ density at pressure level 26 for rotating and rotationally synchronised planets.

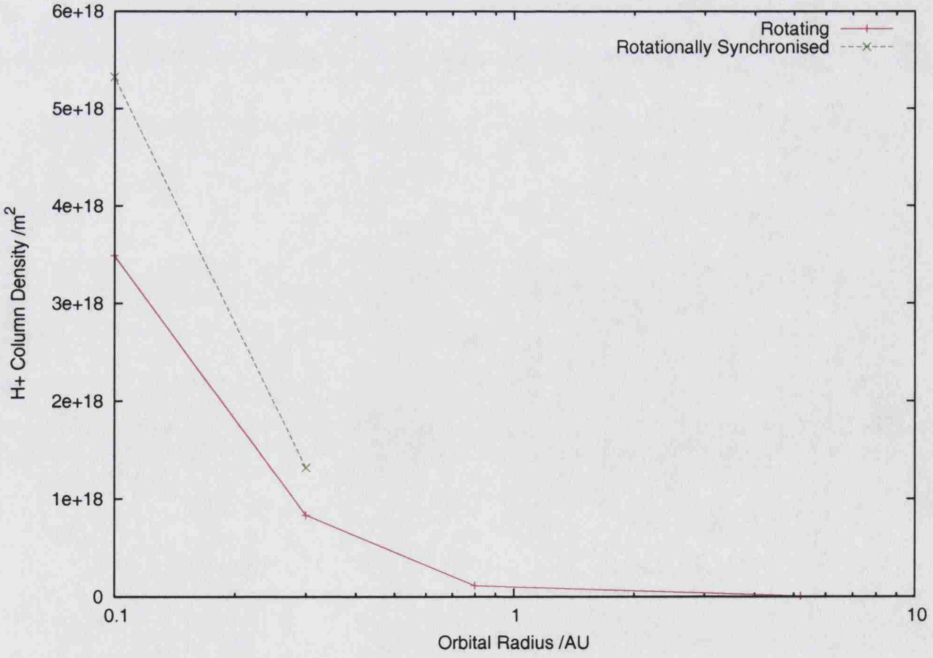

Figure 4.25: Subsolar H^+ column density for rotating and rotationally synchronised planets.

The case of H_3^+, with its significantly shorter lifetime and indirect dependence on H^+ is different. Figure 4.26 shows that, compared to H^+, the increase in density from 0.8AU to 0.1AU is small, and the total increase from 5.2AU is only an order of magnitude. This figure also shows that as the planet is brought in towards the star a double-peak structure begins to form, and at 0.1AU the peak H_3^+ density has shifted to the bottom of the model atmosphere. The short H^+ lifetime and low production rate in this region means that H_3^+ lifetime is less actively surpressed by free electrons, hence the increasing density.

This shift in the peak density to lower in the atmosphere raises questions as to whether the H_3^+ peak energy emission also follows this trend. However, examining figure 3.1 shows that energy emission is considerably dependent on temperature and that the enhanced density low in the thermosphere is not sufficient to allow this region to dominate. Also, the considerably lower neutral density at high altitude implies a much higher H_3^+ to neutral atmospheric density ratio, leading to a strongly enhanced cooling rate over that at the more dense lower thermosphere.

Plotting both rotating and rotationally synchronised H_3^+ density profiles at 0.1AU and 0.3AU is somewhat confusing, as the densities are so close together it makes interpretation difficult. However, the profiles at 0.3AU (figure 4.27) show the expected high altitude deviation between the two cases, with the rotationally synchronised density being somewhat lower.

Again, plotting the local density at pressure level 26 (figure 4.28) makes the flattening H_3^+ trend clear.

Comparing this to a plot of H_3^+ density at pressure level 5 (figure 4.29) shows the opposite density trend lower in the atmosphere.

What, then, can one say from these results? Firstly, the H^+ ion densities of the subsolar point for both rotating and synchronised cases are not as different as

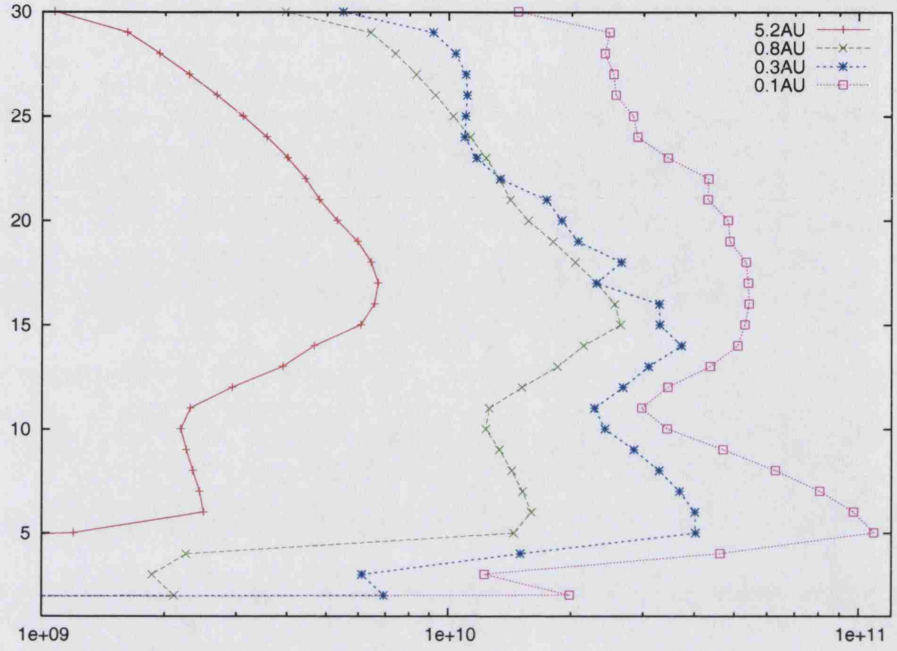

Figure 4.26: H_3^+ density profile at the subsolar point for the rotating-magnetised model.

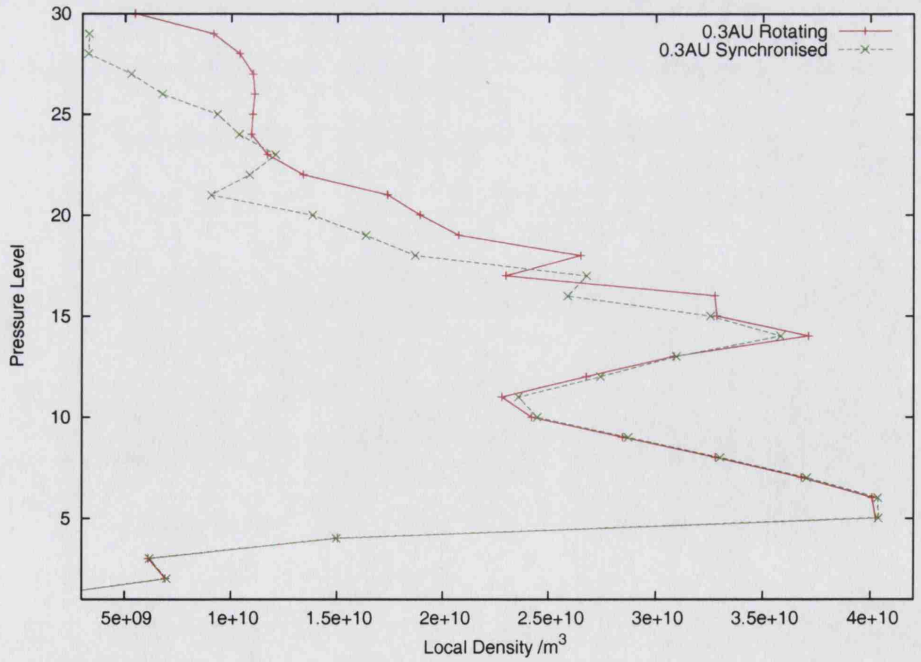

Figure 4.27: Comparison of H_3^+ density profiles of the rotating and rotationally synchronised planets at 0.3AU.

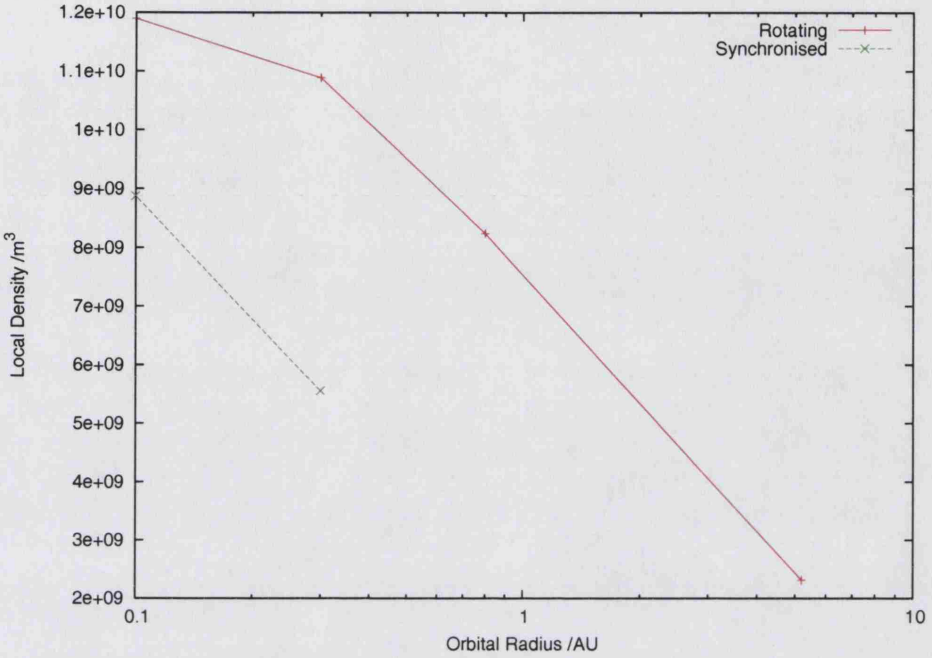

Figure 4.28: Subsolar H_3^+ density at pressure level 26 for rotating and rotationally synchronised planets.

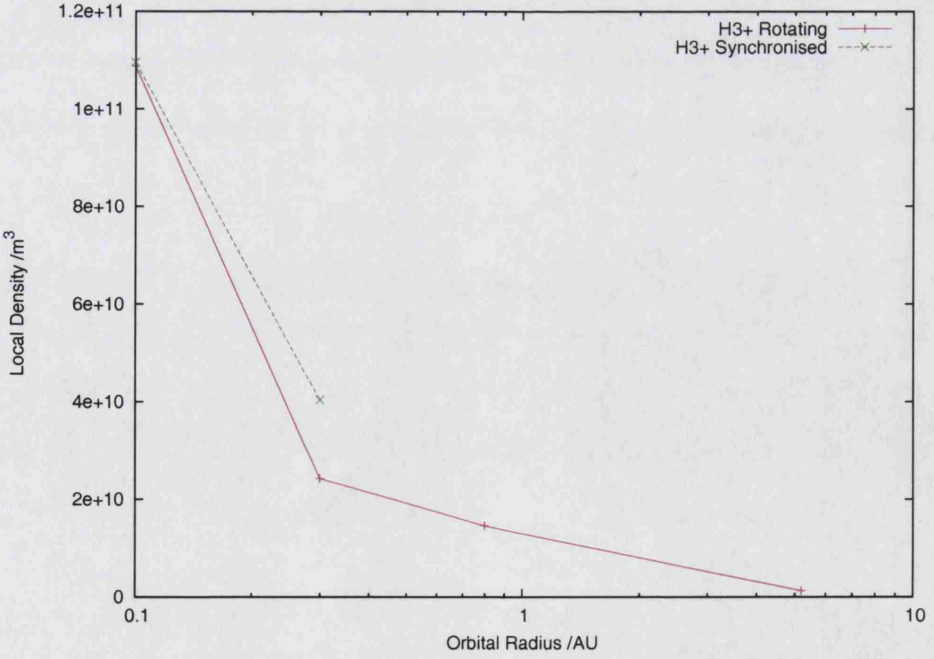

Figure 4.29: Subsolar H_3^+ density at pressure level 5 for rotating and rotationally synchronised planets.

might be expected, due to the long lifetime of the ion. However the difference that does exist influences the H_3^+ density with the result being that not only will the day side of a rotationally synchronised planet be hotter due to being permanently illuminated, but energy loss due to H_3^+ cooling will also be reduced.

4.8.2 Temperature

A successful attempt to achieve temperature equilibrium at 0.1AU for the rotating model is discussed in section 4.6.3. This section will consider how maximum and minimum temperatures change with orbital radius. Unfortunately, due to time constraints and model stability it was not possible to achieve temperature equilibrium at every orbital radius, but these results are still useful when their limitations are taken into account. Individual model temperature profiles may be found in Appendix A.

Figure 4.30 shows how the temperature changes with orbital radius at pressure level 26. The temperature at 5.2 AU is not considered as this model is considered to have an artificially high temperature due to the lack of H_3^+ cooling. At 0.8AU and beyond the temperature difference between midday and midnight is negligible.

For the rotating model the difference between maximum and minimum temperature at 0.3AU is significant, and at 0.1AU the difference has grown to approximately 500K. In the case of the rotationally synchronised model the temperature difference at 0.3AU is already large and at 0.1AU it has grown to greater than 1300K. As expected, the maximum temperature of the synchronised model is greater than that of the rotating model.

Noticeably the temperature of the night side of the rotationally synchronised model remains low. At 0.3AU and 0.1AU the night side is never illuminated and therefore energy input would be primarily due to the rapid nightwards directed hot winds carrying energy from the day side.

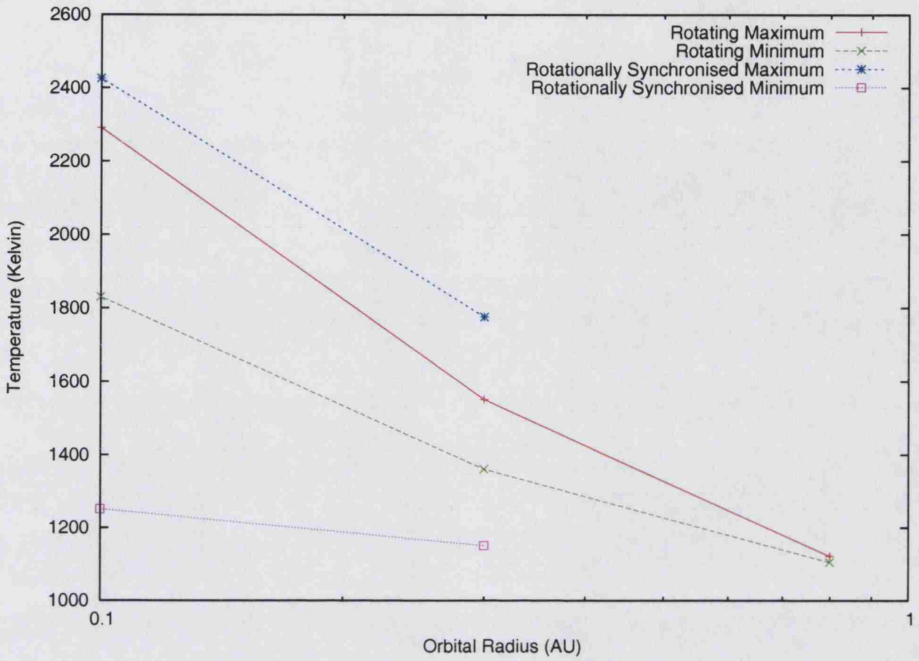

Figure 4.30: Peak and minimum temperatures for the rotating and rotationally synchronised planets at pressure level 26.

It is interesting to note that at 0.3AU the hottest point of the rotating model is not at the subsolar point, but a small number of grid points duskwards of it, whereas at 0.1AU the hottest point has retreated closer to the subsolar point.

Chapter 5

Conclusions and Future Work

In this thesis I have documented the development of **JIME**, the Enhanced Jovian Ionospheric Model, and provided an extended summary of the current theories of extrasolar planetary formation and evolution required to justify its existence. I have then used JIME in order to examine the chemical processes and temperatures expected to exist in the thermosphere of a model 51-Peg type planet. In this chapter I will summarise the results presented in section 4 and what conclusions can be drawn from them. I will then go on to examine the consequences for hot exoplanets and suggest what further work may be useful in order to obtain a deeper understanding of the planets and their properties.

5.1 Conclusions

The goal of this study has been to examine the thermospheric conditions expected to exist in the previously examined 51-Peg type planets under extreme stellar irradiation, with particular emphasis on H_3^+ in its role of upper atmosphere cooling. The results documented in chapter 4 have led to the following conclusions:

- H_3^+ **column densities** for a planet at 0.1AU are $\simeq$ 2 orders of magnitude greater than exist on Jupiter, with correspondingly higher contribution to H_3^+ cooling. At pressure level 26, near the top of the thermosphere, the H_3^+ number density is an order of magnitude greater at 0.1AU than at Jovian distance. This density increase might be expected to be even greater if not for the dramatically shorter H_3^+ lifetime at 0.1AU, determined by the e^- density and indirectly the H^+ density. The increasing dominance of $[H^+]$ over $[H_3^+]$ with stellar flux due to shortened H_3^+ lifetime is a phenomenon that has been predicted by Moore et al. (2003) as described in section 1.3.2.

- The **altitude of the H_3^+ peak density** shifts from the top of the model thermosphere to near the bottom by the time the 51-Peg region is reached. This is due to H_3^+ being preferentially destroyed in regions of high ionisation. However, a combination of lower temperatures at the bottom of the thermosphere and considerably lower [ion]/[neutral] ratio in this region mean that temperatures at the top of the thermosphere are most rapidly affected by the presence of H_3^+.

- The difference in day-side **ion densities** between the rotating and synchronised models are not large and are significantly smaller than change induced by altering the orbital radius by the chosen step.

- **Temperatures** in the upper region of the JIME model at 0.1AU appear to reach equilibrium in a time equivalent to one Jovian rotation or less. In both the rotating and rotationally synchronised cases the resulting subsolar equilibrium temperature is no higher than 4000K, whereas without H_3^+ cooling the temperature undergoes runaway increase beyond 7000K. This demonstrates the importance of H_3^+ cooling in maintaining atmospheric stability in the 51-

Peg region. For a rotating planet at 0.3AU the equilibrium temperature is obtained in approximately 20 hours, reaching a value of approximately 1750K. In both the 0.1AU and 0.3AU cases at the top of the atmosphere, stellar UV and H_3^+ emission are seen to be the dominant heating and cooling processes respectively, increasingly so with decreasing orbital radius. This implies that the lower thermospheric boundary temperature, and hence the rate of downwards heat conduction, has very little effect on the upper thermospheric temperature.

- The variable H_3^+ lifetime between dawn and dusk in the rotating model produces a phenomenon known as the **dawn peak** in the upper pressure levels, in which the difference in production rate of H^+ and H_3^+, and related e^- build up, causes the peak in H_3^+ density to occur shortly after dawn before decaying rapidly and stabilising through to dusk. This feature decays in prominence with decreasing altitude as the initial burst of H_3^+ formation at dawn is reduced with decreasing stellar UV flux through the greater thickness of atmosphere.

- For magnetised cases, the vertical component of the **B**-field either side of the Joviomagnetic equator combined with the local electric field generated by temperature gradient induced atmospheric flow through this **B**-field generates an $E \times B$ force that causes downward ion drift. At the equator the magnetic field dip angle is zero, and so there is no downwards drift. This results in an elevated H^+ ion density high in the thermosphere manifesting itself as a ridge following the magnetic equator, and thus a reduced H_3^+ density leading to a lowering of the local cooling rate.

- For the rotationally synchronised model with offset-tilted magnetic dipole in the Jovian configuration, the azimuthal neutral wind flow through the vertical component of the **B**-field, probably due to unequal stellar flux either side of the

magnetic equator, induces East-west directed $U \times B$ electric field, producing strong ion winds in the region of the magnetic equator. These winds result in a strong North/South asymmetry in the ion density and related temperature. As expected, this phenomenon is not seen when the rotational and magnetic axes are orthogonal to the line from the star to the planet, as would be expected for a rotationally synchronised planet.

- The **temperature profile** in both the rotating and non-rotating models shows strong enhancement in the upper thermosphere where stellar UV heating is most dominant. In both cases the temperature is modulated by the presence of H_3^+ cooling, reducing the subsolar equilibrium temperature to $\sim 3000K$ for the rotating model and $\sim 4000K$ for the rotationally synchronised model. With H_3^+ cooling disabled the subsolar temperature reaches $7000K$ with the rate of increase showing no sign of slowing. In both cases, although near temperature equilibrium may have been reached at the top of the atmosphere, the temperature profile through the lower atmosphere is still in flux and would require considerably longer than feasible to reach a final configuration.

- The **upper thermosphere temperature difference** between the day an night sides is considerably greater in the case of the rotationally synchronised model compared to the rotating model. In both cases the temperature difference increases with reduced orbital radius.

- Strong **Neutral winds** in the upper atmosphere, with peaks velocities greater than $1000\,ms^{-1}$ play a strong part in transporting energy from the subsolar point to the night side, in the case of the rotationally synchronised model.

5.1.1 H_3^+ Thermal Dissociation Calculations

The case for H_3^+ cooling as a moderator of thermospheric temperature is clearly demonstrated. In order to determine its importance it is useful to study the latest observations of 51-Peg atmospheres and what they can tell us about atmospheric stability at these extreme orbital distances.

Studies by Lammer et al. (2003a),(2003b) have examined the rate of atmospheric evaporation of 51-Peg type planets based on estimated exospheric temperatures greater than $10000K$. Temperatures of this magnitude induce thermospheric expansion leading to hydrodynamic escape. Calculations of the present mass loss rate for HD 209458b under these conditions yield a rate of escape of $\approx 10^{12} gs^{-1}$, under which conditions a planet may fully evaporate over a main sequence timescale.

It is interesting to note, however, that Lammer et al. discount the contribution of auroral H_3^+ cooling, stating that thermal dissociation of H_2 limits H_3^+ production in exospheric regions, and ignore low-latitude H_3^+ production completely. Despite the likelihood that this statement is true as far as it goes and that thermal dissociation does indeed indirectly reduce the H_3^+ density below what would be expected otherwise, no evidence is given to follow up this statement or to calculate predicted H_2 or H_3^+ densities. This dismissal of H_3^+ cooling out of hand would appear to be, at best, premature.

Similar research using a 1D model has been undertaken by Yelle (2004), who considers the effect of thermal dissociation to become significant at $\sim 2000K$. Just how significant is not stated and the fact that this value is not constrained more tightly shows how difficult the effect of thermal dissociation is to accurately model.

Thus, the thermosphere is differentiated into two distinct regions; the lower thermosphere which consists primarily of molecular hydrogen, and the upper ther-

mosphere which is mostly dissociated.

This value is above the JIME predicted exospheric dayside temperature for a rotating planet at 0.3AU but well below that of a planet at 0.1AU. Whereas Lammer et al. discount the effect of H_3^+ cooling entirely, Yelle recognises its importance to atmospheric structure, albeit in the lower regions of the thermosphere where neutral H_2 is the dominant species. This, however, takes into consideration an upper thermospheric temperature of $12000K$, well above what is obtained by JIME even at 0.1AU. Despite this figure, Yelle calculates that while atmospheric escape rates are high, atmospheres are stable over a typical main sequence lifetime, somewhat at odds with the Lammer et al. conclusion despite the similar thermospheric temperatures.

Additionally, neither of the previous two experiments take into account the effects of planetary rotation or atmospheric circulation. As has been shown in section 4.5.2, even in the case of a rotationally synchronised planet winds reaching $2000\,ms^{-1}$ transport hot atmosphere midnightward whilst gas rises up at the subsolar point to replace it. Thus the atmosphere is not static or uniform and even at 0.1AU the temperature at night is well below the nominal figure for thermospheric dissociation provided by Yelle, suggesting that the composition of the two hemispheres may differ significantly and that undissociated H_2 may flow into illuminated regions where H_3^+ may be formed rapidly.

We have seen in the JIME 0.1AU model results that auroral H_3^+ is dominated by low latitude production due to photoionisation, something that Lammer et al. do not consider, lowering the temperature to the point where thermal dissociation is clearly not as important as at $10000K$. Whereas Lammer considers the composition of the atmosphere *in situ* it may be argued that since the planet will have formed beyond the ice line and migrated inwards at a rate depending on both the structure of the planet and disc (see section 2.4.1), thermal dissociation will not initially be an

issue and H_3^+ cooling may prevent the thermospheric temperature rising to the point where the process seriously inhibits H_3^+ formation. Clearly there is the possibility of a feedback loop here, where increasing temperature inhibits H_3^+ formation which results in further increasing temperature, and this area will have to be studied in more detail for any conclusions to be formed. Section 3.3.2 describes the process of adding a high altitude exponential modifier to the H_3^+ cooling code in order to artificially restrain the energy removed from the diffuse upper thermosphere in an effort to simulate the conditions of non-thermodynamic equilibrium.

Therefore, whilst the fact of thermal dissociation is not disputed, it is clear that the upper atmosphere of a 51-Peg planet is far from the static model assumed in 1-D calculations.

Given the number of uncertain variables it is clear that there is significant grounds for speculation as to the exact effect of H_3^+ cooling on the atmosphere. The results presented in this thesis, however, suggest that H_3^+ is the dominant species in upper thermosphere stability, in the absence of significant thermal H_2 thermal dissociation.

5.1.2 Observations of Transiting Planet Evaporation

Given that most other mathematical studies of planetary evaporation utilise T_{eff}, the effective temperature, or T_{eq}, the radiative equilibrium temperature rather than T_∞, the exospheric temperature, both of the former of which are below $2000K$ for a typical 51-Peg planet, the next step is to turn to observations in order to examine atmospheric evaporation.

Studies of the transiting planet HD 209458b (Vidal-Madjar et al., 2003) have observed atomic hydrogen absorption in the stellar *Lyman* α line beyond the predicted Roche limit of the planet, suggesting that atmospheric escape is taking place.

The authors have calculated a minimum escape flux of around $10^{10} gs^{-1}$, although note that a flux a couple of orders of magnitude higher would produce a similar absorption signature. They also suggest that a high escape flux may lead to the planet evaporating entirely over a main sequence timescale or evolving into a hydrogen deficient Neptune-like object.

Initial observations of OGLE-TR-56 (Udalski et al., 2002b) suggest that the closest orbiting planet yet discovered is also physically one of the smallest. As suggested this may be due to mass loss in the process of halting orbital decay rather than thermal evaporation of the outer layers, something that may be determined by further observation.

With only two transiting planets presently known the true rate of atmospheric evaporation and its possible variability is unknown and it will require further observations to constrain these values. The fact that there exists a large number of low-eccentricity giant planets in the region of 0.1AU or less around main sequence stars suggests that whilst evaporation may occur at a significant rate, circularisation timescales predict that planetary stability even in these extreme conditions is possible. The study of H_3^+ cooling in this thesis suggests that the molecule may play a significant part in both determining thermospheric temperature and maintaining overall stability against evaporation.

5.2 Future Work

In order to understand what may be required from a next generation exoplanet model it is useful to examine some of the latest studies into 51-Peg planetary formation and evolution.

5.2.1 51-Peg Internal Structure

The observed size of a planet, determined from transit observations, is of great importance as it allows us to calculate the density and therefore theorise the internal energy sources supporting the atmosphere.

Using the best studied transiting planet, that orbiting the star HD 209458, observations have shown that for $M_p = 0.63 M_{Jup}$, a derived value of $R_p = 1.27 R_{Jup}$ (Charbonneau et al., 2000) is obtained, corresponding to an average density, $\rho = 0.38 gcm^{-3}$. Another study by Mazeh et al. (2000) obtains the same mass but a radius $R_p = 1.42 \pm 0.08 R_{Jup}$ due to a more accurate assumption of stellar radius. Whichever is the case it clearly shows that the strongly irradiated planet is significantly distended when compared with a solar system gas giant. It may be expected that this is down to thermal expansion due to the proximity of the star.

However, a paper by Burrows et al. (2000) suggests that this is not the case, indeed rather the opposite. They examine the formation process of gas giant planets in isolation, where cooling by radiation loss from the surface causes the planet to contract, and compare this to the situation where a planet is undergoing intense irradiation. They conclude that the consequent growth of an outer radiative zone (Guillot et al., 1996) contributes to the retardation in the contraction of the planet and predict a value of R_p between 1.4 and 1.6 R_{Jup} for HD 209458b, in line with observations. Since this process requires early proximity to the star it provides further evidence for rapid early migration with Burrows predicting that the planet could not have dwelled for longer than $\sim 10^7$ years beyond 0.5AU.

A later study by Baraffe et al. (2003) which includes a more detailed connection between the outer irradiated atmosphere and the interior structure also predicts retardation in contraction due to irradiation but not to the same degree as pro-

posed by Burrows, suggesting that either a further energy source is required, such as deposition of kinetic wind energy (Guillot and Showman, 2002) or ongoing tidal circularisation (Bodenheimer et al., 2001), or there are additional processes contributing to the retardation.

Clearly a thermospheric model requires good data regarding the lower atmospheric layers on which to base itself, and although models are available (eg. (Barman et al., 2001), (Showman and Guillot, 2002)) they are not self-consistent or generally extend upwards as far as the atmospheric regions that JIME models. Therefore at the current stage of exoplanet modelling JIME can use predicted lower boundary temperature and pressure values and wait for theory to catch up.

The lower thermospheric boundary layer in JIME has been fixed at the same level as that of JIM due to the stated uncertainties in this value. It was also considered that, at 0.1AU the timescale of temperature change in the upper thermosphere due to H_3^+ cooling is so short that the rate of energy conduction downwards, which is partially determined by the lower boundary temperature, is not significant. At 0.1AU the vast majority of energy absorbed is due to stellar UV and, assuming a transparent atmosphere, it is mostly radiated away into space. Clearly the atmosphere is not 100% transparent to IR radiation, and this would be another area in which the model could be enhanced.

Bearing all this in mind, future work on JIME may benefit from a further study into predicted mesopause temperatures and a series of simulated planets with varying boundary conditions in order to examine how upper thermosphere conditions vary. This would be combined with pressure and density data taken from the examinations of HD 209458b. It may also be useful to attempt to model exoplanets at varying stages of evolution, considering the uncertainty in the contraction retardation theory.

5.2.2 The Next Stage of JIME

In conclusion, from the discussion of both the results presented in this thesis and the selection of relevant ongoing research, it is considered that future work on JIME and in the field of thermospheric study should concentrate on the following topics:

- An in depth study of both the theory of thermal dissociation of H_2 and consequences for H_3^+ formation in the upper thermosphere of a 51-Peg planet. This will require the addition of H_2 thermal dissociation chemistry into the model. Following this there should be two series of runs performed, one set with the planet in the 51-Peg region with initial H_3^+ densities as suggested by Lammer; the second set commencing in the Jovian region with reduction of orbital radius along the lines of the cl and cm runs detailed in this thesis. This will allow a comparison between the *in situ* calculations performed by Lammer et al. and a slower build up of stellar UV input that may allow H_3^+ cooling to partially offset temperature buildup that leads to H_2 thermal dissociation. Additionally, examination of the dynamics of such an atmosphere with a perpetually dark hemisphere may provide information as to the increased H_3^+ formation due to H_2 flowing into illuminated regions over that of a static model.

- An observational study of transiting exoplanets. With only two known transiting planets the range of available data is limited. HD 209458b has an extended hydrogen atmosphere beyond the Roche lobe, suggesting that it is losing its upper atmosphere into space, possibly by a process of hydrodynamic flow, although at a rate that is not constrained by less than two orders of magnitude. Is this typical of hot exoplanets? It's too early to tell, of course, and considerably more observations will be required in order to obtain a range of hydrogen escape rates. The space-based transit satellites described in section B.2 along

with data obtained from large scale astrometric brightness variability surveys will put HD 209458b in perspective.

- It has been shown that for a rotationally synchronised planet the temperature difference between the two hemispheres is considerable. An investigation into the rate of atmospheric escape over each hemisphere may prove enlightening as to the potential structure of the thermosphere.

- A series of runs with varying lower boundary conditions in an attempt to examine how the rate of downwards energy conduction effects the equilibrium temperature at the top of the thermosphere.

- Further examination of planetary contraction retardation theory and the on-going studies attempting to explain unknown sources of energy input leading to larger than predicted planetary radii.

- A concerted attempt to enable JIME to run for as long as possible. As previously stated, JIME is relatively stable at 0.3AU and will run at 0.1AU with a 1 second timestep for at least a Jovian rotation. Unfortunately the amount of computation time required for the latter timestep length is considerable, requiring at least 10 days per rotation on the fastest supercomputer that University College London has to offer. It has been proposed that the rate of ion chemistry is the major determining factor in the timestep length. However, it has been seen that H^+ and H_3^+ should reach equilibrium values after a period of time, and so fixing these values and then turning ion chemistry off should be feasible and should allow considerably longer timesteps to be used. As seen in figure 4.3 the ion densities do not reach a stable equilibrium value in a short period of time, but do not vary by more than approximately 30% in 23

hours, suggesting that an average over this period may be suitable. Further investigation into the equilibration of the two principle ions would benefit.

Appendix A

JIME Run Output

A.1 Original Jupiter

Orbital Radius /*AU*	Orbital Period /*hours*	Timestep /*seconds*
5.2	9.92	3.97

This section contains data obtained from the original JIM, simulating Jupiter at 5.2AU. It is provided mainly for comparison with JIME and contains no H_3^+ cooling code.

Notice the H^+ spikes occurring around the auroral regions at pressure level 26, an demonstration of why the original JIM was not particularly stable. Also note that the auroral regions have been overexposed in order to provide more accurate density readings around the equator. A better estimate of the auroral ion densities may be found by studying the ce08 plot which follows this section.

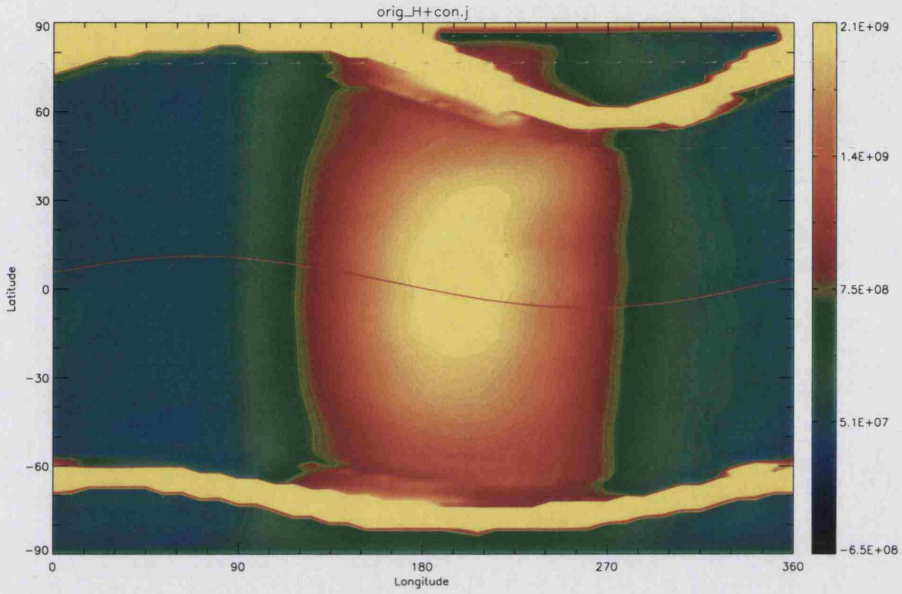

(a) H^+

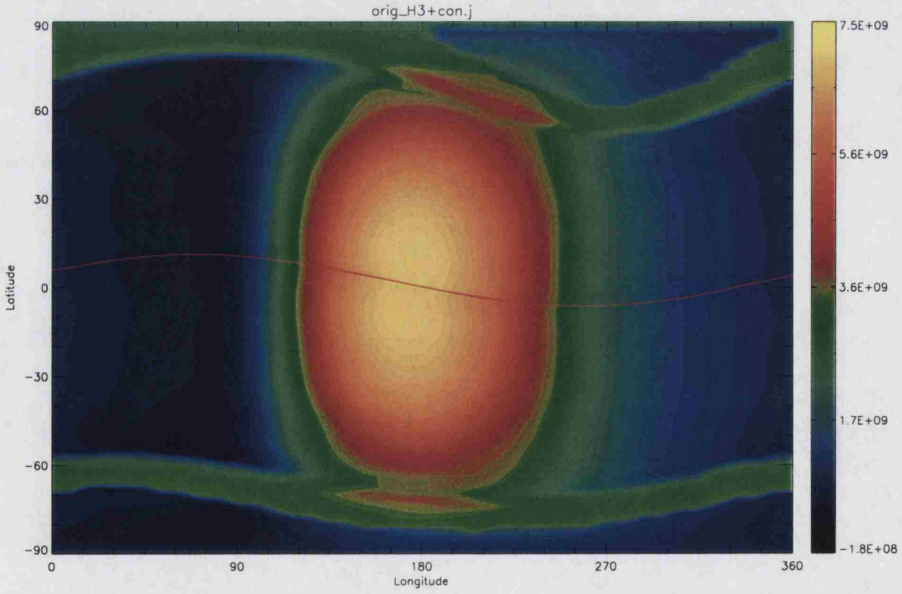

(b) H_3^+

Figure A.1: Pressure Level 16 Local Density

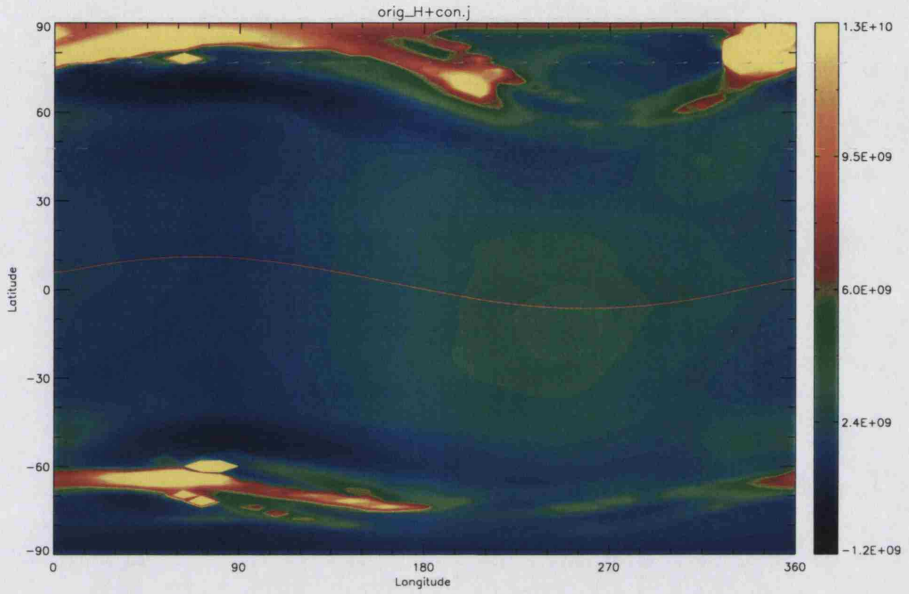

(a) H^+

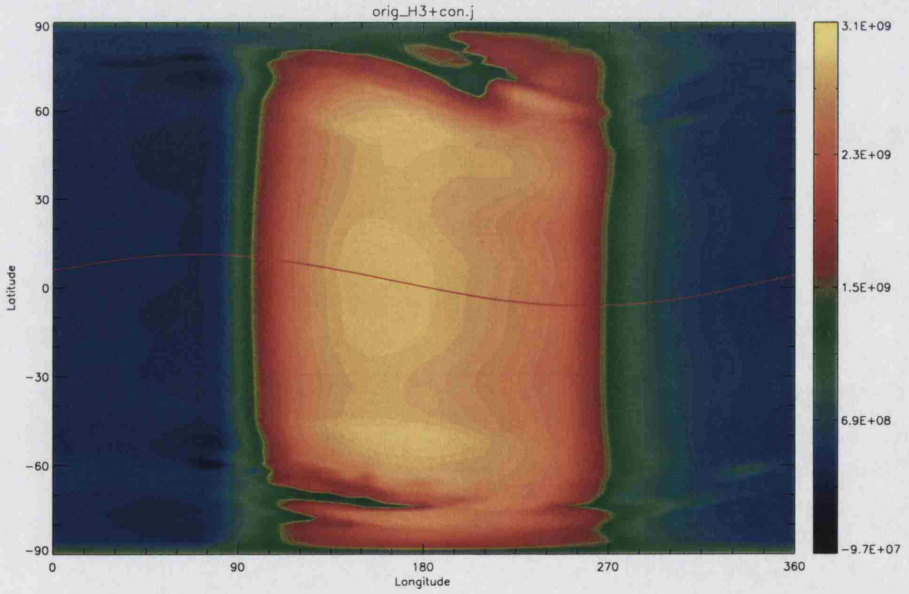

(b) H_3^+

Figure A.2: Pressure Level 26 Local Density

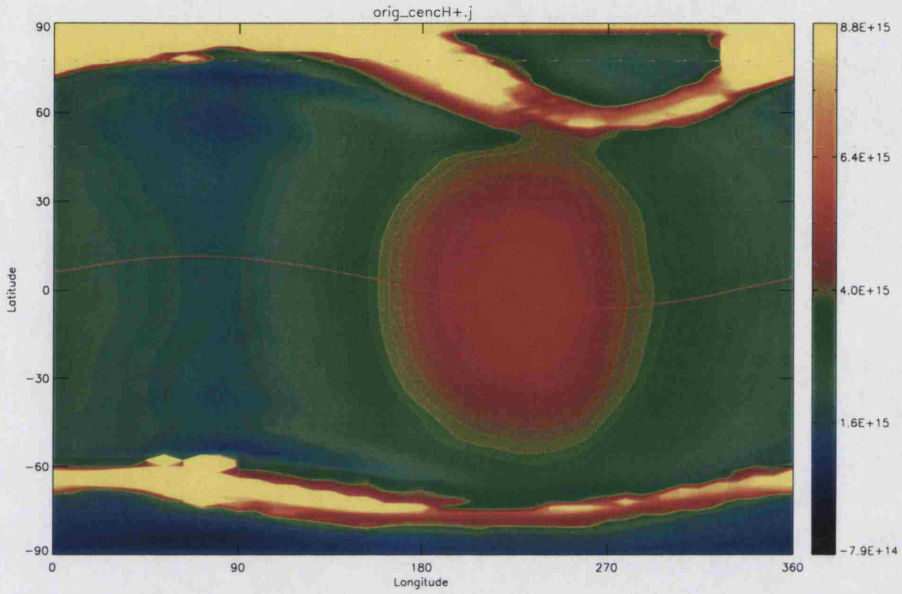

(a) H^+

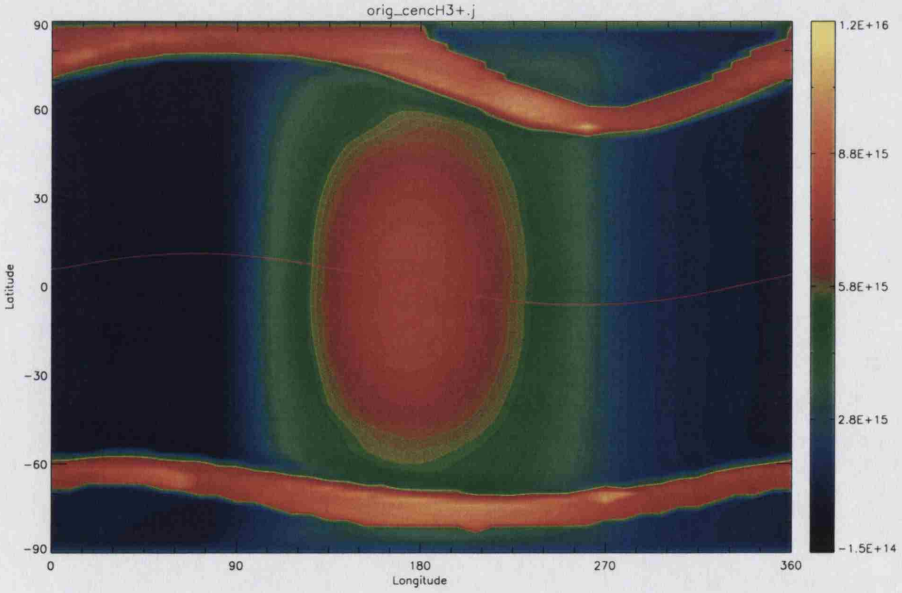

(b) H_3^+

Figure A.3: Column Density

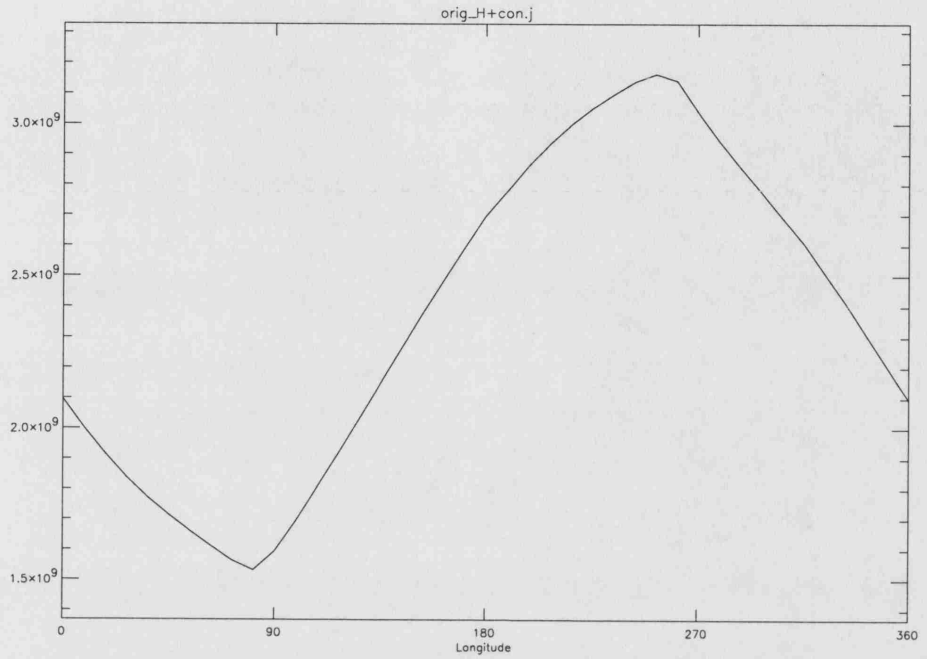

(a) H^+

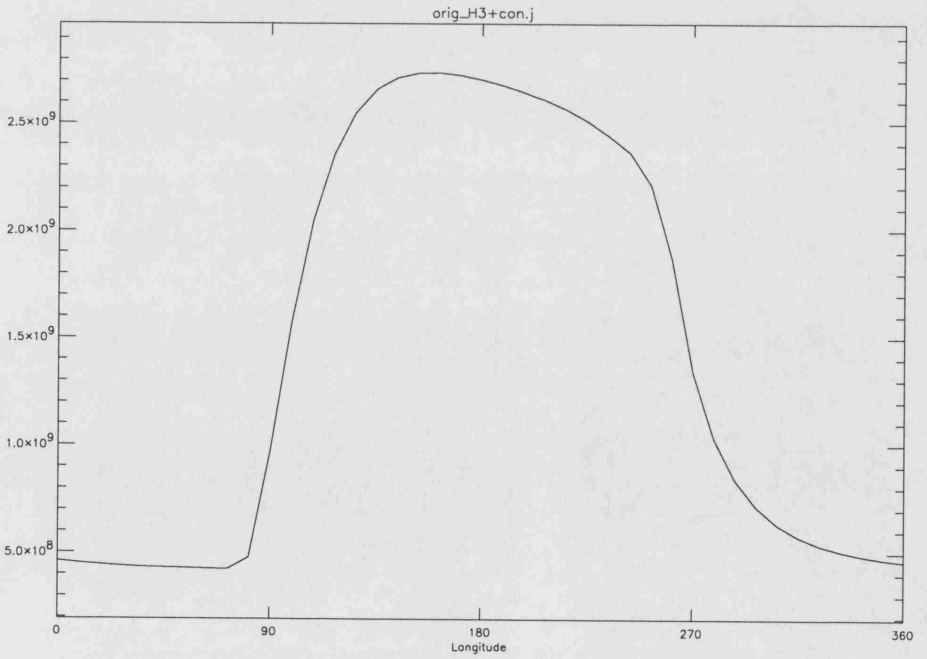

(b) H_3^+

Figure A.4: Longitude-Local Density at Pressure Level 26

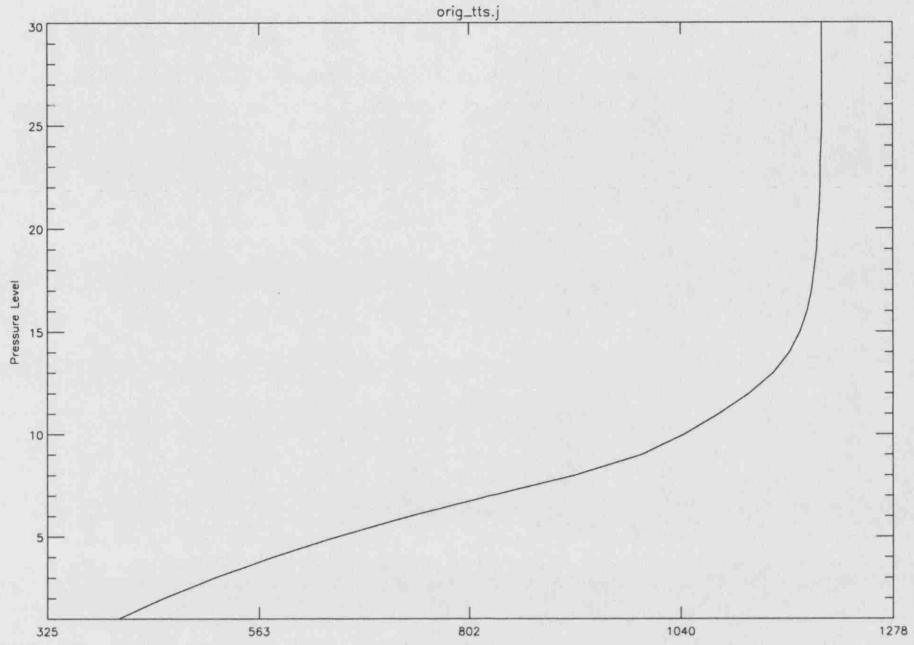

(a) Subsolar Point

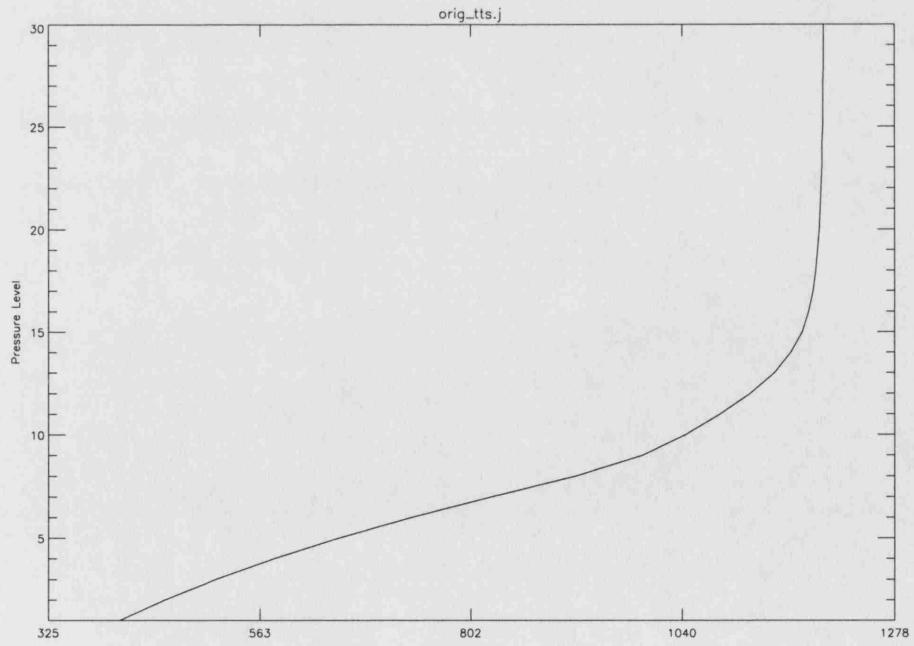

(b) Midnight

Figure A.5: Temperature Profile

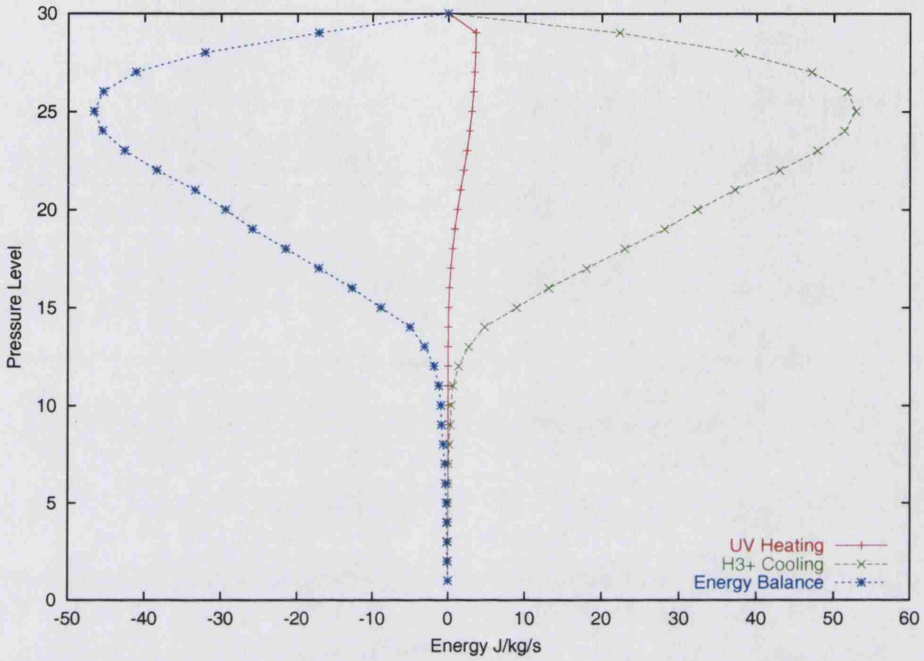

(a) Subsolar Point

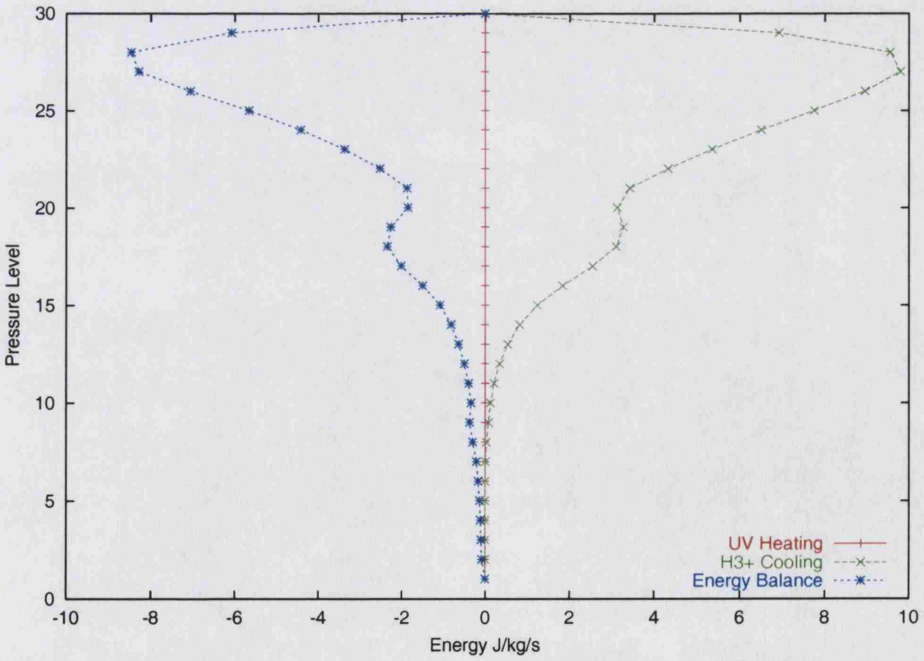

(b) Midnight

Figure A.6: Energy Balance

A.2 ce08

Orbital Radius /*AU*	Orbital Period /*hours*	Timestep /*seconds*
0.8	9.92	3.97

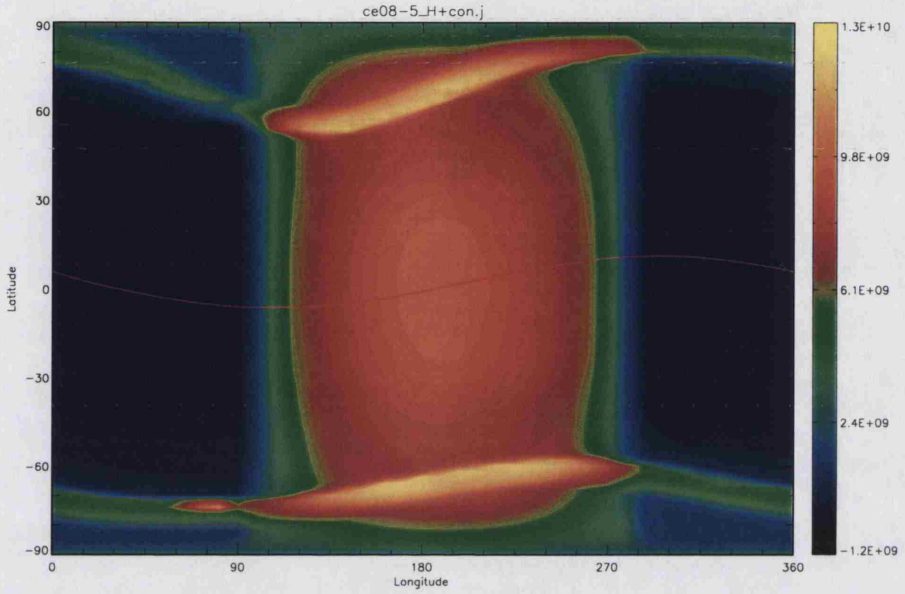

(a) H^+

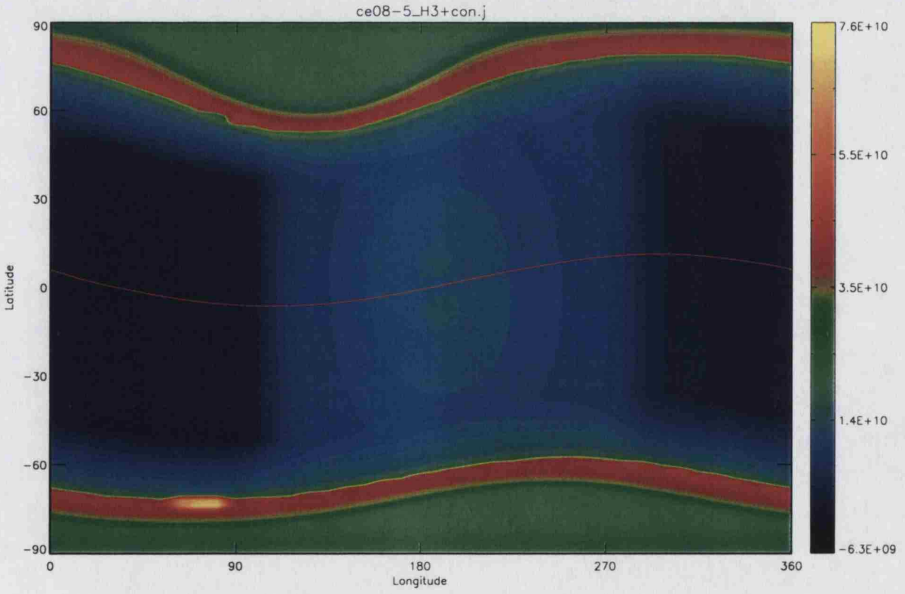

(b) H_3^+

Figure A.7: Pressure Level 11 Local Density

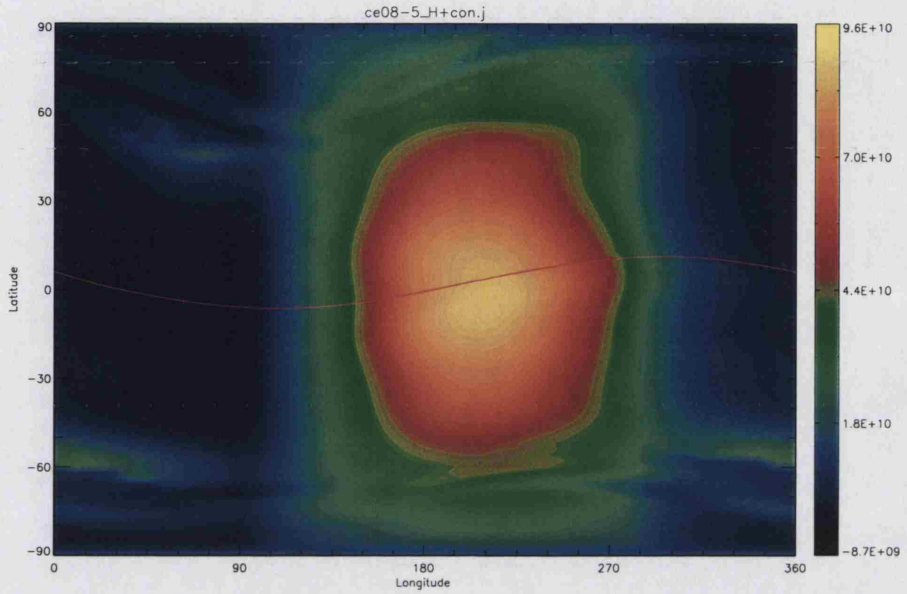

(a) H^+

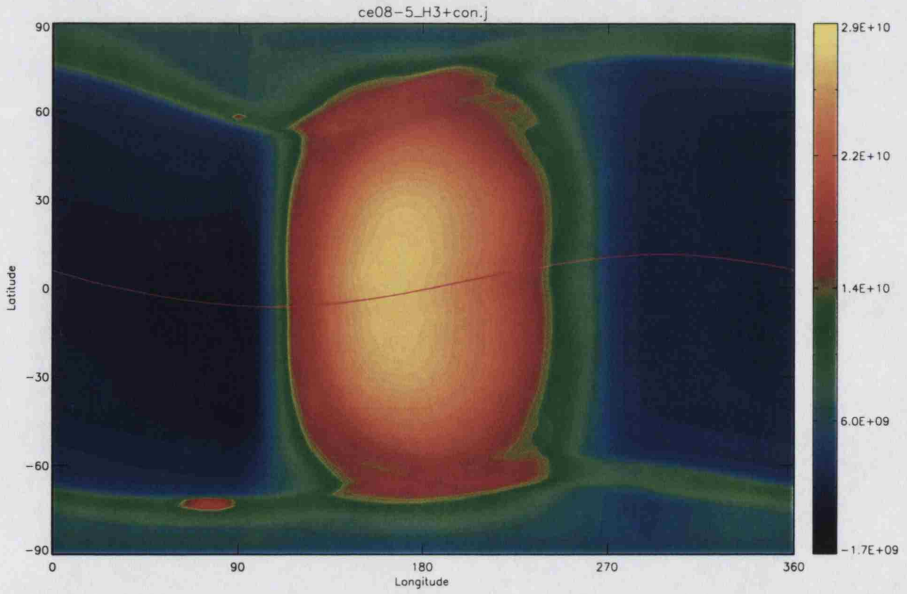

(b) H_3^+

Figure A.8: Pressure Level 16 Local Density

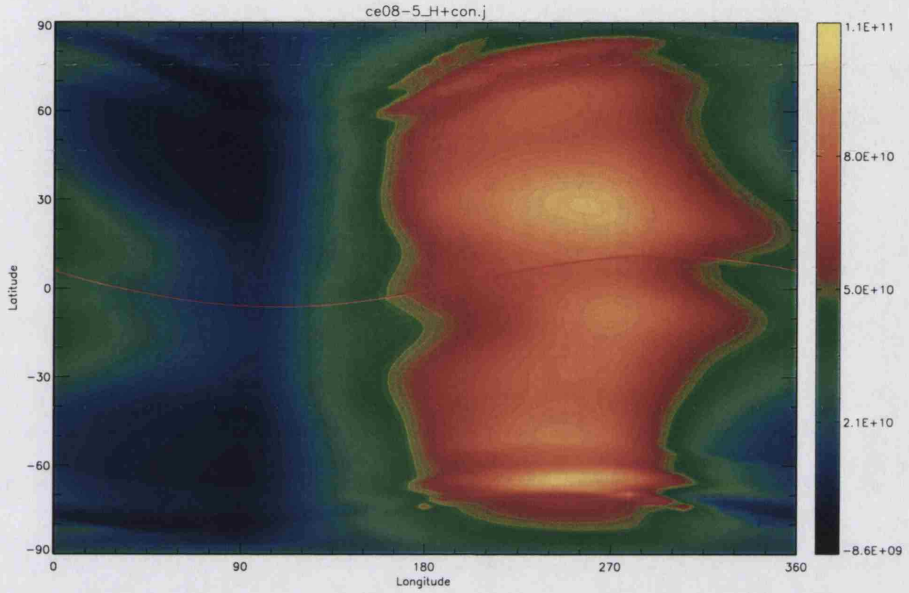

(a) H^+

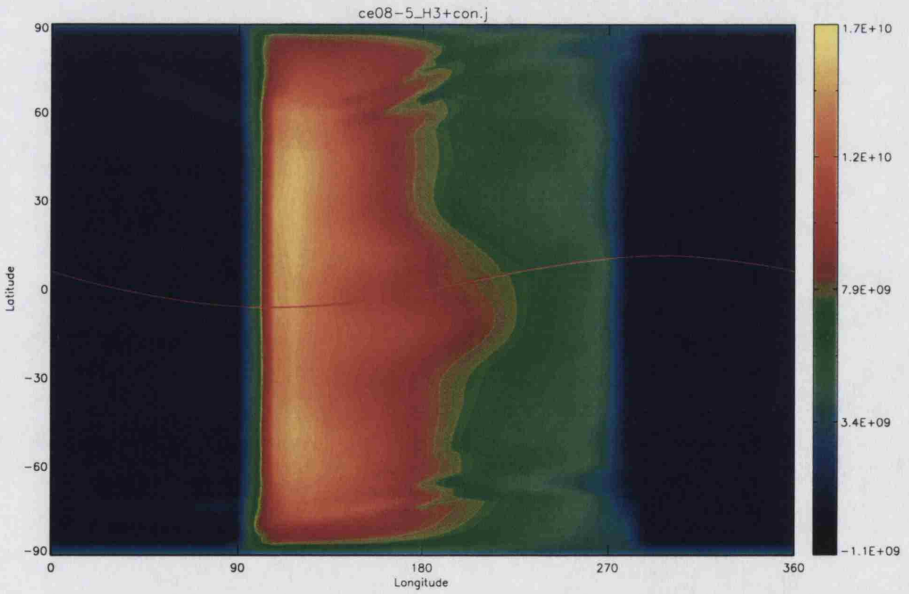

(b) H_3^+

Figure A.9: Pressure Level 26 Local Density

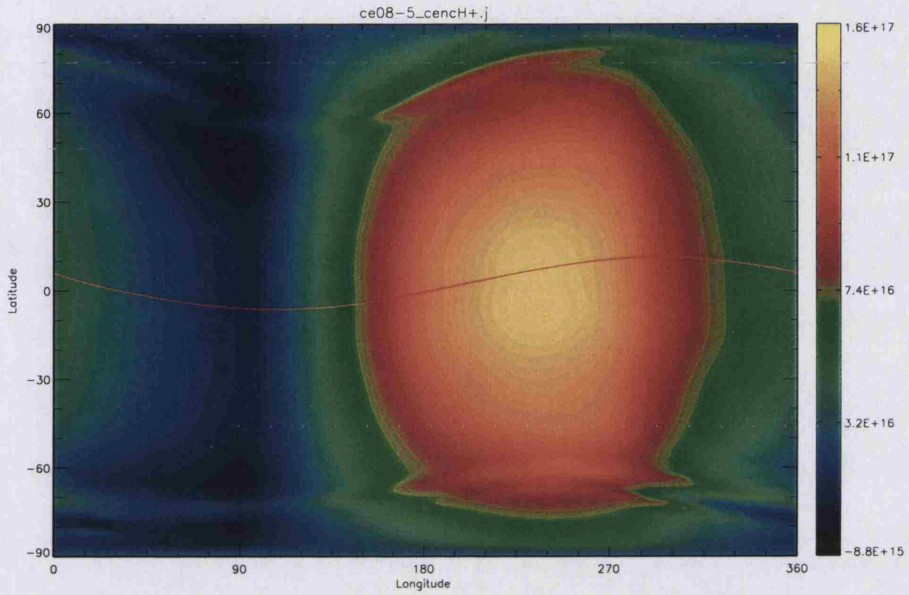

(a) H^+

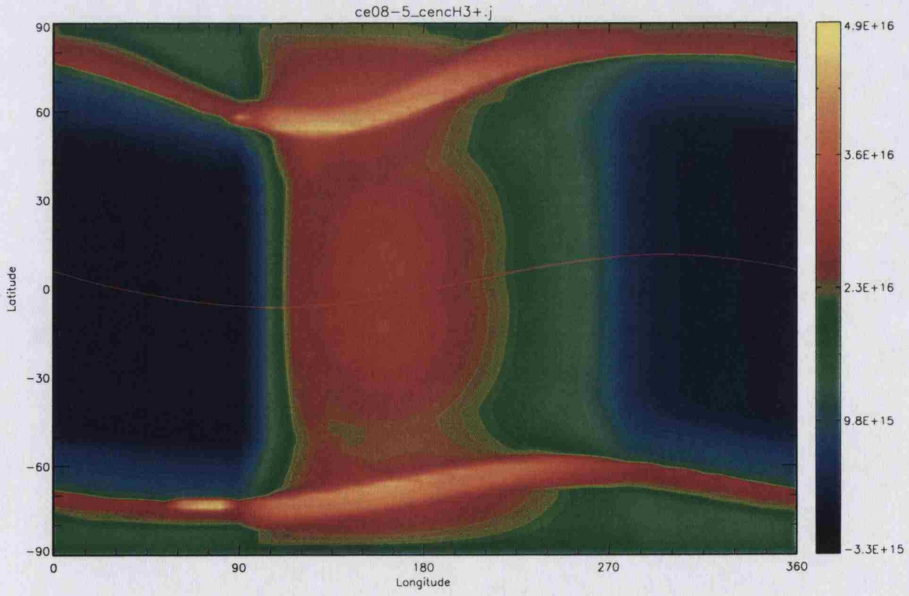

(b) H_3^+

Figure A.10: Column Density

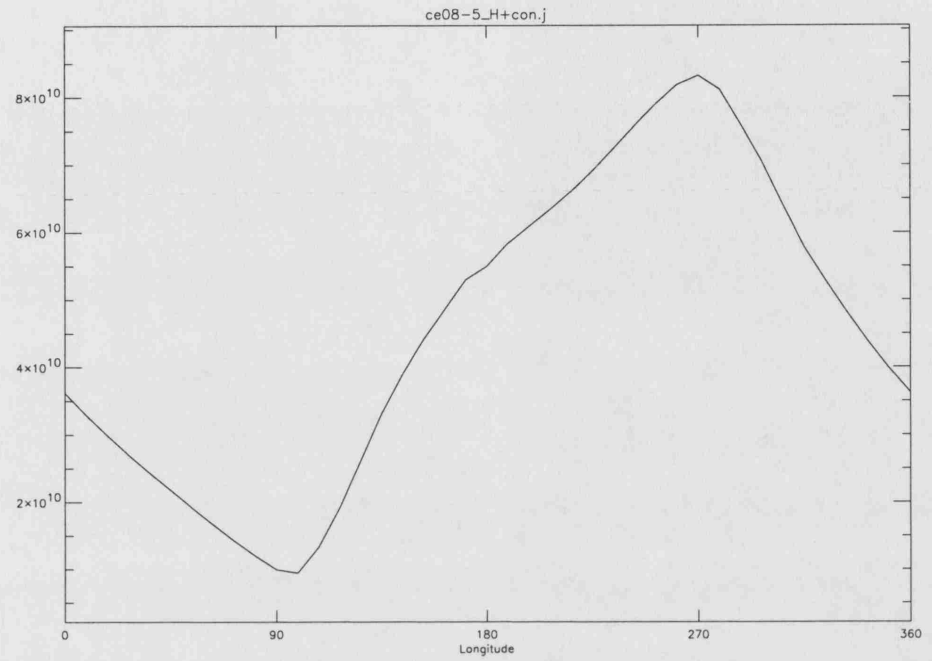

(a) H^+

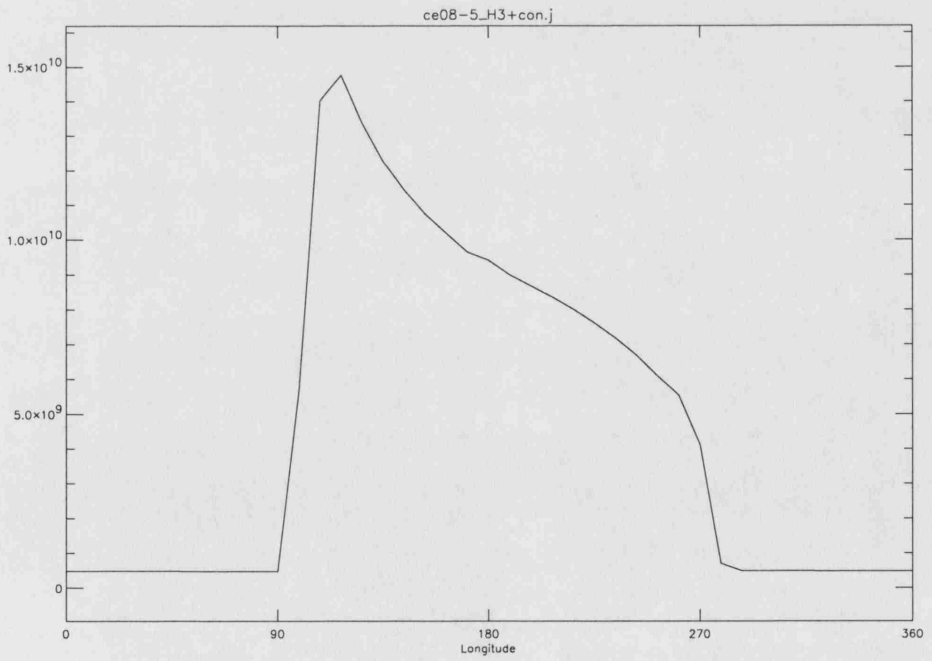

(b) H_3^+

Figure A.11: Longitude-Local Density at Pressure Level 26

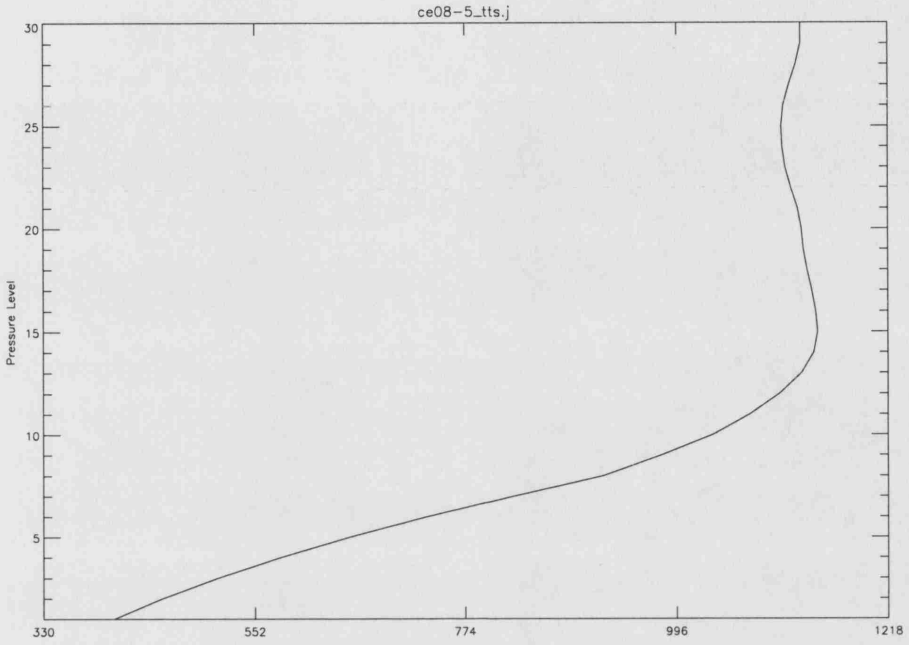

(a) Subsolar Point

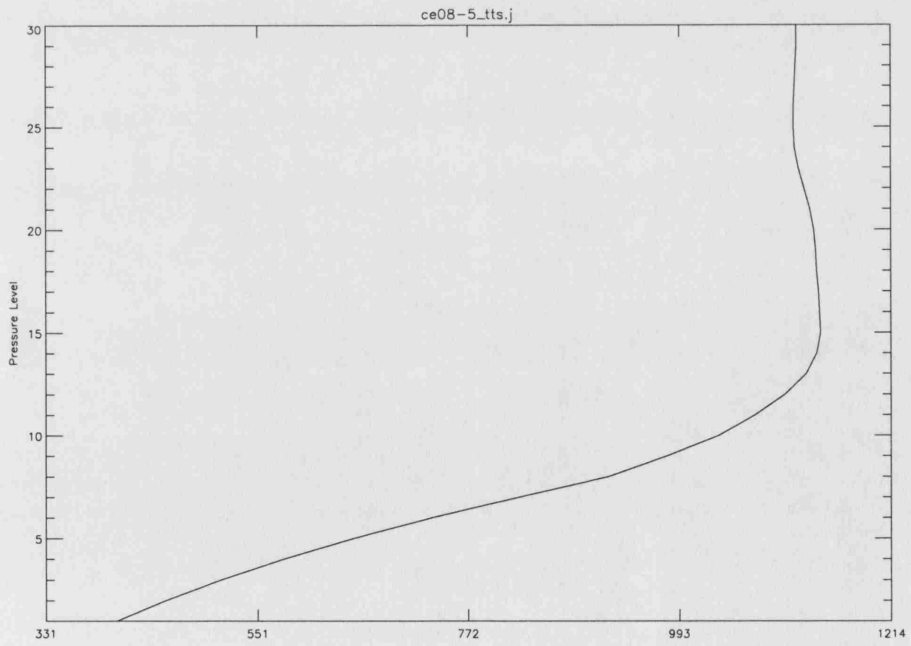

(b) Midnight

Figure A.12: Temperature Profile

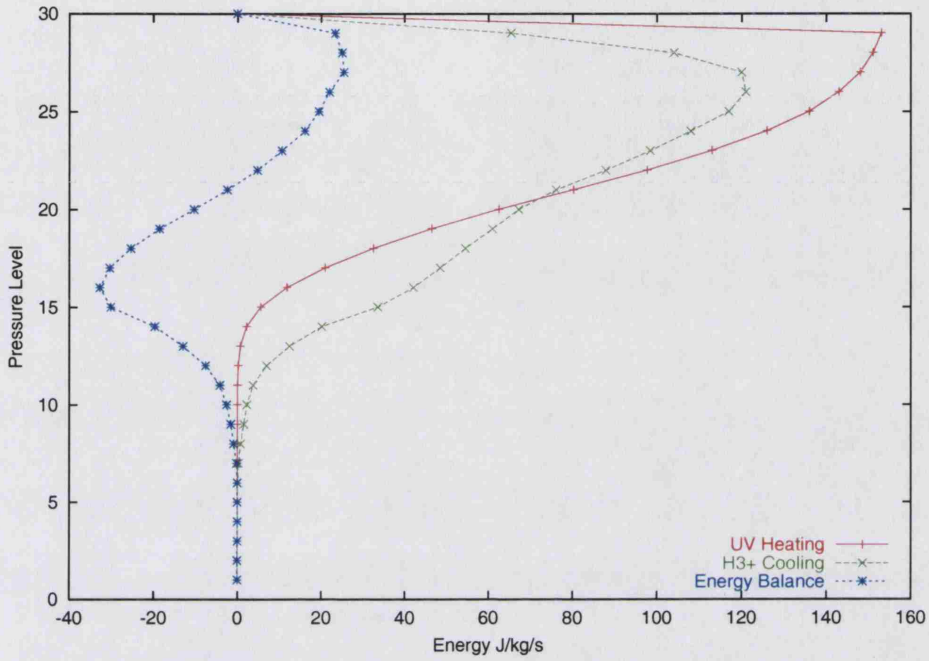

(a) Subsolar Point

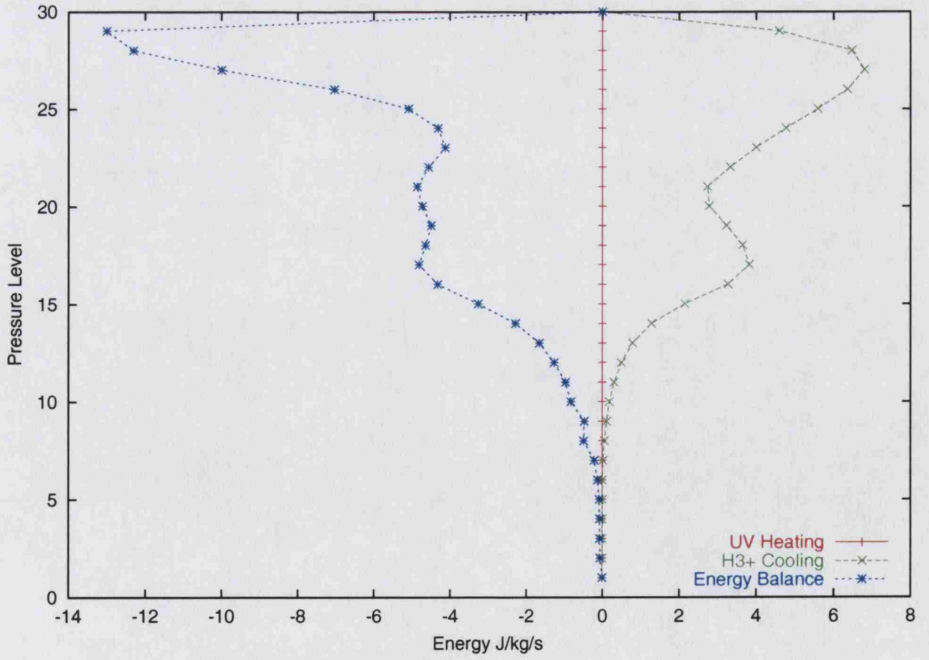

(b) Midnight

Figure A.13: Energy Balance

A.3 ce03

Orbital Radius /*AU*	Orbital Period /*hours*	Timestep /*seconds*
0.3	9.92	3.97

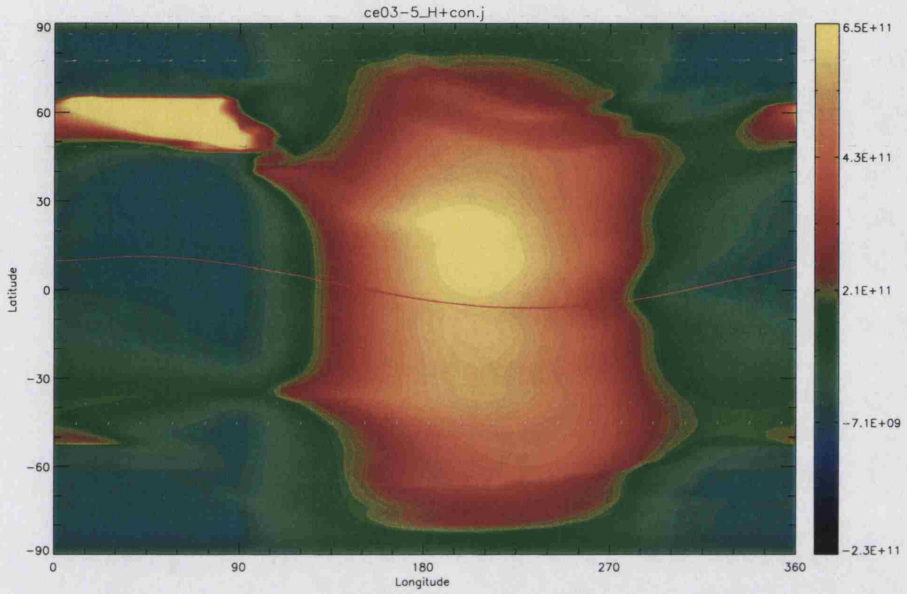

(a) H^+

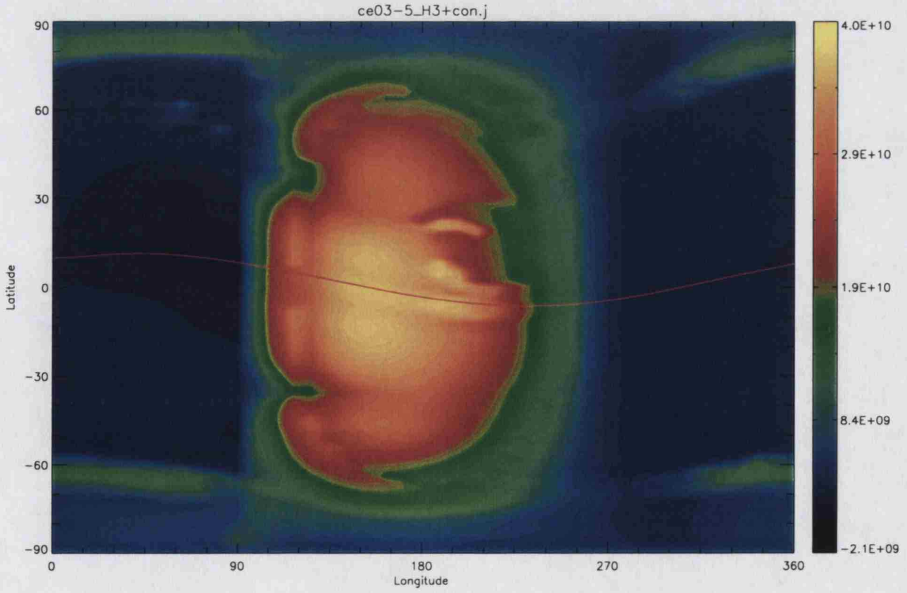

(b) H_3^+

Figure A.14: Pressure Level 16 Local Density

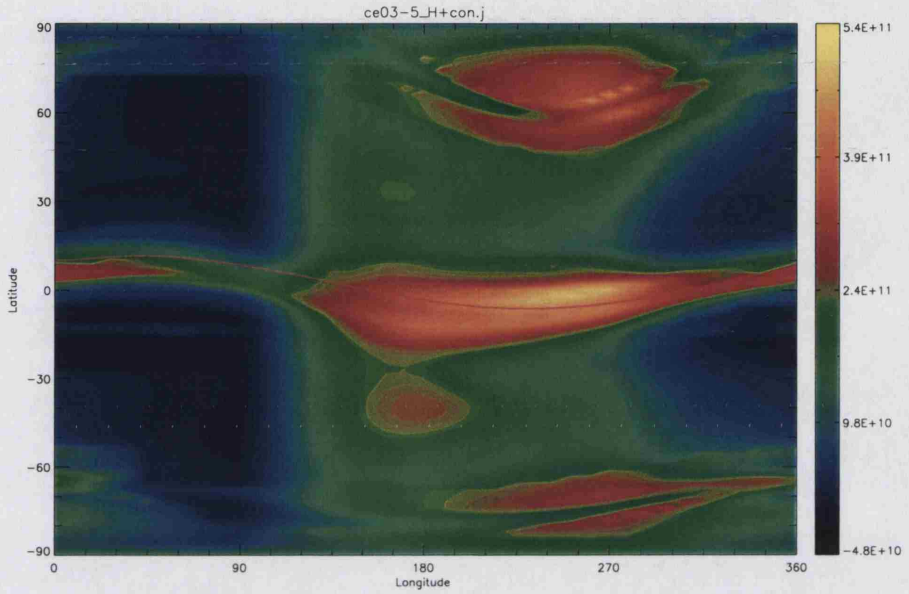

(a) H^+

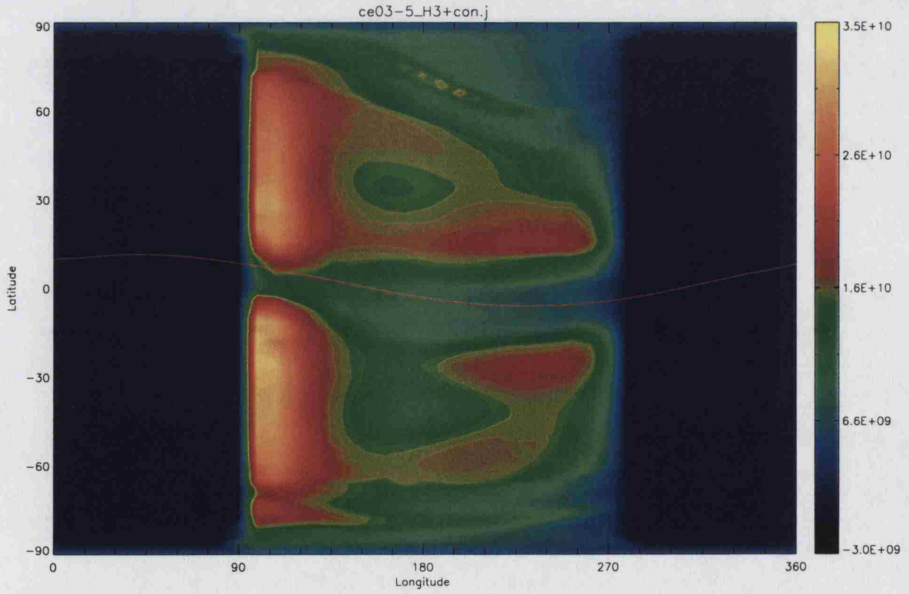

(b) H_3^+

Figure A.15: Pressure Level 26 Local Density

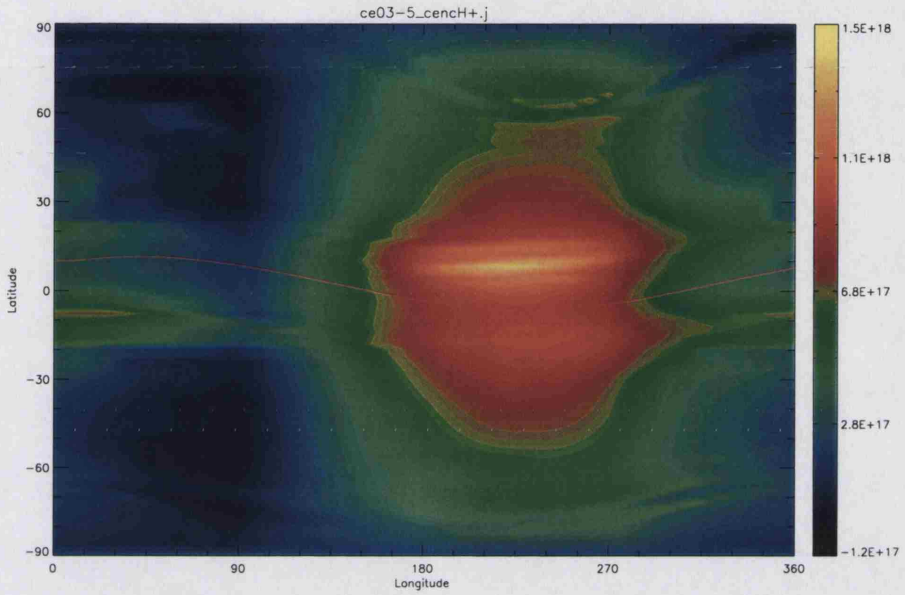

(a) H^+

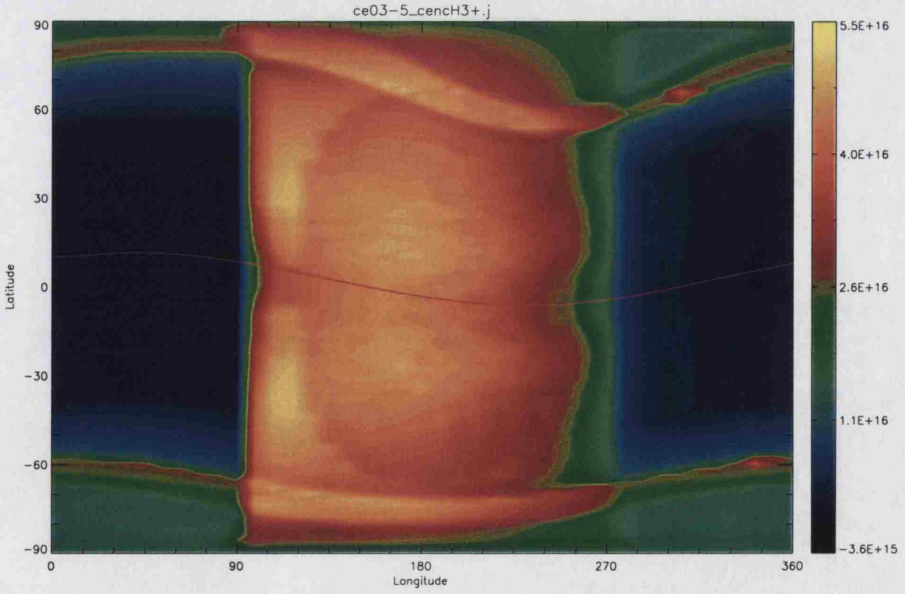

(b) H_3^+

Figure A.16: Column Density

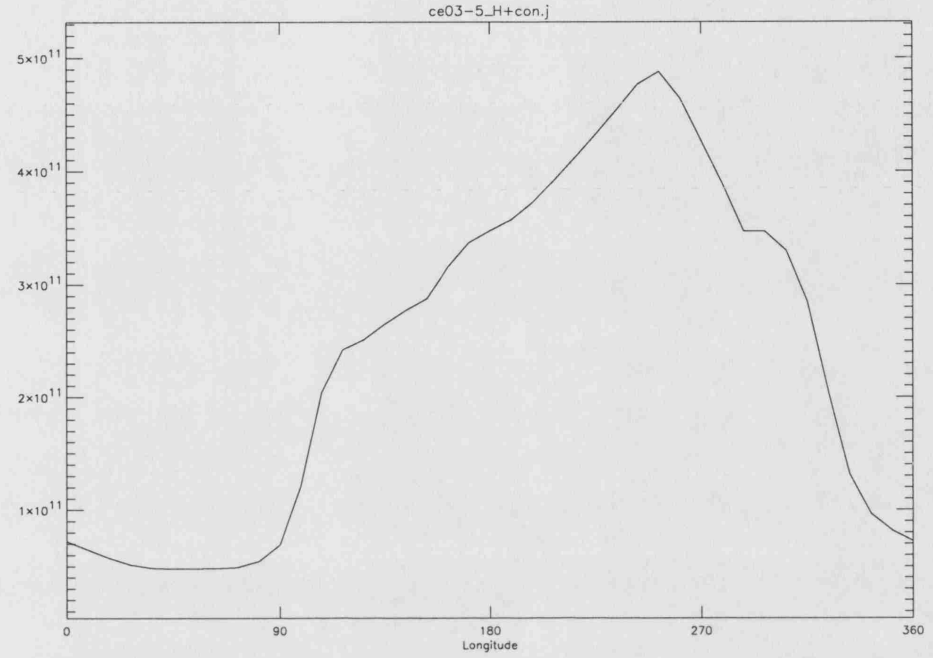

(a) H^+

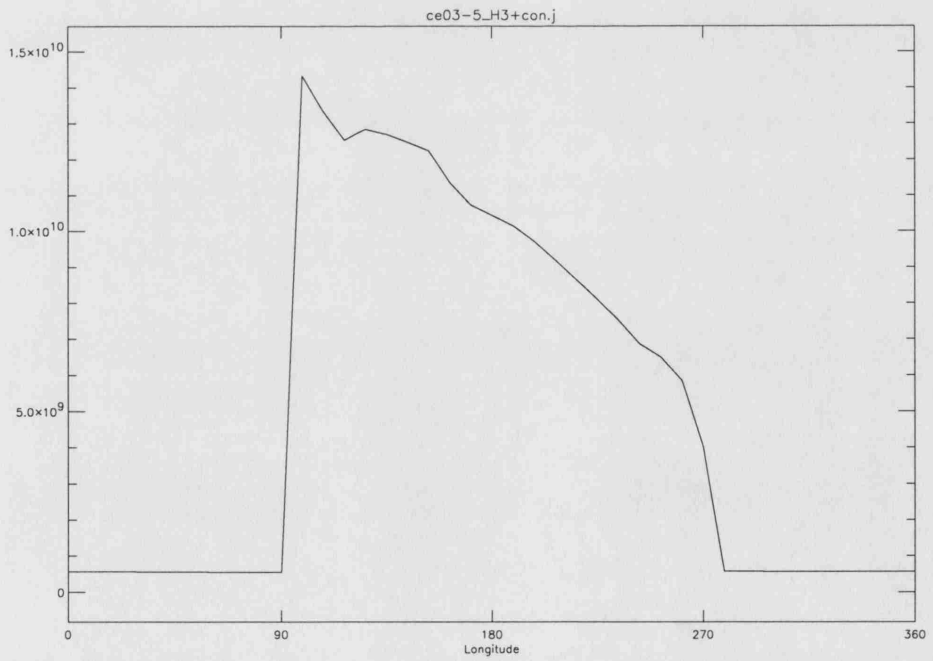

(b) H_3^+

Figure A.17: Longitude-Local Density at Pressure Level 26

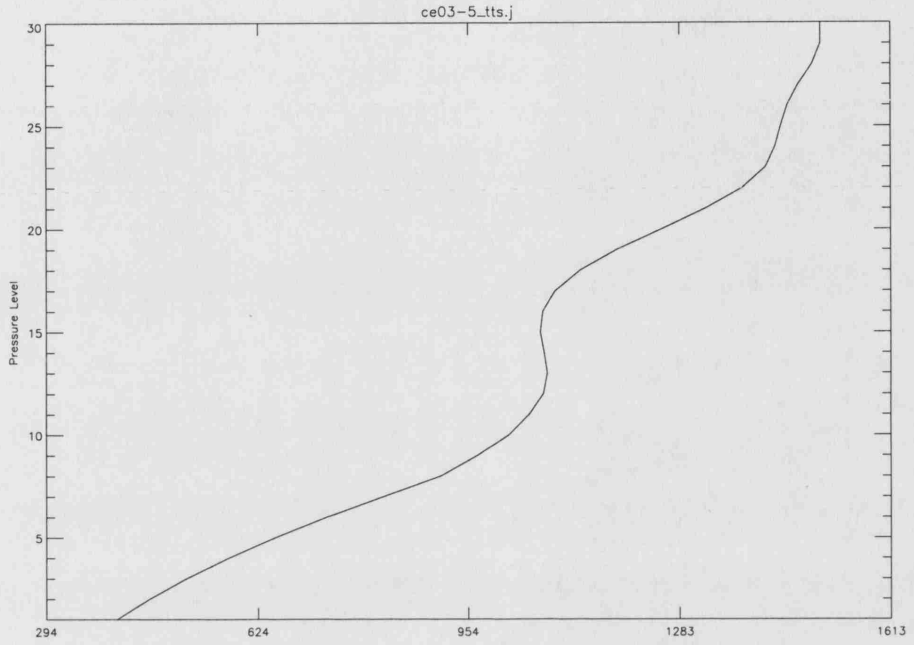

(a) Subsolar Point

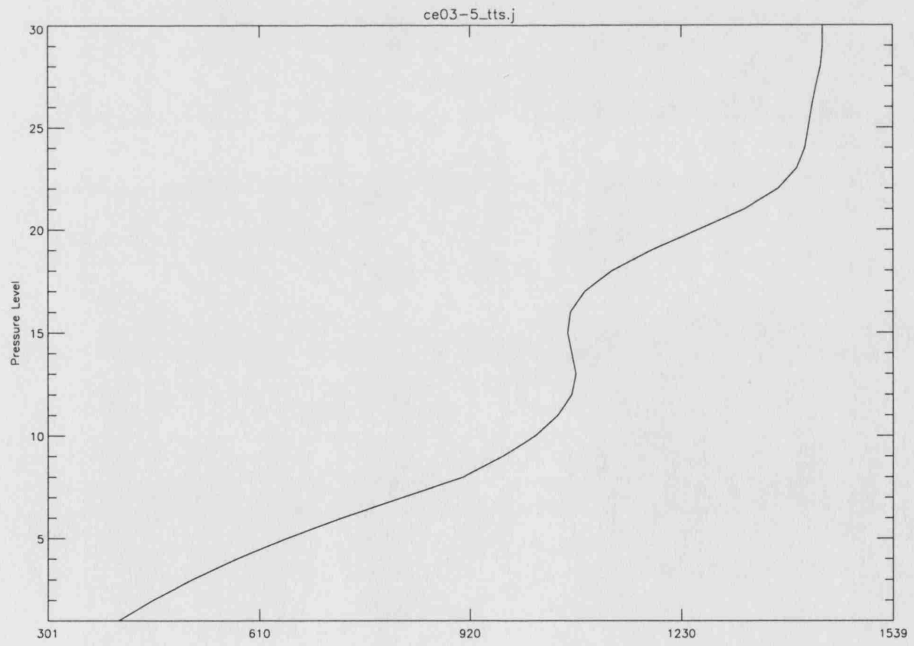

(b) Midnight

Figure A.18: Temperature Profile

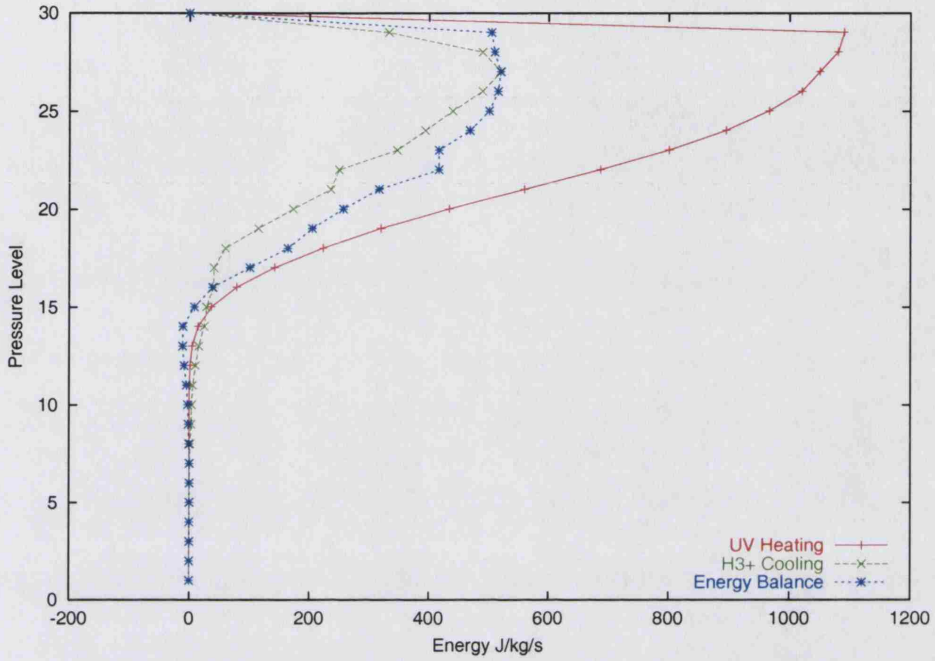

(a) Subsolar Point

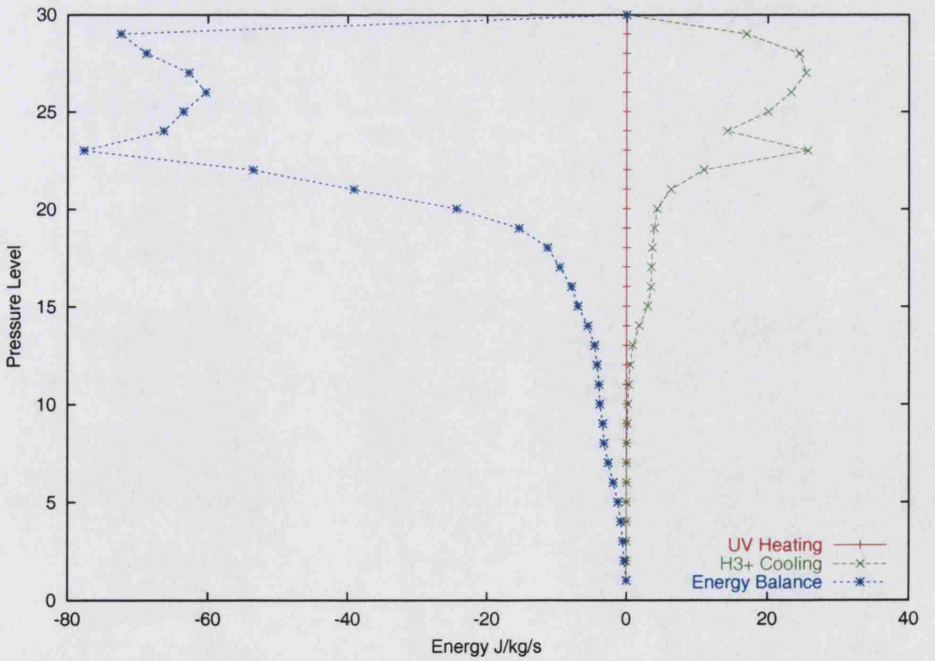

(b) Midnight

Figure A.19: Energy Balance

A.4 ce01

Orbital Radius /*AU*	Orbital Period /*hours*	Timestep /*seconds*
0.1	9.92	3.97

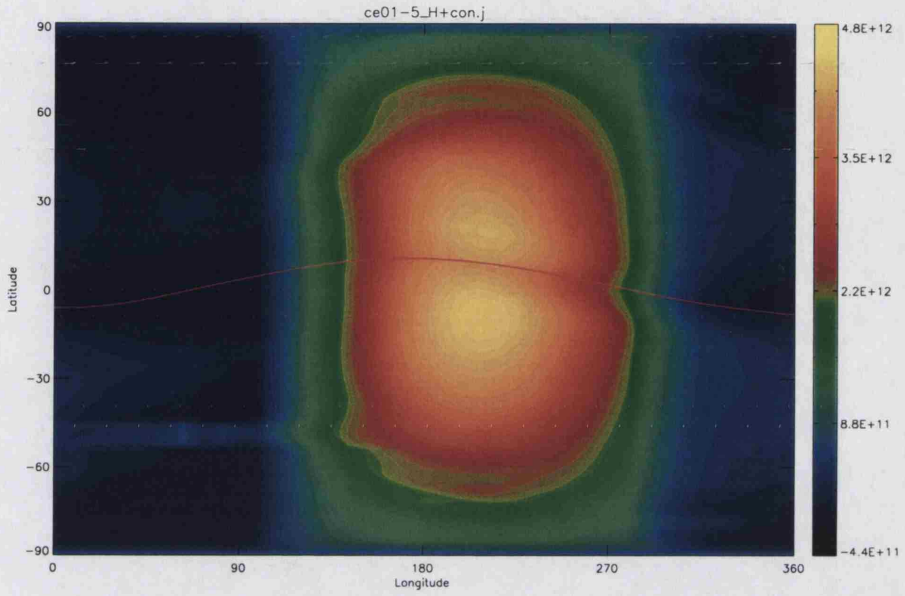

(a) H^+

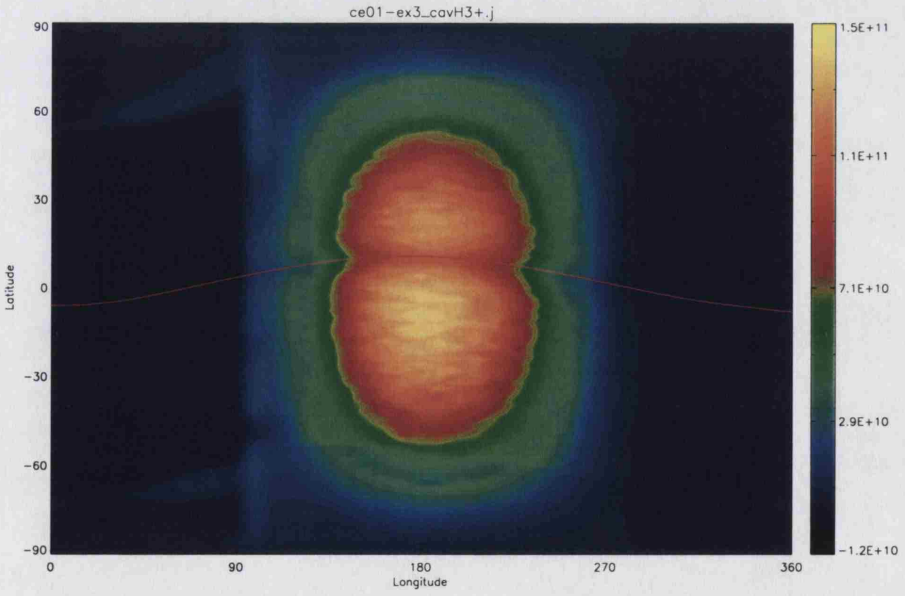

(b) H_3^+

Figure A.20: Pressure Level 16 Local Density

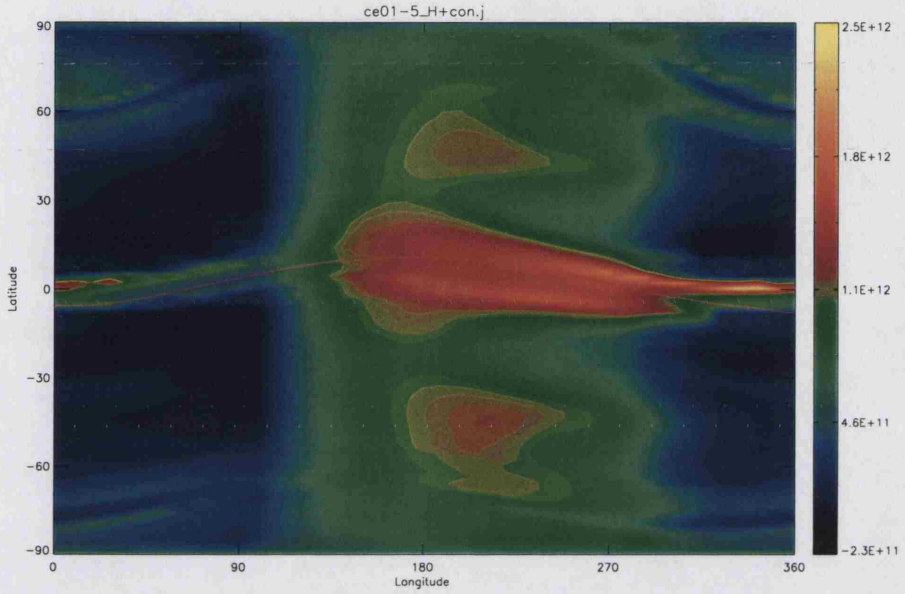

(a) H^+

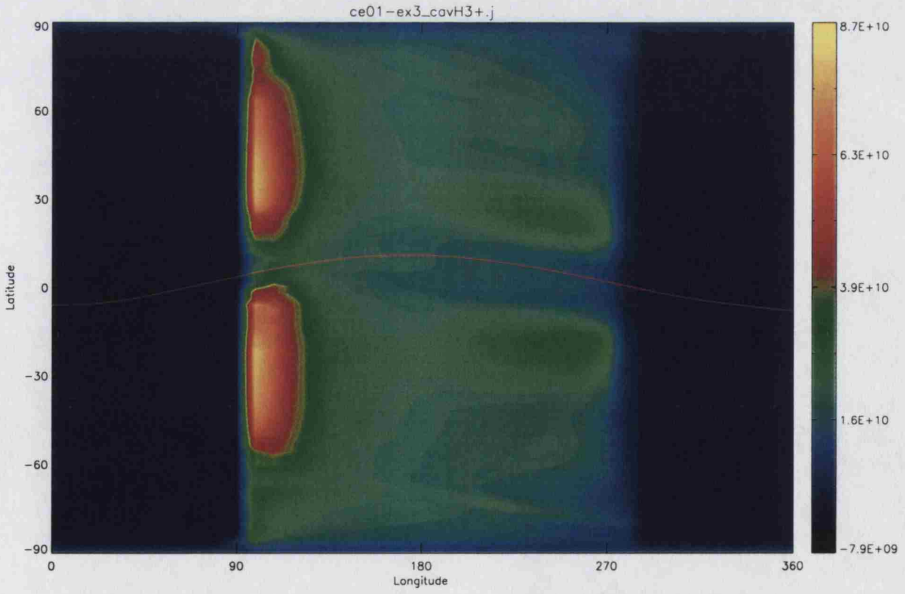

(b) H_3^+

Figure A.21: Pressure Level 26 Local Density

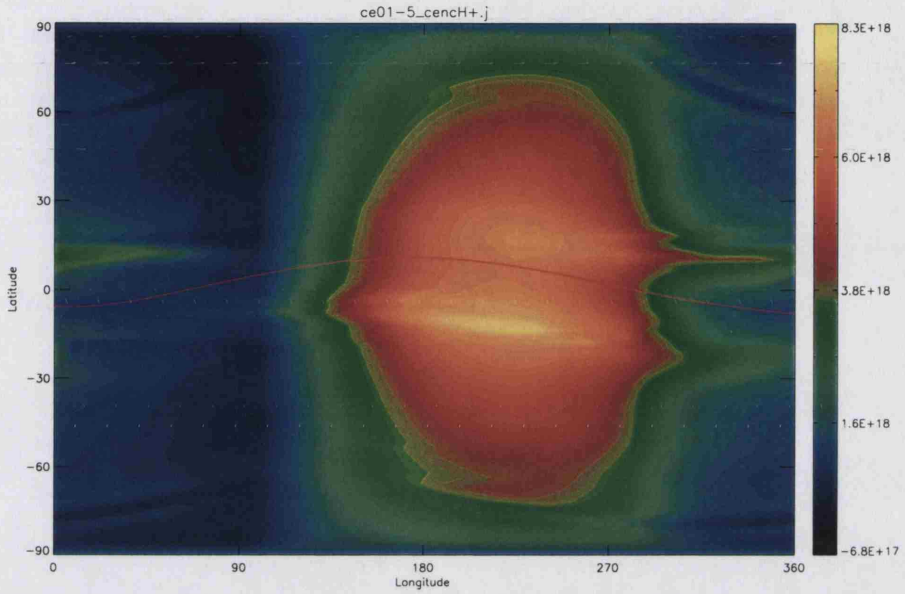

(a) H^+

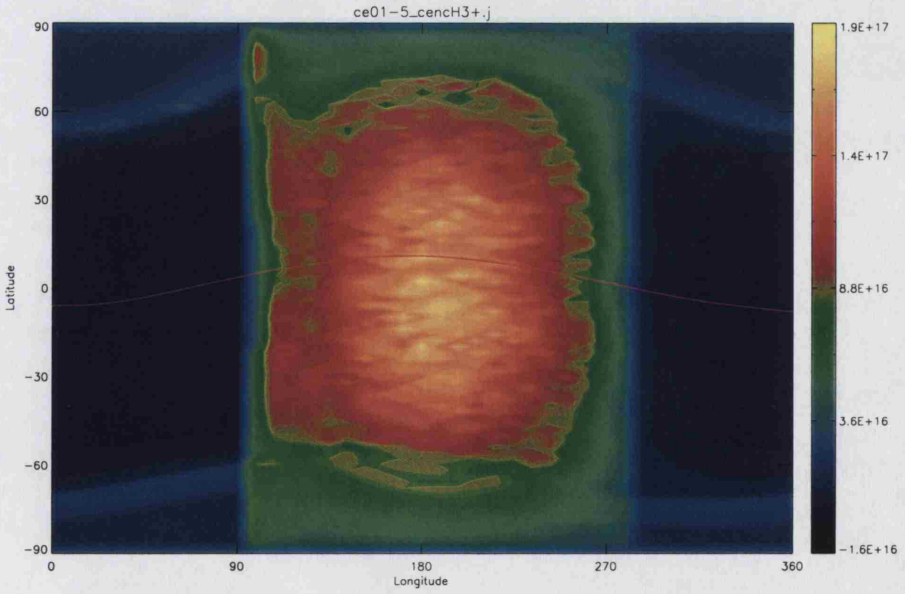

(b) H_3^+

Figure A.22: Column Density

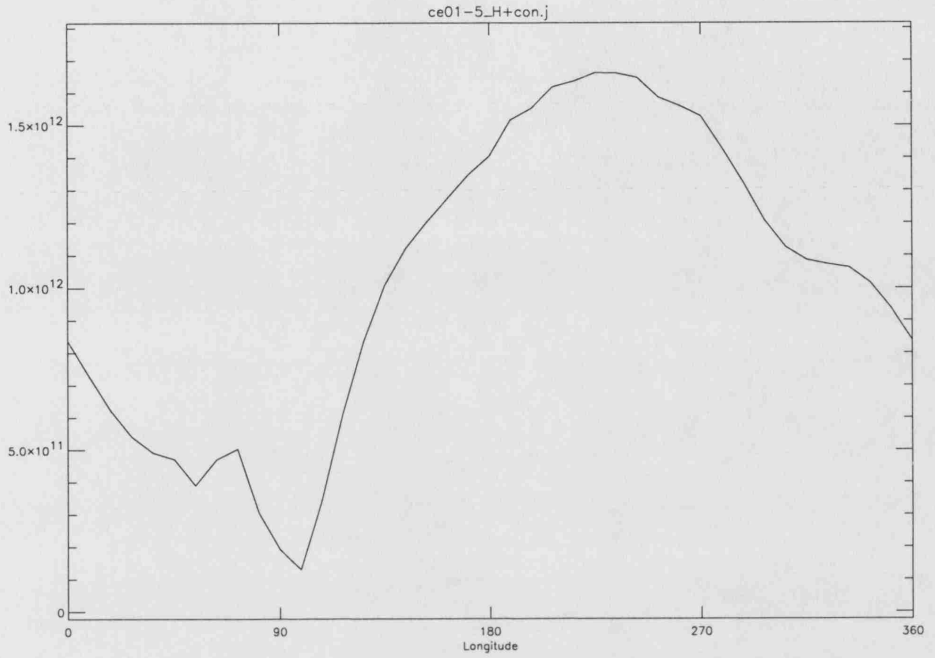

(a) H^+

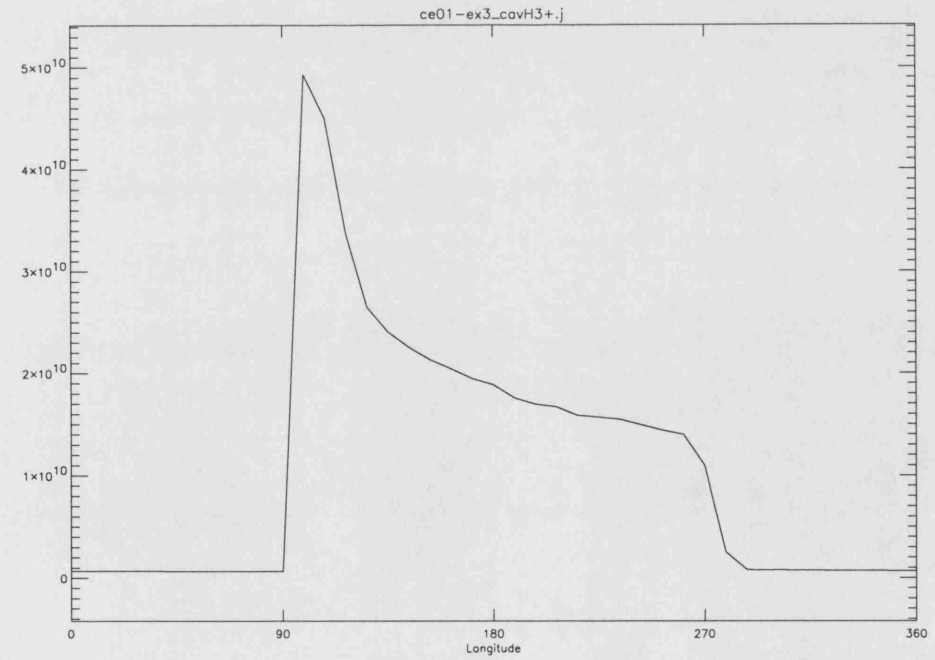

(b) H_3^+

Figure A.23: Longitude-Local Density at Pressure Level 26

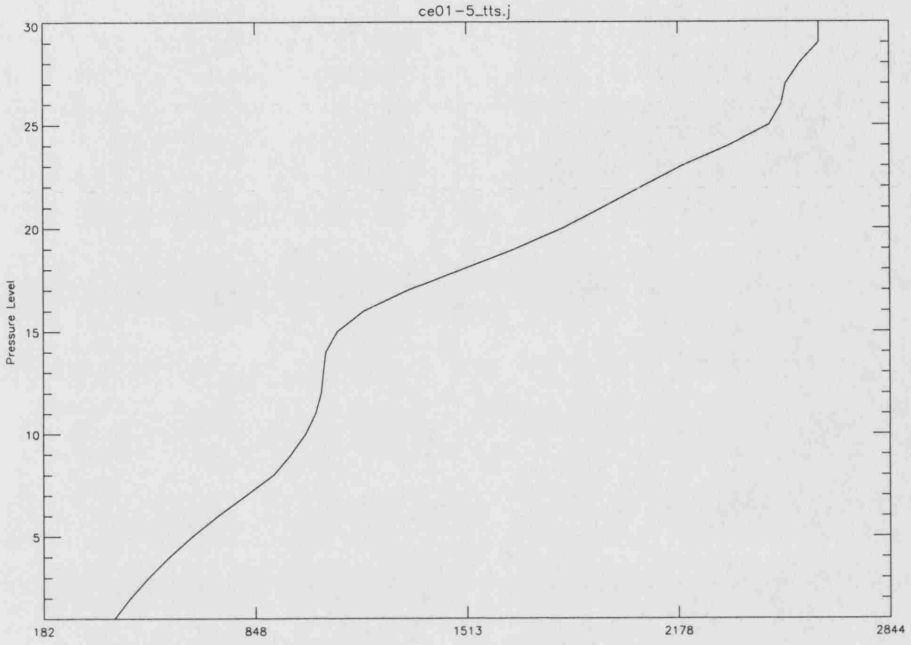

(a) Subsolar Point

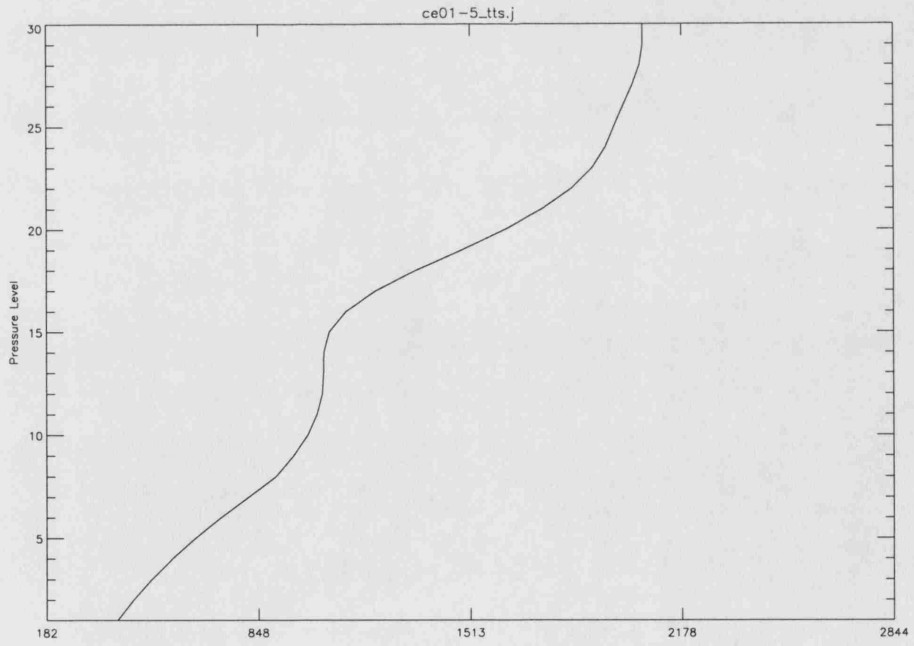

(b) Midnight

Figure A.24: Temperature Profile

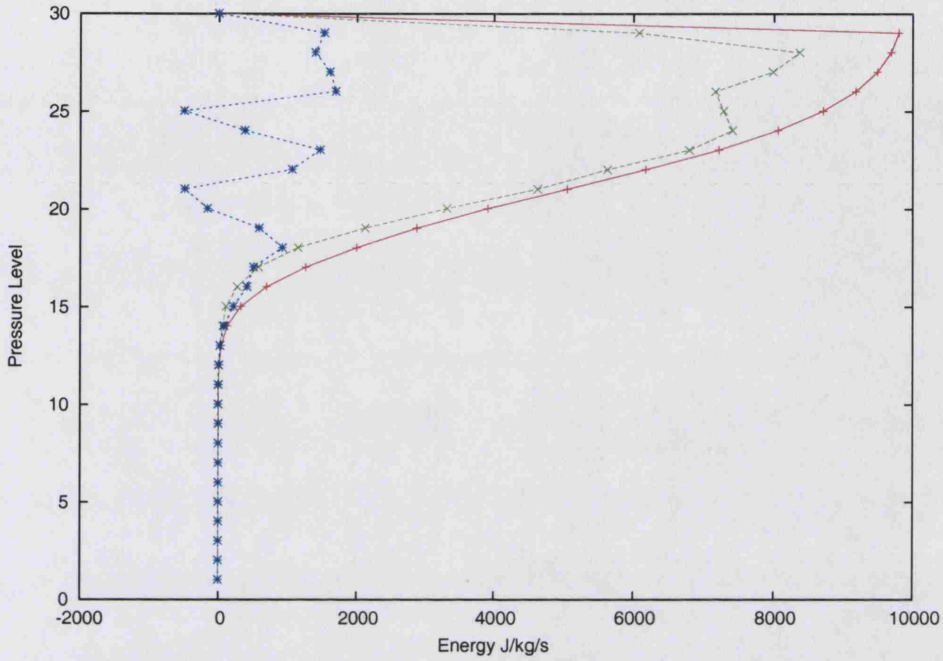

(a) Subsolar Point

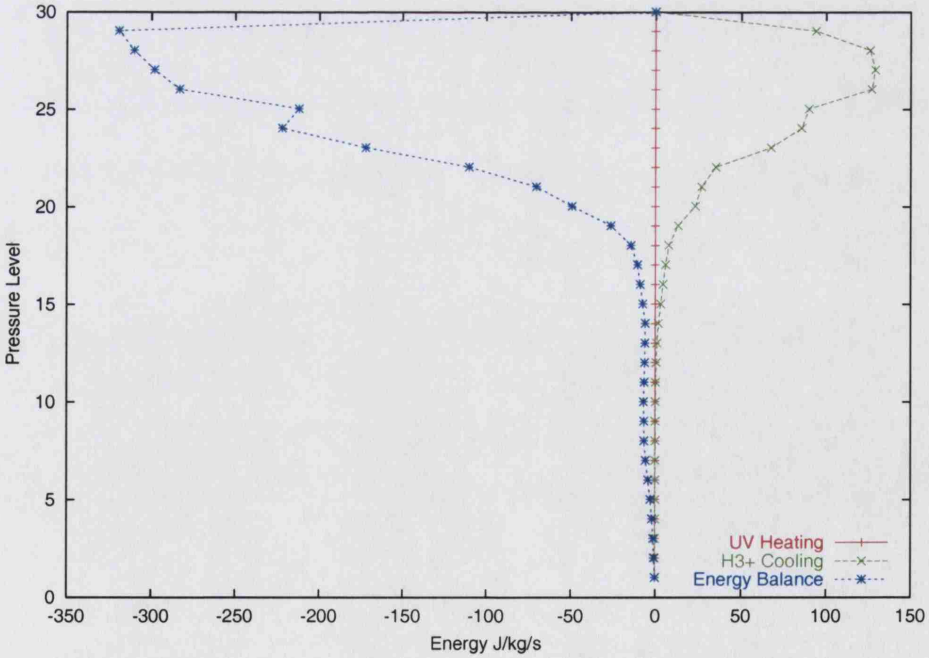

(b) Midnight

Figure A.25: Energy Balance

A.5 cl01

Orbital Radius /*AU*	Orbital Period /*hours*	Timestep /*seconds*
0.1	200	3.97

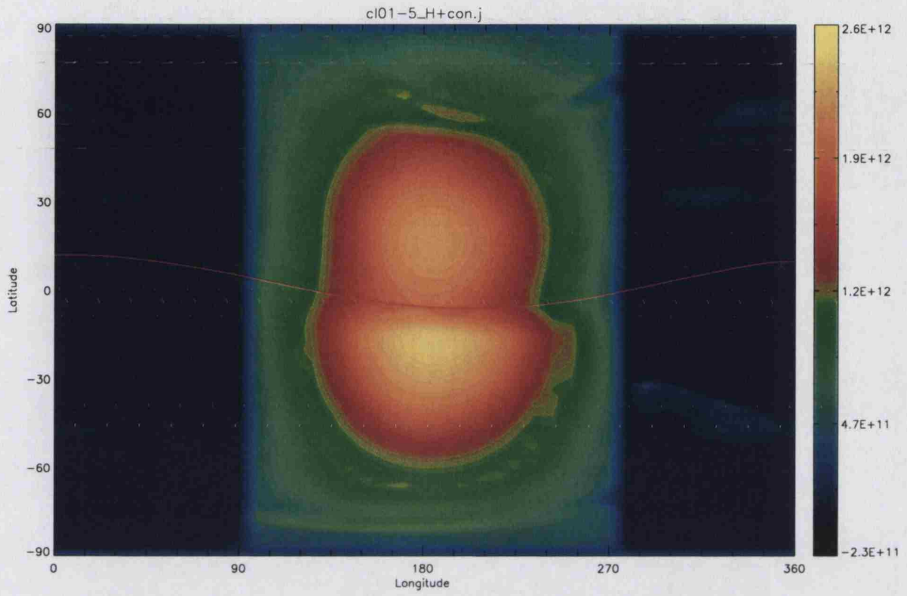

(a) H^+

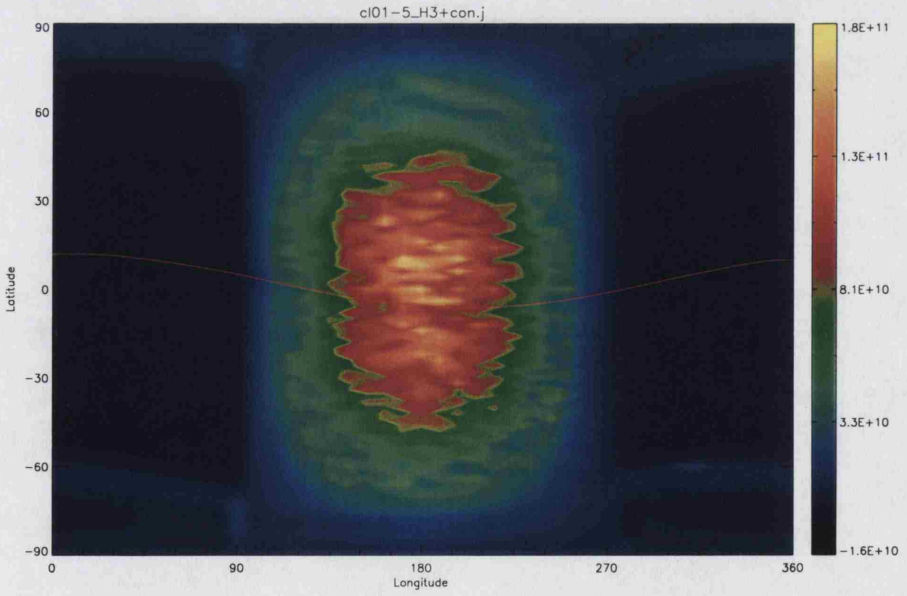

(b) H_3^+

Figure A.26: Pressure Level 16 Local Density

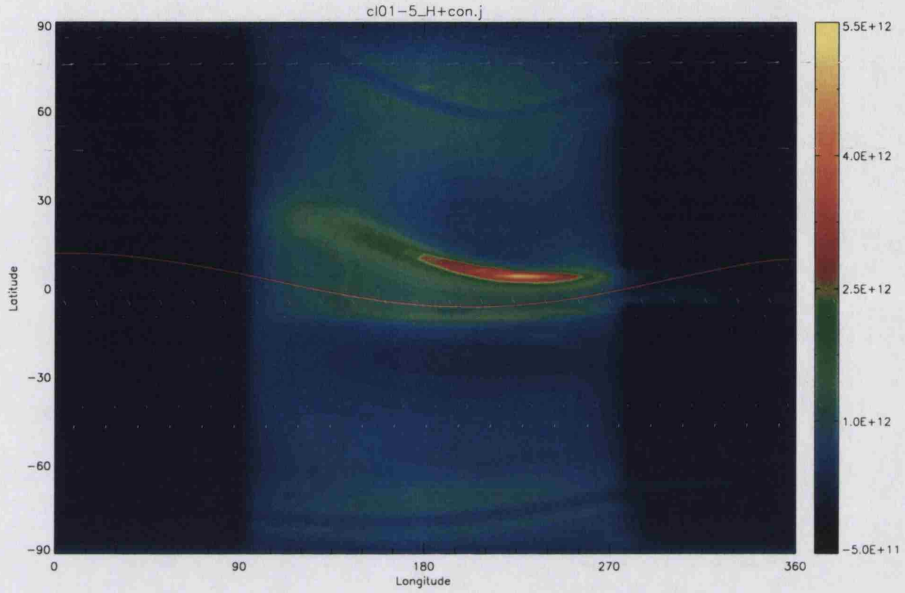

(a) H^+

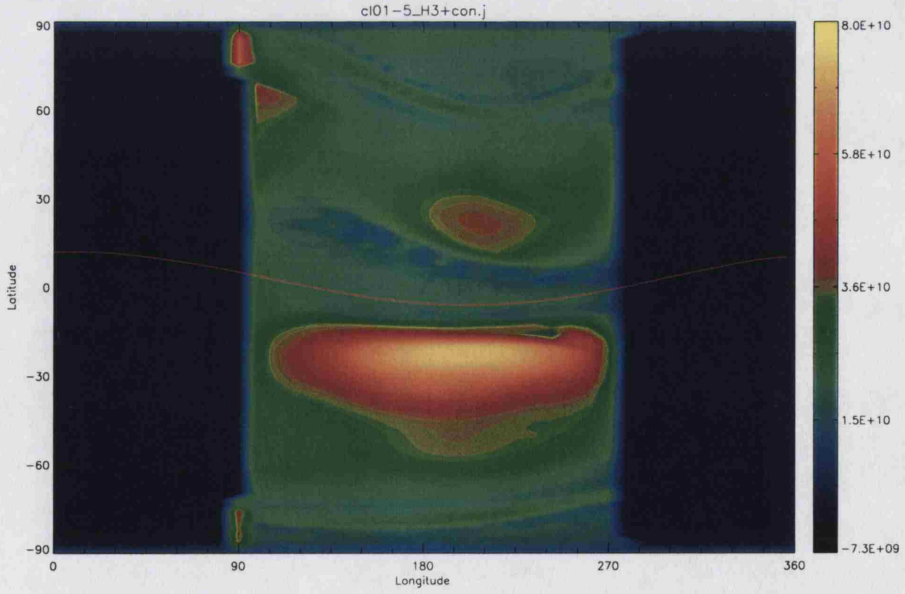

(b) H_3^+

Figure A.27: Pressure Level 26 Local Density

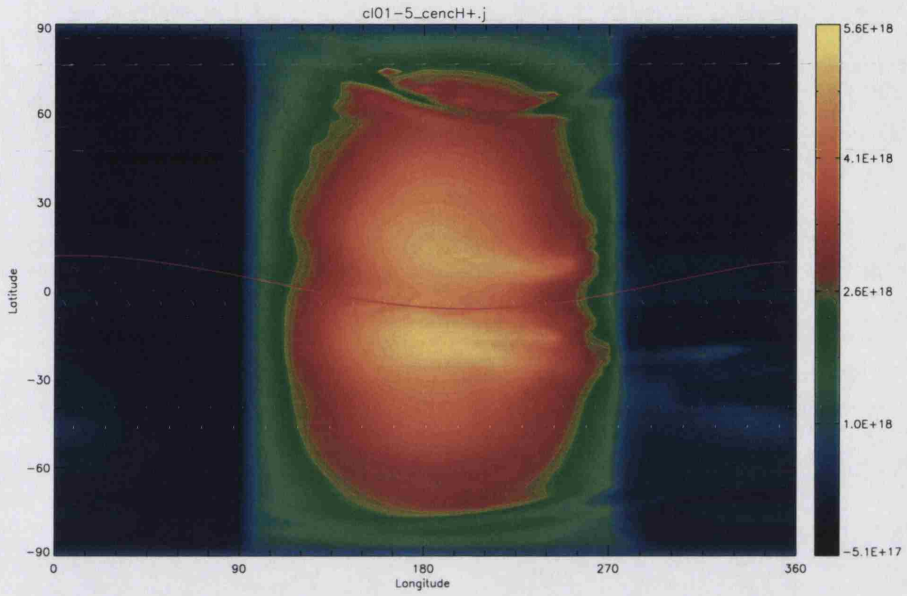

(a) H^+

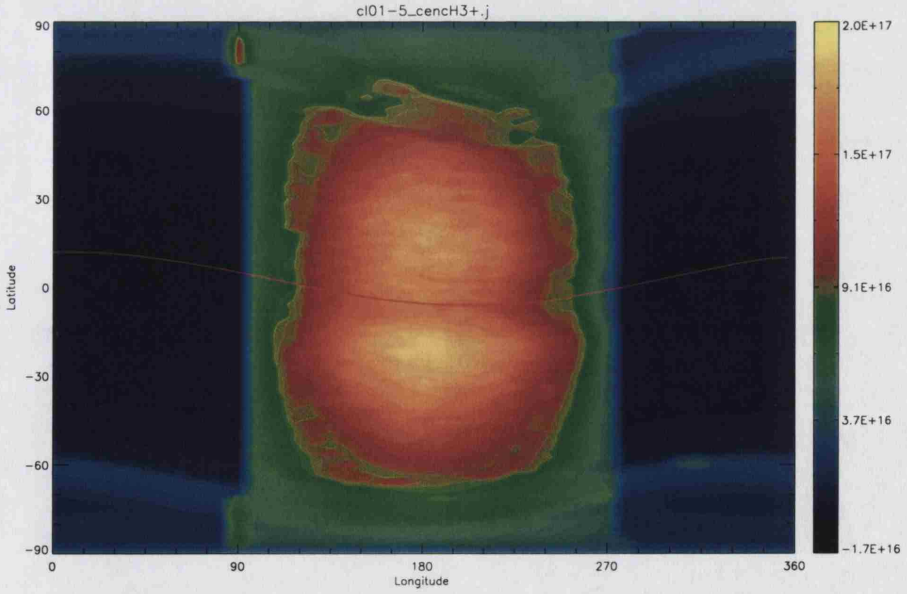

(b) H_3^+

Figure A.28: Column Density

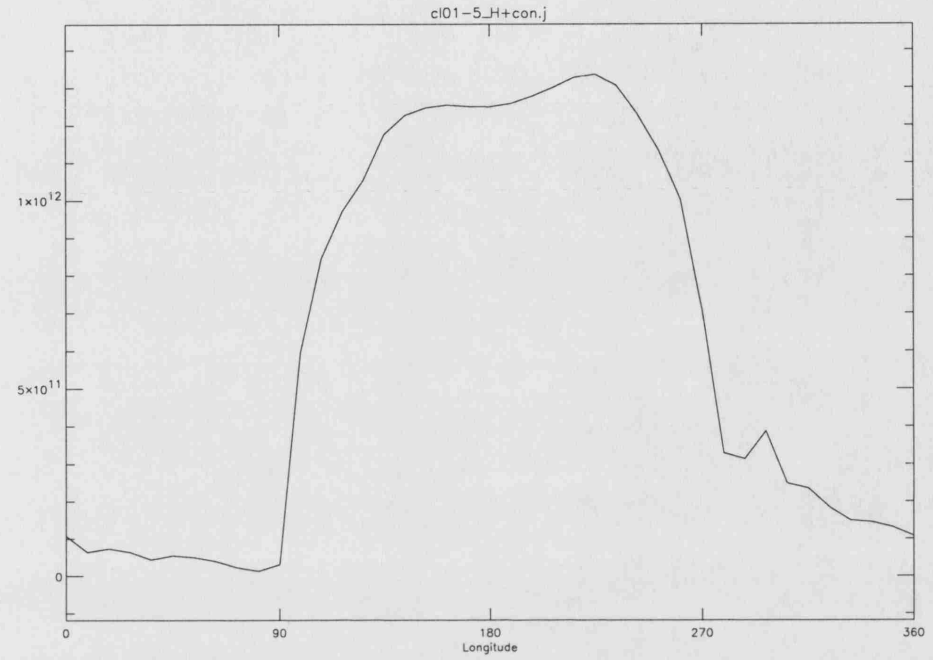

(a) H^+

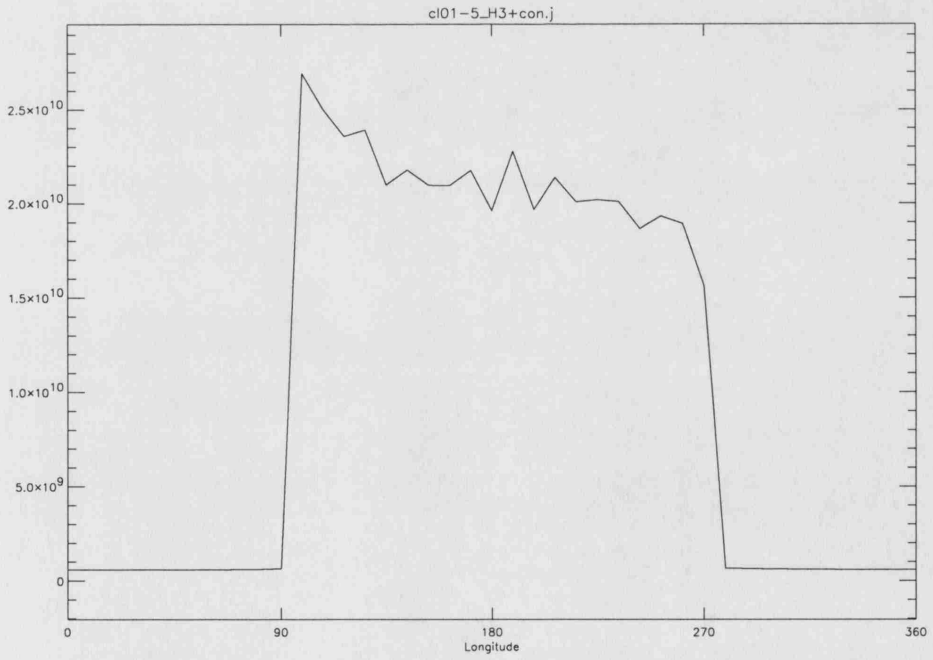

(b) H_3^+

Figure A.29: Longitude-Local Density at Pressure Level 26

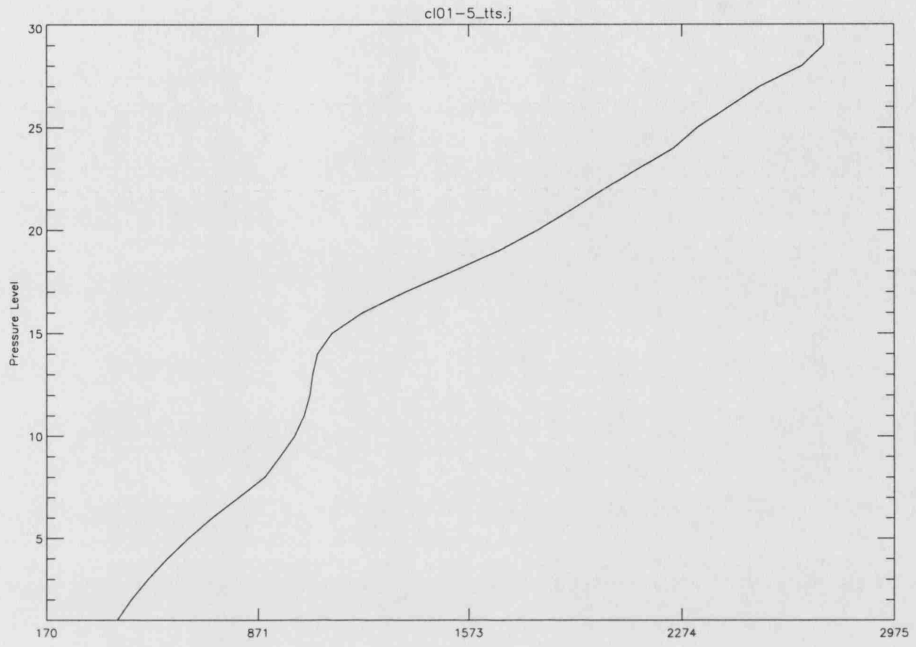

(a) Subsolar Point

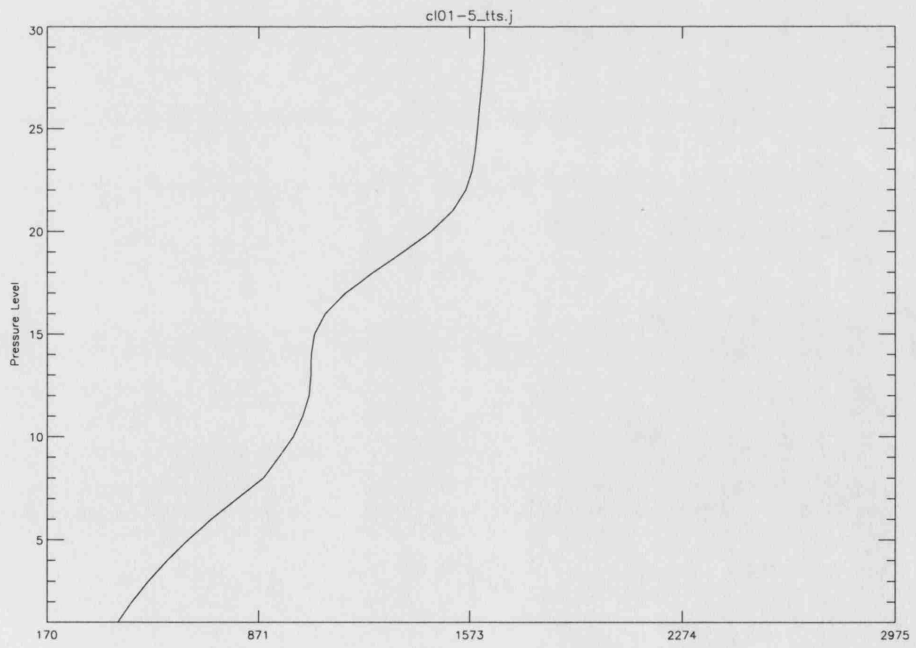

(b) Midnight

Figure A.30: Temperature Profile

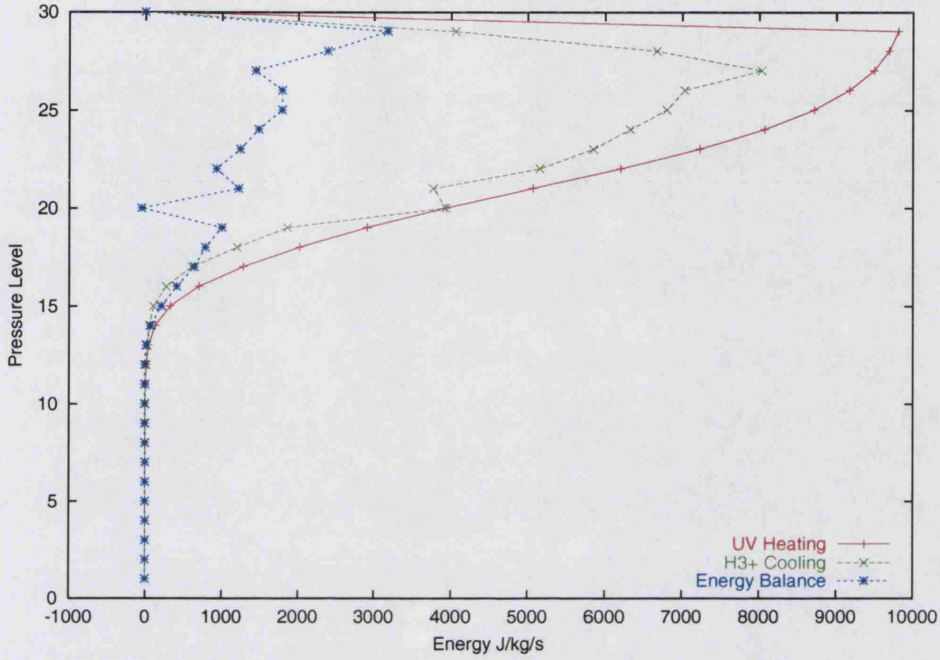

(a) Subsolar Point

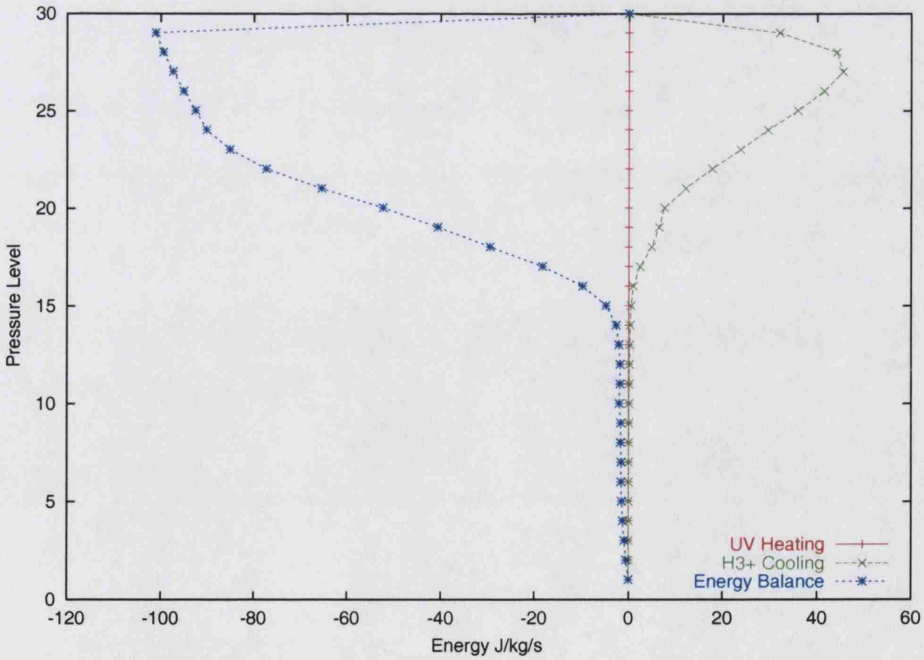

(b) Midnight

Figure A.31: Energy Balance

A.6 cm03

Orbital Radius /*AU*	Orbital Period /*hours*	Timestep /*seconds*
0.3	200	3.97

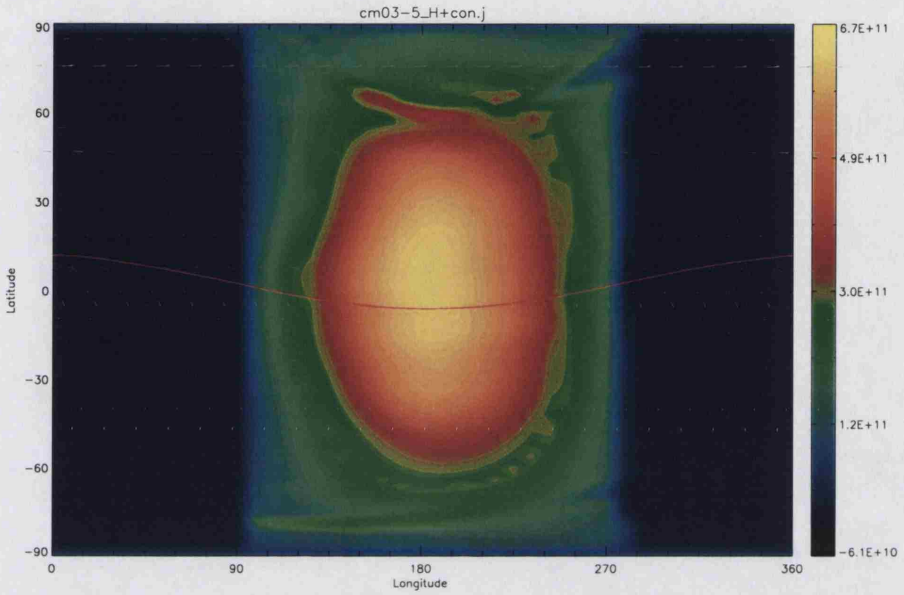

(a) H^+

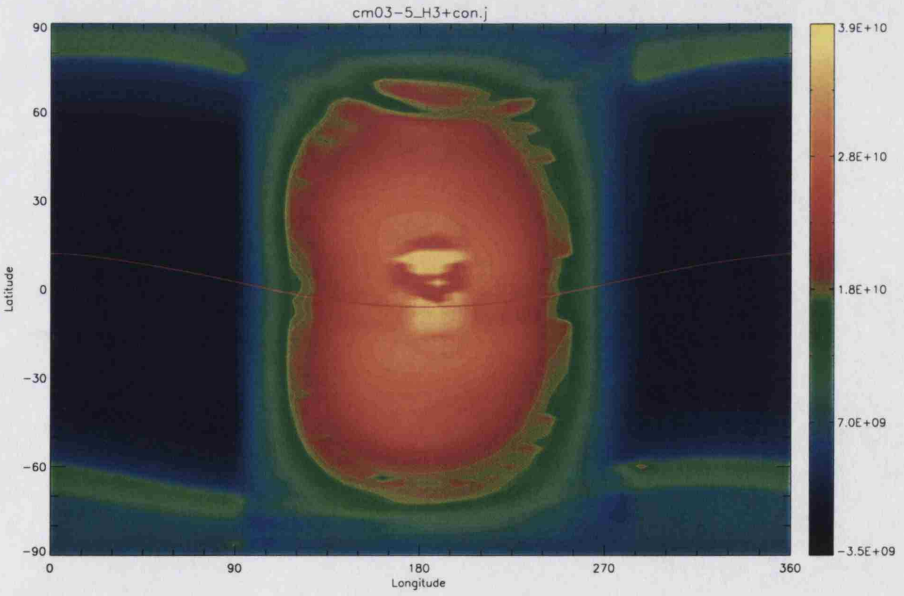

(b) H_3^+

Figure A.32: Pressure Level 16 Local Density

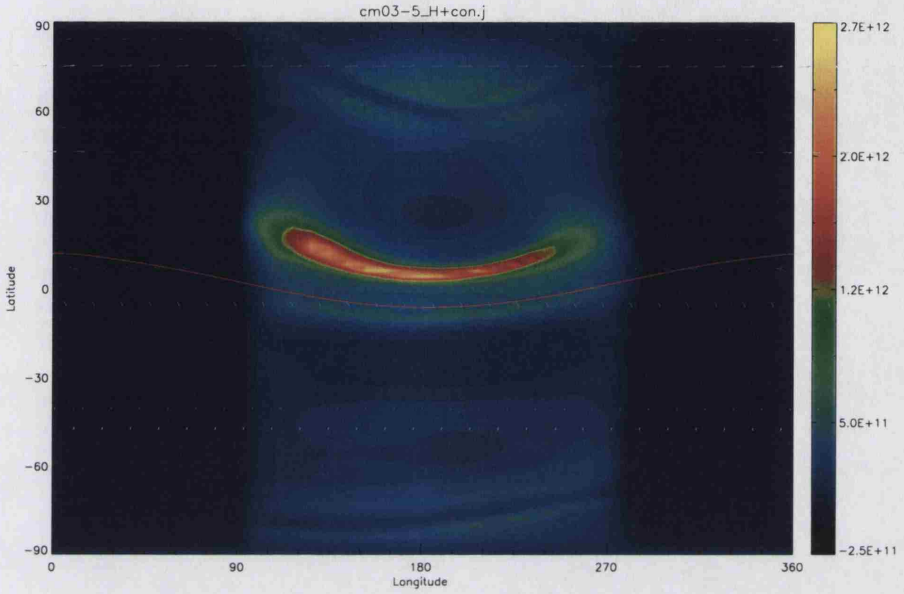

(a) H^+

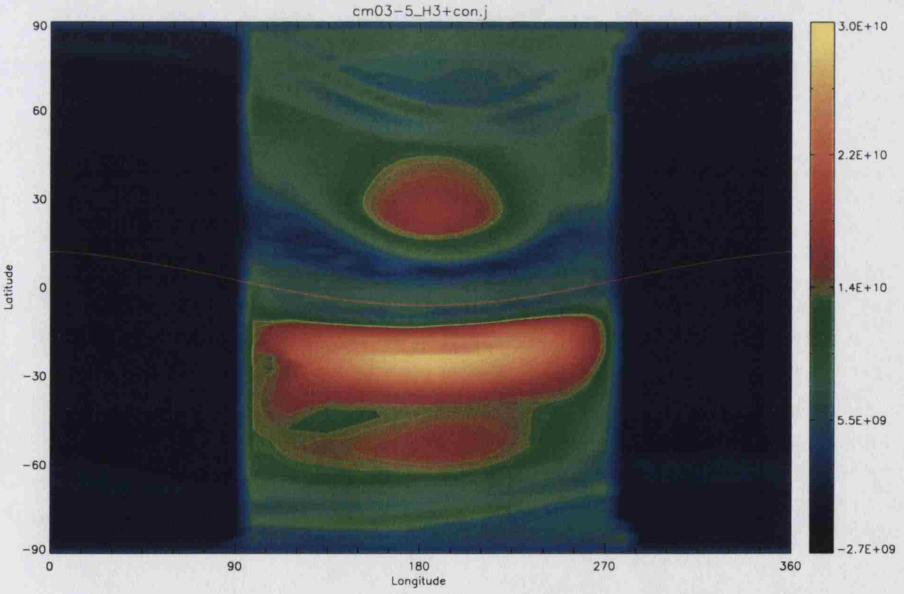

(b) H_3^+

Figure A.33: Pressure Level 26 Local Density

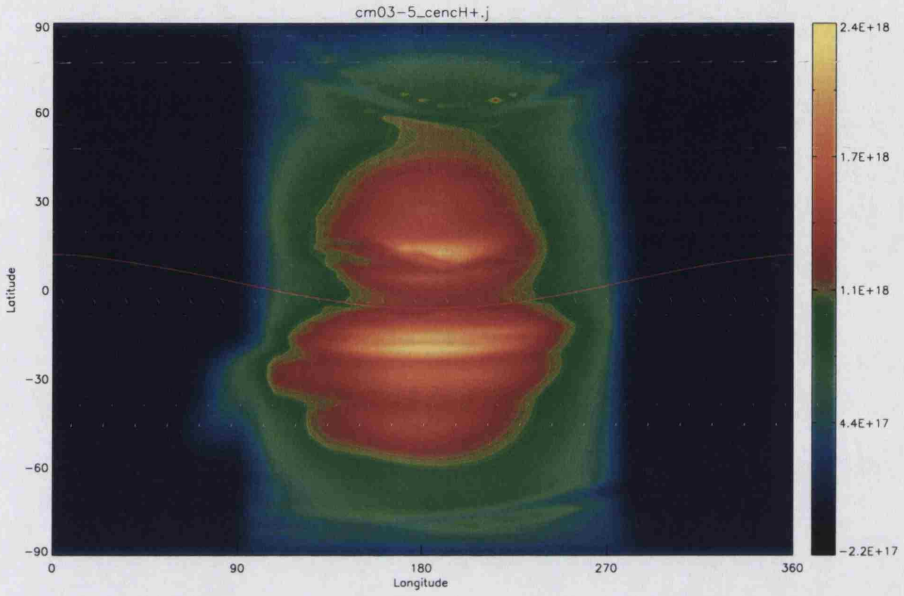

(a) H^+

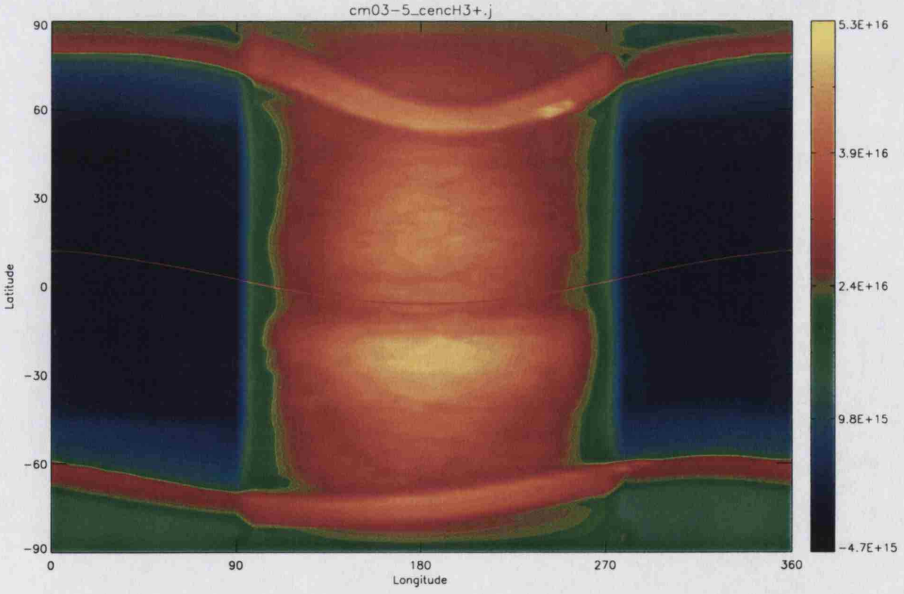

(b) H_3^+

Figure A.34: Column Density

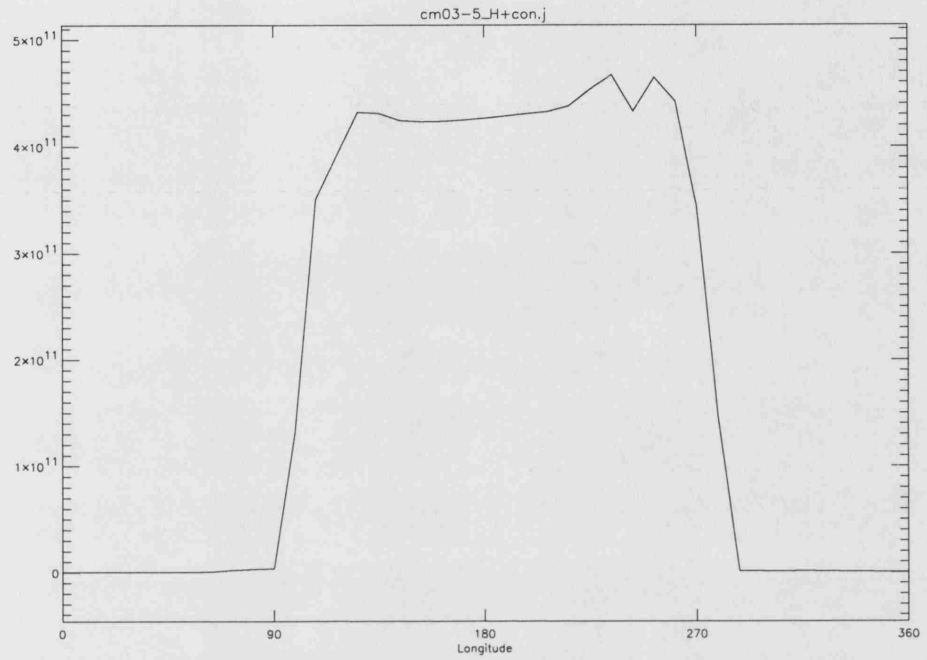

(a) H^+

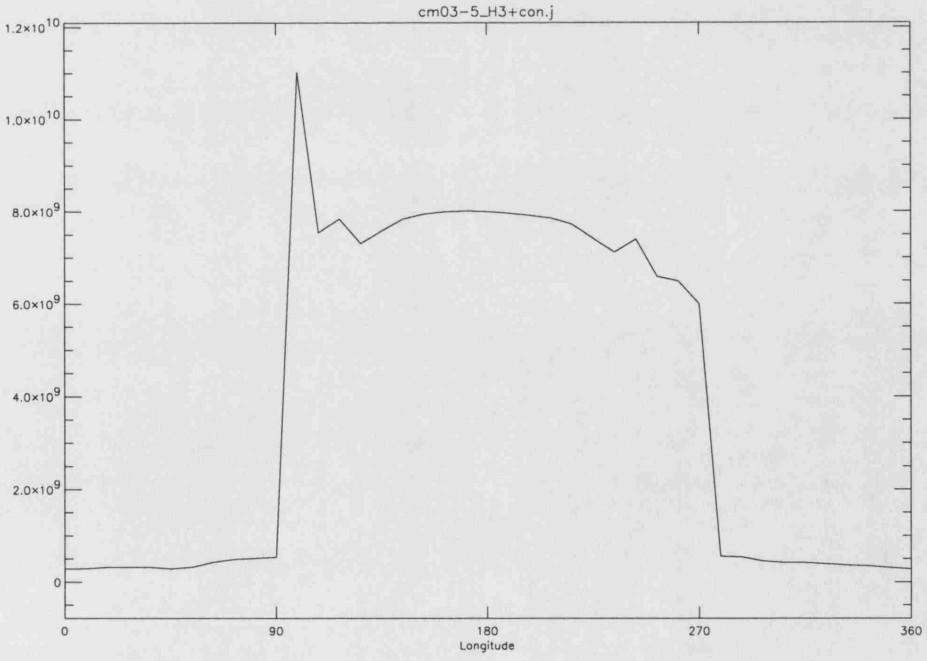

(b) H_3^+

Figure A.35: Longitude-Local Density at Pressure Level 26

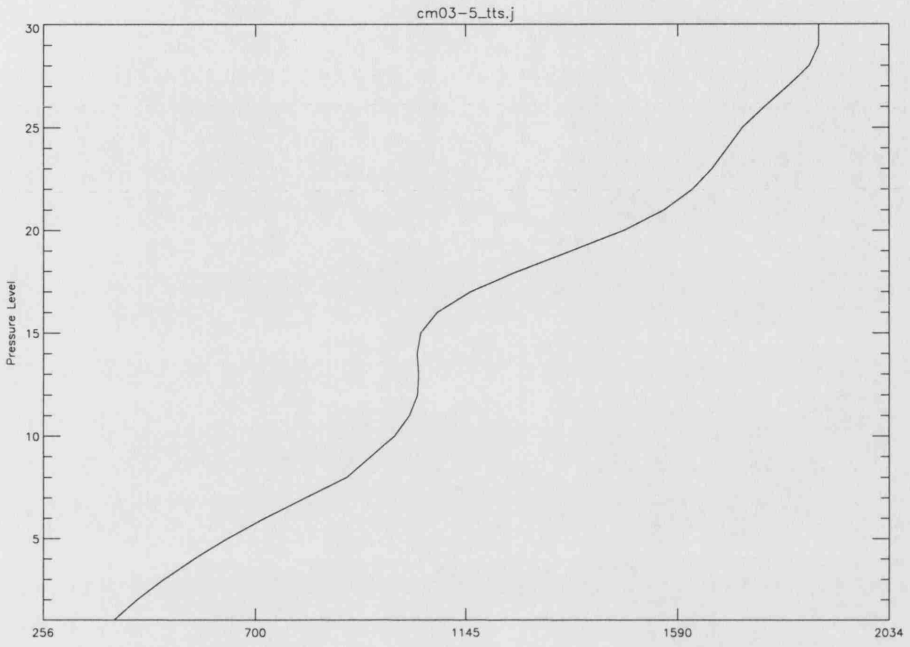

(a) Subsolar Point

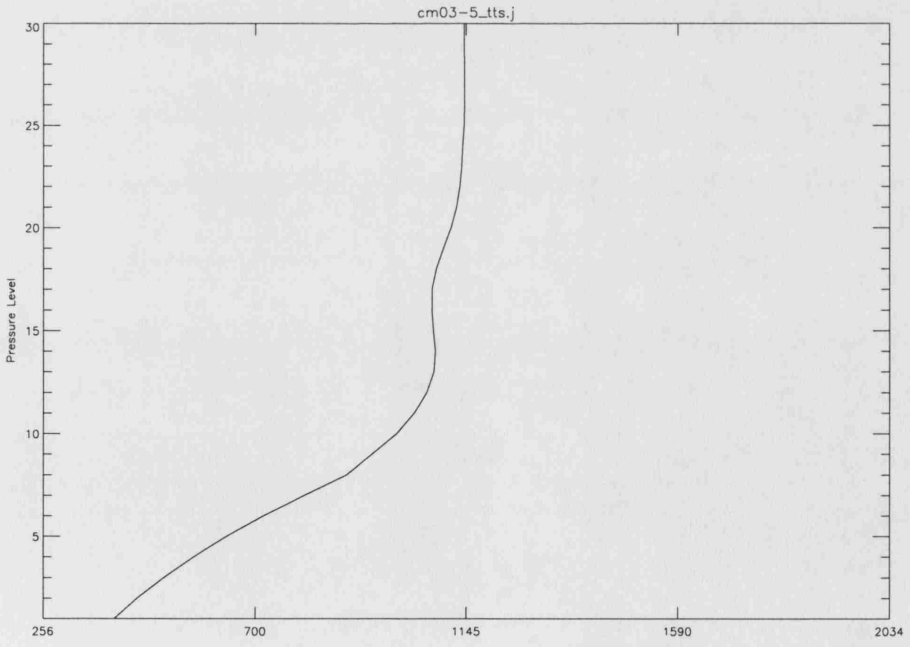

(b) Midnight

Figure A.36: Temperature Profile

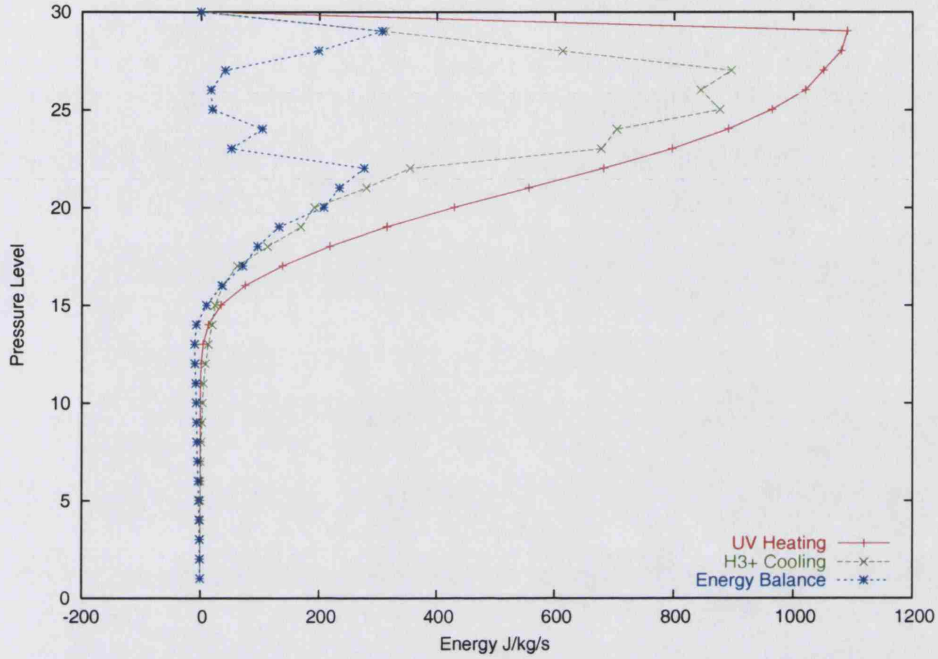

(a) Subsolar Point

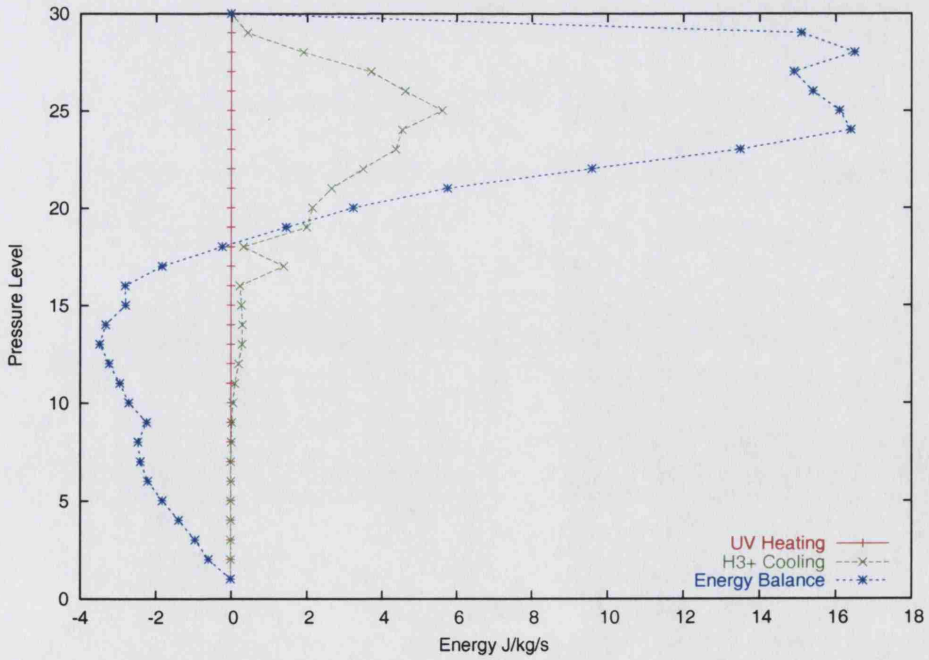

(b) Midnight

Figure A.37: Energy Balance

A.7 cm01

Orbital Radius /*AU*	Orbital Period /*hours*	Timestep /*seconds*
0.1	200	3.97

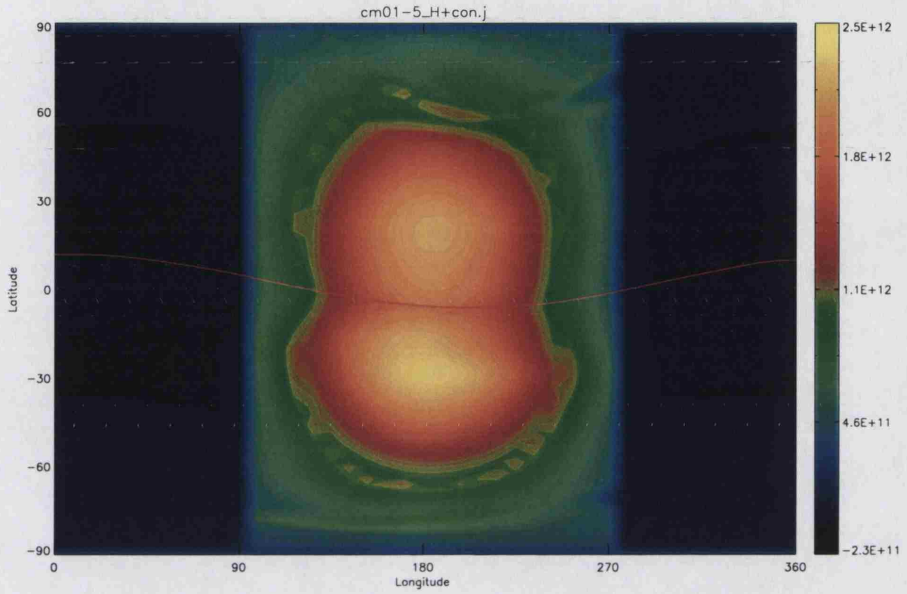

(a) H^+

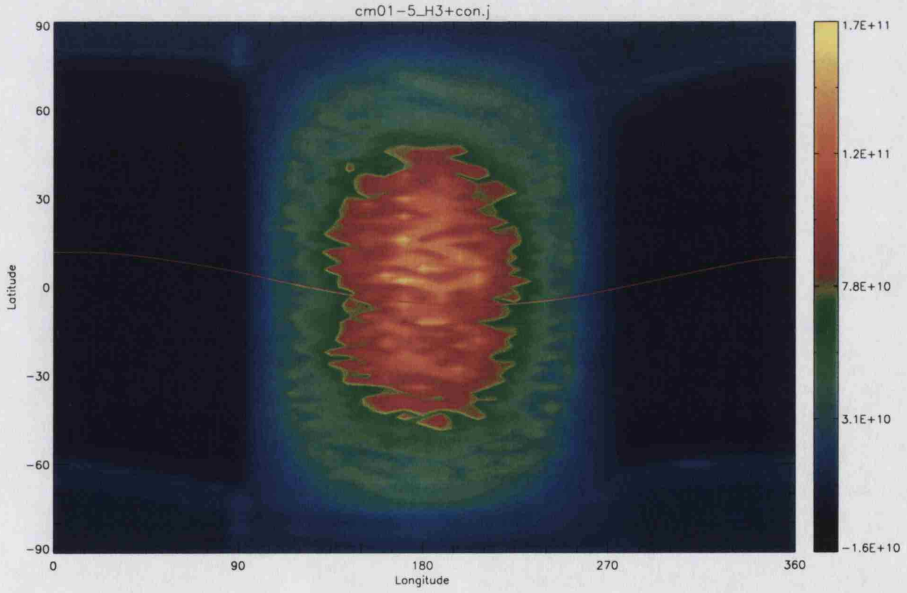

(b) H_3^+

Figure A.38: Pressure Level 16 Local Density

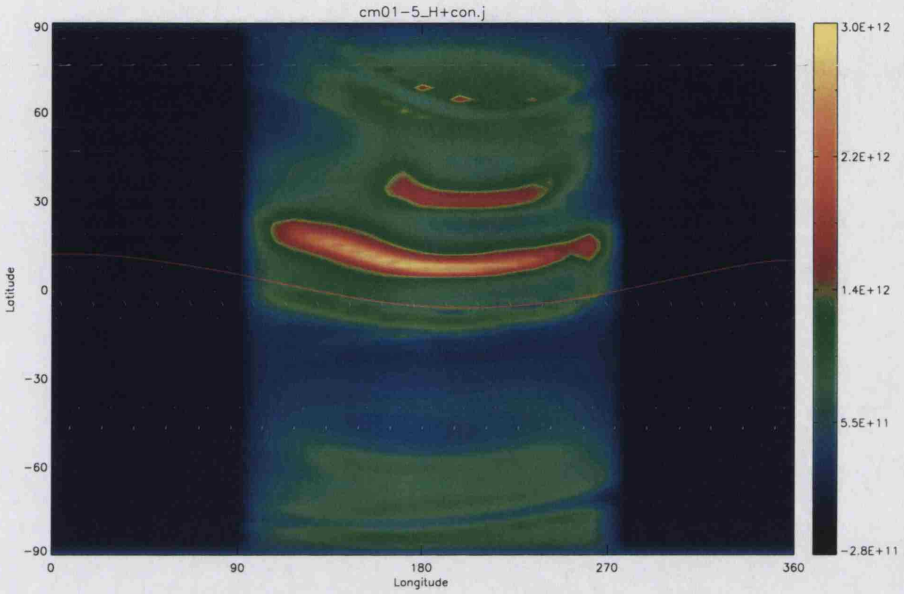

(a) H^+

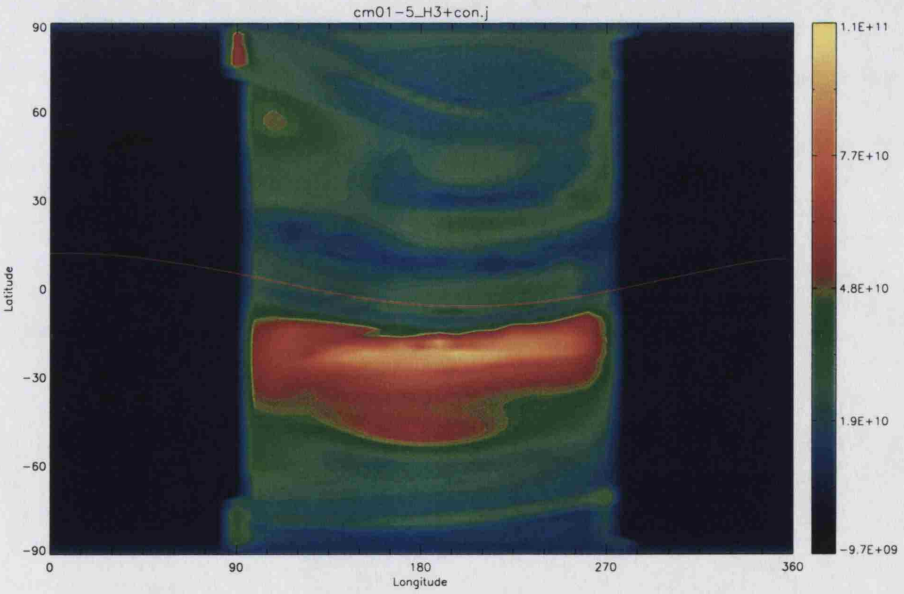

(b) H_3^+

Figure A.39: Pressure Level 26 Local Density

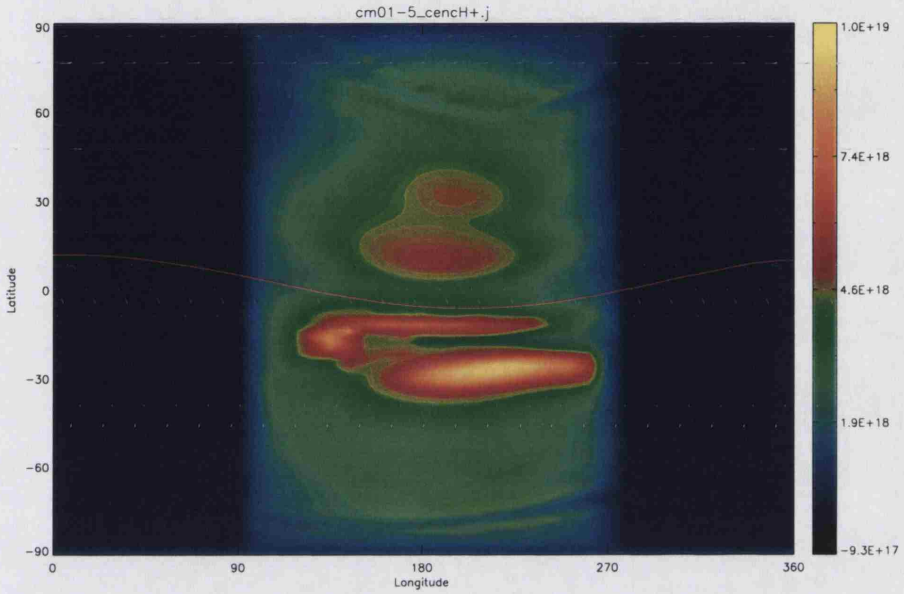

(a) H^+

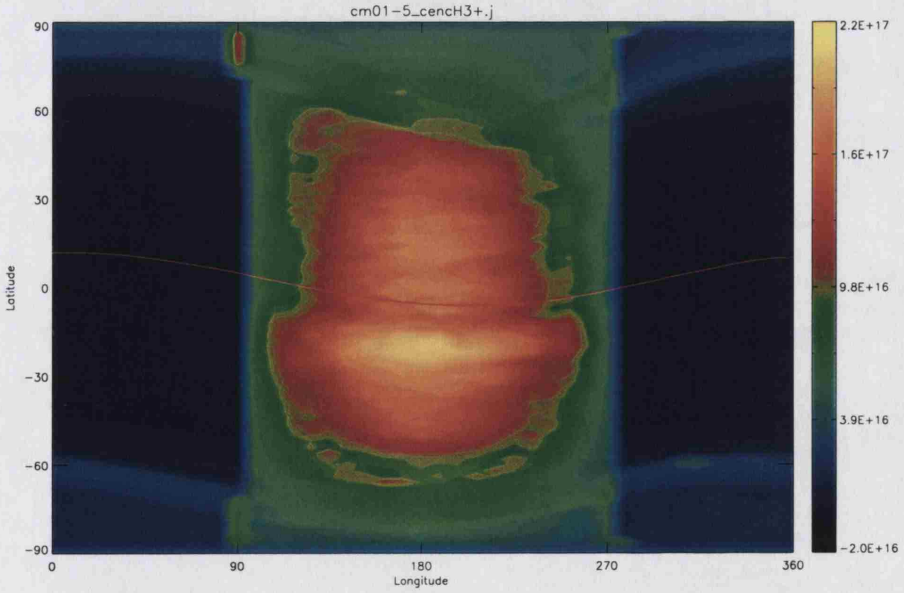

(b) H_3^+

Figure A.40: Column Density

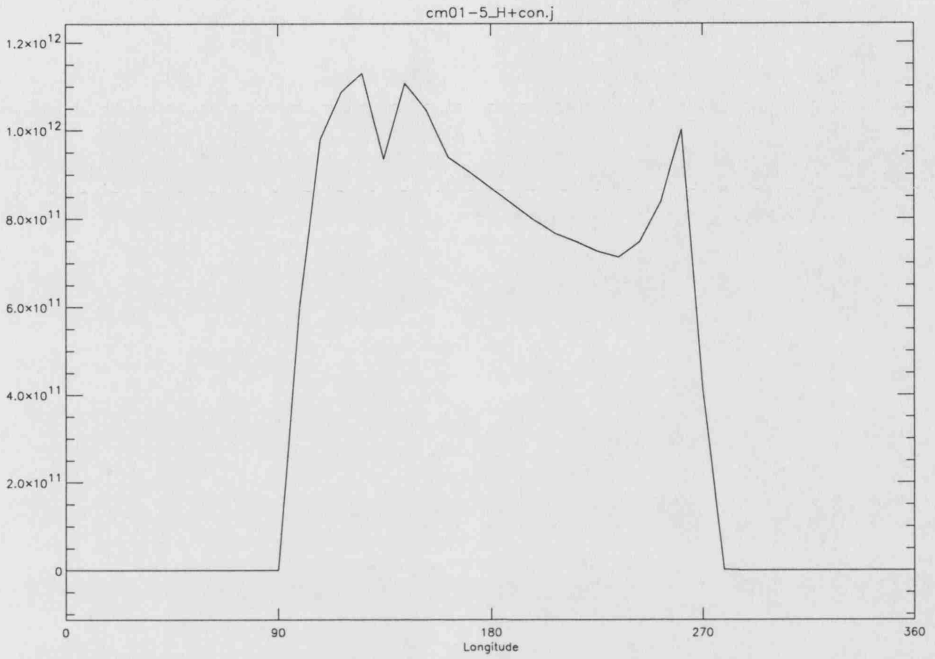

(a) H^+

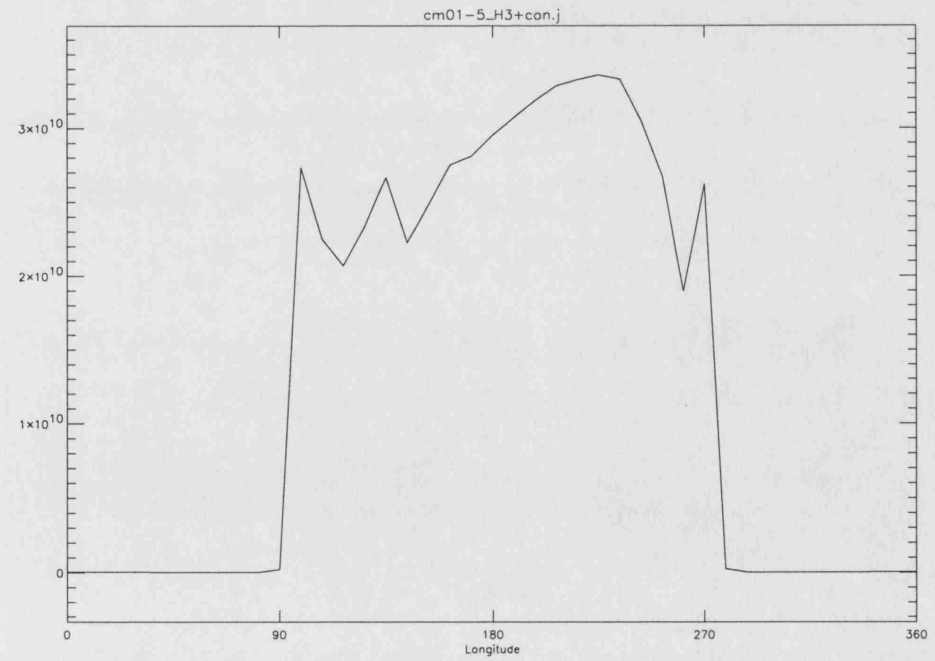

(b) H_3^+

Figure A.41: Longitude-Local Density at Pressure Level 26

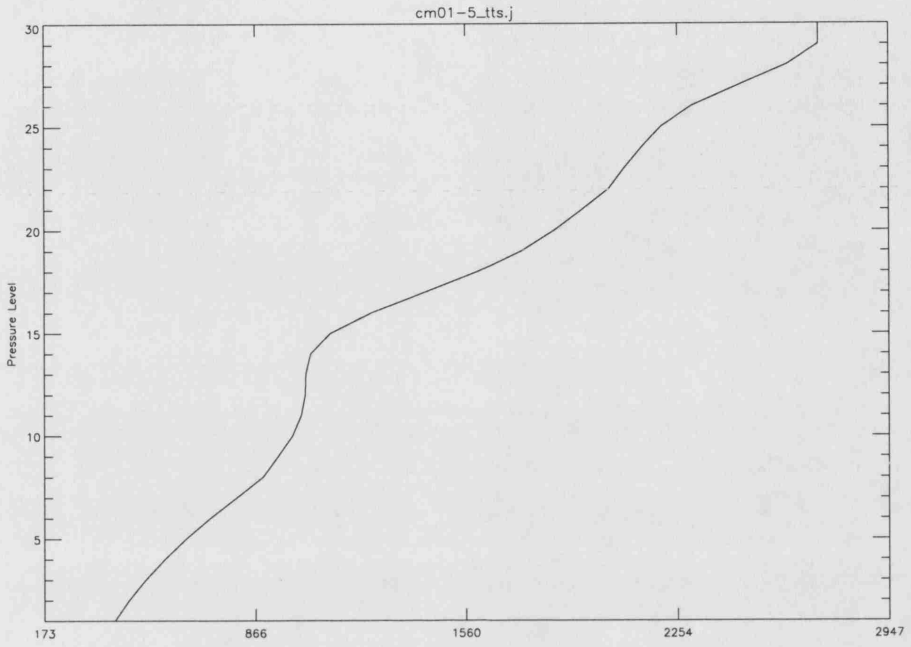

(a) Subsolar Point

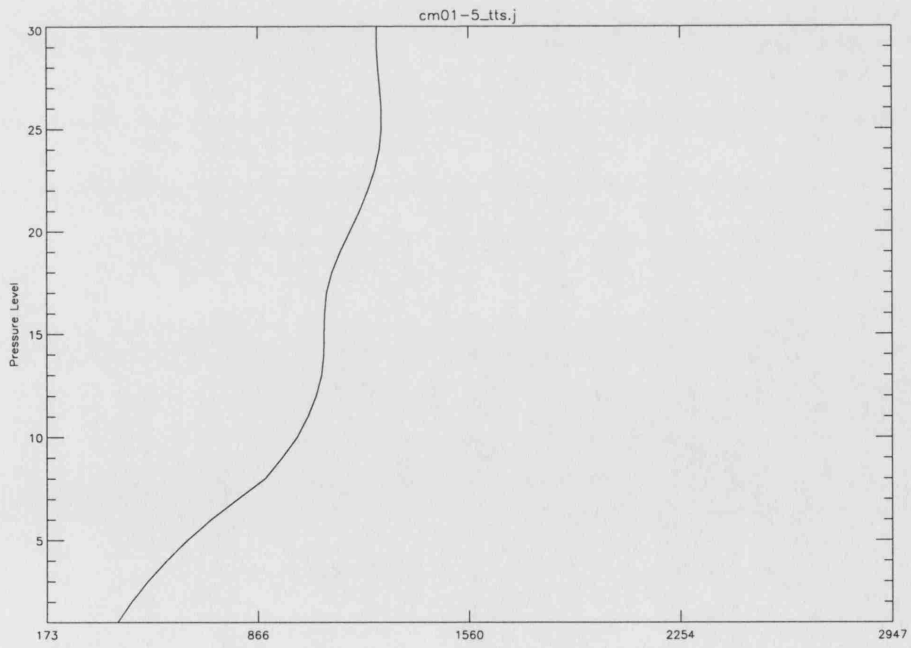

(b) Midnight

Figure A.42: Temperature Profile

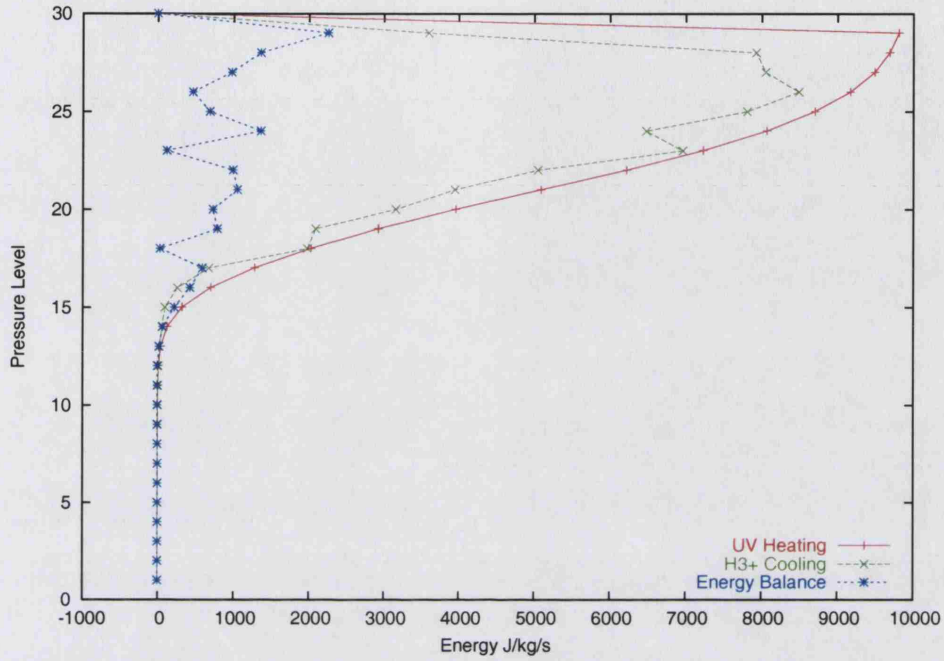

(a) Subsolar Point

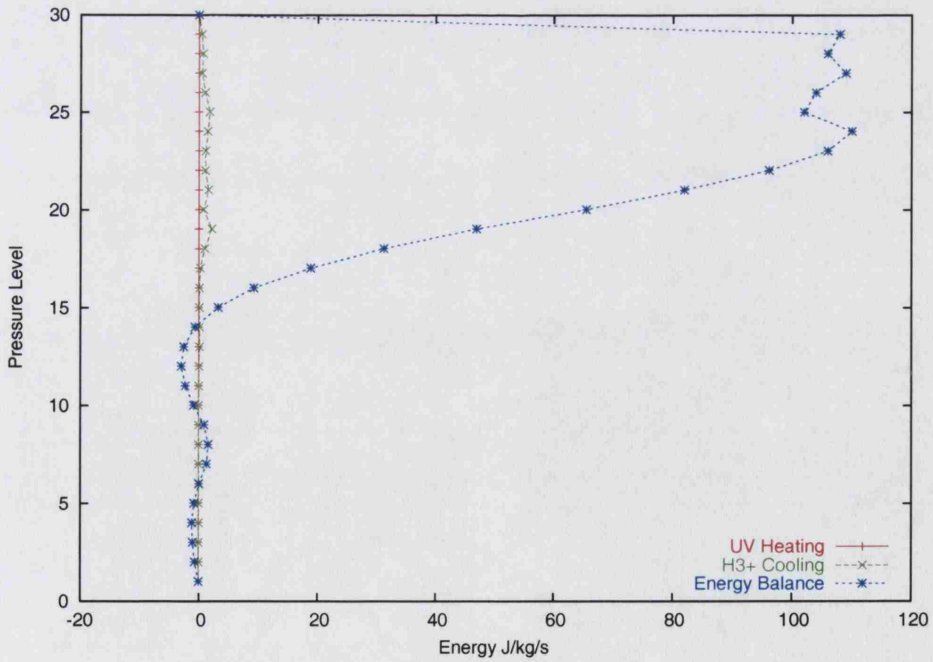

(b) Midnight

Figure A.43: Energy Balance

A.8 cm03-me

Orbital Radius /*AU*	Orbital Period /*hours*	Timestep /*seconds*
0.3	200	3.97

The **cm-me** runs use the same input parameters as the original cm runs but with rotational axis and magnetic dipole set to 90° to the orbital plane. Note that the cm-me runs were obtained with an earlier version of JIME with some patches added, due to a system crash which resulted in the loss of the final version of JIME. Thus there are some spikes and irregularities in the data which should not be taken as genuine features.

Note that the midnight energy balance is still negative at this point. By the time the planet has been brought in to 0.1AU the balance is significantly positive, as in the original cm runs.

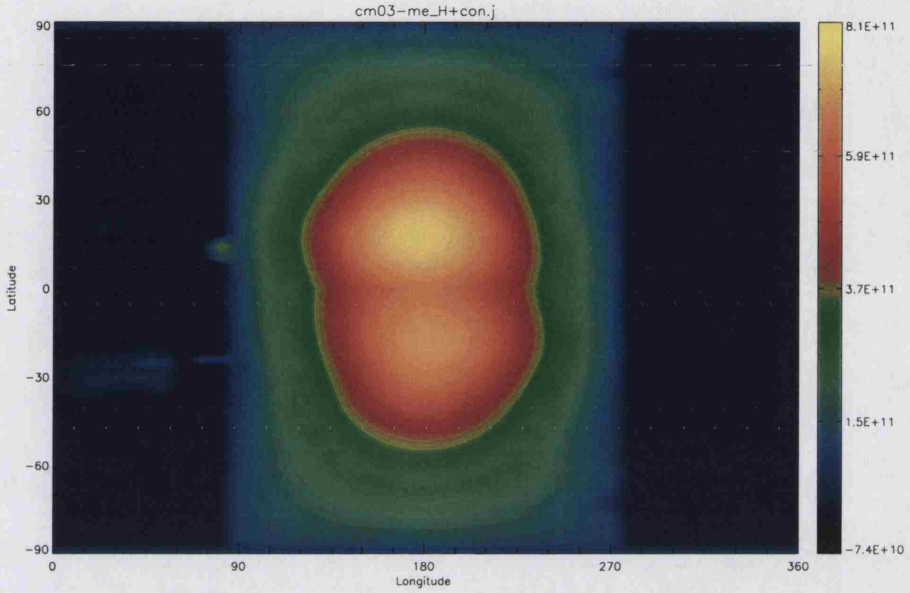

(a) H^+

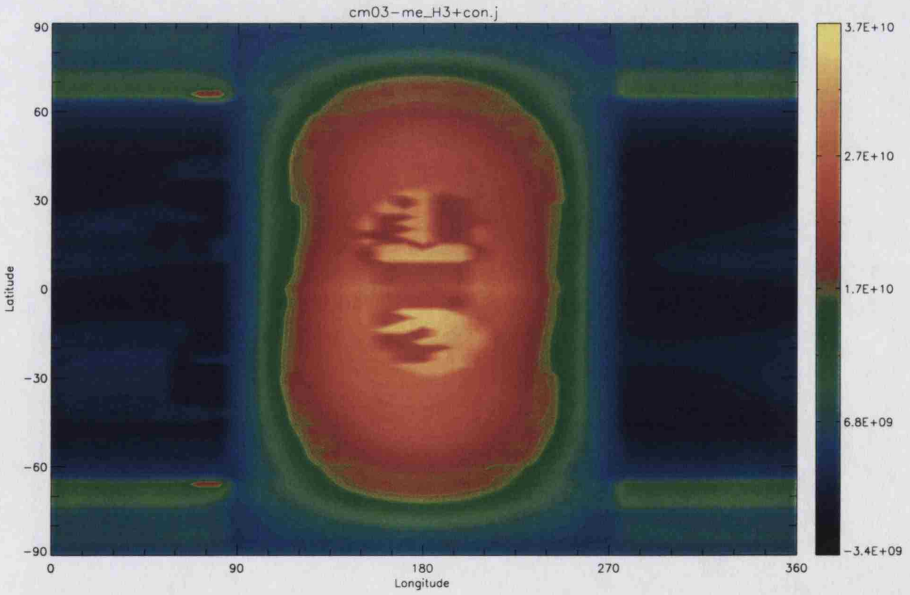

(b) H_3^+

Figure A.44: Pressure Level 16 Local Density

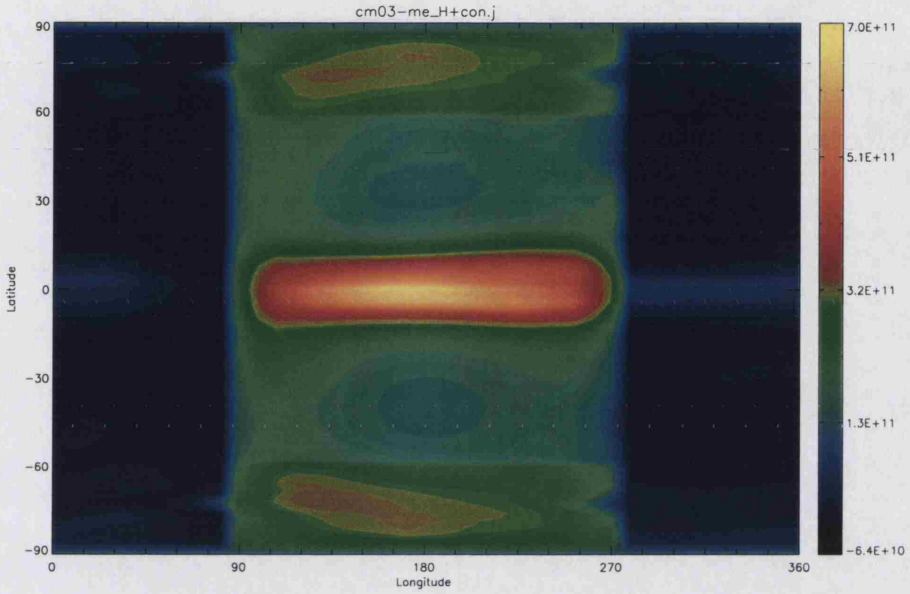

(a) H^+

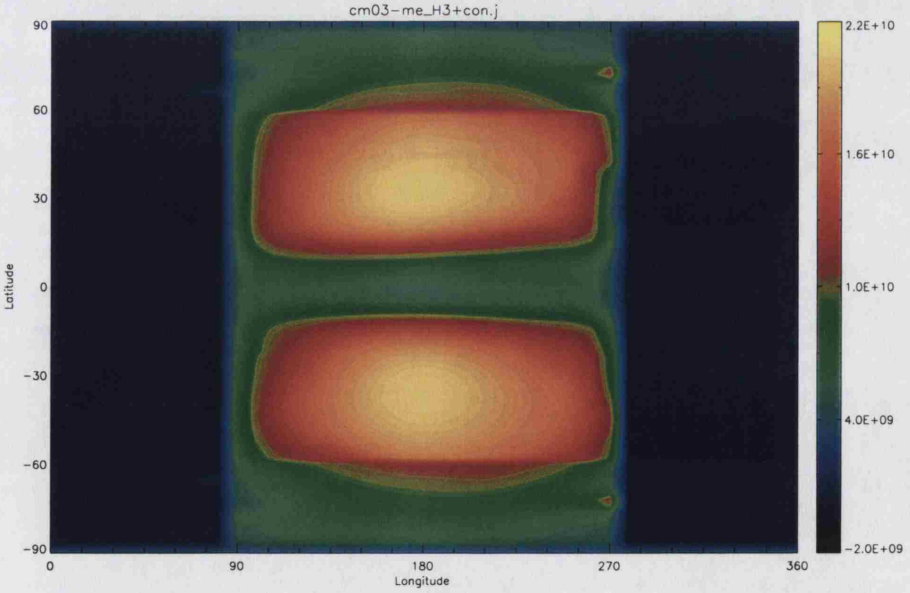

(b) H_3^+

Figure A.45: Pressure Level 26 Local Density

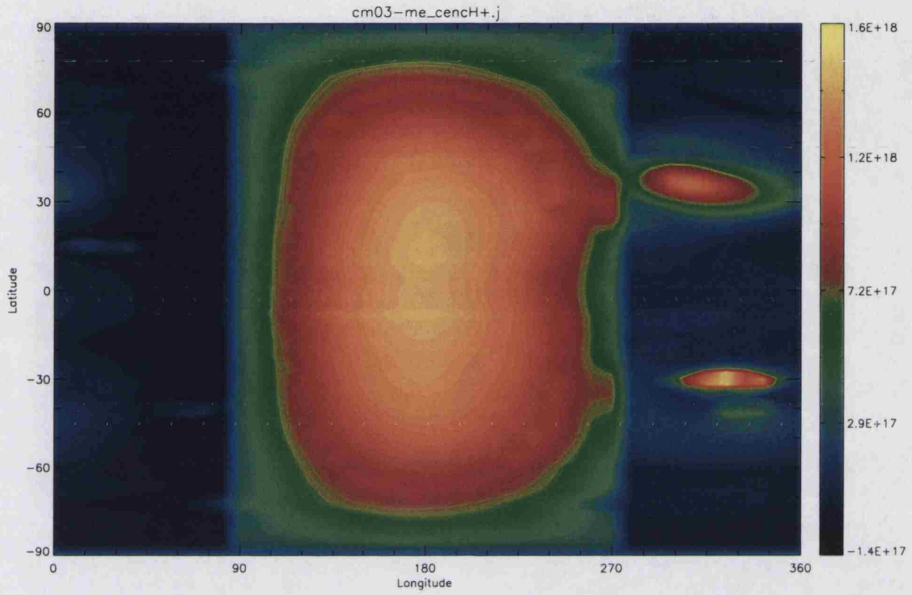

(a) H^+

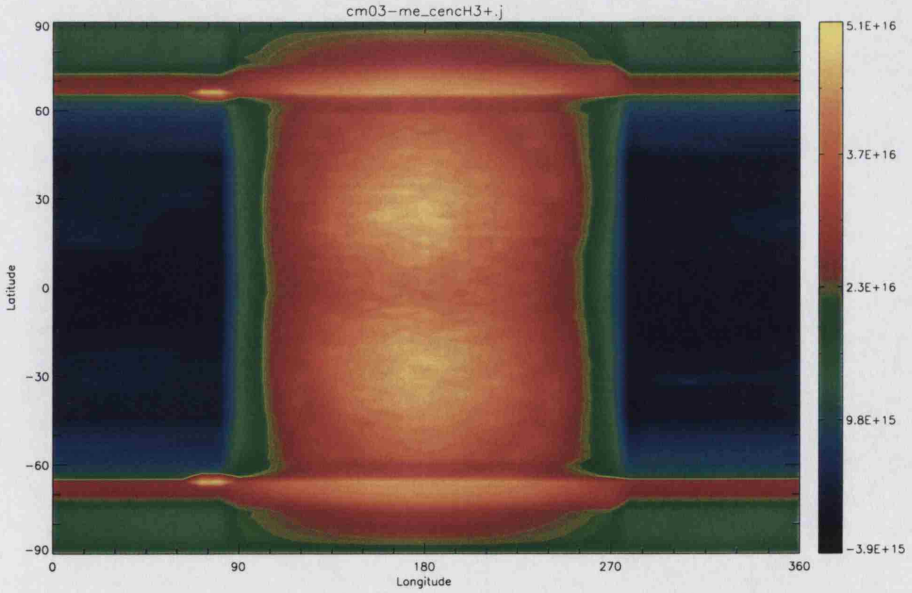

(b) H_3^+

Figure A.46: Column Density

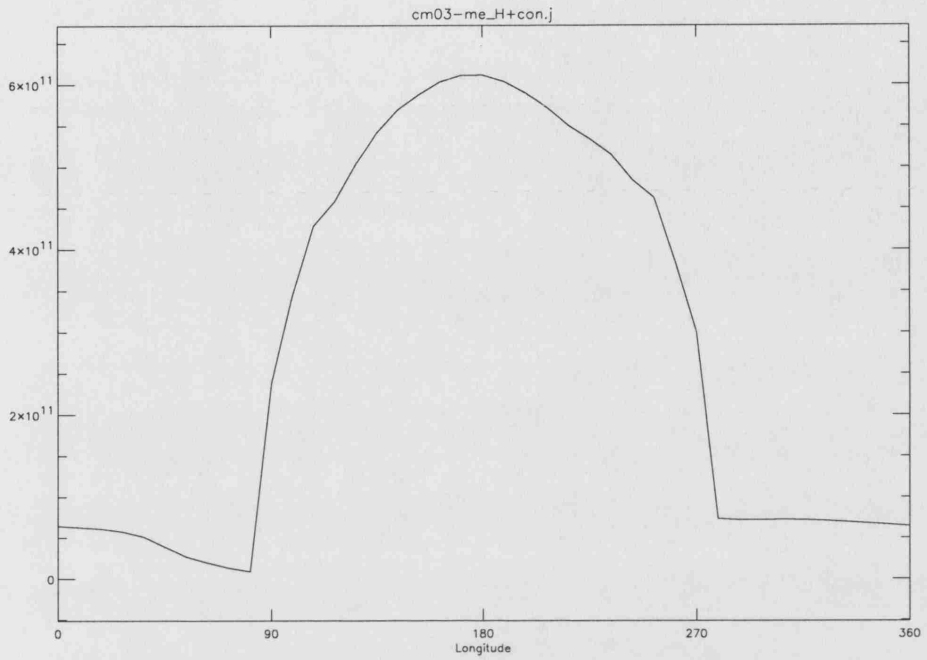

(a) H^+

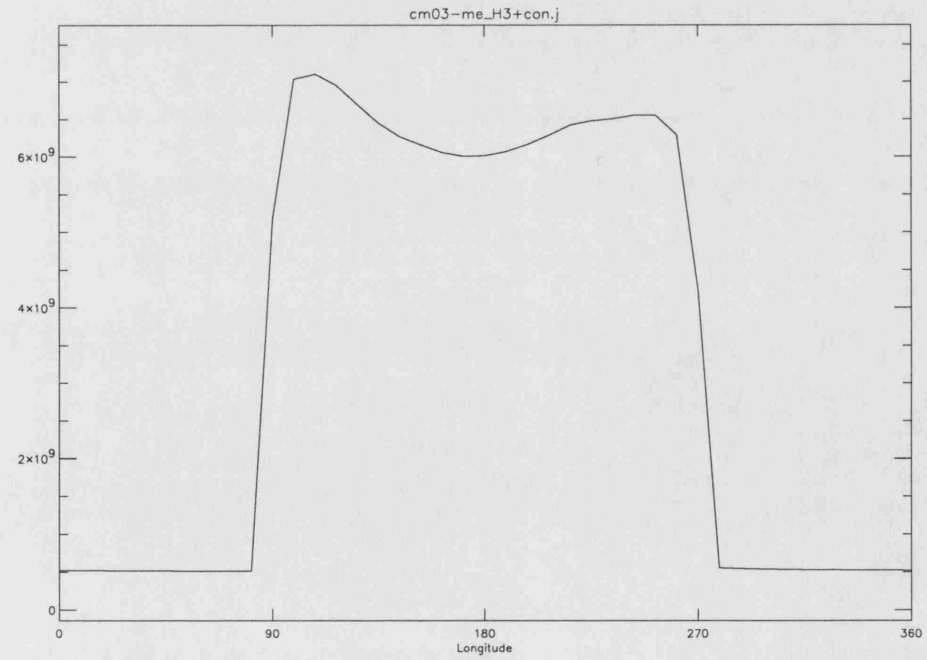

(b) H_3^+

Figure A.47: Longitude-Local Density at Pressure Level 26

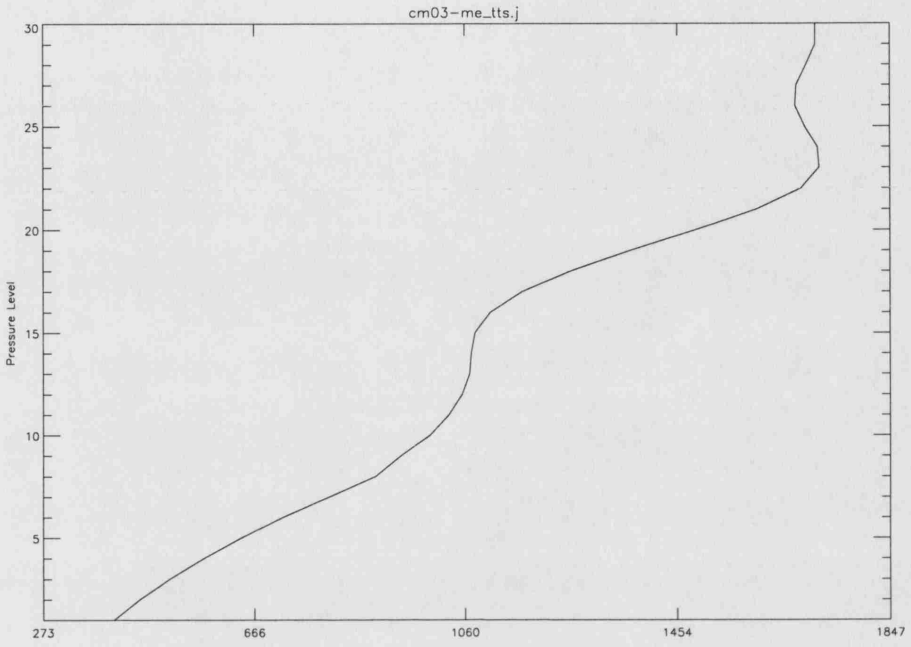

(a) Subsolar Point

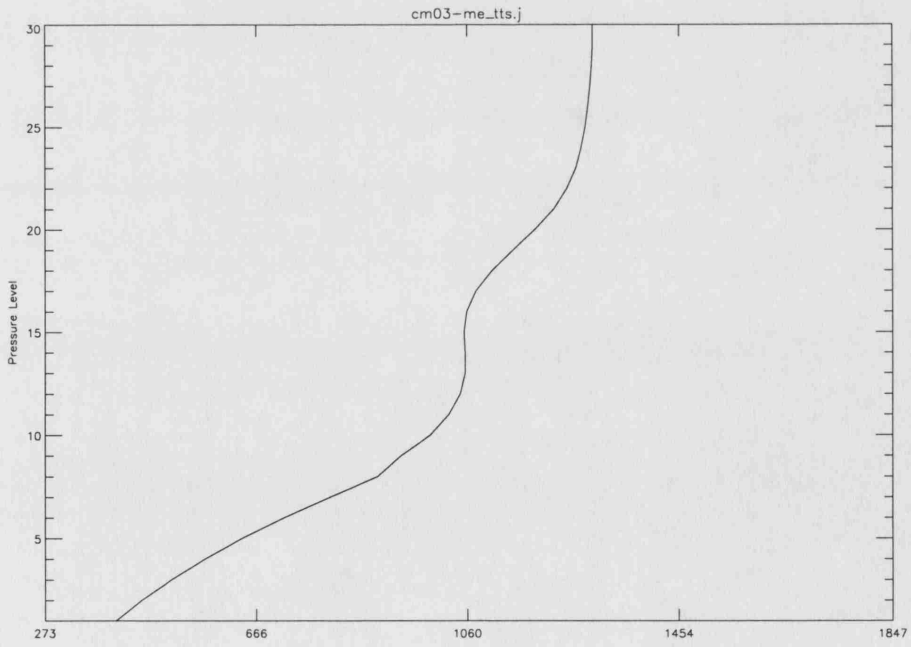

(b) Midnight

Figure A.48: Temperature Profile

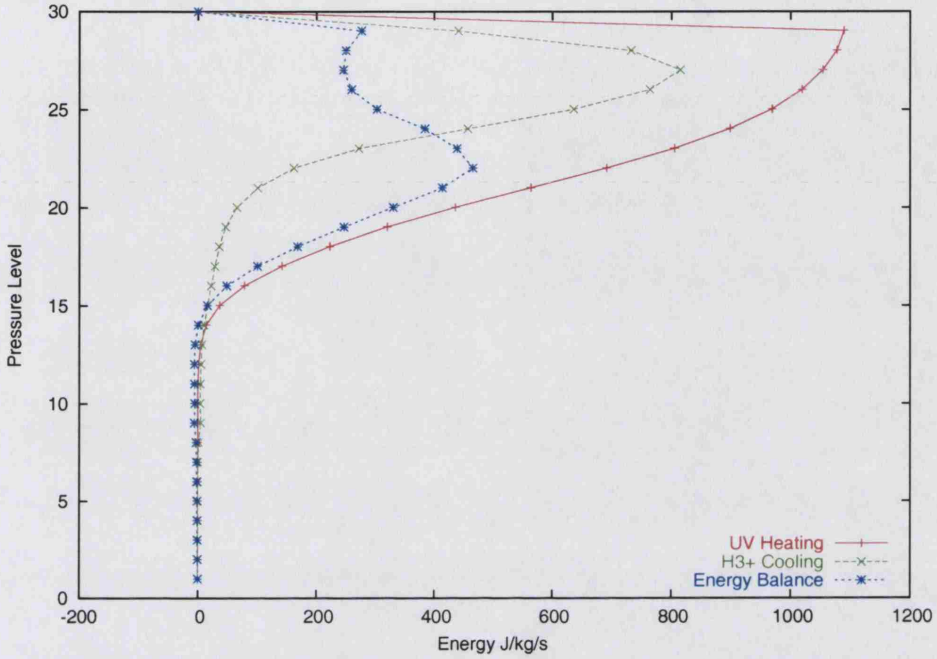

(a) Subsolar Point

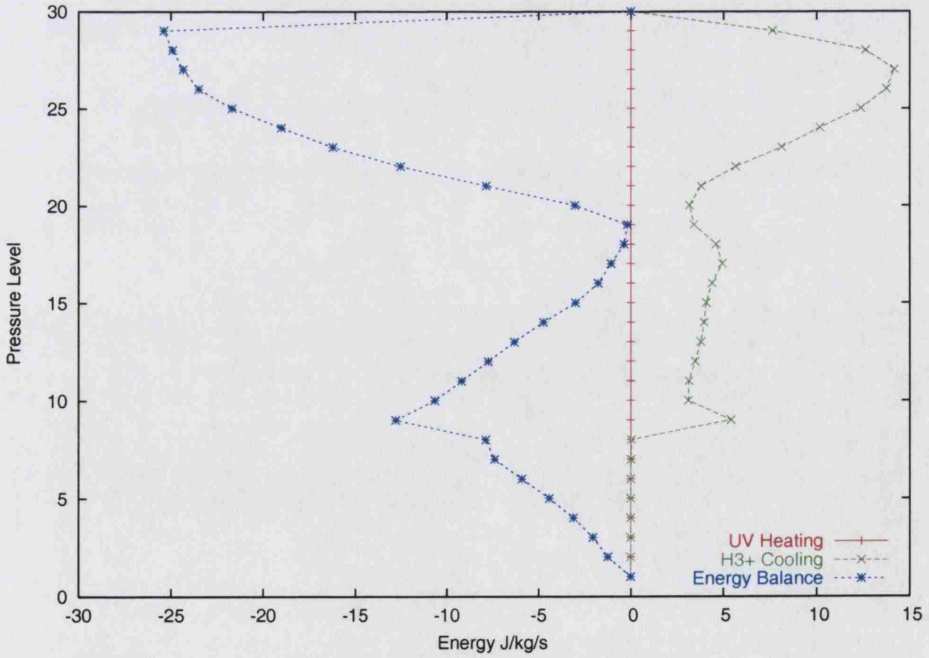

(b) Midnight

Figure A.49: Energy Balance

A.9 cm03-j0

Orbital Radius /*AU*	Orbital Period /*hours*	Timestep /*seconds*
0.3	200	3.97

The **cm-j0** run series has the same parameters as the **cm-me** series but with the magnetic field turned off. Due to certain complications with the magnetic field integration into the model, removal has broken the heating/cooling code. Thus the temperature and energy plots are considered invalid and not displayed here.

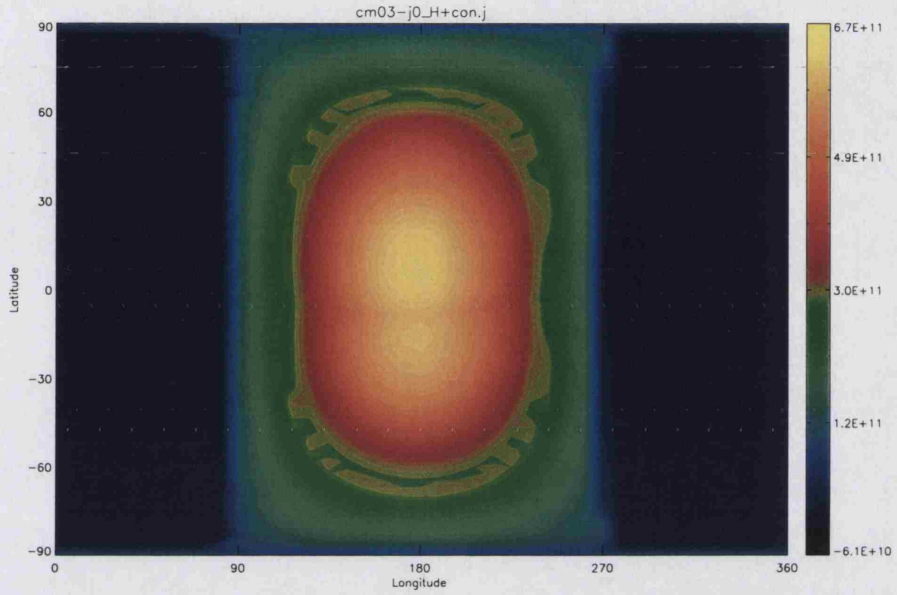

(a) H^+

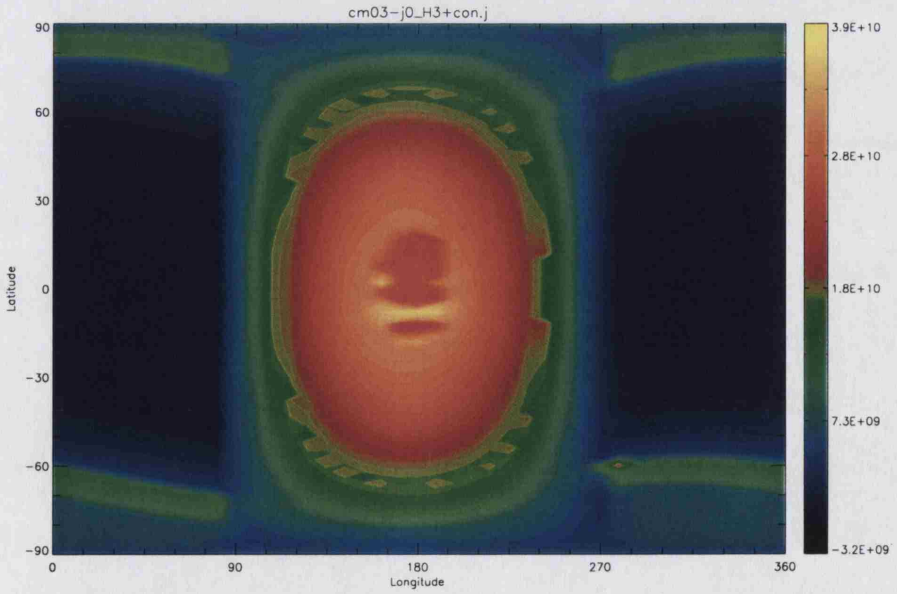

(b) H_3^+

Figure A.50: Pressure Level 16 Local Density

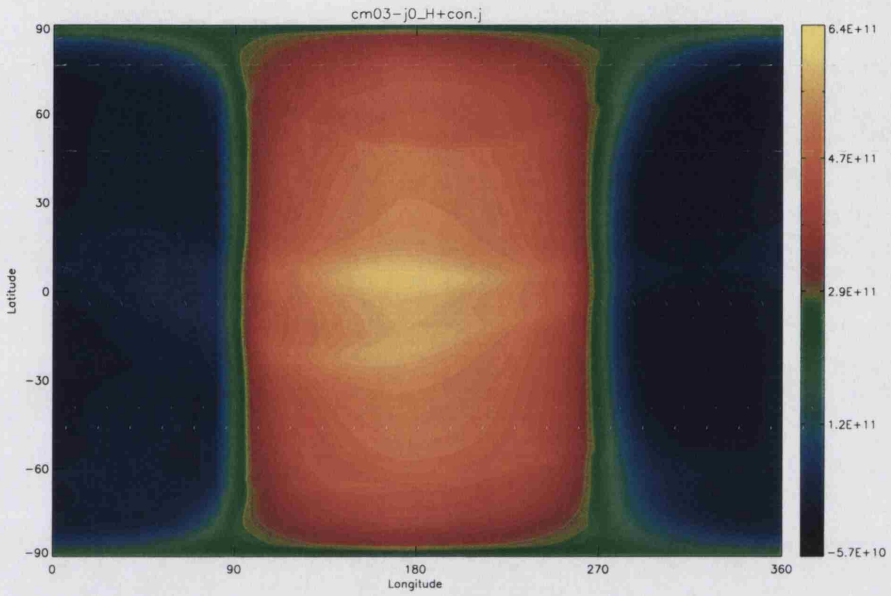

(a) H^+

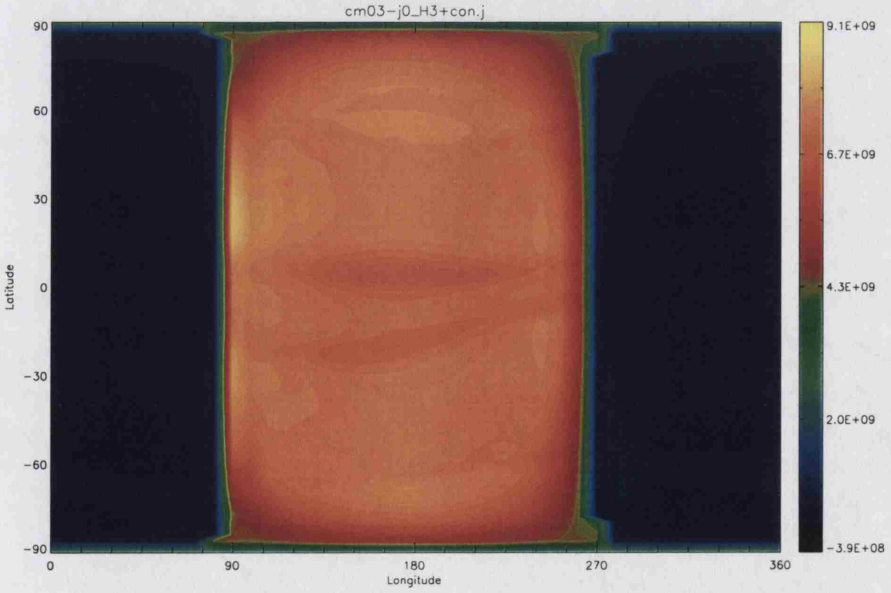

(b) H_3^+

Figure A.51: Pressure Level 26 Local Density

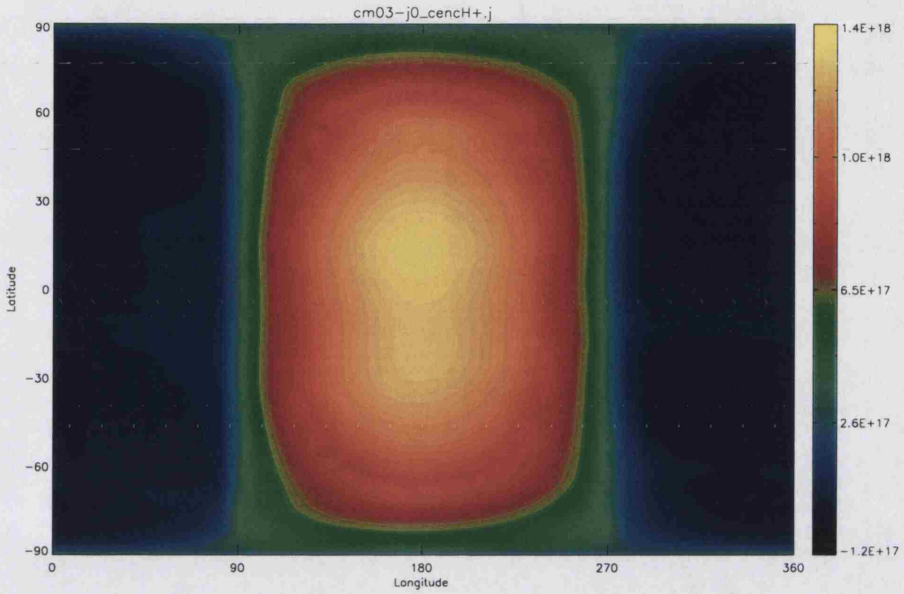

(a) H^+

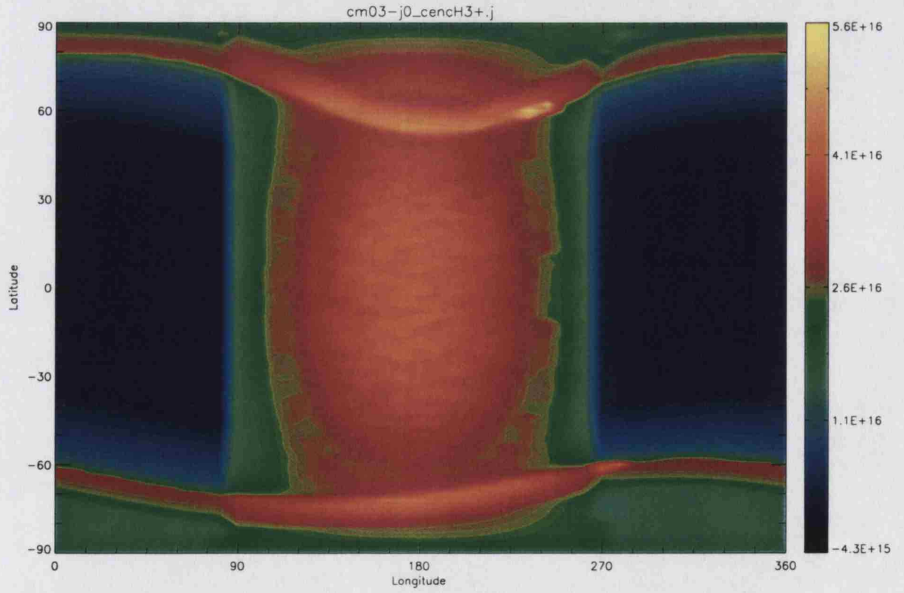

(b) H_3^+

Figure A.52: Column Density

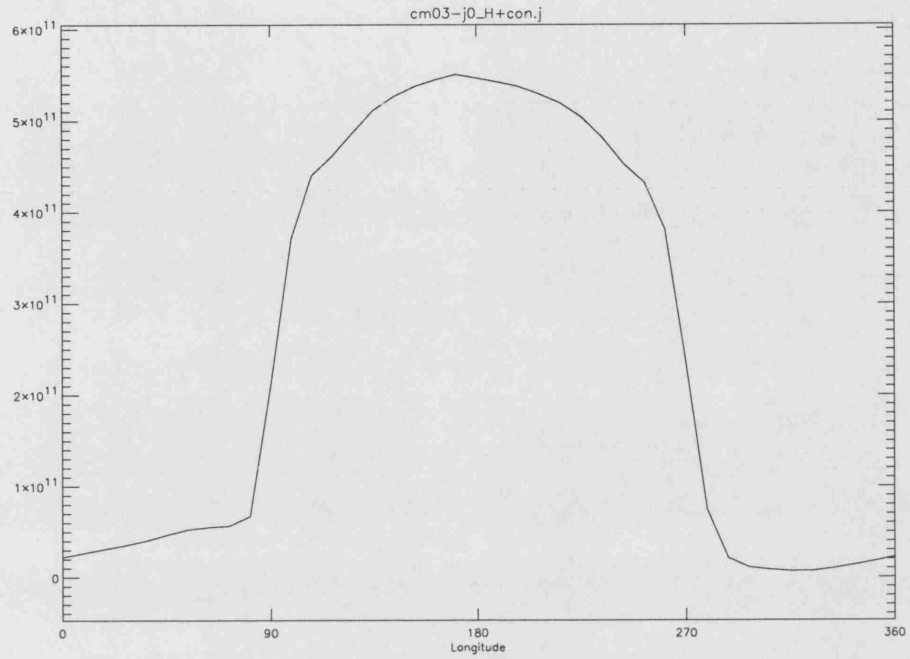

(a) H^+

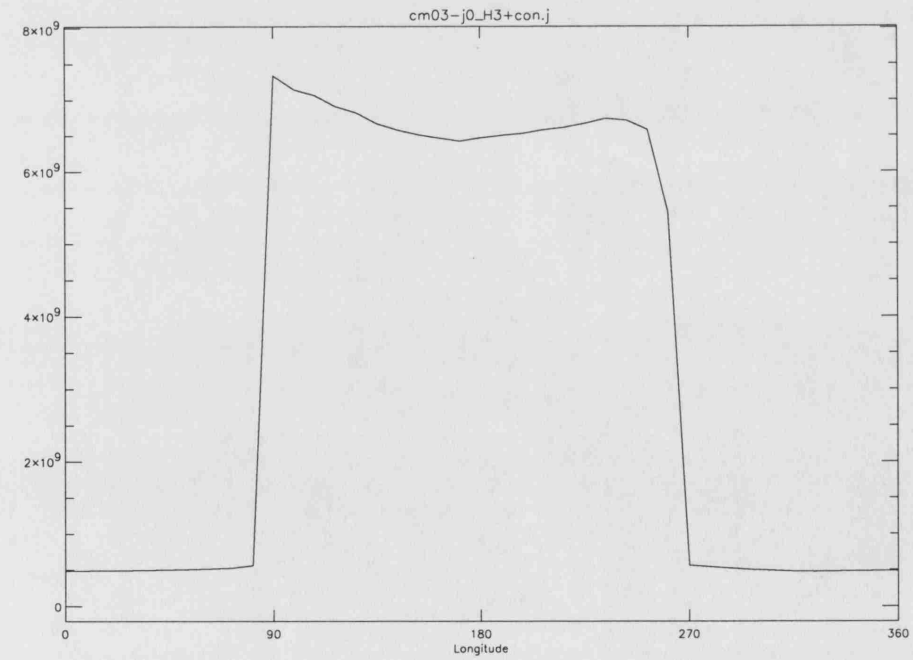

(b) H_3^+

Figure A.53: Longitude-Local Density at Pressure Level 26

A.10 cm01-j0

Orbital Radius /*AU*	Orbital Period /*hours*	Timestep /*seconds*
0.1	200	3.97

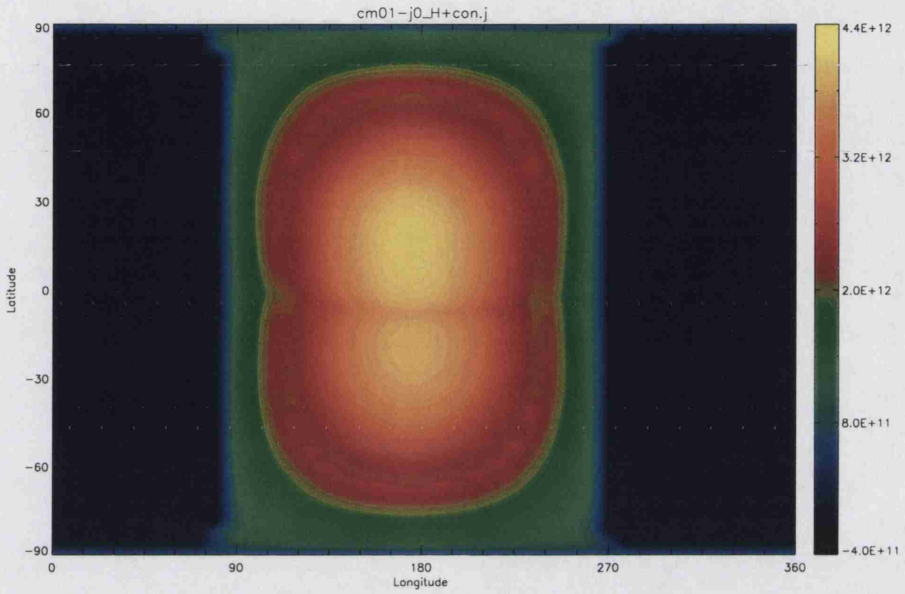

(a) H^+

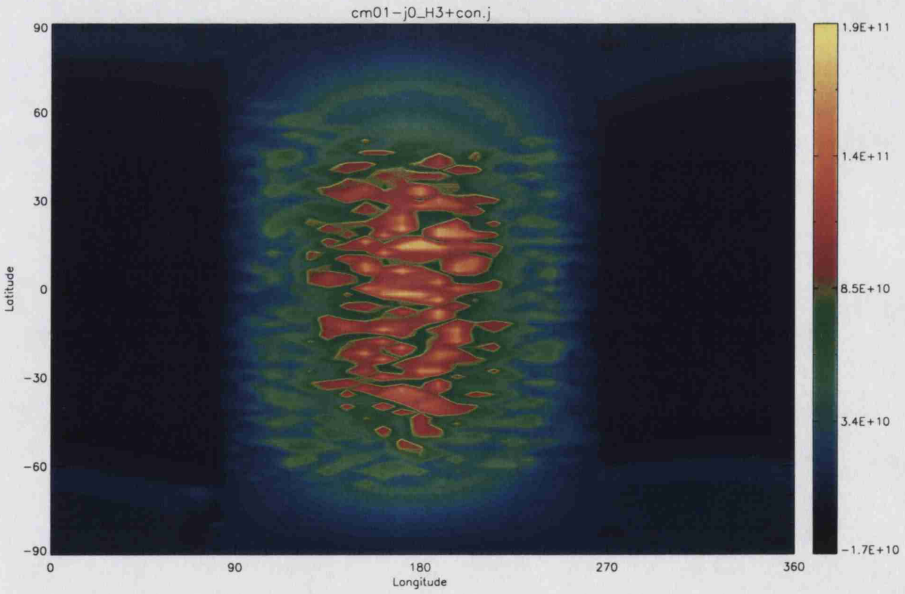

(b) H_3^+

Figure A.54: Pressure Level 16 Local Density

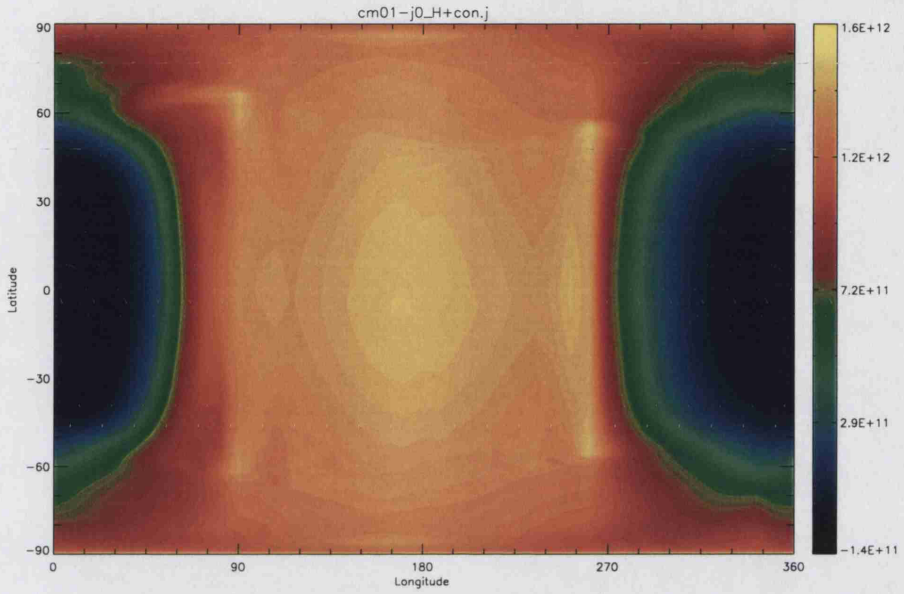

(a) H^+

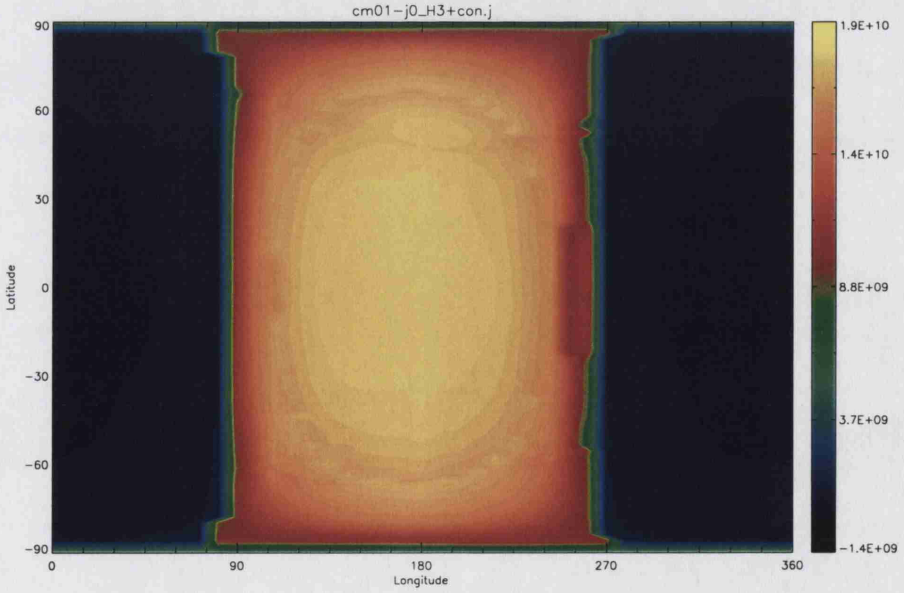

(b) H_3^+

Figure A.55: Pressure Level 26 Local Density

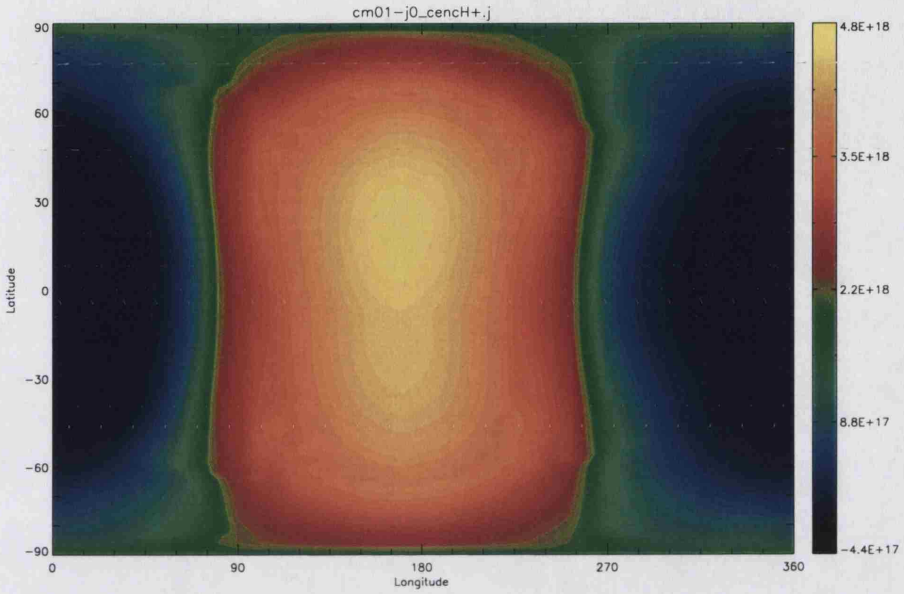

(a) H^+

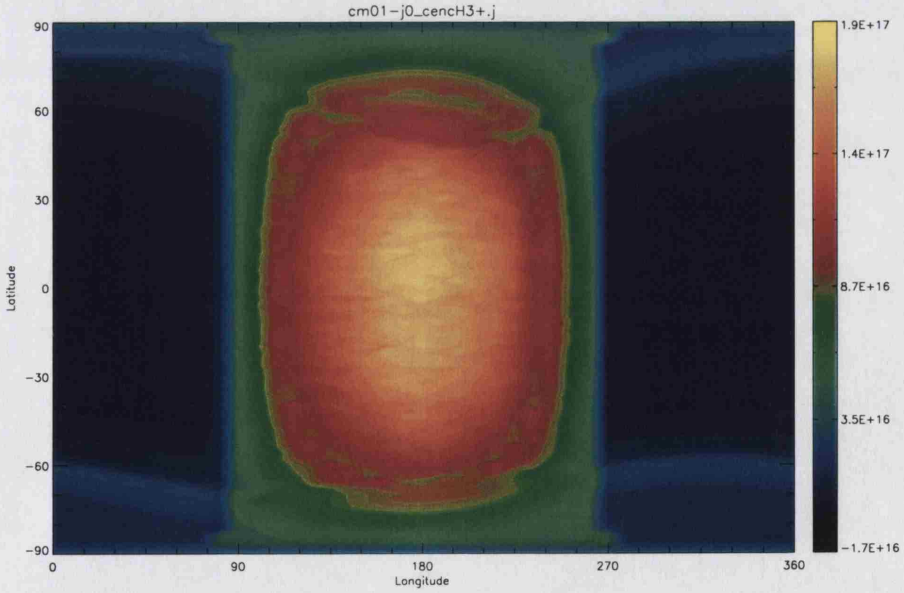

(b) H_3^+

Figure A.56: Column Density

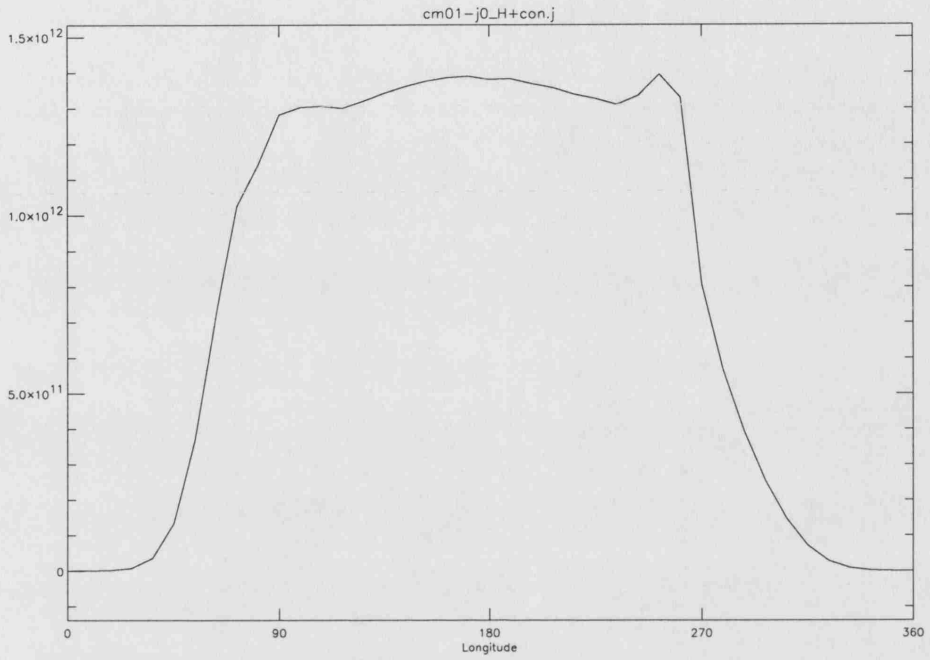

(a) H^+

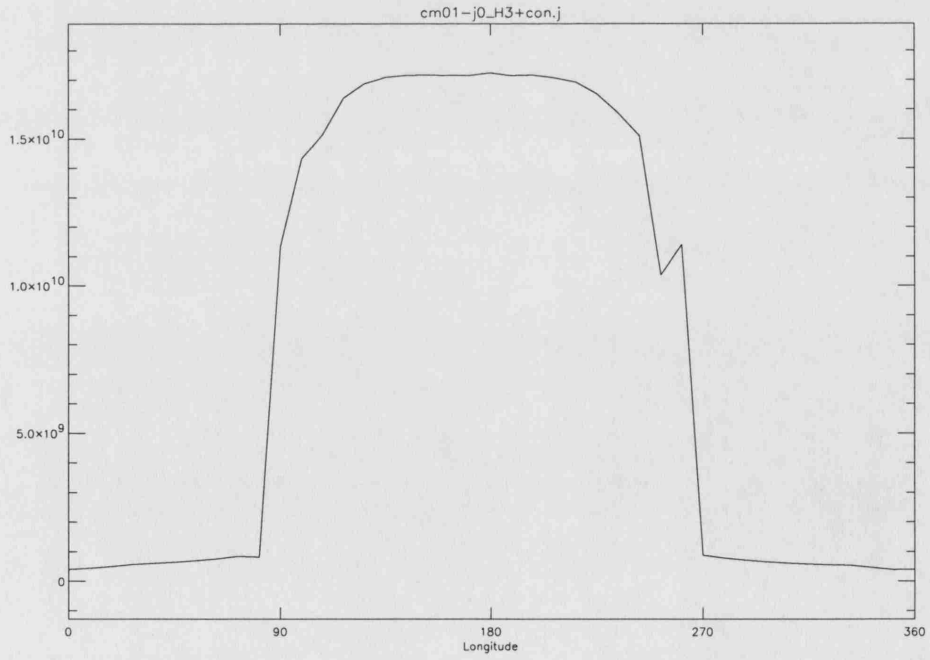

(b) H_3^+

Figure A.57: Longitude-Local Density at Pressure Level 26

Appendix B

Planetary Detection Studies

B.1 Ongoing Experiments

B.1.1 The Geneva Extrasolar Planet Search

The Geneva team currently runs two radial velocity survey experiments, *ELODIE* and *CORALIE*, with another, *HARPS* in development.

Further information may be obtained from: **http://obswww.unige.ch/~udry/planet/planet.html**

ELODIE, the twin fibre-fed échelle spectrograph in place at Observatoire de Haute-Provence (OHP) (Baranne et al., 1996) is one of the more elderly of the current generation of radial velocity experiments and, as befits its vintage it has the twin historical distinction of being the first experiment to unequivocally detect an exoplanet, 51-Pegasi and the first to detect a transiting planet, HD 209458.

CORALIE (Queloz et al., 2000) is ELODIE's twin located at the ESO Observatory in La Silla, Chili. ELODIE is able to provide an accuracy of better than $15ms^{-1}$ in 30 minutes for a 9^{th} magnitude star using a process known as cross-correlation spectroscopy, in which the spectrum of the star is dynamically compared with the

spectrum of a thorium-argon lamp (Bouchy and Carrier, 2001). The spectral image is captured on a 1024x1024 CCD cooled to 183K with a resolution of 42,000 ($\lambda/\Delta\lambda$). CORALIE is able to provide slightly higher resolution due to its 2000x2000 CCD.

ELODIE and CORALIE together span both the Northern and Southern hemispheres with an initial target inventory of nearly 2000 G and K type stars, chosen for low stellar variability.

HARPS (Benz et al., 1999), the High Accuracy Radial velocity for Planetary Search spectrograph, mounted on the 3.6m telescope at La Silla will provide a significant increase in performance over its two predecessors with a stated maximum radial velocity accuracy of $1ms^{-1}$ and resolution of 100,000 ($\lambda/\Delta\lambda$).

The HARPS project primarily aims to use their increased resolution to build up a distribution of parent star metallicities as a function of planetary mass, as well as obtain a distribution of the masses of 51-Peg planets as a function of orbital radius to test for mass loss.

B.1.2 The Advanced Fibre-Optic Échelle Spectrometer

AFOE (Brown et al., 1994), or the Advanced Fibre-Optic Échelle spectrometer, is a fibre-fed, bench-mounted échelle spectrograph attached to the Tillinghast 1.5m telescope at the Fred Lawrence Whipple Observatory, Mt. Hopkins, near Tucson, Arizona (Brown et al., 1994), and is a joint project of the Smithsonian Astrophysical Observatory (SAO) and the High Altitude Observatory (HAO).

The spectrograph is coupled to a 2000x2000 CCD and is capable of a spectral resolution of ~50,000. Its novel feature is the dual calibration method, consisting of both a thorium-argon chamber (as used in ELODIE) and an iodine vapour absorption cell.

B.1.3 The California & Carnegie Planet Search

The California & Carnegie planet search group runs surveys on two telescopes, described below.

The Lick Radial Velocity survey is based at Lick Observatory, Mt. Hamilton, California, using the facility's 3-m Shane reflector (Cumming et al., 1999) which is operated by the University of California. Connected to the telescope is a échelle spectrograph which uses the iodine vapour calibration technique to achieve a precision of $\sim 5\text{ms}^{-1}$ with a 10 minute exposure time for an apparent magnitude of 5. In operation since the late 1980s the initial survey consisted of 76 F, G and K type stars, since extended to more than 100 including M dwarfs.

The Keck survey has been operating on the Keck I telescope, Mauna Kea, Hawaii since 1996 (Vogt et al., 2000). It utilises the HIRES échelle spectrometer which operates at a resolution of R=80,000, achieving a stated precision of 3ms^{-1} for a range of 530 main-sequence target stars of spectral types F7 to M5 for a nominal 10 minute exposure time. The stars were primarily obtained from the Hipparcos (G and K) and Gliese (M) catalogues and are mostly located within 50 pc of the sun. The list of acceptable stars was trimmed to remove evolved stars, stars less than 2 Gyr in age and stars that showed intrinsic periodicity in the range 10 to 50 ms^{-1} possibly related to magnetic fields, rapid rotation or spots. In addition stars with known spectroscopic binaries were removed to avoid spectral contamination.

B.1.4 Anglo-Australian Planet Search

The Anglo-Australian Planet Search (AAPS) (Butler et al., 2001) commenced operation in 1998 and is expected to run until 2010 with the goal of complementing the major northern hemisphere radial velocity searches such as Lick and Keck by pro-

viding high precision all-sky coverage, with a stated aim for long term precision of $3ms^{-1}$. Prior to AAPS, the only southern hemisphere (south of -20°) radial velocity surveys were those at La Silla (CORALIE).

AAPS is being conducted using the 3.92m equatorially mounted Anglo-Australian Telescope (AAT) located at Siding Spring Mountain, Australia, a site renowned for its exceptionally dark skies. The spectrograph is the University College of London Echelle Spectrograph (UCLES) which uses an Iodine vapour absorption cell and provides a resolution R$\sim$45,000.

the target sample chosen for AAPS consists of approximately 200 stars with $\delta < -20°$, and consists of 178 late (V-VI) F, G and K stars of V magnitude < 7.5 and age > 3 Gyr where age or activity information is available, 7 M dwarfs with V < 11.5 and 16 metal rich ($[Fe/H] > +0.3$) G dwarfs, with the only overlap with Lick and Keck being the star Tau Ceti.

The limiting magnitude on the F, G and K stars is chosen in order to achieve sufficiently high signal to noise in order to obtain photon-limited precision of $3ms^{-1}$ with exposure times of 10 minutes or less.

B.1.5 The ESO Coudé Echelle Spectrometer

The ESO-CES program is a precise radial velocity survey operating at ESO La Silla in Chili using the facility's fibre-fed Coudé Echelle Spectrometer (Endl et al., 2001), initially attached to the 1.4m CAT telescope and continuing using the 3.6m telescope after the CAT's decommissioning in 1998. With a resolving power of up to 235,000 in the 346 - 1028 nm region, CES is ESO's highest resolution spectrograph.

Initial radial velocity precision tests on a small number of well known planetary systems, including 51 Peg and 70 Vir yielded precision of between 8-15 ms^{-1}, comparable with CORALIE but significantly lower than the $3ms^{-1}$ aimed at by the

Anglo-Australian Planet Search program, the two other main experiments looking at the southern sky. The target sample of the CES includes 40 solar-type stars which it has been observing since 1992.

B.1.6 The Optical Gravitational Lensing Experiment

OGLE, a gravitational lensing program utilising the 1.3m Warsaw telescope at Las Campanas Observatory, Chile, belonging to the Carnegie Institution of Washington (Udalski et al., 2002a), (Udalski et al., 2002b), has been in operation for almost a decade with the goal of microlensing event detection via photometric monitoring of of millions of stars in the densest stellar regions of the sky. Following a CCD upgrade in 2001 a third phase of observations, OGLE-III, commenced in June of that year.

The system was used to monitor three regions of sky in the direction of the galactic core over the course of 45 days for photometric transits, and the most promising candidates were selected for followup studies. It was in this way that the transiting planet OGLE-TR-56b was discovered, the first detection by a method other than radial velocity surveys.

B.2 Future Missions

B.2.1 Kepler

The Kepler project is is significantly different from the majority of the current ground based detectors in that it's aim is to search out terrestrial-type planets, which for the purposes of their study the Kepler team have assumed to be planets with a mass $< 10M_{\oplus}$ (Koch et al., 1998). The main scientific objectives are to determine

the terrestrial planet abundance and the stellar and orbital characteristics of these systems, along with such fundamental planetary properties as albedo, mass and density. With such a range of requirements, only the transit method of detection could possibly be viable.

The main advantage of putting such a mission in space, apart from the obvious seeing advantages, is that Kepler can train itself on a single object for a long period of time and thus obtain an uninterrupted light curve, unlike equivalent ground-based experiments which suffer the constraints of a day-night cycle.

The Kepler photometer consists of a 0.95 meter aperture Schmidt telescope with an exceptionally large field of view of 105 square degrees. This enables an extremely large number of stars to be imaged simultaneously. In fact Kepler will monitor 160000 stars with magnitudes as faint as m_v=14. The system will theoretically provide the sensitivity in order to detect the transit of an Earth-sized planet across a 12th magnitude G2V (Sun-type) star with a precision of 4σ after 6.5 hours integration.

Kepler is part of NASA's Discovery series of missions and at the time of writing has only just received the go ahead. The current nominal launch date is October 2006.

B.2.2 COROT

COROT, the Convection, Rotation and planetary Transits mission is multi-purpose astroseismology and transit-based extrasolar planet detection project (Antonello and Ruiz, 2001). It was selected as part of the Small Mission Program of the French Space Agency, CNES and is seen as a precursor to the considerably more expensive Kepler mission, for although it cannot hope to compete in terms of resolution it has the advantage of being expected to enter service in 2004, at least a year ahead of

Kepler.

The two main goals of the program, astroseismology and planet detection share a single 27 cm telescope with the exoplanet program utilising two dedicated 2048x2048 CCDs cooled to -40°C (Léger et al., 2000) and providing a field of view of 3.5^{o2}.

The 2.5 year mission will allow for 5 separate fields of stars to be observed continuously for 150 days, each containing between 6000 to 12000 stars with m_v from 11 to 16.5. In order to achieve such a long observing duration on a fixed field the telescope will be in a polar inertial orbit (Baglin, 2000).

COROT, despite its limitations and small size will be the first of the new generation of space-based transit experiments. The photon-noise limited resolution is sufficient to detect planets down to around 1.5 times the radius of the Earth (Rouan et al., 1998). It may well therefore be the first experiment ever to detect the presence of a terrestrial-type planet outside the solar system.

B.2.3 Eddington

The Eddington project is a space-based astrometry mission with the dual purpose of the use of astroseismology in order to examine the evolution of stars and habitable-zone terrestrial-type extrasolar planet detection using the transit method (Favata, 2001). Currently Eddington is still in the design phase, so the final satellite configuration is subject to completion.

Eddington's large field of view allows high-resolution observation of a very large number of targets, with transits searched for on approximately 500,000 stars during the course of the 3 year mission (10^3 at V<18), whilst simultaneously returning lower resolution astroseismic data.

In addition to simple detection, Eddington is estimated to be sensitive enough to be able to records transit shapes and timings with sufficient accuracy to be able

to to predict the presence of planetary moons and possibly rings for relatively close and bright stars.

At the time of writing it has just been announced that Eddington has been cancelled by the ESA, although it remains to be seen as to whether the project will be reinstated in a revised form or at a later date.

B.2.4 GAIA

GAIA, the Global Astrometric Interferometer for Astrophysics is the recently approved selection for the ESA Astrophysics Cornerstone Mission, due to be launched in 2012 with a planned lifetime of 5 years (Lattanzi et al., 2002).

Seen as a successor to Hipparcos, the GAIA observatory is equipped to provide an extremely precise astrometric, photometric and radial velocity survey of the galaxy, accurately obtaining and classifying a three dimensional map of approximately one billion stars with both positions and motions (Gilmore et al., 2000). The astrometric precision is predicted to be as high as 10 microarcsec at V=15.

GAIA will continuously scan the sky, utilising two astrometric viewing detectors, each with an aperture of 1.7x0.7 m^2 measuring one-dimensional coordinates along great circles in two simultaneous fields of view separated by an angle of 106° (Perryman et al., 2001).

The detector consists of an array of 250 CCDs with an integration time of approximately 0.9s per CCD. In addition to the astrometric equipment is a radial velocity spectrometer with a telescope aperture of 0.75x0.7 m^2.

In order to provide a stable observing environment with the smallest amount of target occultations and thermal variations it was decided against placing GAIA in low earth orbit. Hence, GAIA is to be launched into a Lissajous orbit around the Earth-Sun Lagrange L2 point. In this position it will revolve on its axis at a rate of

120 arcsec s^{-1} with a precession period of 76 days.

B.2.5 Darwin

Darwin, an ESO Cornerstone mission and part of ESA's Horizons 2000 programme is currently in the early design stages and not due for launch until around 2015 (Penny, 2001). Darwin's goal during its five year lifespan is to search for terrestrial-type planets orbiting within the habitable zone of approximately 200 G, K and M stars up to 20 parsecs away. This procedure will be split into an initial 1-year imaging survey intended to seek out targets for the follow-up 4-year R=20 spectroscopy phase, with particular emphasis on detection of biological signatures such as oxygen and water.

Darwin consists of a fleet of 6 free-flying telescope satellites and a central light-combining hub operating in what is known as a Laurance Configuration acting as an interferometer system, with telescope-hub separations ranging from 20 to 200m. The technology employed by Darwin is by necessity extremely advanced. Precision formation of the individual telescope satellites is required to achieve 10^5 order nulling of the on axis star and a pointing accuracy of 24 mas. In addition, as the telescopes are operating in the infra-red, highly effective solar shields are employed to keep the optics temperature down to 40K, thereby keeping the thermal noise down to a minimum.

Darwin is intended to be launched into a L2 Lagrange halo orbit, the location of which has the double advantage of providing effective radiative cooling and avoiding Earth occultations (Nakagawa et al., 1998).

Appendix C

JIM Session Data

In this section I will describe the additional switches contained in the JIME input file over the original JIM, their purpose and usage. I shall be using for example a typical input file used to run the model for 6000 timesteps at at 0.1AU with a tidally locked planet. Only items commented are specific to JIME. Note that this is not the complete extent of the file but simply the beginning, the section in which the extended JIME switches are located.

```
/usr/people/scratch/adw/cm02-5/cm02-5-e
/usr/people/scratch/adw/cm01-5/cm01-5
cm01-5
ttftfftff
f
0.40
1.8988E+27
7.1398E+07
0.01     | Dfac - stellar flux dilution factor (effectively
         | distance)
1        | Cooling code? 1 = yes  0 = no
0        | Blank output files each timestep? 1 = yes 0 = no
         | This feature enable JIME to overwrite the previous
         | output, effectively allowing the model to run
         | indefinitely without taking up any more disk space
         | than a single timestep
```

```
0       | Output the average temperature at various latitudes
        | and pressure levels to a file for examination
0       | Outputs the contents of a number of important
        | variables such as number densities, temperature,
        | mixing ratios and solar input / H3+ cooling energy
        | balance. Output file can get VERY large so use with
        | caution.
0       | flatten average H3+ density per latitude.
        | Made Obsolete by the arcspring cleaning code.
0       | Read file containing modifications to ion densities.
        | Commented out so don't use.
0       | spring cleaning interval. Turned off by default as
        | made obsolete by arcspring cleaning code.
4       | how many spring cleaning iterations. This selects how
        | many times the (arc)spring cleaning code is looped
        | over. Odd numbers calculate the average and even
        | numbers use this value to compute the median used
        | in spring cleaning. The more loops the more
        | aggressive the smoothing, but be sure to use an
        |  even number.
10      | Calls arcspring cleaning code every x timesteps. Set
        | to 0 to turn the code off.
2       | Number of longitude cells to use for calculating the
        | median on either size of the current cell.
1       | ...and add on +1 and -1 latitude values?
1       | 1:smooth high values 2:low 3:both. This controls
        | whether spikes, holes or both are checked for.
1       | H3+ cooling exponential decay with pressure level;
        |  1=on 0=off
0       | Do we want temperature & ion density output? This
        | outputs a file with extension .numden allowing
        | average densities and temperatures to be followed.
-0.1    | h3+ exponential decay variable f1
9       | h3+ exponential decay variable f2
0       | attempt to fill in 2.5E-9 'dead' H3+ values.
        | Commented out in favour of simplified, permanently
        | active code. Don't use.
0       | Outputs electron lifetimes.
1       | Outputs major components of energy balance, solar EUV
        | and H3+ cooling, H+ and H3+ densities and neutral
        | density in formatted ASCII form for easy plotting.
1.0
200.0   | Rot period (dec hours) 200.0 = tidally locked.
10460.9
```

```
5.2
86.88
4.30E+05
9.40 159.90
-0.103 -0.059 0.003
7.1788E+07
180000  | No. of time steps per rotation period (integer)
2615
5.0 15.0 6.0 0.50
10000.0
1.875e12
2.0 5.0
7.0 15.0  2.0e6
1.0
1 1 0 0
17 -4
165.
f f  1
5
1 8 4.00 20.0E6
90
6
12
35.
2000.0
90.0
107001          | nnstrt=first iteration (time)
113001          | nnstop=last iteration (time)
100             | iwrite6=output freq. control unit 6
100             | iwrite2=output freq.control  unit 2 et al
1.3
600.,0.0,600.
```

Appendix D

Code Fragments

D.1 coolh3

```
 SUBROUTINE COOLH3(volel,t,den3d,np,
&IR,IRH2,l,m,nlong,nlat,xnion,Ps2,howcool,h3f1,h3f2,
&h3eng,h3ind,h2den)

 integer np,l,m,nlong,nlat,m2,howcool
 real xnion(4,np,nlat,nlong)
 real t(np,nlat,nlong)
 real den3d(np,nlat,nlong)
 real IR(np),IRH2(np)
 real numh2,numh3
 real h2lev, h3lev
 real tpres
 real pi
 real h31,h32,h33,h34,h35
 real h21,h22,h23,h24,h25
 real volel(nlat,nlong,np)
 real Ps2(np,nlat,nlong)
 real amu, n2a(np)
 real H3func,h3f1,h3f2
 real h3eng(nlat,nlong)
 real h3ind(np,nlat,nlong)
 real h2den(np,nlat,nlong)
```

```
Caw   Molecular weight of H2 (m2) = 2
      m2 = 2
      amu = 1.6605402E-27
      pi=3.141592654
      h3eng(m,l)=0

      do n=2, np-1

         numh3=volel(m,l,n)*xnion(3,n,m,l)
         tpres=t(n,m,l)

Caw      Energy output per element is
Caw      number of H3+ molecules per mesh volume
Caw      * fitted energy equation
Caw      * number of steradians
Caw      * conversion factor from ergs to Joules.
Caw      Done this long-winded way to check for errors
Caw      in the calculation.

         h31 = 1.42033e-13
         h32 = (tpres)*3.07162e-16
         h33 = (tpres**2)*2.31182e-19
         h34 = (tpres**2)*7.46270e-22
         h34 = h34 * tpres
         h35 = (tpres**2)*1.35837e-25
         h35 = tpres*h35
         h35 = tpres*h35

         h3lev=numh3*(h31-h32-h33+h34-h35)*4*pi*(1E-7)

Caw      Below is the cooling rate in
Caw      Joules/sec divided by the volume we are looking at
Caw      to get the cooling rate per unit volume. Then divide
Caw      by the neutral density to get the cooling rate per
Caw      unit mass.

         IR(n)=(h3lev/volel(m,l,n))/den3d(n,m,l)

Caw      The H3+ cooling modifier. H3+ cooling rate drops off
Caw      with decreasing pressure so that above pressure level
Caw      25, there is effectively no cooling. Variables h3f1
Caw      & h3f2 allow the shape of the drop off curve to be
Caw       modified.
```

```
   IF (howcool.eq.1) THEN
     IF (n.ge.10.and.n.le.30) THEN
       H3func = dexp(h3f1*(n-h3f2)) - dexp(-2.1)
       h3lev=h3lev*H3func
       IR(n)=IR(n)*H3func
     ENDIF
   ENDIF

   h3ind(n,m,l)=IR(n)
   h3eng(m,l)=h3eng(m,l)+h3lev
ENDDO
RETURN

END
```

D.2 springtimearc

```
Caw This is the spring cleaning code for averaging
Caw over an arc of longitude.
Caw Simplified version for presentation purposes.

      IF (sprtimearc.ne.0) THEN
      IF (nnloop.eq.nnstrt.OR.MOD((nnloop-nnstrt),
     &                          sprtimearc).eq.0) THEN
      write (*,*),'Arc Spring cleaning at timestep ',nnloop
       DO sprun=1,springruns
        DO dbpres=2,npres
 DO dblat=3,(nlat-2)
         numinsprav=0
  DO sprion=1,4
   oldsprav(sprion,dbpres,dblat)=springionav
     &                            (sprion,dbpres,dblat)
          springionav(sprion,dbpres,dblat)=0
         ENDDO
         DO sprion=1,4
          DO dblong=1,nlong

Caw Is this the first run through the loop? If so then
Caw get the values we're going to average over. A bit messy
Caw as in JIMworld 40 + 1 = 1!

           IF (MOD(sprun,2).ne.0) THEN
             arcav(sprion,dbpres,dblat,dblong)=0
             arcavruntot=0
             DO arcpos=(dblong-sprtimearcnum),
     &                 (dblong+sprtimearcnum),1
              IF (arcpos.gt.40) THEN
               arcposval = arcpos - 40
              ELSEIF (arcpos.lt.1) THEN
               arcposval = 40 + arcpos
              ELSE
               arcposval = arcpos
              ENDIF
              arcavruntot=arcavruntot+xnion(sprion,dbpres,
     &                                      dblat,arcposval)
              arcpostemp=arcpos-((dblong+sprtimearcnum)-
```

```
     &                            ((2*sprtimearcnum)+1))
              arcposvarr(arcpostemp)=xnion(sprion,dbpres,
     &                                    dblat,arcposval)
             ENDDO
             arcav(sprion,dbpres,dblat,dblong)=arcavruntot /
     &                              ((sprtimearcnum*2)+1)

Caw Add on the values for m+1 and m-1, above and below the
Caw current element. Controlled by the variable 'extramed'
Caw in the input file.

             IF (extramed.eq.1) THEN

              arcposvarr((sprtimearcnum*2)+2)=
     &         xnion(sprion,dbpres,(dblat+1),dblong)
              arcposvarr((sprtimearcnum*2)+3)=
     &         xnion(sprion,dbpres,(dblat-1),dblong)
             ENDIF

Caw Bubble sort routine to find the median

             IF (extramed.eq.1) THEN
              extramedval=3
             ELSE
              extramedval=1
             ENDIF
510    continue
             medorder=0
              DO medloop=1,((sprtimearcnum*2)+extramedval)
              IF (arcposvarr(medloop).gt.arcposvarr(medloop+1))
     &                                       THEN
               medcalctmp=arcposvarr(medloop)
               arcposvarr(medloop)=arcposvarr(medloop+1)
               arcposvarr(medloop+1)=medcalctmp
               medorder=1
              ENDIF
             ENDDO

             IF (medorder.eq.1) GOTO 510

Caw Now get the value one up from the median.

             IF (extramed.eq.1) THEN
              arcmedian(sprion,dbpres,dblat,dblong)=
```

```
     &         arcposvarr(sprtimearcnum+1)
               ELSE
                arcmedian(sprion,dbpres,dblat,dblong)=
     &         arcposvarr(sprtimearcnum+0)
               ENDIF

Caw  Check for bad median caused by 'dead h3+ cell'.
Caw  Primary H3+ hole killer before dedicated code brought
Caw  the problem under control.

               DO arcmedbad=(sprtimearcnum+1+extramed),
     &                (sprtimearcnum*2+1+(2*extramed))
                IF ((arcmedian(3,dbpres,dblat,dblong).le.(0.1E8))
     &          .AND.(arcposvarr(arcmedbad).ge.(0.1E8))) THEN
                 arcmedian(3,dbpres,dblat,dblong) =
     &                     arcposvarr(arcmedbad)
                 GOTO 520
                ELSE IF (arcmedian(3,dbpres,dblat,dblong).
     &                  gt.(0.1E8)) THEN
                 GOTO 520
                ELSE
                ENDIF
               ENDDO
520    continue

Caw Is the median in a H3+ hole? Then don't use it.

               IF (arcmedian(3,dbpres,dblat,dblong).le.(0.1E8))
     &         THEN
                badsmooth(dbpres,dblat,dblong)=1
               ELSE
                badsmooth(dbpres,dblat,dblong)=0
               ENDIF

Caw If the ion density is greater than twice the mean or less
Caw than 0.6 of the median then replace it with the median.

               IF (xnion(sprion,dbpres,dblat,dblong).gt.
     &            (2.0*arcmedian(sprion,dbpres,dblat,dblong)))
     &           THEN
                IF (badsmooth(dbpres,dblat,dblong).eq.0) THEN
                 IF (updown.eq.1.OR.updown.eq.3) THEN
                  xnion(sprion,dbpres,dblat,dblong) =
     &            arcmedian(sprion,dbpres,dblat,dblong)
```

```
          ENDIF
         ENDIF
        ELSEIF (xnion(sprion,dbpres,dblat,dblong).lt.
&          (0.6*arcmedian(sprion,dbpres,dblat,dblong)))
&         THEN
         IF (badsmooth(dbpres,dblat,dblong).eq.0) THEN
          IF (updown.eq.2.OR.updown.eq.3) THEN
           xnion(sprion,dbpres,dblat,dblong) =
&          arcmedian(sprion,dbpres,dblat,dblong)
          ENDIF
         ENDIF
        ENDIF
       ENDIF
      ENDDO
     ENDDO
    ENDDO
   ENDDO
  ENDDO
 ENDIF
 ENDIF
```

D.3 h3hole

```
Caw Simple routine that checks to see whether the
Caw time derivative of the H3+ number density is
Caw out of bounds due to ion bug and if so:
Caw If the dissociative recombination rate is less
Caw than 1% of the ion density (remembering there
Caw is a 4 second timestep) then set the new time
Caw derivative to be equal to the diss. recomb. rate.
Caw Otherwise set it to be equal to the ion density.

            IF (abs(h3pderiv).gt.(0.01*abs(xnion(kion,n,m,l)))
     &          .and.(h3pderiv.lt.0)) THEN
             IF (abs(dh3p(n,m,l)).lt.(abs(xnion(kion,n,m,l)
     &           *0.01))) THEN
              h3pderiv = dh3p(n,m,l)
             ELSE
              IF (dh3p(n,m,l).lt.0) THEN
               h3pderiv = -xnion(kion,n,m,l)*0.01
              ELSE
               h3pderiv = xnion(kion,n,m,l)*0.01
              ENDIF
             ENDIF
            ENDIF
```

Bibliography

Achilleos, N., Miller, S., Tennyson, J., Aylward, A., Mueller-Wodarg, I., and Rees, D. (1998). JIM: A Time-Dependent, Three-Dimensional Model of Jupiter's Thermosphere and Ionosphere. *J. Geophys. Res.*, 103(E9):20089.

Agnor, C. B. and Ward, W. R. (2000). Secular Resonant Damping of Planetary Eccentricities. In *31st Annual Lunar and Planetary Science Conference.*

Angel, J. R. P. and Woolf, N. J. (1997). An Imaging Nulling Interferometer to Study Extrasolar Planets. *Astrophys. J.*, 475:373.

Antonello, E. and Ruiz, S. (2001). The COROT Mission. In *Multifrequency Behaviour of High Energy Cosmic Sources*, Proceed. of Frascati Workshop 2001, Vulcano, May 21-26. Mem. Soc. Astr. Ital.

Bagenal, F. (1992). Jupiter's Magnetosphere. *Ann. Rev. Earth Pl. Sci.*, 20:289.

Baglin, A. (2000). COROT: A Minisat for Pioneer Science, Asteroseismology and Planets Finding. *Adv. Space. Res.*, 31:345–349.

Baraffe, I., Chabrier, G., Barman, T. S., Allard, F., and Hauschildt, P. H. (2003). Evolutionary Models for Cool Brown Dwarfs and Extrasolar Giant Planets. The Case of HD 209458. *A&A*, 402:701–712.

Baranne, A., Queloz, D., Mayor, M., Adrianzyk, G., Gnispel, G., Kohler, D., Lacroix, D., Meunier, J.-P., Rimbaud, G., and Vin, A. (1996). ELODIE: A Spectrograph for Accurate Radial Velocity Measurements. *A&A*, 119:373.

Barman, T. S., Hauschildt, P. H., and Allard, F. (2001). Irradiated Planets. *Astrophys. J.*, 556:885–895.

Bate, M. R., Lubow, S. H., Ogilvie, G. I., and Miller, K. A. (2003). Three-dimensional calculations of high- and low-mass planets emb edded in protoplanetary discs. *Mon. Not. R. Astro. Soc.*, 341:213–229.

Baumjohann, W. and Treumann, R. A. (1997). *Basic Space Plasma Physics.* Imperial College Press.

Beckers, J. M. (1993). Adaptive Optics for Astronomy: Principles, Performance and Applications. *Ann. Rev. A&A*, 31:13.

Benz, W., Mayor, M., Udry, S., Bertaux, J.-L., Schmitt, J., Bouchy, F., Naef, D., and Renvoizé, V. (1999). HARPS - Scientific Proposal. Technical report, Observatoire de Genéve, 51, Ch. des Maillettes, CH-1290 Sauverny, Switzerland.

Bodenheimer, P., Lin, D. N. C., and Mardling, R. A. (2001). On the Tidal Inflation of Short-Period Extrasolar Planets. *Astrophys. J.*, 548:466–472.

Boss, A. P. (1997). Giant Planet Formation by Gravitational Instability. *Science*, 276:1836–2839.

Boss, A. P. (1998). Formation of Extrasolar Giant Planets: Core Accretion or Disk Instability? *Earth, Moon & Planets*, 81:19–26.

Boss, A. P. (2002). Formation of Gas and Ice Giant Planets. *Earth Planet Sci. Lett.*, 202:513–523.

Bouchy, F. and Carrier, F. (2001). P-mode Observations on α Cen A. *A&A*, 374:L5.

Briceno, C., Vivas, A. K., Calvet, N., Hartmann, L., Pacheco, R., Herrera, D., Romero, L., Berlind, P., Sánchez, G., Snyder, J. A., and Andrews, P. (2001). The CIDA-QUEST Large-Scale Survey of Orion OB1: Evidence for Rapid Disk Dissipation in a Dispersed Stellar Population. *Science*, 291:93–96.

Brown, T., Noyes, R., Nisenson, P., Korzennik, S., and Horner, S. (1994). The AFOE: A Spectrograph for Precise Doppler Studies. *Pub. Astron. Soc. Pas.*, 106:1285.

Burrows, A., Guillot, T., Hubbard, W. B., Marley, M. S., Saumon, D., Lunine, J. I., and Sudarsky, D. (2000). On the Radii of Close-in Giant Planets. *Astrophys. J.*, 534:L97–L100.

Butler, R., Tinney, C., Marcy, G., Jones, H., Penny, A., and Apps, K. (2001). Two New Planets from the Anglo-Australian Planet Search. *Astrophys. J.*, 555:410.

Butler, R. P., Vogt, S. S., Marcy, G. W., Fischer, D. A., Henry, G. W., and Apps, K. (2000). Planetary Companions to the Metal-Rich Stars BD - 10°3166 and HD 52265. *Astrophys. J.*, 545:504–511.

Cardin, P., Brito, D., Jault, D., Nataf, H.-C., and Masson, J.-P. (2002). Towards a Rapidly Rotating Liquid Sodium Dynamo Experiment. *Magnetohydrodynamics*, 38:177–189.

Chamberlain, J. W. (1978). *Theory of Planetary Atmospheres, An Introduction to Their Physics and Chemistry*, volume 22 of *International Geophysics Series*. Academic Press.

Charbonneau, D., Brown, T. M., Latham, D. W., and Mayor, M. (2000). Detection of Planetary Transits Across A Sun-Like Star. *Astrophys. J.*, 529:L45–L48.

Chiang, E. I., Fischer, D., and Thommes, E. (2002). Excitation of Orbital Eccentricities of Extrasolar Planets by Repeated Resonance Crossings. *Astrophys. J.*, 564:L105–L109.

Collins, G. W. (1991). *Fundamentals of Stellar Astrophysics.* W. H. Freeman & Co.

Cowley, S. W. H. and Bunce, E. J. (2001). Origin of the Main Auroral Oval in Jupiter's Coupled Magnetosphere-Ionosphere System. *Planet Space Sci.*, 49:1067–1088.

Cumming, A., Marcy, G. W., and Butler, R. P. (1999). The Lick Planet Search: Detectability and Mass Thresholds. *Astrophys. J.*, 526:890.

Deeg, H.-J. (1998). Photometric Detection of Extrasolar Planets by the Transit Method. In *Brown Dwarfs and Extrasolar Planets, Proceedings of a Workshop held in Puerto de la Cruz, Tenerife, Spain, 17-21 March 1997*, volume 134 of *ASP Conference Series*, page 216.

Dinelli, B. M., Miller, S., and Tennyson, J. (1992). Bands of H_3^+ up to $4v_2$: Rovibrational Transitions From First Principles Calculations. *J. Mol. Spec.*, 153:718–725.

Drossart, P., Maillard, J.-P., Caldwell, J., Kim, S. J., Watson, J. K. G., Majewski, W. A., Tennyson, J., Miller, S., Atreya, S. K., Waite, J. T., and Wagener, R. (1989). Detection of H_3^+ on Jupiter. *Nature*, 340:539–541.

Endl, M., Els, M. K. S., Hatzes, A., and Cochran, W. (2001). The Planet Search Program at the ESO Coudé Echelle Spectrometer: I I. The α Centauri System: Limits for Planetary Companions. *A&A*, 374:675.

Exell, R. H. B. (2001). Atmospheric Boundary Layer Science. http://www.jgsee.kmutt.ac.th/exell/JEE661/JEE661Lecture4.html.

Farrell, B. (2002). Introduction to Meteorology. http://icg.harvard.edu/ eps132/lecture.dir/lecture4a/notes.html.

Favata, F. (2001). The Eddington Mission. In *4th Annual ROE Workshop*, Occasional Reports of the Royal Observatory Edinburgh.

Ford, E. B., Havlickova, M., and Rasio, F. A. (2001). Dynamical Instabilities in Extrasolar Planetary Systems Containing Two Giant Planets. *Icarus*, 150:303–313.

Fuller-Rowell, T. J. (1982). *A Three Dimensional, Time Dependent, Global Model of the Thermosphere.* PhD thesis, University College London.

Fuller-Rowell, T. J. and Rees, D. (1980). A Three-Dimensional, Time-Dependent, Global Model of the Thermosphere. *J. Atmos. Sci.*, 37:2545–2567.

Geballe, T. R., Jagod, M.-F., and Oka, T. (1993). Detection of H_3^+ Emission Lines in Saturn. *Astrophys. J.*, 408:L109–L112.

Giampapa, M. S., Craine, E. R., and Hott, D. A. (1995). Comments on the Photometric Method for the Detection of Extrasolar Planets. *Icarus*, 118:199.

Gilmore, G., de Boer, K., Favata, F., g, E. H., Lattanzi, M., Lindegren, L., Luri, X., Mignard, F., Perryman, M., and de Zeeuw, P. (2000). GAIA: Origin and Evolution of the Milky Way. In *UV, Optical, and IR Space Telescopes and Instruments*, volume 4013 of *Proceedings of the International Society for Optical Engineering*, page 453.

Goldreich, P. and Sari, R. (2003). Eccentricity Evolution for Planets in Gaseous Disks. *Astrophys. J.*, 585:1024–1037.

Goldreich, P. and Tremaine, S. (1980). Disk-Satellite Interactions. *Astrophys. J.*, 241:425–441.

Gonzalez, G., Laws, C., Tyagi, S., and Reddy, B. E. (2001). Parent Stars of Extrasolar Planets, VI. Abundance Analyses of 20 New Systems. *Astron. J.*, 121:432–452.

Gould, A. (2000). A Natural Formalism for Microlensing. *Astrophys. J.*, 542:785.

Gould, A. (2001). Applications of Microlensing to Stellar Astrophysics. *Pub. Astron. Soc. Pas.*, 113:903.

Greenberg, R., Hartmann, W. K., Chapman, C. R., and Wacker, J. F. (1978). Planetesimals to Planets - Numerical Simulation of Collisional Evolution. *Icarus*, 35:1–26.

Guillot, T., Burrows, A., Hubbard, W. B., Lunine, J. I., and Saumon, D. (1996). Giant Planets at Small Orbital Distances. *Astrophys. J.*, 459:L35–L38.

Guillot, T., Gautier, D., and Hubbard, W. B. (1997). New Constraints on the Composition of Jupiter from Galileo Measurements and Interior Models. *Icarus*, 130:534–539.

Guillot, T. and Showman, A. P. (2002). Evolution of '51 Pegasus b-like' Planets. *A&A*, 385:156–165.

Han, C. and Kang, Y. W. (2003). Probing the Spatial Distribution of Extrasolar Planets with Gravitational Microlensing. *Astrophys. J.*, 596:1320–1326.

Hanson, W. B. and Moffett, R. J. (1966). Ionization Transport Effects in the Equatorial F Region. *J. Geophys. Res.*, 71:5559.

Herbst, E. and Klemperer, W. (1973). The Formation and Depletion of Molecules in Dense Interstellar Clouds. *Astrophys. J.*, 185:505–533.

Hinz, P. H., Angel, J. R. P., Hoffmann, W. F., McCarthy, D. W., McGuire, P. C., Cheselka, M., Hora, J. L., and Woolf, N. J. (1998). Imaging Circumstellar Environments with a Nulling Interferometer. *Nature*, 395:251.

Hollas, J. M. (1987). *Modern Spectroscopy.* John Wiley.

Houghton, J. T. (2002). *The Physics of Atmospheres.* Cambridge University Press.

Howell, S., Everett, M., Esquerdo, G., Davis, D., Weidenschilling, S., Lew, T. V., and Foxley, A. (1999). Photometric Search for Extra-Solar Planets. In *Precision CCD Photometry*, volume 189 of *ASP Conference Series*, page 170.

Kim, Y. H., Fox, J. L., and Porter, H. S. (1992). Densities and Vibrational Distribution of H_3^+ in the Jovian Auroral Ionosphere. *J. Geophys. Res.*, 97:6093–6101.

Koch, D., Borucki, W., Webster, L., Dunham, E., Jenkins, J., Marriott, J., and Reitsema, H. (1998). Kepler: A Space Mission to Detect Earth-Class Exoplanets. In *Space Telescopes and Instruments V*, volume 3356 of *Proceedings of the International Society for Optical Engineering*, page 599.

Konacki, M., Torres, G., Jha, S., and Sasselov, D. D. (2003). An Extrasolar Planet that Transits the Disk of its Parent Star. *Nature*, 421:507–509.

Kuchner, M. J. and Lecar, M. (2002). Halting Planetary Migration in the Evacuated Centers of Protoplanetary Disks. *Astrophys. J.*, 574:L87–L89.

Lammer, H., Selsis, F., Ribas, I., Guinan, E. F., Bauer, S. J., and Weiss, W. W. (2003a). Atmospheric Loss of Exoplanets Resulting from XUV Heating. *Astrophys. J.*, submitted.

Lammer, H., Selsis, F., Ribas, I., Guinan, E. F., Bauer, S. J., and Weiss, W. W. (2003b). Hydrodynamic Escape of Exoplanetary Atmospheres. In *Proceedings of the 2nd Eddington Workshop 'Stellar Structure and Habitable Planet Finding', Palermo, 9-11 April 2003.* ESA Publications Division.

Lattanzi, M., Casertano, S., Sozzetti, A., and Spagna, A. (2002). The GAIA Astrometric Survey of Extra-Solar Planets. In *Proceedings of the Summer School, GAIA: a European Space Project*, Journal de Physique IV. EDP Sciences.

Lee, M. H. and Peale, S. J. (2002). Dynamics and Origin of the 2:1 Orbital Resonances of the GJ 876 Planets. *Astrophys. J.*, 567:596–609.

Léger, A., Baglin, A., Barge, P., Bordé, P., Defay, C., Deleuil, M., Rouan, D., Schneider, J., and Vuillemin, A. (2000). Detecting Earth-Uranus Class Planets with the Space Mission COROT. In *Observation, Formation and Evolution*, Proceedings of the IAU Symposium 202, Manchester aug 2000.

Levison, H. F. and Stewart, G. R. (2001). Remarks on Modelling the Formation of Uranus and Neptune. *Icarus*, 153:224–228.

Lin, D. N. C. and Papaloizou, J. (1986). On the Tidal Interaction between Protoplanets and the Protoplanetary Disk. III. Orbital Migration of Protoplanets. *Astrophys. J.*, 309:846–857.

Lui, L. and Wan, W. (2001). The Evolution of Equatorial Trough of Ionospheric F-Region Ionization. *TAO*, 12:559–565.

Lynden-Bell, D. and Pringle, J. E. (1974). The Evolution of Viscous Discs and the Origin of the Nebular Variables. *Mon. Not. R. Astro. Soc.*, 168:603–637.

Mao, S. and Paczyński, B. (1991). Gravitational Microlensing by Double Stars and Planetary Systems. *Astrophys. J.*, 374:L37–L40.

Markwardt, C. (2002). IDL Curve Fitting and Function Optimization. http://cow.physics.wisc.edu/ craigm/idl/fitting.html.

Matsuyama, I., Johnstone, D., and Murray, N. (2003). Halting Planet Migration by Photoevaporation from the Central Source. *Astrophys. J.*, 585:L143–L146.

Mayor, M. and Queloz, D. (1995). A Jupiter-Mass Companion to a Solar-Type Star. *Nature*, 378:355.

Mazeh, T., Naef, D., Torres, G., Latham, D. W., Mayor, M., Beuzit, J.-L., Brown, T. M., Buchhave, L., Burnet, M., Carney, B. W., Charbonneau, D., Drukier, G. A., Laird, J. B., Pepe, F., Perrier, C., Queloz, D., Santos, N. C., Sivan, J.-P., Udry, S., and Zucker, S. (2000). The Spectroscopic Orbit of the Planetary Companion Transiting HD 209458. *Astrophys. J.*, 532:L55–L58.

McCall, B. J. (2000). Laboratory Spectroscopy of H_3^+. *Phil. Trans. R. Soc. Lond.*, A358:2385–2401.

McCall, B. J., Geballe, T. R., Hinkle, K. H., and Oka, T. (1999). Observations of H_3^+ in Dense Molecular Clouds. *Astrophys. J.*, 522:338–348.

Mennesson, B. and Mariotti, J. M. (1997). Array Configurations for a Space Infrared Nulling Interferometer Dedicated to the Search for Earthlike Extrasolar Planets. *Icarus*, 128:202.

Miller, S., Achilleos, N., Ballester, G. E., Geballe, T. R., Joseph, R. D., Prangé, R., Rego, D., Stallard, T., Tennyson, J., Trafton, L. M., and Waite, J. H. (2000). The Role of H_3^+ in Planetary Atmospheres. *Phil. Trans. R. Soc. Lond.*, 385:2485–2502.

Miller, S., Achilleos, N., Ballester, G. E., Lam, H. A., Tennyson, J., Geballe, T. R., and Trafton, L. M. (1997). Mid-to-Low Latitude H_3^+ Emission from Jupiter. *Icarus*, 130:57–67.

Mitchell, J. B. A., Ng, C. T., Levac, D. P., Mitchell, R. E., Mul, P. M., Claeys, W., Sen, A., and McGowan, J. W. (1983). Measurement of the Branching Ratio for the Dissociative Recombination of H_3^+ + e. *Phys. Rev. Lett.*, 51:885–888.

Mizuno, H. (1980). Formation of the Giant Planets. *Prog. Theo. Phys.*, 64:544–557.

Moore, L., Mendillo, M., Muller-Wodarg, I., and Murr, D. (2003). Photochemical Modeling of Global Variations and Ring Shadowing in Saturn's Ionosphere. *Icarus, in press.*

Murray, N. and Chaboyer, B. (2002). Are Stars with Planets Polluted? *Astrophys. J.*, 566:442–451.

Nakagawa, T., Hayashi, M., Kawada, M., Matsuhara, H., Matsumoto, T., Murakami, H., Okuda, H., Onaka, T., Shibai, H., and Ueno, M. (1998). HII/L2 Mission: Future Japanese Infrared Astronomical Mission. In *Space Telescopes and Instruments V*, volume 3356 of *Proceedings of the International Society for Optical Engineering*, page 462.

O'Byrne, J. (1996). Sharper Eyes on the Sky. *Sky & Space*, December:20.

Oka, T. (1980). Observation of the Infrared Spectrum of H_3^+. *Phys. Rev. Lett.*, 45:531–534.

Oka, T. (1981). A Search for Insterstellar H_3^+. *Phil. Trans. R. Soc. Lond.*, A303:543–549.

Oka, T. (2000). Introductory Remarks. *Phil. Trans. R. Soc. Lond.*, A358:2363–2369.

Oka, T. and Geballe, T. R. (1990). Observations of the 4 Micron Fundamental Band of H_3^+ in Juipter. *Astrophys. J.*, 351:L53–L56.

Paczyński, B. (1996). Gravitational Microlensing in the Local Group. *Ann. Rev. A&A*, 34:419–459.

Pan, F. and Oka, T. (1986). Calculated Forbidden Rotational Spectra of H_3^+. *Astrophys. J.*, 305:518–525.

Penny, A. (2001). Darwin and the UK - How UK Academia Could Get Involved. In *4th Annual ROE Workshop*, Occasional Reports of the Royal Observatory Edinburgh.

Perryman, M., de Boer, K., Gilmore, G., Hog, E., Lattanzi, M., Lindegren, L., Luri, X., Mignard, F., Pace, O., and de Zeeuw, P. (2001). GAIA: Composition, Formation and Evolution of the Galaxy. *A&A*, 369:339.

Perryman, M. A. C. (2000). Extra-solar Planets. *Rep. Prog. Phys.*, 63:1209.

Peters, B. (2001). A Martian Thermosphere/Ionosphere Global Circulation Model. Master's thesis, University College London.

Pollack, J. B., Hubickyj, O., Bodenheimer, P., Lissauer, J. J., Podolak, M., and Greenzweig, Y. (1996). Formation of the Giant Planets by Concurrent Accretion of Solids and Gas. *Icarus*, 124:62–85.

Pravdo, S. H. and Shaklan, S. B. (1996). Astrometric Detection of Extrasolar Planets: Results of a Feasibility Study with the Palomar 5 Meter Telescope. *Astrophys. J.*, 465:264.

Quegan, S., Bailey, G. J., Moffett, R. J., Heelis, R. A., Fuller-Rowell, T. J., Rees, D., and Spiro, R. W. (1982). A Theoretical Study of the Dirstribution of Ionization in the High-Latitude Ionosphere and the Plasmasphere - First Results on the Mid-Latitude Trough and the Light-Ion Trough. *J. Atmos. Ter. Phys.*, 44:619–640.

Queloz, D., Mayor, M., Weber, L., Blécha, A., Burnet, M., Confino, D., Naef, D., Pepe, F., Santos, N., and Udry, S. (2000). The CORALIE Survey for Southern Extra-Solar Planets I. A Planet Orbiting the Star Gliese 86. *A&A*, 354:99.

Rego, D., Miller, S., Achilleos, N., Prangé, R., and Joseph, R. D. (2000). Latitudinal Profiles of the Jovian IR Emissions of H_3^+ at 4 μm with the NASA Infrared Telescope Facility: Energy Inputs and Thermal Balance. *Icarus*, 147:366–385.

Rishbeth, H. (1972). Thermospheric Winds and the F-Region: A Review. *J. Atmos. Ter. Phys.*, 34:1–47.

Rouan, D., Baglin, A., Copet, E., Schneider, J., Barge, P., Deleuil, M., Vuillemin, A., and Léger, A. (1998). The Extrasolar Planets Program of the COROT Satellite. *Earth, Moon & Planets*, 81:79.

Sambou, E., Vila, P. M., and Kobea, A. T. (1998). Non-Trough foF2 Enhancements at Near-Equatorial Dip Latitudes. *Ann. Geophysicae.*, 16:711–720.

Sandquist, E. L., Dokter, J. J., Lin, D. N. C., and Mardling, R. A. (2002). A Critical Examination of Li Pollution and Giant Planet Consumption by a Host Star. *Astrophys. J.*, 572:1012–1023.

Santos, N. C., Israelian, G., and Mayor, M. (2000). Chemical Analysis of 8 Recently Discovered Extra-Solar Planet Host Stars. *A&A*, 363:228–238.

Santos, N. C., Israelian, G., Mayor, M., Rebolo, R., and Udry, S. (2003). Statistical Properties of Exoplanets II. Metallicity, Orbital Parameters and Space Velocities. *A&A*, 398:363–376.

Sasaki, S. (1989). Gas Capture of Outer Jovian Planets - Critical Mass for Core Instability. *Abs. Lunar Plan. Sci. Conf.*, 20:944–945.

Sasselov, S. D. (2003). The New Transiting Planet OGLE-TR-56b: Orbit and Atmosphere. *Astrophys. J.*, submitted.

Satoh, T. and Connerney, J. E. P. (1999). Jupiter's H_3^+ Emissions Viewed in Corrected Jovimagnetic Coordinates. *Icarus*, 141:236–252.

Schneider, J. (1999). Les Planètes Extrasolaires: Méthodes de détection, premières découvertes et perpectives futures. Serie IIb, n. 6, page 621. C. R. Acad. Sci. Paris.

Seiff, A., Kirk, D. B., Knight, T. C. D., Young, L. A., Milos, F. S., Venkatapathy, E., Mihalov, J. D., Blanchard, R. C., Young, R. E., and Schubert, G. (1997). Thermal Structure of Jupiter's Upper Atmosphere Derived from the Galileo Probe. *Science*, 276:102–104.

Shakura, N. I. and Sunyaev, R. A. (1973). Black Holes in Binary Systems. Observational Appearance. *A&A*, 24:337–355.

Showman, A. P. and Guillot, T. (2002). Atmospheric Circulation and Tides of '51 Pegasus b-like' Planets. *A&A*, 385:166–180.

Smoluchowski, R. (1971). Metallic Interiors and Magnetic Fields of Jupiter and Saturn. *Astrophys. J.*, 166:435–439.

Spiro, R. W., Heelis, R. A., and Hanson, W. B. (1978). Ion convection and the formation of the mid-latitude F region ionization trough. *J. Geophys. Res.*, 83:4255–4264.

Takeuchi, T., Miyama, S. M., and Lin, D. N. C. (1996). Gap Formation in Protoplanetary Disks. *Astrophys. J.*, 460:832–847.

Tanaka, H., Takeuchi, T., and Ward, W. R. (2002). Three-Dimensional Interaction Between a Planet and an Isothermal Gaseous Disk. I. Corotation and Lindblad Torques and Planet Migration. *Astrophys. J.*, 565:1257–1274.

Terquem, C. E. J. M. L. J. (2003). Stopping Inward Planetary Migration by a Toroidal Magnetic Field. *Mon. Not. R. Astro. Soc.*, accepted.

Thommes, E. W., Duncan, M. J., and Levison, H. F. (1999). The Formation of Uranus and Neptune in the Jupiter-Saturn Region of the Solar System. *Nature*, 402:635–638.

Thommes, E. W. and Lissauer, J. J. (2002). Planet Migration. In *Proceedings of STSci Astrophysics of Life symposium.* Not yet published.

Trafton, L. M., Geballe, T. R., Miller, S., Tennyson, J., and Ballester, G. E. (1993). Detection of H_3^+ from Uranus. *Astrophys. J.*, 405:761–766.

Trilling, D. E., Benz, W., Guillot, T., Lunine, J. I., Hubbard, W. B., and Burrows, A. (1998). Orbital Evolution and Migration of Giant Planets: Modelling Extrasolar Planets. *Astrophys. J.*, 500:428–439.

Udalski, A., Paczyński, B., Żebruń, K., Szymański, M., Kubiak, M., Soszyński, I., Szewczyk, O., Wyrzykowski, L., and Pietrzyński, G. (2002a). The Optical Gravitational Lensing Experiment. Search for Planetary and Low-Luminosity Object Transits in the Galactic Disk. Results of 2001 Campaign. *Acta Astronomica*, 52:1–37.

Udalski, A., Żebruń, K., Szymański, M., Kubiak, M., Soszyński, I., Szewczyk, O., Wyrzykowski, L., and Pietrzyński, G. (2002b). The Optical Gravitational Lensing Experiment. Search for Planetary and Low-Luminosity Object Transits in the Galactic Disk. Results of 2001 Campaign - Supplement. *Acta Astronomica*, 52:115–128.

Vidal-Madjar, A., des Etangs, A. L., Désert, J.-M., Ballester, G. E., Ferlet, R., Hébrard, G., and Mayor, M. (2003). An Extended Upper Atmosphere Around the Extrasolar Planet HD209458b. *Nature*, 422:143–146.

Vogt, S., Marcy, G., Butler, R., and Apps, K. (2000). Six New Planets from the Keck Precision Velocity Survey. *Astrophys. J.*, 536:902.

Wambsganss, J. (1997). Discovering Galactic Planets by Gravitational Microlensing: Magnification Patterns and Light Curves. *Mon. Not. R. Astro. Soc.*, 284:172–188.

Ward, W. R. (1997a). Protoplanet Migration by Nebula Tides. *Icarus*, 126:261–281.

Ward, W. R. (1997b). Survival of Planetary Systems. *Astrophys. J.*, 482:L211–L214.

Ward, W. R. and Hahn, J. M. (2000). Disk-Planet Interactions and the Formation of Planetary Systems. In *Protostars and Planets IV*, page 1135. University of Arizona Press.

Wetherill, G. W. (1990). Formation of the Earth. *Ann. Rev. Earth Pl. Sci.*, 18:205–256.

Winters, W. F., Balbus, S. A., and Hawley, J. F. (2003). Gap Formation by Planets in Turbulent Protostellar Disks. *Astrophys. J.*, 589:543–555.

Witte, M. G. and Savonije, G. J. (2002). Orbital Evolution by Dynamical Tides in Solar Type Stars. Application to Binary Stars and Planetary Orbits. *A&A*, 386:222–236.

Wolszczan, A. and Frail, D. A. (1992). A Planetary System Around the Millisecond Pulsar PSR1257 + 12. *Nature*, 355:145–147.

Yano, J.-I., Talagrand, O., and Drossart, P. (2003). Origin of Atmospheric Zonal Winds. *Nature*, 421:36.

Yelle, R. V. (2004). Aeronomy of Extra-Solar Giant Planets at Small Orbital Distances. *Icarus*, 170:167–179.

Yelle, R. V. and Miller, S. (2004). Jupiter's Thermosphere and Ionosphere. In *Jupiter*. Cambridge University Press.

Yildiz, M. (2003). Modeling Dissimilar Components of the Eclipsing Binary EK Cep: Does the Primary Star Have a Rapidly Rotating Core? *A&A*, 409:689–695.